

**Aero-structural Design and Optimisation of Tethered Composite Wings
Computational Methods for Initial Design of Airborne Wind Energy Systems**

Candade, A.A.

DOI

[10.4233/uuid:c706c198-d186-4297-8b03-32c80be1c6df](https://doi.org/10.4233/uuid:c706c198-d186-4297-8b03-32c80be1c6df)

Publication date

2023

Document Version

Final published version

Citation (APA)

Candade, A. A. (2023). *Aero-structural Design and Optimisation of Tethered Composite Wings: Computational Methods for Initial Design of Airborne Wind Energy Systems*. [Dissertation (TU Delft), Delft University of Technology]. <https://doi.org/10.4233/uuid:c706c198-d186-4297-8b03-32c80be1c6df>

Important note

To cite this publication, please use the final published version (if applicable).
Please check the document version above.

Copyright

Other than for strictly personal use, it is not permitted to download, forward or distribute the text or part of it, without the consent of the author(s) and/or copyright holder(s), unless the work is under an open content license such as Creative Commons.

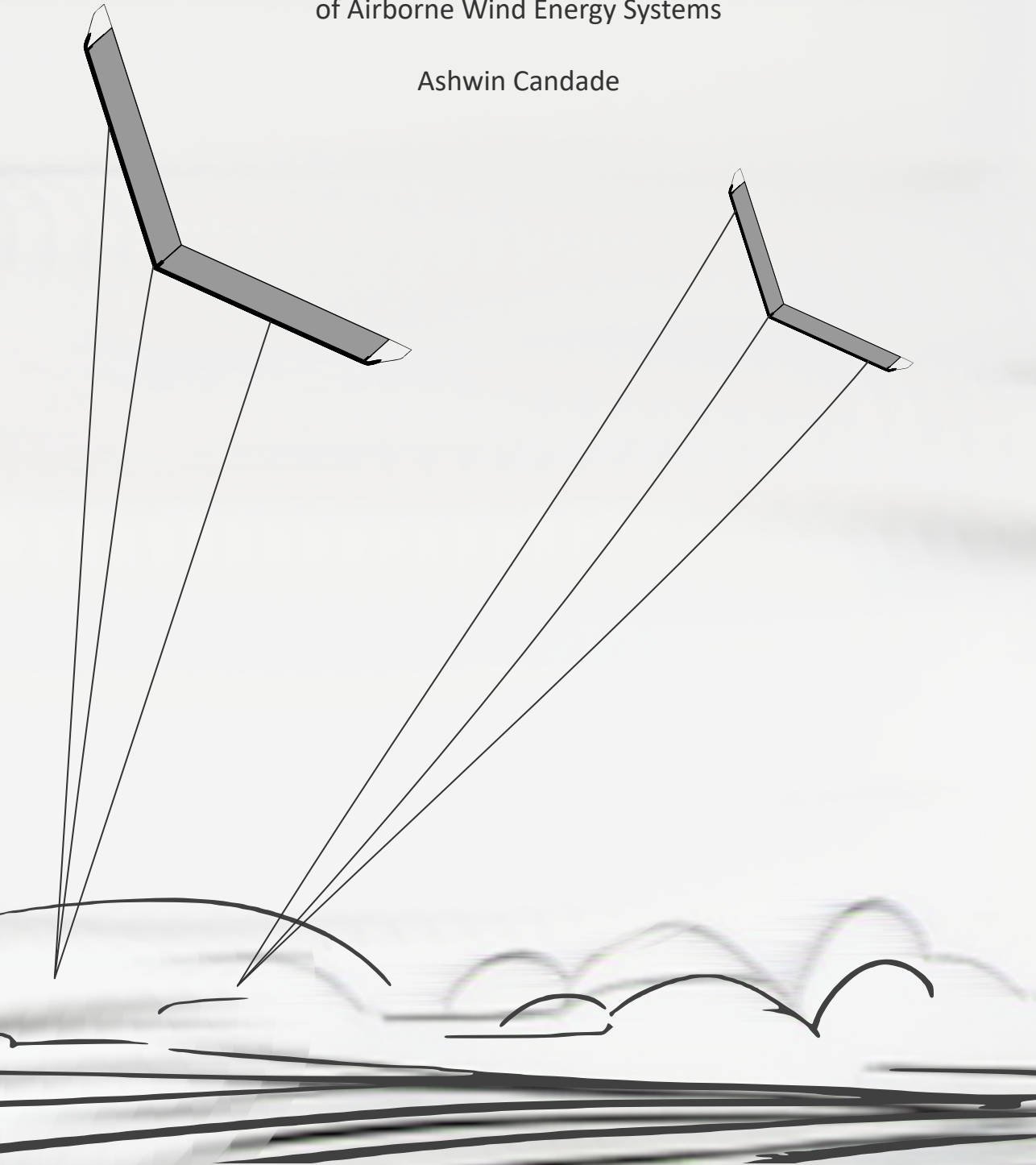
Takedown policy

Please contact us and provide details if you believe this document breaches copyrights.
We will remove access to the work immediately and investigate your claim.

Aero-structural Design and Optimisation of Tethered Composite Wings

Computational Methods for Initial Design
of Airborne Wind Energy Systems

Ashwin Candade



Aero-structural Design and Optimisation of Tethered Composite Wings

Computational Methods for Initial Design
of Airborne Wind Energy Systems

Ashwin Candade

Aero-structural Design and Optimisation of Tethered Composite Wings

Computational Methods for Initial Design
of Airborne Wind Energy Systems

Proefschrift

ter verkrijging van de graad van doctor
aan de Technische Universiteit Delft,
op gezag van de Rector Magnificus prof. dr. ir. T.H.J.J. van der Hagen,
voorzitter van het College voor Promoties,
in het openbaar te verdedigen
op woensdag 6 december 2023 om 10.00 uur

door

Ashwin CANDADE

Ingenieur in de Luchtvaart- en Ruimte,
Technische Universiteit Delft, Nederland,
geboren te Chennai, India.

Dit proefschrift is goedgekeurd door de promotoren.

Samenstelling promotiecommissie bestaat uit:

Rector Magnificus,	voorzitter
Prof. dr. G.J.W. van Bussel,	Technische Universiteit Delft, promotor
Dr.-Ing. Roland Schmehl,	Technische Universiteit Delft, promotor

Onafhankelijke leden:

Prof. dr. ir. Rinze Benedictus,	Technische Universiteit Delft
Prof. dr. ir. Joris Degroote,	Universiteit Gent
Dr. Paolo Tiso,	Eidgenössische Technische Hochschule Zürich
Dr.-Ing. Markus Kleineberg,	Deutsches Zentrum für Luft- und Raumfahrt
Dr. ir. Roeland De Breuker,	Technische Universiteit Delft
Prof. dr. ir. C.J.Simão Ferreira,	Technische Universiteit Delft, reservelid



EnerKite



This research has been supported financially by the project AWESCO (H2020-ITN-642682), funded by the European Union's Horizon 2020 research and innovation program under the Marie Skłodowska-Curie grant agreement No. 642682.

Keywords: AWE, Initial Design Methods, Composite Structures, Aeroelasticity

Printed by: Koninklijke Rijnsja

Front & Back: DeaYayPea

Copyright © 2023 by A. Candade
ISBN 978-94-6384-508-3

An electronic version of this dissertation is available at
<https://repository.tudelft.nl>.

*He took his vorpal sword in hand:
Long time the manxome foe he sought—
So rested he by the Tumtum tree,
And stood awhile in thought.*

– Lewis Carroll

Propositions

accompanying the dissertation

AERO-STRUCTURAL DESIGN AND OPTIMISATION OF TETHERED COMPOSITE WINGS

COMPUTATIONAL METHODS FOR INITIAL DESIGN
OF AIRBORNE WIND ENERGY SYSTEMS

by

Ashwin CANDADE

1. Composite topology optimisation devoid of manufacturing constraints is a wild goose chase for real world applications (this thesis).
2. Semi-rigid bridled wing's true potential will be significantly amplified when scaling airborne wind to utility scale systems (this thesis).
3. When considering the Pareto principle for mass minimisation of semi-rigid wings, the bridle subsystem design is the 20% that achieves 80% of the goal (this thesis).
4. An optimal AWES design first requires a consensus on an ideal AWES business case (this thesis).
5. Industrial PhDs are analogous to semi-rigid pumping AWE systems.
6. Implementing simulation/optimisation frameworks from scratch is a Sisyphean task.
7. PhD research at times is like being inside a black hole – time slows down only for you, while it continues to march outside the event horizon.
8. The distinction between assumptions, approximations, and model complexity distinguishes an engineer from a scientist.
9. Just as the flow of resources from the East to the West facilitated the Industrial Revolution, the Climate Revolution will gain momentum only with accumulated knowledge capital flowing back from the West to the East.
10. Climate activists are anthropocentrism activists in disguise.

These propositions are regarded as opposable and defensible and have been approved as such by the promoters prof. dr. G.J.W. van Bussel promoters and Dr.-Ing Roland Schmehl.

Contents

Summary	vii
Samenvatting	viii
Acronyms	xi
Nomenclature	xiii
1 Introduction	1
1.1 Conventional wind energy	4
1.2 Airborne wind energy	6
1.3 AWE design drivers	9
1.3.1 The tri-tethered fixed-wing system	11
1.4 Summary and thesis outline	12
2 Design methods for composite AWE wings: State of Art	15
2.1 Reference tri-tethered swept wing for fixed-wing AWE applications	17
2.2 Design process for complex systems	19
2.2.1 Deriving system requirements	20
2.2.2 Iterative design and testing	20
2.3 Simulation models for AWE wing design	21
2.3.1 Performance estimation for AWE systems	21
2.3.2 Steering, controls, and flight mechanics	23
2.3.3 Aerodynamic domain	26
2.3.4 Wing structural domain	27
2.3.5 Aero-structural domain	30
2.4 Research motivation and approach	32
2.5 Research questions	33
3 Simulation of aerodynamic and bridle loads	35
3.1 Computational overview	37
3.1.1 Loads on AWE wings	37

3.1.2	Assumptions and model simplifications	37
3.1.3	Model overview and interfaces	38
3.2	Aerodynamic domain	39
3.2.1	Linear boundary conditions	40
3.2.2	Nonlinear conditions	41
3.3	Bridle domain	43
3.3.1	Model assumptions	43
3.3.2	Single pulley system	44
3.3.3	Multi-pulley bridle system	45
3.4	Summary and conclusions	47
4	Design and simulation of composite AWE wings	51
4.1	Structural Domain	53
4.1.1	Anisotropic laminate structures	53
4.2	Structural laminate domain \mathcal{S}_{lam}	54
4.2.1	Classical Laminate Theory	55
4.2.2	Lamination parameters	58
4.3	Structural geometric domain \mathcal{S}_{2D}	60
4.3.1	Cross-section topology parametrisation and discretisation	60
4.3.2	Stiffness parameters - analytical approach	63
4.3.3	Stiffness parameters - FE approach	66
4.3.4	Numerical case studies	66
4.3.5	Multi-fidelity expression of \mathcal{S}_{2D}	69
4.4	Structural stiffness domain \mathcal{S}_{1D}	70
4.4.1	Constitutive equations and displacement field	72
4.4.2	Equilibrium and compatibility equations	73
4.4.3	Finite element implementation	74
4.4.4	Framework specific implementation details	76
4.5	Coupled aero structural solver	77
4.5.1	Coupling methodology	78
4.5.2	Dynamic load stepping	80
4.5.3	Interface mapping $\mathcal{A} \rightleftharpoons \mathcal{S}$	81
4.6	Summary and conclusions	83
5	Structural design space	87
5.0.1	The D-box – an atypical wing box	89
5.1	Wing box internal geometry and structural optimisation	92
5.1.1	Laminate layup tailoring	92

5.1.2	Laminate thickness parameterisation	93
5.2	Case Study: Cross-sectional topology optimisation.	96
5.3	Case Study: Cross-sectional laminate layup optimisation.	98
5.4	Summary and conclusions	101
6	Bridle design space	105
6.1	Bridle configuration design.	107
6.2	Impact of bridle design on load introduction	107
6.2.1	Bridle and wing design	109
6.2.2	Power generation with multiple tethers	110
6.3	Case Study: Bridle influence on structural response	111
6.3.1	Structural deflection response	112
6.4	Summary and conclusions	112
7	Aero-structural design space	117
7.1	Introduction	119
7.2	Aero-structural-bridle coupling strategy	120
7.3	Design drivers	121
7.4	Case Study: Bridle configurations	122
7.5	Case Study: D-box stiffness	126
7.5.1	Stiffness domain \mathcal{S}_{1D}	126
7.5.2	Geometry domain \mathcal{S}_{2D}	129
7.6	Summary and conclusions	133
8	Conclusions and discussion	137
8.1	Conclusions	139
8.2	Future recommendations	142
8.2.1	Aerodynamic domain	142
8.2.2	Bridle domain.	142
8.2.3	Structural domain	143
8.2.4	Flight dynamics of bridled wings	143
8.2.5	Design load cases	143
8.3	Lessons learnt	144
A	The EnerKite system	147
A.1	Early generation kites	149
A.1.1	Improving power generation.	151
A.1.2	Pursuing light-weight wings for AWE	153
A.1.3	Launching and landing system	154

A.2	The EnerKite system concept.	155
A.2.1	Technical demonstrator.	155
A.2.2	Airborne subsystem	156

Bibliography	161
---------------------	------------

List of publications	169
-----------------------------	------------

Acknowledgments	170
------------------------	------------

Curriculum vitae	171
-------------------------	------------

Summary

Airborne wind energy (AWE) is an emerging renewable energy technology that harnesses wind energy using tethered flying systems. The extra degrees of freedom allow these systems to harvest wind resources at altitudes currently unrealisable by conventional turbines. These flying devices, often resembling kites or drones, are typically divided into two classes. The first converts kinetic energy into electricity using onboard generators and transmits it to the ground via a conductive tether. The second class transfers aerodynamic forces via the tether to the ground, where the mechanical energy is converted into electrical energy using an electrical machine. As the tether's length constrains the system, once the flying device reaches this tether length limit, some energy must be used to retract it back to its initial position. This cycle of traction and retraction is known as a pumping cycle. Therefore, AWE systems must be designed to maximise the harvesting or traction phase while minimising the retraction phase to ensure a net positive power output.

From the AWE system landscape, this thesis is based on tethered aircraft-style fixed-wing systems. Typically, such systems utilise composite structures owing to their high stiffness-to-weight ratios. Designing these composite structures demands special attention due to their anisotropic nature, which results in complex load-deflection couplings. Here, a multi-disciplinary simulation framework for tethered composite aircraft wings is developed. The research focuses on methods used during the iterative phases of initial (conceptual and preliminary) design that are commonly employed in a spiral system engineering approach. The proposed framework integrates computational methods for the design of the aerodynamic \mathcal{A} , bridle \mathcal{B} , and structural \mathcal{S} domains. The bridle is a system of segments of tether and pulleys that distribute the tether forces into the wing structure. The aerodynamic and structural domains are divided into 2D and 1D models, which are then integrated to determine the 3D response of the wing. A nonlinear vortex-lattice method (VLM) is utilised for the aerodynamic domain. For the structural domain, an anisotropic 1D finite element (FE) model is developed that is coupled with a 2D FE sectional solver. In addition, methods are proposed that enable detailed topology optimisation.

For tailless swept-wings, like those used by EnerKite, the aero-structural-bridle interactions are crucial. The developed framework is used to investigate the impacts of different wing and bridle configurations to determine the sufficient level of fidelity required at the initial design phases. Typically, such aeroelastic phenomena are captured during detailed design stages wherein full 3D structural and aerodynamic simulations are employed. However, this mandates design knowledge typically unknown at the initial design stages. This motivates a multi-fidelity modelling approach to include these coupling effects while abstracting the composite ply level details during the design exploration. This is achieved by combining geometric discretisation approaches with lamination parameters. Thus, the framework aims to provide viable design options during the initial stages while considering aero-structural-bridle couplings.

Samenvatting

Airborne wind energy (AWE) is een opkomende hernieuwbare energietechnologie die windenergie opwekt met behulp van vliegende apparaten. Dankzij de extra vrijheidsgraden kunnen deze systemen windenergie opwekken op hoogtes die voor conventionele windturbines onbereikbaar zijn. Deze vliegende apparaten, die vaak op vliegers of drones lijken, worden doorgaans in twee klassen verdeeld. De eerste zet kinetische energie om in elektriciteit met behulp van generatoren aan boord en transporteert deze naar de grond via een geleidende kabel. De tweede klasse trekt aan de kabel van een lier op de grond, waar de mechanische energie omzet in elektrische energie met behulp van een generator. Wanneer de kabel volledig is uitgerold, moet er energie gebruikt worden om het vliegende apparaat terug naar beneden te halen. Deze cyclus van het uittrekken en inhalen van de kabel staat bekend als de pompcyclus. De AWE-systemen worden ontworpen zodat het maximaal haalbare vermogen wordt opgewekt bij het uittrekken en zo min mogelijk vermogen wordt verbruikt bij het inhalen.

Dit proefschrift is gebaseerd op AWE-systemen waarvan de vliegers een vaste vleugel hebben en lijken op vliegtuigen. Dergelijke systemen maken meestal gebruik van composiet constructies vanwege hun hoge stijfheid-gewichtsverhouding. Bij het ontwerpen van deze composiet constructies moet rekening worden gehouden met hun anisotrope aard, wat resulteert in complexe belasting-doorbuiging koppelingen. In dit proefschrift wordt een multidisciplinair simulatieraamwerk ontwikkeld voor composiet vliegers. Het onderzoek richt zich op methoden die gebruikt worden tijdens iteraties van het initiële (conceptuele en voorlopige) ontwerp die gewoonlijk gebruikt worden in een spiral systeem engineering aanpak. Het voorgestelde raamwerk integreert rekenmethodes voor het ontwerp van de aerodynamische \mathcal{A} , bridle \mathcal{B} , en structurele \mathcal{S} domeinen. De bridle is een systeem van kabels en katrollen die de belasting op de vleugelconstructie verdeelt. De aërodynamische en structurele domeinen worden verdeeld in 2D en 1D modellen, die vervolgens worden geïntegreerd om de 3D responsie van de vleugel te bepalen. Een niet-lineaire vortex-lattice method (VLM) is gebruikt voor het aerodynamische domein. Voor het structurele domein is een anisotroop 1D eindige elementen model ontwikkeld dat is gekoppeld aan een 2D eindige elementen model van de dwarsdoorsnede. Daarnaast worden methoden gebruikt die een gedetailleerde topologieoptimalisatie mogelijk maken.

Voor staartloze geveegde vleugels, zoals die gebruikt worden door EnerKite, zijn de aëro-structuur-bridle interacties bepalend. Het ontwikkelde raamwerk wordt gebruikt om de effecten van verschillende vleugel- en bridleconfiguraties te onderzoeken en daarmee te bepalen welke mate van betrouwbaarheid nodig is in de eerste ontwerpfasen. Dergelijke aëro-elastische fenomenen worden gewoonlijk pas geanalyseerd tijdens de detailontwerpfasen met volledige 3D structurele en aërodynamische simulaties. Dit vereist echter kennis over het ontwerp die meestal onbekend is in de eerste ontwerpfasen. Om deze koppelingseffecten mee te nemen en tegelijkertijd de details van het composiet materiaal te abstraheren tijdens de ontwerpverkenning is een multi-fidelity modelbenadering gebruikt. Dit wordt bereikt door geometrische

discretisaties te combineren met lamineerparameters. Het raamwerk heeft dus als doel om haalbare ontwerpties te bieden tijdens de eerste fasen, waarbij rekening wordt gehouden met aëro-structuur-bridle interacties.

Acronyms

AoA	angle of attack
AUW	all up weight
AWE	airborne wind energy
AWEP	Aerodynamics, Wind Energy, Flight Performance and Propulsion
AWES	airborne wind energy system(s)
AWESCO	Airborne Wind Energy System Modelling, Control and Optimisation
CFD	computational fluid dynamics
CLT	classical lamination theory
COTS	commercial off-the-shelf
CST	class shape transformation
DLC	design load cases
DoF	degrees of freedom
EASA	European Aviation Safety Agency
EV	electric vehicle
FAA	Federal Aviation Administration
FE	finite element
FEM	finite element method
FRP	fibre reinforced polymer
FSI	fluid structure interaction
GDP	gross domestic product
GHG	green house gasses
GMST	global mean surface temperature
HALE	high altitude long endurance
IEC	International Electrotechnical Commission
LCOE	levelized cost of electricity
LEI	leading edge inflatable
MDO	multidisciplinary optimisation
ML	machine learning
NAL	National Aerospace Laboratories
NREL	National Renewable Energy Laboratory
PV	photo voltaic
RANS	Reynolds averaged Navier-Stokes
ROM	reduced order model
SHM	structural health monitoring
SIMP	solid isotropic materials with penalization
UAV	unmanned aerial vehicle

uRANS **u**nsteady **R**eynolds **a**veraged **N**avier-**S**tokes
uVLM **u**nsteady **v**ortex-lattice **m**ethod
VAM **v**ariational **a**symptotic **m**ethod
VAWT **v**ertical **a**xis **w**ind **t**urbine
VLM **v**ortex-lattice **m**ethod
VSM **v**ortex-step **m**ethod
VTOL **v**ertical **t**ake-off and **l**anding

Nomenclature

Latin Symbols

A	Projected wing area	[m ²]
A_b	Turbine blade area	[m ²]
AC	Aerodynamic Center	[-]
A_r	Projected rotor area	[m ²]
\mathcal{A}	Aspect ratio	[-]
\mathcal{A}	Airfoil polynomial weight coefficient matrix	[-]
B	CST parameterisation shape coefficients	[-]
\mathbf{x}_i	Bridle attachment position vector	[-]
c	Aerodynamic chord	[m]
\bar{c}	Mean aerodynamic chord	[m]
C_D	Aerodynamic drag coefficient	[-]
C_g	Center of gravity	[-]
C_L	Aerodynamic lift coefficient	[-]
C_M	Aerodynamic pitching moment coefficient	[-]
C_N	Aerodynamic yawing moment coefficient	[-]
C_p	Aerodynamic centre of pressure	[-]
$C_{P,r}$	Rotor power coefficient	[m ²]
\mathcal{N}	Element shape function	[-]
\mathbf{F}	Force vector (components in $\mathbf{F} \in \mathbb{R}^3$)	[N]
\mathbf{I}	Inertia tensor	[kgm ²]
$l_{1,\dots,n}$	Length of pulley segments in bridle subsystem	[m]
l_p	Total length of single pulley loop in bridle subsystem	[m]
$\frac{L}{D}$	Lift to drag ratio	[-]
\mathbf{M}	Mass tensor	[kg]
$N_{1,2}$	CST parameterisation class coefficients	[-]
P	Power	[W]
\mathbf{P}_{sp}	Reference set of points along airfoil spline parameterisation	[-]

\mathbf{x}_p	Bridle pulley position vector	[-]
R_p	Pulley radius in bridle subsystem	[m]
\mathbf{S}	Stiffness tensor	[-]
U	Strain energy (principle of virtual work)	[Nm]
V	Work done by external forces (principle of virtual work)	[Nm]
v_a	Apparent velocity	[m/s]
v_∞	Free stream velocity	[m/s]
v_w	Wind velocity	[m/s]
$\mathbf{x}_{1,\dots,n}$	Wing attachment position in bridle subsystem ($\mathbf{x} \in \mathbb{R}^3$)	[m]
\mathbf{x}_p	Pulley position in bridle subsystem ($\mathbf{x} \in \mathbb{R}^3$)	[m]

Greek Symbols

α_a	Angle of attack	[°]
Γ_d	Dihedral angle	[°]
Π	Potential energy (principle of virtual work)	[Nm]
Ψ	Non-dimensional position along airfoil chord	[-]
σ_{rotor}	Rotor solidity	[-]
b	Wing span	[m]
γ	Sweep angle	[°]
λ	Taper ratio	[-]
ϵ_{tol}	Convergence tolerance	[-]
Ω	Twist angle	[°]
ξ	Normalised element coordinate	[-]
ζ	Non-dimensional position along airfoil thickness	[-]

Other Symbols

$\mathcal{C}(\)$	Convergence function
\mathcal{A}	Aerodynamic domain
\mathcal{B}	Bridle domain
\mathcal{S}	Structural domain
\mathcal{S}_{lam}	Structural laminate domain
\mathcal{S}_{1D}	Structural stiffness domain
\mathcal{S}_{2D}	Structural geometry domain
\mathcal{Q}	Forces in domain

NOMENCLATURE

$\xi(\)$ Input space of domain

$\varphi(\)$ Solver space of domain

\mathcal{X} Position of domain

$\mathcal{F}(\)$ Response space of domain



Chapter 1

Introduction

Since the Neolithic Revolution, humanity's domestic way of life has required energy in some form. Historically, the motivation for energy sources was based on utility, availability, and cost. In the 21st century, our world is heavily dependent on fossil fuels due to their great utility, abundance, and cheap transportation worldwide, facilitated by two centuries of infrastructure development. However, this dependence has led to a significant increase in greenhouse gas emissions.

Fossil fuels have accumulated in the Earth's crust over millennia. With increased fossil fuel usage, all this accrued carbon is being released as CO₂ into the atmosphere in a comparatively shorter timespan, leading to an unprecedented increase in global temperatures. Paleoclimate reconstructions suggest that the warmest period, prior to the current observed history, was a $\Delta 1^\circ\text{C}$ increase in the global mean surface temperature (GMST) around 6500 years ago. In contrast, a similar $\Delta 1^\circ\text{C}$ has already been surpassed in the past ≈ 180 years of the Post-Industrial Era, with anthropogenic green house gasses (GHG) emissions being the main contributor to this increase. This temperature rise is the most rapid in the last 2000 years, only surpassed by historical events such as volcanic events and asteroid impacts associated with mass extinction.

Staying on this trajectory could lead to a $\approx 2^\circ\text{C}$ increase in average surface temperature by 2030, a point at which many climate scientists believe the damage would be irreversible [1–3]. Already, in 2020, more than one-fifth of the world's population live in regions that have experienced warming greater than 1.5°C in at least one season [1]. Figure 1.1 plots the historical GHG emission data for the world in the post-Industrial Era categorised by sector. The largest contributor to global GHG emissions is the energy sector, responsible for 76% (37.2 GtCO₂e) of total GHG emissions in 2019. Within the energy sector, heating and electricity accounted for 31.9% (15.6 GtCO₂e) of all GHG emissions [4]. Over the last 20 years, globally reported GHG emissions have increased by 50%, with the energy sector being the most significant contributor [4, 5].

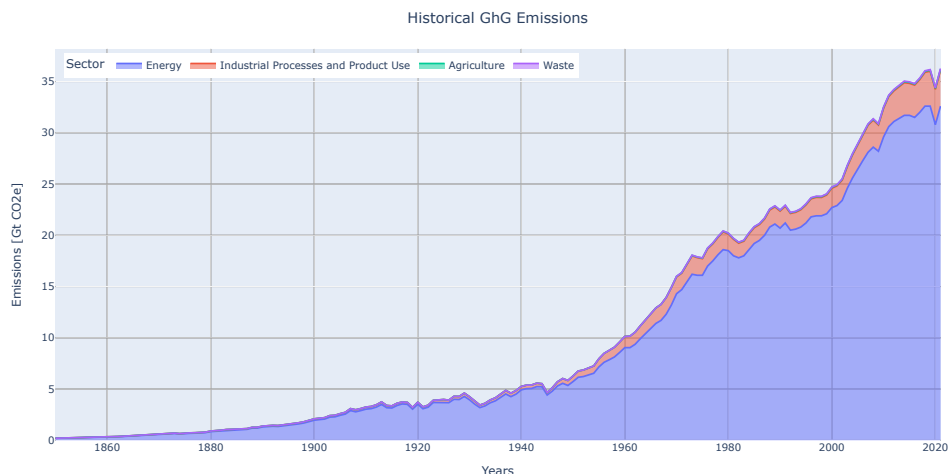


Figure 1.1 | Historical GHG emissions expressed in GtCO₂e, split into sectorial contributions (Data source: World Resources Institute [6]).

Considering that this energy demand has been increasing monotonically since the 1800s, with only globally disruptive events such as wars and pandemics causing setbacks, our dependency

on fossil fuels for energy requires serious attention. While they have been advances in reducing fossil fuel dependency, such as the increasing adoption of electric vehicle (EV) in the transportation sector, care must be taken to avoid simply shifting these emissions to the electricity sector. Current estimates put the global electricity demand at over 1000 TWh in 2021, which unsurprisingly is over five times more than during the global shutdown in 2020 [4, 5].

With the technological advances made in the renewable sector in the last years, 2019 marked a new positive milestone — more than 56% of newly installed renewable energy that year achieved a levelized cost of electricity (LCOE) lower than that of their coal rivals. Thus, for developing regions that are predicted to have the largest energy demand in the subsequent years, investing in new renewables is progressively getting cheaper than new coal capacity. This is quite a remarkable feat, as, in 2010, solar photo voltaic (PV) cost 7.6 times the cheapest fossil fuel power alternative [7]. New renewable projects have already started winning the all-important cost battle against coal power plants. Predictions show that replacing the current most expensive coal-generated power (around 500 GW) with renewables would reduce annual CO_2 emissions by 5% (1.8 GtCO₂e) of the total GHG emissions, while also being cheaper by about 1% of the global gross domestic product (GDP) [7]. There is no denying that compared to a decade ago, the same amount of capital invested results in far higher renewable energy yield.

However, even after all these advances, only around 30% of the electricity generated in 2021 was from renewable sources [4]. An optimistic deduction from this data would show that this is the highest ever contribution of renewables to the energy sector in the entire Post Industrial Era. However, subjectively examining this reveals a mere 3% increase in renewables contribution from 2019 [4]. With more studies illuminating the irreversible changes to our planet that are already in motion, incremental increases in renewable contribution might not be sufficient given the current threats affecting not only our generation but also future ones [1–3].

1.1. CONVENTIONAL WIND ENERGY

Conventional wind turbines have evolved substantially from the early beginnings in the 1800s, requiring substantial engineering effort and multiple iterations to reach the current multi-megawatt power outputs. Other concepts explored are depicted in Figure 1.2, ranging from vertical axis wind turbine (VAWT)s, multi-blade turbines, dual blade, to the now ubiquitous tri-bladed designs.



Figure 1.2 | Evolution of Wind turbine designs used for power generation [8].

The power a wind turbine can generate can be represented as follows

$$P = \frac{1}{2} C_{P,r} \rho A_r v_w^3, \quad (1.1)$$

where the swept area of the rotor is given by A_r , the wind speed by v_w and the power coefficient for the rotor by $C_{P,r}$. Given that the air density is considered constant ($\rho = 1.225 \text{ kg/m}^3$), and the theoretical maximum for the power coefficient is prescribed by the Betz limit $C_P \leq 0.593$ [9], the remaining parameters in maximising the power output P are the swept area A_r and the wind speed v_w . This, however, is a strongly simplified view. In reality, multiple other aspects, such as materials and manufacturing capabilities, transportation and installation, and the essential factor of economics, need to be balanced to achieve a commercially viable energy source. Even with current environmental concerns, economic profit is still a key incentive for the energy market. Thus, maximising the swept area while remaining economically viable is the challenge for conventional wind. An additional challenge is reducing the cut-in wind speed, allowing wind turbines to increase full-load hours at lower wind speeds.

In Europe, the average rated power of wind turbines deployed in 2018 was 6.8 MW offshore and 2.7 MW onshore, increasing to 8.2 MW and 3.3 MW respectively by 2020 [10–13]. The increase in the operating wind speed and rotor area can be seen clearly from wind turbine designs in the last few years. These systems are multi-disciplinary machines, pushing the boundaries of tower heights and blade lengths. As more wind farms move offshore, where wind resources are typically stronger and more consistent at a given height, turbine designs are getting taller to harness these strong winds and employing longer blades (increasing swept area A_r).

The current largest manufactured and deployed turbine in Europe is the Haliade-X prototype, commissioned in 2019, measuring 260 m at the tip, with blades 107 m long and a 12 MW generator. There are already other turbines challenging these numbers, such as a direct-drive 14 MW turbine, the SG 14-222 DD from Simens-Gamesa, with a rotor diameter of 222 m [14]. At a nacelle mass of 500 t, this turbine features one of the lightest nacelles for such a class of machines. Other turbine companies develop similar large offshore turbines, with Vestas's recently announced 15 MW design, the V236-15.0 being the largest machine as of 2021, with a rotor diameter of 236 m [15].

The primary motivation behind these massive machines is to consolidate the expenses and infrastructure required to sink foundations and assemble, construct and erect towers. The economic reality is that a single larger tower is less expensive to build and maintain than multiple smaller towers. Turbine structural scaling can be expressed at an elementary level using the square-cube law stating that an increase in dimensions implies a quadric increase of the energy capturing blade swept area and a cubic increase in the material mass of the wind turbine [16]. This engineering law gives significant insight, as the material mass is an excellent first-order cost indicator. Considering the Haliade-X, the turbine has a nacelle mass of 600 t and blades of 165 t. This totals to a mass of 825 t including the hub and other systems, that requires to be hoisted and supported at a hub height of 135 m. The energy capturing portion of the machine is thus 825 t, with a specific mass of 68.8 t/MW for the 12 MW rated system. This energy-generating part of the system is supported by a tower that weighs about 2.7 times more at $\approx 2250 \text{ t}$.

Such wind turbines are already some of the tallest man-made structures, competing with skyscrapers. However, these designs are not without a fair share of technical challenges, driven

by structural loads arising from gravitational effects and aero-servo-elastic effects. These aero-elastic effects become more pronounced as designs strive for a low solidity ratio ($\sigma_{\text{rotor}} = nA_b/A_r$), defined by the ratio of the area A_b of the n blades to the swept area of the rotor A_r . Lower solidity ratios are desired for direct drive machines that spin at a higher speed, reducing the extra mass and complexity of gearboxes in the nacelle.

The research community, in the meantime, is exploring even larger, more optimised blades, such as the 15 MW design IEA-15-240-RWT of the National Renewable Energy Laboratory (NREL) with 117 m long carbon fibre blades at 73 t each [17, 18]. Other research with larger blades, for 20 MW designs, hints at the direction wind turbines are heading towards in the future [19–22]. With the shift towards new composite materials, these designs focus on reducing the material required in the blade for a similar swept area, thus mitigating the consequences of the square-cubed law.

While advances in material technology and computational analysis have provided the stimulus for designing larger and lighter turbine blades, the supporting tower structures are still a challenging environment to hoist the blades onto. An interesting off-shoot of these large offshore turbines is the engineering efforts undertaken in developing the infrastructure for the installation, support and maintenance required for these machines. For example, for the commercial installation of the Haliade-X planned in a location about 130 km off the coast of England, the wind farm operator had to commission the world's largest floating crane. With a capacity of 3000 t and a fully erected height of 325 m from the seabed to the top, the *Voltaire* was used to hoist the 825 t of nacelle and blades atop the 135 m tower. Such unique infrastructural needs further highlight the challenges — progressively larger turbines also necessitate the development of infrastructure required to assemble, commission, and maintain these turbine structures.

With these physical and engineering constraints, the field of wind energy can not expect a step change from just the current conventional wind turbines, even with the continued increase in tower heights and blade lengths. Instead, the concept of airborne wind energy (AWE) proposes a radical shift in the methodology of extracting power from the wind. These systems replace conventional wind turbines' large cement and steel towers with lightweight, flexible tethers and the large blades of turbines with flying devices. Thus, the apparatus that extracts power from the wind is kept in the air and hence denoted as the airborne part of the system. This concept eliminates the requirement of tower structures that conventional turbines need to support the wind power extracting blades. A schematic comparison is illustrated in Figure 1.3. The concept depicted converts the traction force from the airborne element into torque at the ground level that is utilised to generate electric power.

1.2. AIRBORNE WIND ENERGY

Kites in various forms have been used for thousands of years, from recreation, art, and religion to signalling and observation applications. Since the late middle ages, they have contributed to science and engineering, culminating in the use of kites for atmospheric research and as a precursor of powered flight in the “golden age of kites” from around 1860 until 1920 [23]. Until the late 1970s, there were no significant changes in the status of the kite. With a looming oil crisis after the Six-Day-War and the resulting oil embargo, the late 70s saw a sudden interest in alternative energy sources, leading to the proposed utilisation of kites for energy generation. Multiple pioneering researchers and inventors have explored the concept of AWE, the most

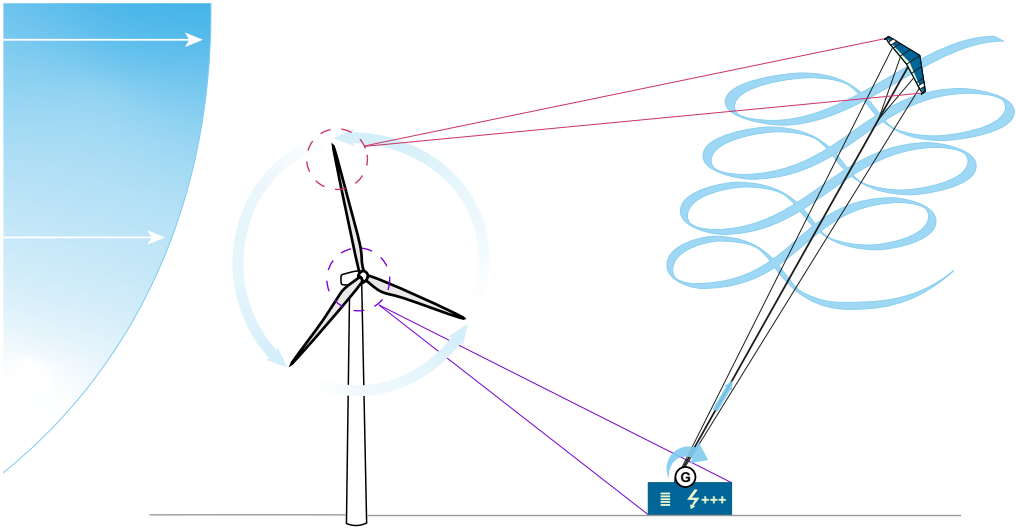


Figure 1.3 | Comparing a conventional wind turbine to an airborne wind energy system(s) (AWES), motivating the potential to reach higher altitude winds with less material.

recognised being Loyd’s work on “Crosswind Kite Power” [24–26].

Loyd outlined two working principles for crosswind kites, one using onboard generators and another with ground-based towed generators [27, 28], as visualised in Figure 1.4. However, as with most of the alternative energy research explored in the 1980s, AWES were soon forgotten with the resurgence of cheap oil. Less complex wind turbines were not forgotten and developed into today’s pillar of renewable energy.

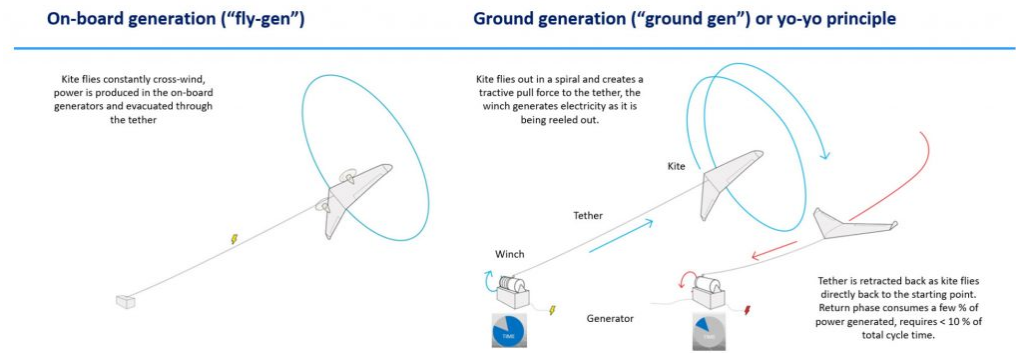


Figure 1.4 | System operational concepts, with traction and retraction phases of pumping cycle AWE. Adapted from [29].

Resurging interest in renewable energy research in the early 2000s has led to re-examining alternative renewable energy. With the developments in the unmanned aerial vehicle (UAV) sector in the last decade, advances in compact computational power and sensor technologies have rejuvenated interest in AWE as a solution for the energy transition [30]. Next to the lower material requirements AWE can harvest stronger and less interrupted winds at increased heights. Compared to a conventional wind turbine’s square-cubed law-based scaling, AWE

systems have practically no mass penalty to increase the operating altitude of the device. This technology is a growing field, with about 60 research groups and companies across the globe pursuing active research and development, as outlined in Figure 1.5 [31]. As with any novel technology, there are many variations to the approach to the technology [32, 33].

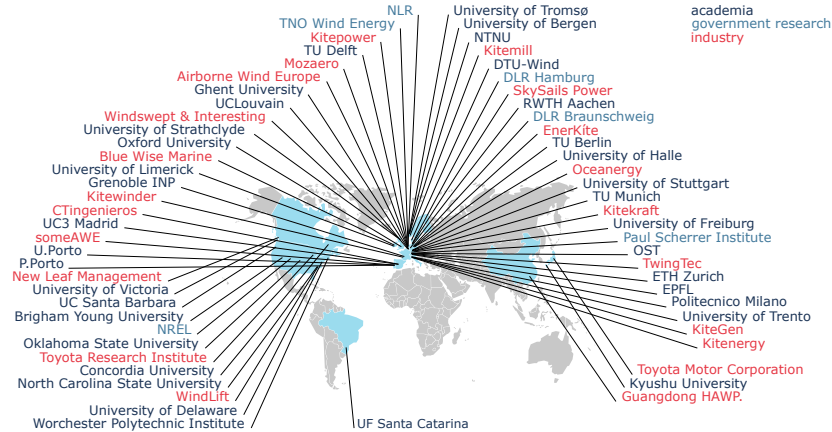


Figure 1.5 | Overview of global research organisations actively investigating and developing AWE concepts [31].

The implemented concepts can be classified into multiple categories based on Loyd’s terminology. The first criterion distinguishes airborne and ground-based electricity generation. Concepts that utilise electrical machines in the airborne part of the system, such as wing-mounted rotor-driven machines, fall into this category, commonly denoted as “fly-gen”. In contrast, other concepts place the generator on the ground and utilise tensile members to transfer the tensile forces, commonly called “ground-gen” systems. Ground-based generators can further be sub-classified into fixed and mobile ground-based units. An overview of these classifications is depicted in Figure 1.6.

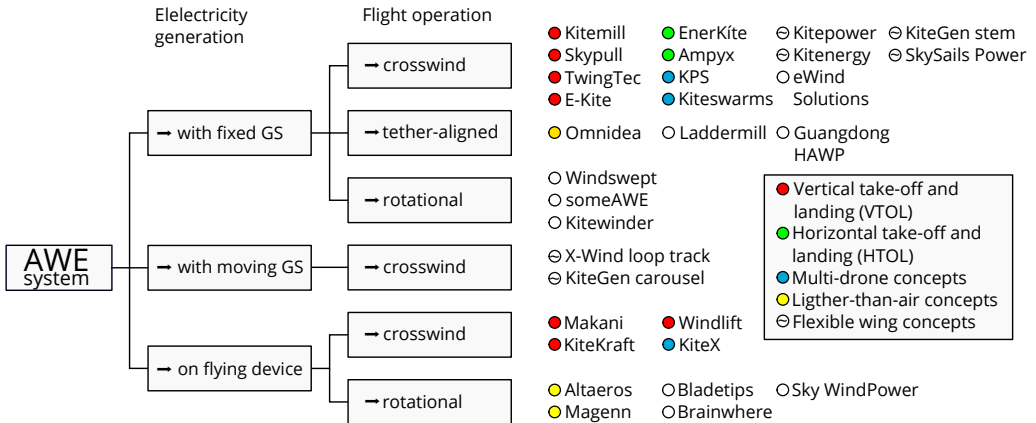


Figure 1.6 | AWE system classification organised by operational principles as pursued in 2019 [31]. There have been multiple companies that have emerged and retired since.

Of the onboard and ground-based energy conversion topologies, this study considers the ground-based conversion concepts. Specifically, an implementation based on a tethered wing oper-

ated in cyclic flight patterns driving a set of ground-based generators. Denoted as pumping cycles, these flight patterns alternate between the energy-generating traction phases, during which the tether forces are maximised by flying the wing in crosswind manoeuvres and energy-consuming retraction phases, in which the tether forces are substantially reduced by reducing the angle of the wing concerning the relative flow. This cyclic process is illustrated in Figure 1.4.

The employed airborne devices range from flexible membrane kites to tethered fixed-wing aircraft including propulsion systems, fuselage and landing gear. An overview of some of these typical configurations is provided in Figure 1.7.

Based on the material composition of the airborne device, AWE systems are commonly classified into soft-wing and fixed-wing kites. Soft-wing kites are made of woven fabric membranes with additional stiffened sections to maintain the wing and aerofoil shape. These can be fabric pockets that are inflated during flight (ram-air kites), or pre-inflated tubes (leading edge inflatable (LEI) tube kites). Fixed-wing kites implement a more conventional aircraft-type configuration that includes fuselage and wing structures. These wings use carbon or glass fibre composite structures on account of their high strength-to-weight ratio. It should be noted that the “rigid” classification for fixed-wing kites is a physical idealisation in comparison to the flexible nature of fabric-based soft-wing kites. Fixed-wing systems achieve higher lift-to-drag ratios than soft-wing kites and are subject to wing loadings an order of magnitude higher than conventional aircraft at nominal operating conditions.

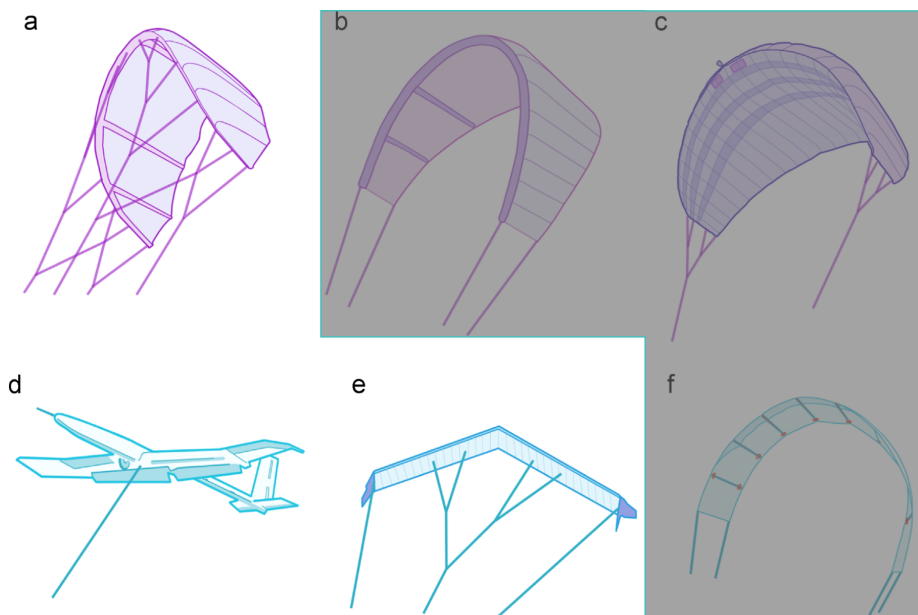


Figure 1.7 | Common types of kites used for AWE systems, as defined in Cherubini *et al.* [34]. Systems in grey are considered deprecated and are no longer commercially pursued.

1.3. AWE DESIGN DRIVERS

Most companies currently focus on ground-based power generation, in two distinct configurations. The first utilises soft-wing kites with a suspended apparatus that actuates the wing. These systems have a single tether from the control unit to the ground station. The other con-

figuration consists of tethered fixed-wing kites that utilise onboard avionics for flight control. The wing is connected to the ground with a single tether in most cases. These fixed-wing systems have significant prior art stemming from the growth of the drone and UAV industry such as commercial off-the-shelf (COTS) systems for flight controllers, propulsion systems, avionics and actuators. For AWE to be a viable energy source, the system must operate autonomously for extended periods. This fact is commonly overlooked at the early research stage, where it is common to repurpose COTS systems from the drone/UAV industry [35, 36]. However, AWE systems have their own set of unique challenges compared to conventional aircraft, summarised below:

1. The tethered connection to the ground. The tether affects the aerodynamics of the airborne system. For example, the pitching moment and effective C_g change with tether parameters such as connecting position on the wing, tether tension and so forth. There is additionally a significant drag component from the tether. The wing loading is an order of magnitude higher, as the tension in the tether is significantly larger than the mass of the wing.
2. Extended "manoeuvre" loads AWE have no cruise phase, with the pumping cycle comprising significant direction changes requiring changes in pitch, roll and yaw.

When asked about the biggest challenge faced by AWE, wing energy pioneer Henrik Stiesdal, commented on how even after multiple years of technical demonstrators, there has been no AWE system that has been operational for ten continuous days, with no operator intervention [37]. Continuous autonomous operation places high demands of robustness both on the system controller and on the kite and ground station hardware. This goal of reliable operation thus depends on system-level robustness and maturity, which is currently being refined.

An area of inspiration for safe and reliable AWE system design would be to build upon the years of research and development that have gone into the field of safety in the aircraft industry. While the aerospace industry has some of the most stringent quality control and certification procedures, one must realise that most aircraft do not operate continuously for days. Instead, passenger aircraft go through some of the most rigorous maintenance and inspection procedures between flights. For perspective, in the energy sector, the typical maintenance interval for solar PV farms is six months, compared to three-six months for conventional wind turbines. While in contrast, "A" checks (requiring a minimum of 10 man hours) in the aircraft industry are typically performed between 400-600 flight hours ($\approx 16 - 25$ days of in-air time) [38-44].

The current (public) record for the longest continuous manned flight in the troposphere is held by two pilots from Las Vegas in 1958, who flew a modified Cessna 172 for 64 days, 22 hours, and 19 minutes [45]. In comparison, the current (public) endurance record for unmanned aircraft is at 25 days, 23 hours, and 57 minutes, set by the Airbus Zephyr S in 2018 [46]. Another category of endurance aircraft is orbital test vehicles that operate autonomously in low Earth orbit. These hybrid spaceplanes, such as the Boeing X-37B, have a flight time record of 780 days, attesting that electro-mechanical flight actuation systems along with current battery technology can operate with long maintenance-free intervals [47]. Achieving continuous, robust, and safe autonomous operation is a significant challenge for AWE systems to become a viable alternative to conventional wind turbines. The complexity of sustaining an aircraft in flight without human inspection or maintenance for extended periods highlights the difficulty

of this task. There is a significant gap that requires traversing when it comes to continuous, robust, and safe autonomous AWE systems, as outlined in subsequent chapters.

1.3.1. The tri-tethered fixed-wing system

This thesis considers a unique hybrid AWE system that is a cross between fixed-wing systems with actuated aerodynamic control surfaces and soft-wing systems, where the wing is a morphing aerodynamic control surface, actuated using tensile members. A tri-tethered system is explored in this work, which employs a fixed-wing kite with no active aerodynamic surfaces. Instead, the system is steered via three tethers differentially actuated from the ground to achieve roll and pitch actuation. Pictured in Figure 1.8 are the operational phases for the AWE system concept considered in this thesis. This hybrid concept is motivated by fundamental use cases and functional requirements.

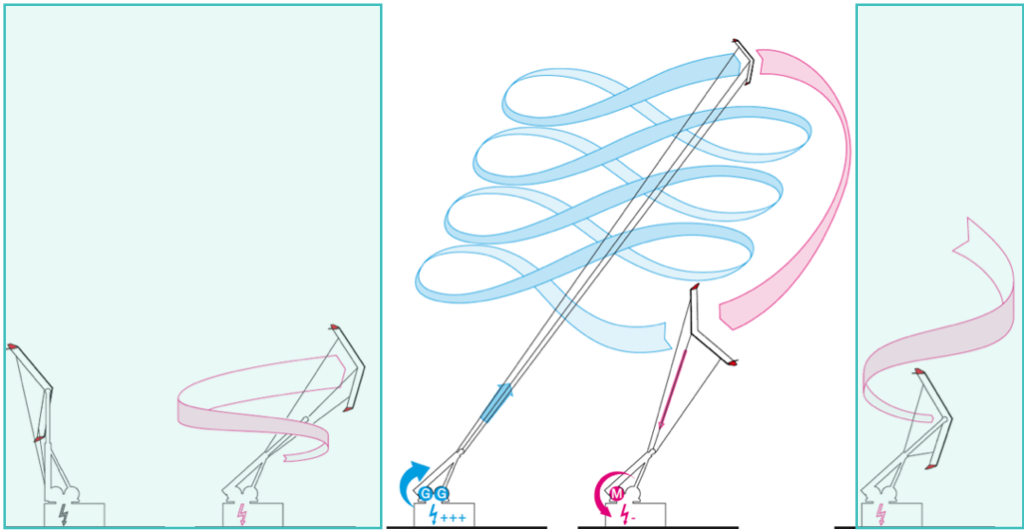


Figure 1.8 | Operational phases of the tri-tethered AWE concept: docked mode, launching, production, retraction and landing phases (from left to right). Pink marks operations that consume power, while blue marks power generation. The phases masked in green are not directly considered in this thesis.

Continuous, reliable operation is a decisive factor for any energy source, making it an important driving factor for design choices. For example, the considered system requires that all safety-critical equipment is situated on the ground. The airborne component thus operates with minimal fail-safe onboard sensors and actuators. All onboard subsystems have no flight-critical functions, allowing the wing to operate in emergency mode, even with multiple onboard failures.

Another driving factor is the economic requirement of high capacity factors and the ability to provide generated energy close to the consumer. This use case mandates that energy is generated in shallow off-shore or on-shore regions and, more importantly, in proximity to human habitation. Such deployment use cases prescribe requirements such as operation at lower wind speeds typically seen on land, in contrast to higher wind speeds available at off-shore locations. To maximise the capacity factor, the system prioritises low cut-in wind speeds by prioritising lightweight wings in the design matrix. This design choice results in a ground-based rotational launching and landing system, minimising the number of onboard components required in this

phase. This serves to reduce the on-board mass, as well as complexity. Because the system has to operate close to inhabited areas, it prioritises robust and safe operations. This leads to system requirements, such as having multiple points of failure, resulting in the choice of redundant tethers and winch drives. Such system requirements motivate the selection of the hybrid AWE configuration with three tethers and actuating the kite from the ground for steering.

This thesis will focus on methods to simulate and design such tri-tethered systems, specifically the aero-structural design of tethered composite wings. Each operational phase (launching, power generation, retraction and landing) needs to be considered for the design of the wing. To narrow down the scope of this research, the design process for each of these phases is not considered. Instead, operational load cases and system constraints from these operational phases are imposed strictly as design requirements and load cases. Furthermore, this hybrid AWE concept poses specific modelling challenges stemming from its operational phases, which require consideration in the computational models employed.

1.4. SUMMARY AND THESIS OUTLINE

Wind turbines continue to grow in size, with new developments increasing the swept area with larger blades and targeting higher wind speeds at taller hub heights. By replacing the tower structure with tensile members, AWE technology can access these wind resources with less material and reduced environmental impact.

From the multiple airborne configuration of kites shown in Figure 1.7, this thesis considers the tri-tethered, tailless swept fixed-wing concept. The wing is operated in pumping cycles using ground-based energy conversion and a ground-based actuation system to control the airborne wing. Unique among the other AWE concepts, this system combines steering via tether manipulation, as seen on soft-wing kites, with composite wing structures of more traditional aircraft-style fixed-wing systems. Such a tri-tethered system concept is in active development by the company EnerKite. Figure 1.9 shows prototype(s) of this minimal, passive wing, seen in operation during testing. The development path towards this specific system design is detailed in Appendix A.



Figure 1.9 | Swept fixed wing prototype(s) in flight with the EK30 technical demonstrator (circa 2015-2022, images courtesy of EnerKite).

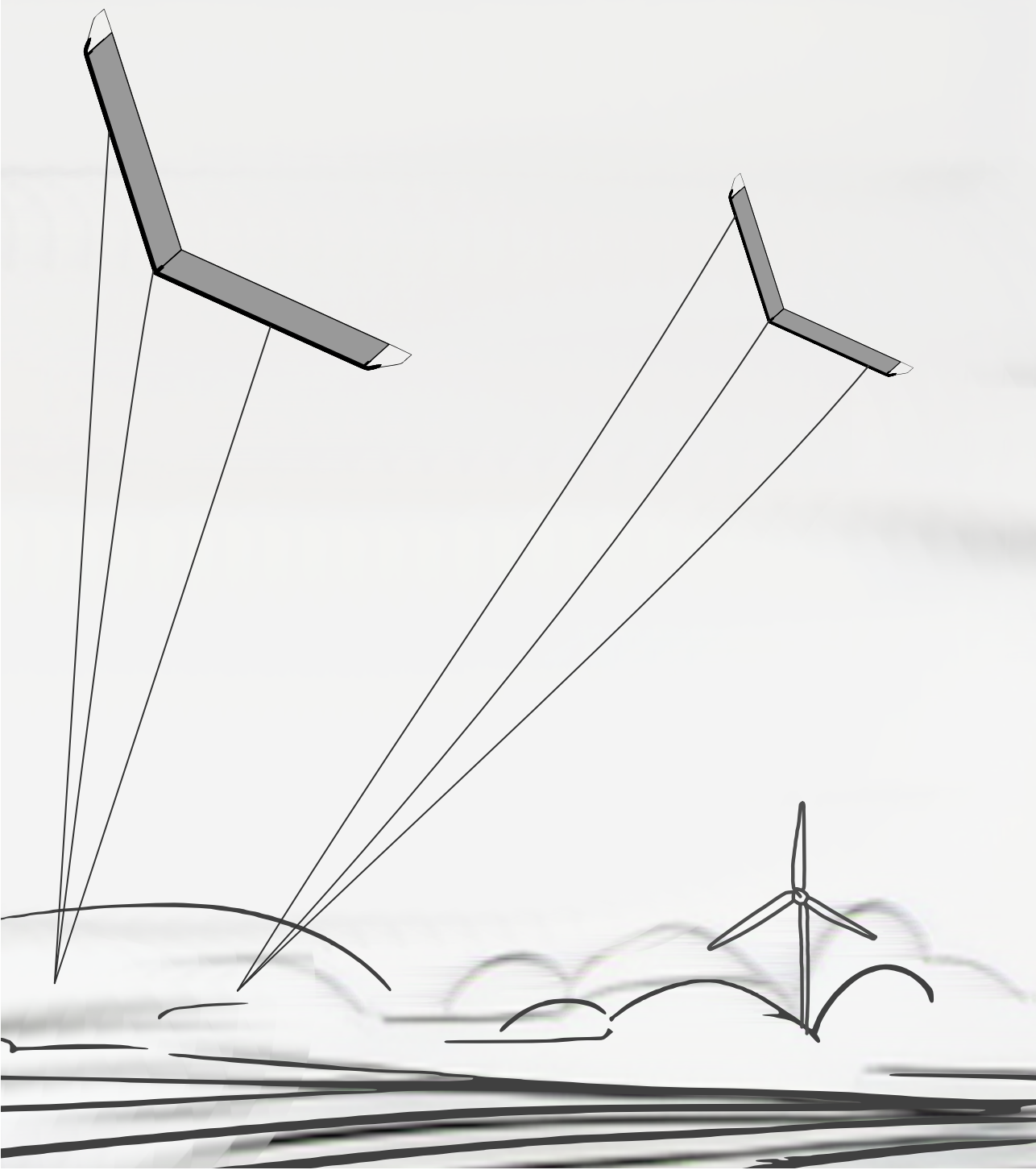
Compared to untethered aircraft wings, the design of AWE wings needs to account for several aspects inherent to the application. Firstly, the presence of the tensioned tether(s) results in a significantly higher wing loading than conventional wings. In conventional wings and rotor blades, composite structures experience both bending, torsion and axial loading effects

during operation. The failure mechanism for such multi-axial loading is often complex and does not correspond to a trivial combination of the load components and instead involves interaction between the loads. For example, a pure bending load in an isotropic material (such as aluminium) results in only bending forces in the structure. In contrast, the same load case in an anisotropic composite could lead to both bending and torsional forces.

Thus, for composite AWE wings, a design process that considers the specific requirements that combine the complexities of anisotropic designs, high wing loading, and additional load introduction from the bridling needs to be developed. Furthermore, specific to the system considered in this thesis, there are no active onboard control surfaces on the wing. Steering is achieved by forcing a change in the wing's attitude using the tethers. As tethers are tensile structures, only tension forces can be transmitted via the tethers. Thus, the force equilibrium of the aerodynamic forces in conjunction with multiple tethers is required to change the wing's attitude and hence steer the kite.

Such aspects require design tools and methods that are at the intersection of wind turbines and aircraft design. Given the current state of AWE development, coupled with the interdisciplinary nature of the system, tools for the rapid exploration of the design space are vital for the initial design. This thesis explores such design methods for AWE with a strong focus on the computationally fast tools, for iterative design optimisation.

The thesis is structured as follows. **Chapter 2** covers the current state of the art in relevant disciplines of wind turbines and aircraft design and the gaps in knowledge that motivate this body of research. **Chapter 3** details the computational methodology to model the aerodynamic and bridle loads. The approach developed for the design of composite wing structures is then described in **Chapter 4**. Following which, the developed framework is utilised to perform design optimisations and case studies. The structural design space is explored with mass minimisation case studies in **Chapter 5**. Then, using the same structural design case, the influence of bridle design space is explored in **Chapter 6**. Subsequently, **Chapter 7** considers the aero-structural design space, with case studies exploring the interaction between aerodynamic forces, composite structures, and tethers. Finally, the findings of this research are presented and discussed in **Chapter 8**. Additionally, **Appendix A** contains a brief interlude into the evolution of the EnerKite system.



Chapter 2

Design methods for composite AWE wings: State of Art

A scientist discovers that which exists. An engineer creates that which never was.

—Theodore von Karman

ABSTRACT

2

Comparing aircraft and wind turbines to airborne wind energy systems — this chapter explores the parallels and differences between the overlapping disciplines that combine to form airborne wind energy. The marked differences that give rise to unique design requirements are underlined. For instance, while conventional aircraft and wind turbines operate in relatively consistent environments, airborne wind energy systems face dynamic and variable wind conditions, frequently flying complex trajectories while performing cross-wind manoeuvres. These increase the demands on the system, from disciplines of control, stability and structural design. The requirements unique to airborne wind energy (AWE) thus require extra consideration while selecting simulation and modelling tools. A literature review of the prior art in the aerospace and wind energy disciplines is provided, highlighting gaps that require further development. Based on this, a set of research questions are posed for this thesis.

An AWE system consists of subsystems that span multiple engineering disciplines, from the aerodynamic design of the wing to the mechanical design of the ground station, the generator to the power electronics required for the energy supply to the grid. Accordingly, AWE is governed by a multi-disciplinary design space. This thesis limits the scope of discussion to the airborne portion of the system, specifically the design of the wing subsystem. Figure 2.1 shows representative commercial AWE systems in operation, with the more “kite” like soft-wing systems on the left, followed by the fixed-wing “aircraft” systems on the right.



Figure 2.1 | Various commercial AWE systems with kite-like and aircraft-like airborne systems. Adapted from [33].

The present work solely addresses the design of fixed-wing airborne wind energy system(s) (AWES), focusing on the tri-tethered tailless swept wing configuration like the EnerKite system seen in the centre of Figure 2.1. This design combines the tether-based steering of soft-wing kites with more aircraft-like features including rigid aerofoils and structural elements.

2.1. REFERENCE TRI-TETHERED SWEEP WING FOR FIXED-WING AWE APPLICATIONS

The studies of this thesis are based on the ground actuated, tri-tethered swept wing concept for AWE. The concept utilises a high-aspect ratio swept wing, wherein the forces are transferred and controlled through a system of multi-element bridles that connect the three tethers to the wing.

A standard reference wing that brings to light design challenges associated with such high aspect ratio swept wings is introduced to aid in the discussion of the results of this thesis. The wing consists of a high aspect ratio swept planform as detailed in Table 2.1 and illustrated in Figure 2.2. It should be noted that the winglets depicted in the figure are treated as additional loads, and their design is not considered in this work.

The design comprises a non-tapered constant chord geometry with a sweep angle of 24° . The total wing area is $\approx 8 \text{ m}^2$ with a target design all up weight (AUW) 24 kg. The aerofoil families in this reference wing are typical slender profiles common to high-lift, low-Reynolds number applications. The wing also has top and bottom winglets to provide yaw stability during the different phases of operation (rotational launching and landing, traction and retraction). The loads from these winglets’ aerodynamic forces and masses are considered in the studies in this work. However, the current analysis does not consider the winglets’ aerodynamic design and flight physics.

Similar to aircraft design, the aerodynamic performance of fixed-wing AWES depends on both

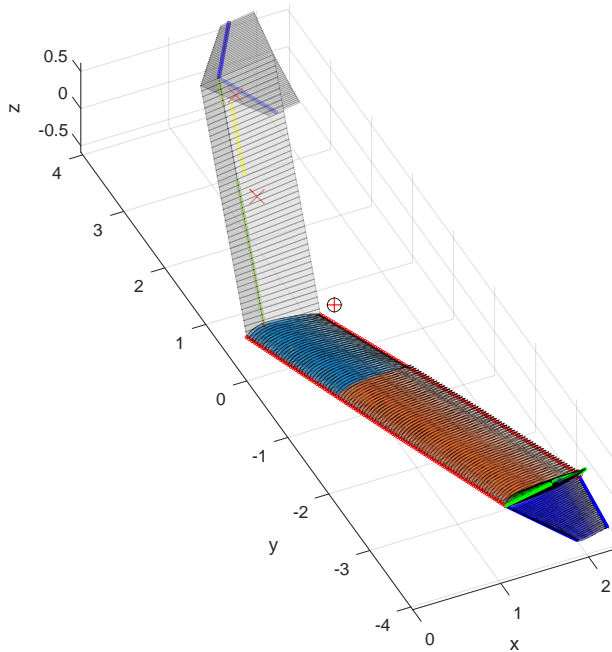


Figure 2.2 | Schematic reference wing geometry, showing planform and profile geometry, with two characteristic root and tip cross-sectional profiles along the span of the wing.

Table 2.1 | Details of the reference wing geometry.

Wing planform		
Area A	8.3 m ²	Projected
Wing span b	10.5 m	
Chord c	0.8 m	
Aspect Ratio \mathcal{R}	12.6 –	
Taper Ratio λ	1 –	
Sweep γ	24°	
Dihedral Γ_d	3°	
Target Mass	24 kg	
Wing sectional profiles		
Root	$0 < \text{root} < 0.4 \frac{b}{2}$	Selig type aerofoil
Tip	$0.4 \frac{b}{2} < \text{tip} < \frac{b}{2}$	Selig type aerofoil

the aerodynamic section(s) and the planform design of the wing. The addition of the tether introduces a force that is of multiple orders of magnitude larger than the wing weight, thus significantly increasing the wing loading. This makes the structural design of fixed-wing **AWES** more challenging than aircraft wings of comparative sizes. The hybrid fixed-wing considered in this work thus results in a system that encapsulates both the challenges and benefits of both the soft and fixed-wing **AWES**. Furthermore, the flight physics and loads on the wing from the

launching and landing system must also be addressed. This makes the engineering design process critical in determining the optimal system configuration. The subsequent sections of this chapter outline design aspects that require consideration and methodology for designing such bridled composite wings.

2.2. DESIGN PROCESS FOR COMPLEX SYSTEMS

A robust energy converter requires multiple subsystems to interact and work in synergy. A systematic methodology for the design and development of the subsystems is critical for the success of AWE systems. In other multi-disciplinary systems such as aircraft and spacecraft, the design lifecycle is split into the conceptual, preliminary, and detailed design stages [48]. The concept design phase outlines configuration choices of the design, such as the number of engines, wing location, empennage configuration. Driven by requirements, designs are iteratively refined to find viable solutions. At the end of the conceptual design phase, the configuration, size and mass targets for the aircraft are frozen. Some typical milestones targeted during the conceptual design phase are given in **Interlude 1**.

Subsequently, in the preliminary design stage, analysis and design of each discipline (aerodynamics, propulsion, structures, controls, etc.) are carried out, for the targets from the conceptual design stage. During this phase, scale models for experimental analysis are commonly built. The preliminary design stage culminates with a detailed proposal of the design.

The detailed design stage marks the go-ahead of the project. In this stage, the actual design of the parts that need to be built is undertaken. As the design is refined, the estimated weights and performance are updated, ensuring initial requirements are still met. The detailed design ends when all parts of the aircraft are designed, and ready for manufacturing.

In classical design methodology, a fourth phase is the production or manufacturing design phase, where detailed manufacturing drawings and specifications are made. This phase ends in a fully specified manufacturing design, along with the associated tooling and manufacturing process. Essentially, all the details that are necessary to produce the aircraft. Typically, the production design and manufacturing are done in parallel, as it is inevitable that parts require modification, for example, to improve manufacturability or reduce costs.

Interlude 1 | Intellectual pivot points for conceptual aircraft design

1. Determine the requirements;
2. Make a first estimate of the weight (frequently based on previous aircraft);
3. Determine the necessary critical performance parameters such as maximum lift coefficient, lift-to-drag ratio, wing loading, and thrust-to-weight ratio;
4. Make an initial configuration layout: shape and size of the airplane on a drawing board or a computer screen;
5. Obtain a better weight estimate;
6. Carry out a performance analysis: Does the design meet or exceed requirements?
If not, return to step 3;
7. Evaluate design at the end of the preceding iterative process: Is it the best design?

Anderson [49]

The conceptual and preliminary phases are commonly grouped into the initial design phase, as they focus on determining specific requirements for the system and making initial estimates.

These estimates are often derived from similar/existing designs and prior experience. Despite this, the typical design lead time from product announcements to maiden flights for a new commercial transport aircraft takes around 6-8 years [48]. After that, it commonly takes additional time for certification and staff training before the aircraft can be deployed into fleet operations. The large lead times are predominantly because designs are driven by norms and certification requirements in the civil aviation sector. Given the human life at stake, these requirements for safe operations are very stringent and exhaustive. This timeline and certification procedures are also a common reason why the civil aviation sector has many “variant” aircraft derived from older certified designs rather than new aircraft designed from scratch.

2.2.1. Deriving system requirements

AWES combine the multi-disciplinary aspects of both aircraft and wind turbine sectors. **AWES** designs thus include system complexities from both sectors, over and above the intrinsic engineering and technological challenges. Hence, a requirements-based certification-driven design for **AWES** is a logical choice.

In the aerospace and wind energy sectors, a product line targets representative operation profiles and multiple design load cases (DLC)s. These **DLCs** are determined by prior experience and simulation models. A subset of these **DLCs** is then prescribed by certification norms. For aircraft, aviation authority bodies such as the Federal Aviation Administration (FAA) and the European Aviation Safety Agency (EASA) are responsible for prescribing, assessing and certifying an aircraft. Examples would range from CS-22 for gliders, CS-23 for normal transport aircraft, to CS-25 for large aircraft [50–52]. Similarly, in the wind energy sector, the International Electrotechnical Commission (IEC) provides standards such as the IEC 61400-1:2019, that define wind gust spectra and resulting load cases along with other design requirements [53].

Certification-driven practices are the path that **AWE** is slowly but steadily heading towards [54, 55], but at the current pre-commercial phase of the technology, gaining technical and operational experience, ultimately proving reliable long-term operations of these machines is the main focus. As with most hardware-centric technical innovations, a significant amount of capital is raised and invested in these technical demonstrators. A system failure can thus cause significant capital loss and, in extreme cases, lead to the insolvency of commercial entities. The rise and fall of Alphabet (erstwhile Google) backed Makani is a prime example of this [56, 57]. Nevertheless, there is a significant drive for commercial entities to be the first to market with their solution, motivating rapid design cycles [58].

2.2.2. Iterative design and testing

For nascent technology such as **AWE**, a balance of risk minimisation along with a rapid pace of progress is paramount for systems design. While wind and aerospace sectors typically follow the established waterfall or V-model of systems engineering, an emerging systems engineering strategy employed in such high-risk development is the spiral system model pioneered by the software industry [59]. As depicted in Figure 2.3, the core principle is to reduce risks by starting with a subset of the requirements, proving a viable concept prototype, and then progressively appending more functionality to arrive at the final design solution iteratively. This approach minimises the sunken resource costs, allowing for non-viable designs to “fail-fast” at an earlier stage.

While this technique allows for rapid iteration, it needs to be backed by design tools that can explore, simulate and analyse design candidates with reasonable fidelity and computational

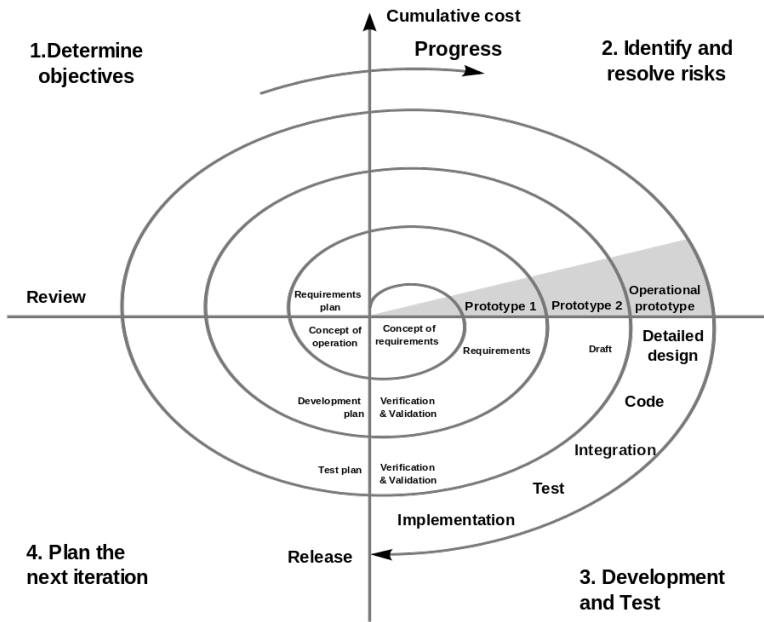


Figure 2.3 | Spiral systems engineering development model focused on iterative design [59].

effort. This design paradigm thus requires harmony between requirements, simulation capabilities, prototyping, manufacturing and testing.

Utilising a spiral development process is advantageous for AWE design, given the uncertainty and lack of prior expertise. It allows for the realisation of multiple prototypes towards the development of the final product. For example, the first iteration (prototype 1) could focus only on landing and launching requirements, not considering power production. Once a satisfactory design is achieved, the next prototype could address power production. Thus, with each iteration, the system is refined systematically. Such a spiral process strategy allows for fast feedback, facilitating vital experience gathering during the design process.

The work in this thesis aims to facilitate such a spiral “design -> implement -> deploy” approach. This motivates the research into design-oriented simulation models that provide suitable fidelity, for each phase in the spiral system design process.

2.3. SIMULATION MODELS FOR AWE WING DESIGN

This section covers prior research from the field AWE, complemented by relevant contributions from the broader domains of aerospace and wind turbine development. Literature particular to analytical methodology and models is described in greater detail in Chapter 3 and Chapter 4.

2.3.1. Performance estimation for AWE systems

Loyd derived a theoretical model describing the traction power of a kite [26]. The lift-to-drag ratio L/D of the kite governs the traction power, given by the ratio of the lift force’s cube to the drag force’s square C_L^3/C_D^2 .

$$P = \frac{2}{27} \frac{C_L^3}{C_D^2} \rho A v_w^3 \quad (2.1)$$

where A is the projected wing surface area of the kite, and v_w is the wind speed.

Loyd's relation provides an analytical metric based on several simplifications and assumptions, of which some are highlighted below:

1. The wind velocity is considered constant and uniform.
2. Only the traction phase is considered, neglecting the retraction phase that completes a pumping cycle.
3. The tether is estimated as a massless single, inelastic, straight line connecting the wing to the ground with no drag.
4. The wing is assumed to fly at the moment of maximum traction power, during which the tether is aligned to the wind vector. Thus, both the elevation and azimuth angles are zero.
5. No inertial effects are considered. Thus a static equilibrium state of the forces is considered, neglecting the mass and trajectory of the wing.

From this simple relation, it is clear that to maximise power during the traction phase, the lift-to-drag ratio C_L^3/C_D^2 should be maximised. Loyd did not consider the additional drag from the tether, which was only accounted for in subsequent research. Thus, to compensate for the additional tether drag an even higher lift contribution of the wing is required to maintain the desired power.

Multiple refinements to the analytical model have been made since, accounting for gravitational and inertial effects, elevation and azimuth angle effects, non-uniform vertical wind profiles, as well as improved tether models that consider tether mass, aerodynamic drag and the related tether sag [60–62]. While these analytical estimates are crucial for preliminary design exploration, they still do not provide the level of detail required to calculate the power generated over a complete pumping cycle, for a prescribed trajectory.

Complete dynamic models, on the other hand, typically consider a state space model of the airborne system and model the entire trajectory of the kite prescribed during traction and retraction phases [63–68]. Such models are commonly used in dynamic simulations for controller design. Deriving from these, a subset of models have been utilised for trajectory optimisation and power prediction using [36, 69]. However, such models require detailed system knowledge commonly unknown at the initial design stage and are often computationally expensive for iterative design exploration.

Quasi-steady performance models allow for a computationally efficient parameter sensitivity analysis determining critical design parameters early in the design process. These models discretise the pumping cycle into its characteristic phases: traction, retraction and transition. Each phase is then described by analytical relations, assuming a steady-state force equilibrium. Typically, the problem parameters are consolidated into airborne system parameters

such as wing area, mass, lift-to-drag ratio, tether diameter, etc. and ground station parameters like electrical machine capabilities, storage medium, storage capacity, etc.. Pumping cycles can then be simulated by varying system parameters and solving at different operational wind conditions to predict the harvested energy. To improve the accuracy of the description of the traction phase, the trajectory of the kite can be discretised further as depicted in Figure 2.4, solving for the equilibrium of forces at each trajectory point allowing for a computationally fast performance prediction [70–72]. More recently, non model-based approaches using machine learning (ML) trained on experimental data have also been explored [73].

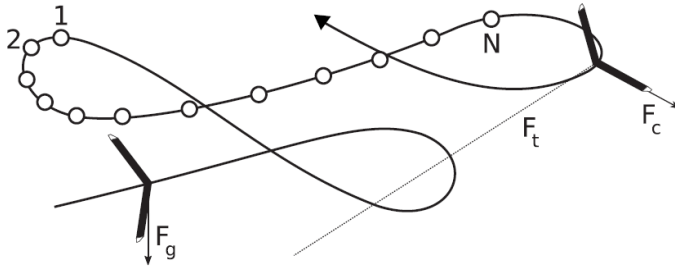


Figure 2.4 | Traction phase trajectory discretisation for power prediction models, where F_g is the gravitational force, F_c the centrifugal forces, and F_t the forces in the tether [71].

Akin to conventional wind turbines, **AWES** need to account for the stochastic nature of wind. Hence, power curves that correlate various wind speeds with the generated power prove to be an apt metric to compare different system design points. Aspects of the system, such as cut-in, rated, and cut-out wind speeds, can be ascertained for a particular design using such quasi-static performance models.

The varying operational environment necessitates the system to extract kinetic wind energy even during low wind situations efficiently but also dynamically control power output such that no failures occur at high wind speeds. Conventional wind turbines account for this by using active or passive control systems that allow for stalling and pitching of the blades. Analogues in **AWES** would be control methods to change the C_L of the system, either by pitch or wing camber control. Additionally, **AWES** have an added degrees of freedom (DoF), which is the operational height of the system, allowing for more flexible operations leading to more complex target power tracking strategies.

Synopsis 1 | Energy yield and wing design

Quasi-static performance models provide a balance of accuracy and system parameter knowledge. By abstracting the system design to such yield models, parameter sensitivity studies to identify critical areas that require consideration during the subsystem design can be undertaken. Such design trade studies can thus be utilised during the conceptual design phase to derive requirements and baseline parameters such as operational wind speed, mass, area, lift-to-drag ratios, etc., for the preliminary design of the wing subsystem.

2.3.2. Steering, controls, and flight mechanics

AWES have either “parafoil-like” for soft-wings or more conventional “aircraft-like” steering solutions and flight mechanics for fixed-wing kites. Soft-wing **AWES** do not have active control

surfaces or mechanisms embedded in the wing. Instead, they are controlled by actuating bridle lines that induce warping/deformation of the flexible \cap shaped wing. This allows for the control of the pitching, yawing, and rolling motion of the kite — essentially utilising the entire wing as an aerodynamic actuator. The actuation for this control is achieved either via multiple lines directly from the ground station (EnerKite ram-air wing [74]) or via an airborne control unit that directly manipulates the bridle lines (Skysails [75], TU Delft/Kitepower [76]). Steering is achieved either by wing-tip warping and/or by the differential actuation of the wing-tip bridle lines, leading to a roll of the lift vector. Warping steering mechanisms have an inherent disadvantage — observations show that the control inputs (magnitude and frequency) impact the flexible membrane material, negatively impacting the lifetime of the kite [75].

Fixed-wing AWE systems with empennages akin to conventional aircraft use control surfaces for both steering and power/depower control. Examples of this concept employed by the industry are systems from Makani, TwingTec, and Ampyx Power, among others [30, 77–79]. As with conventional aircraft, they are placed far away from the centre of rotation to increase the lever arm (flaps near wing tips and rudder and elevator on the tailplane) to increase the effectiveness of the control surfaces. The centre of rotation for tethered aircraft need not coincide with the C_g due to the presence of the tether.

In contrast, the wing considered in this thesis consists of a tailless high aspect ratio swept wing as introduced in Figure 1.9. This bridled, swept, fixed wing utilises a mix of both of the above concepts for control. The kite has no aerodynamic actuators and is steered via manipulation of the tethers similar to the soft-wing kites. The system is controlled from the ground via three tether lines — two steering lines and one power line. EnerKite is a company that develops such a type of AWE system. Details about their development path, as well of their typical launch and landing phases can be found in [Appendix A](#).

The tailless design of the wing attains the required pitch damping and stability by planform design (wing sweep, washout, dihedral, etc.) as well as by manipulating the resultant centre of aerodynamic pressure by the 2D aerodynamic profile design. This, along with a suitable bridle design, is used to obtain the desired static stability. A schematic of the typical forces occurring in this system is shown in Figure 2.5. Aerodynamic forces, in conjunction with the forces transferred via the tethers, determine the system's attitude. This steering concept is described in further detail subsequently.

A schematic representation of pitch and roll control achieved by manipulating the tether lengths is seen in Figure 2.6. The reference zero pitch and roll configuration is shown in Figure 2.6a. Here the datum positions of the three tethers are also marked across all figures to serve as a visual reference. A pitch-up manoeuvre is achieved by a symmetric reeling in the two control lines while arresting the main line. This is visualised in Figure 2.6b. Similarly, a rolling manoeuvre is achieved by an asymmetric actuation of the control lines, with the main line fixed again, as seen in Figure 2.6c.

The differential actuation of the two steering lines causes the lift vector (aligned perpendicular to the airspeed and parallel to the tethers) to roll, thus resulting in a net effect akin to rolling in a conventional aircraft. For such ground-actuated wings, the bridling positions relative to the aerodynamic centre of pressure highly influence the control effectiveness. For effective pitch control, the longitudinal stability is determined from the resultant force \mathbf{F}_m of the main line and the forces \mathbf{F}_c of the control lines along with the aerodynamic centre of pressure, and C_g of the wing as depicted in Figure 2.5. As seen from the illustration, the wing's planform

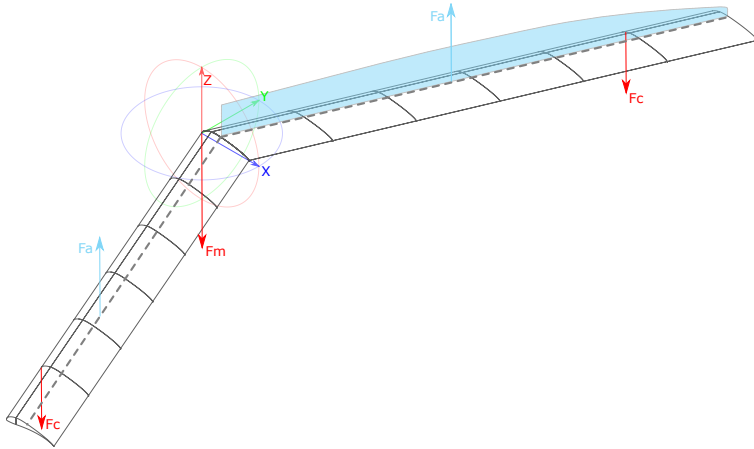


Figure 2.5 | Simplified forces acting on the reference tri-tethered swept wing AWE wing [80].

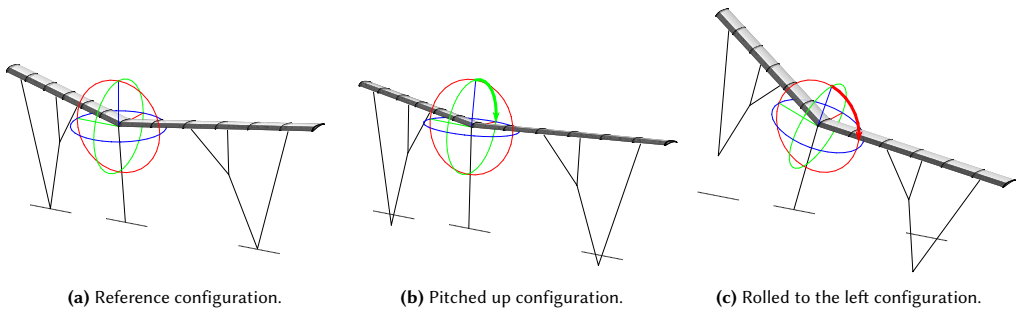


Figure 2.6 | Control of the reference tri-tether rigid wing via asymmetric line actuation [80].

effect plays a significant part in the stability. Depending on the spanwise (YX plane) location of the tether attachment point, there is a coupled effect on both the lateral and longitudinal stability of the wing, which is naturally additionally influenced by the attachment's chordwise (ZX plane) location. It should also be noted that there is an additional challenge for control – as the tethers transmit no compressive forces and can only transfer tensile forces.

Flight mechanics

When considering the flight mechanics and simulations of these systems, models range from simple point mass models to 6DoF aircraft models along with tether models of varying levels of fidelity [81–85].

As the name implies, point mass models consider the kite as a concentrated mass point subjected to quasi-steady equations of motion to determine the kite's orientation. A common modelling approach is to use a multi-point system (usually a four-point system) that discretises the kite into three lifting surfaces, approximating the typical \cap shape of the kite as linear lifting surfaces attached perpendicularly to form a \sqcap . Aerodynamic and mass parameters for these surfaces are then calculated and prescribed to individual mass points that are connected via a spring damper system. These points are subsequently used to determine a fourth virtual

mass point representing the kite dynamics [86, 87].

In contrast, a full dynamic rigid body aircraft model considers inertial effects and provides higher fidelity. Such dynamic models are especially crucial for control system development. Specific to AWES, the aircraft model is combined with a suitable tether and winch model [88–91]. Specific to bridle lines and the accompanied system response, Terink *et al.* investigated the effect of the layout of the bridle line configuration that distributes the forces from the tether into the wing structure, showing that there are some constraints on the rigid body motion to a certain degree, specifically for highly flexible wings [92]. The reader is encouraged to consult the review by Vermillion *et al.*, which provides a comprehensive summary of the advances in AWES controls [93].

Unlike conventional aircraft configuration, swept wings with no fuselage i.e. so-called flying wings, have unique flight characteristics owing to their lack of empennage. Considering longitudinal stability, most aircraft with empennage are naturally stable. Designs typically ensure the C_g is located ahead of the aerodynamic centre AC of the aircraft, resulting in an adverse change in pitching moment for a positive change in α_a . In contrast, flying wings typically have a small static stability margin, requiring active pitch control for gust tolerance. The EnerKite concept requires a balance of a passively stable wing to be steered from the ground while allowing for the switching of aerodynamic states required for the different phases of AWE operations. This results in the definition of an area of feasible longitudinal and lateral stability parameters as a design requirement [74, 94].

Synopsis 2 | Flight mechanics of bridled wings

Soft-wing kites are steered typically by wing deformations and resulting aerodynamic changes while fixed-wing kites utilise actuated control surfaces. The tri-tether swept wings considered in this work are steered by changing the virtual C_g . This leads to a strong coupling between the wing profiles, planform, bridle configuration, attachment position(s), and the flight mechanic stability of the system.

2.3.3. Aerodynamic domain

Maximising the system's power harvesting factor entails maximising the system's lift-to-drag $\frac{L}{D}$ ratio (Equation 2.1). In conventional aircraft, this requirement would correspond to a "minimum sink" design goal typically found in glider configuration aircraft. A factor to consider for AWE is that this $\frac{L}{D}$ ratio corresponds to the entire airborne system, including the tethers. Additional details on the choice of a swept wing design in this work are described in Section A.1.1.

Solving the governing Navier-Stokes equations to determine aerodynamic performance characteristics requires significant computational resources. This relegates such computational fluid dynamics (CFD) methods to fidelity analysis, close to the final design. The challenges of CFD motivate other medium and low methods for aerodynamic analysis. In the conceptual design phase, semi-empirical methods are commonly utilised. Subsequently, during the preliminary design phase, panel methods that trace their origins back to the 1940s are more common. The governing principle is to discretise the lifting surface into multiple panels, simplify the governing equations to a linear integral equation by assuming potential flow (irrotational, inviscid, incompressible) conditions and solve these at different points in the panel [95].

Full Navier-Stokes CFD requires the discretisation of the volume around the body. In comparison, panel methods reformulate the solution only at the fluid-body boundary, thus requiring only the body to be discretised. With suitable discretisation, panel methods can thus describe

the aerodynamics (defined by the Prandtl-Glauert equations) of a body, such as the full 3D shape of a wing along with a fuselage, without having to discretise the volume around the lifting body. However, as these simplifications discard nonlinear terms from the generalised Navier-Stokes solutions, flow phenomena such as skin drag, separation, and transonic shock are ignored [96, 97]. Despite these limitations, panel methods are still widely used in the industry to date for conceptual design, with tools such as VSAERO and AVL (Athena Vortex Lattice) being well renowned [98].

AWE wings operate predominantly in a region of high lift C_L (: high angle of attack (AoA) α_a), where inviscid aerodynamic design methods fail to accurately model nonlinearities of the lift slope, as well as the dramatic increase in drag is experienced near the stall region. To account for these viscous phenomena, Reynolds averaged Navier-Stokes (RANS) solvers or viscid-inviscid interaction methods are required. For 2D domains, full Navier-Stokes solutions can currently be performed with a reasonable computation effort (hours of CPU time), while viscid-inviscid methods in seconds [99, 100]. However, in the 3D domain, these methods are still too computationally expensive for the iterative initial design phase. Instead, extended lifting line methods incorporating nonlinear 2D (viscous) aerofoil characteristics provide a fast computational strategy for determining 3D aerodynamics. These subsets of methods, commonly called 3D planar lifting surface methods, include panel, vortex step, and vortex-lattice method (VLM). These methods are subsequently discussed in Chapter 3.

Prior-art in the aerodynamic domain specific to AWE suggests that panel methods are still widely utilised both for soft-wing kites [101] as well as rigid planes [102, 103]. Published high fidelity CFD studies consider soft-wing aerodynamics [104, 105].

Synopsis 3 | Aerodynamic evaluation at the initial design stage

AWE wings typically operate continuously in high lift conditions, near stall regimes, where nonlinear and viscous effects such as separation can not be ignored. However, CFD based analysis to accurately predict these phenomena is still prohibitively computationally expensive in the 3D domain, especially for iterative design space exploration.

2.3.4. Wing structural domain

The aerodynamic efficiency of wings typically increases proportionally with the aspect ratio, given the inverse relation to the induced drag. However, the increased aerodynamic efficiency is penalised by increasing structural complexity and the mass arising from countering the more significant bending moments and smaller structural area [106–108]. Hence, the increase in aerodynamic efficiency that high aspect ratio wings produce is dominated by mass penalties.

Thin walled composite structures

With the impetus in the aircraft industry to increase efficiency in the late seventies, research into exploring composite materials as a means to increase structural efficiency was undertaken [109–111]. With advances in material technology in the late 1980s, glass and carbon fibre composites were increasingly used in aerospace structures, owing to their high stiffness-to-mass ratio [112, 113]. The wind turbine industry, in contrast, switched from steel blades to multi-material composite blades already in the late 1950s. Early turbine designs in the 40s using steel blades suffered fatigue-induced failures, motivating the pursuit of composite blades.

In subsequent years, blades with wooden ribs combined with steel spars and aluminium skins were common, such as the Gedser turbines in the late 1950s, which was the pioneer in reliable maintenance-free energy production [114]. Since the early 1970s, the majority of turbines had fibre reinforced polymer (FRP) composite blades, with glass fibre being the most common [115, 116].

Compared to isotropic structures, composite wings require more information to model accurately, as seen thematically in Figure 2.7. Fundamentally, additional details are required to capture the changing direction-dependent material properties. The resulting physics requires a more detailed analysis for the stiffness prediction. More detailed finite element (FE) models and thus higher computational effort are required to solve such simulations [117]. Furthermore, higher mesh density is typically required to capture stress concentrations that arise at composite-composite and composite-metal joint boundaries.

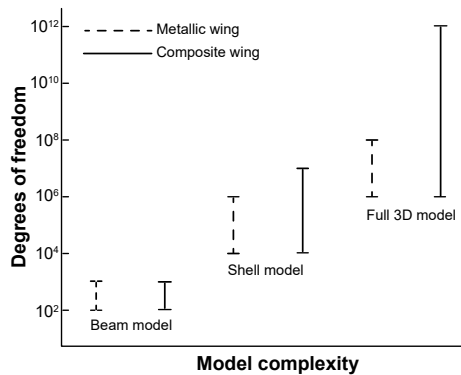


Figure 2.7 | Comparing model complexity for Boeing 777 (metal) vs 777x (composite) scale wings [117].

For slender structures like wings and blades, the span is the spatially dominant direction, with the thickness and chord being orders of magnitude smaller. This is also seen in the internal composition of such structures, wherein thin-walled shells are reinforced with longitudinal stringers along the span, reinforced with ribs for chord-wise strength. Methods for modelling such structures can be broadly classified in increasing order of fidelity and complexity into:

1. Beam models

Based on the simplifications of the linear elastic theory, beams represent the most elementary models for slender structures such as blades and wings. The load-bearing member is represented by a 1D line and can be described analytically, as well as using FE methods for more complicated compositions.

2. Shell based FE models

These models represent the structure as hollow thin-walled shells, considering only the outer “walls” as solid. Thin shell elements neglect the stress component normal to the surface of the shell, while thick shell elements typically consider shear deformations using the midplane stresses. Shell elements are 2D patches or surface elements, with the thickness dimension considered an abstract property.

3. Full 3D FE models

These models consist of the total volumetric representation of the structure, including

various material and component interfaces. Solid FE quadratic elements are utilised in order to obtain stress profiles through the volume of the element.

In the parlance of finite element method (FEM), the DoF of an element/node represents an unknown parameter that requires some mathematical formulations to solve. For structural FE, nodal DoFs correlate to displacement translations and rotations. Thus, depending on the phase of design (conceptual, preliminary, or detailed), a methodology that captures sufficient fidelity should be selected. Conceptual design leans in favour of the lower computational cost of beam and shell models, commonly abstracting the entire wing as a load-bearing wing-box, while for example, critical detailed components such as mounting brackets would normally utilise full volumetric quadratic elements to quantify stress concentrations.

Prior experience shows that for conventional aircraft wings with isotropic materials, beam models provide adequate accuracy in the early design stages [118]. Studies comparing FE beam to shell structural representation reinforce the balance of model complexity to accuracy that beam theory facilitates [119]. However, these studies investigate typical civil aircraft with nominal aspect ratios and isotropic materials. For high aspect ratio wings, non-linearities come into play. As described by Hodges *et al.*, there is a coupling between the flap-wise bending mode to the chord and torsional bending mode, leading to non-negligible structural non-linearities [120]. Librescu *et al.* studied the effects of transverse shear and warping restraints at the wing root in a series of investigations on the role of wing sweep and external stores in composite wings [121–123]. They conclude that the composite laminate ply angles and aspect ratio of the wings induce load deflection couplings, which would not be accounted for in classical beam models [124]. In wind turbines, the influence of biased fibre ply angles is also being explored as a means to increase blade efficiency using passive load alleviation by biased fibre directions with respect to the bending axis [125]. This concept of obtaining favourable structural response by exploiting material anisotropy is further explored while discussing aeroelastic phenomenon in Section 2.3.5.

Given the vast number of approaches to modelling thin-walled composites, the reader is directed towards a comprehensive summary of assumptions, applications and efficiency of approaches [126]. The theme of this work is focused on the initial design space, i.e. conceptual design space exploration, thus limiting the scope to computationally fast models. For such slender thin-walled composite structures being considered here, an alternative to 3D shell and solid FE methods is to attempt to reduce the 3D problem into a set of characteristic 2D cross-sections in addition to a 1D beam model, striking a balance between computational cost and accuracy. Pertinent literature on this methodology is found in Chapter 4.

Airborne wind energy wings

Compared to conventional parafoils and aircraft, the tether in AWE wings introduces a force of equal magnitude to the aerodynamic forces. These forces, under normal crosswind operation, are orders of magnitude larger than the gravitational and inertial forces. Furthermore, AWE wings are subjected to prolonged manoeuvre loads during the harvesting phase. This is again in contrast to most aircraft that are subjected predominantly to cruise loads.

The unconventional location of the load-bearing wing box, located at the leading edge, is unique to the swept wing investigated in this work (Figure 2.8b). As illustrated in Figure 2.8a, a conventional rectangular wing-box is typically aligned to the aerodynamic lift produced by

the wing (commonly at the aerodynamic centre at quarter chord), thus mainly designed to resist bending loads. In comparison, the atypical wing box situated at the leading edge results in a lower moment of inertia to resist bending, torsional loads and other challenges that are described in detail in subsequent chapters of this work.

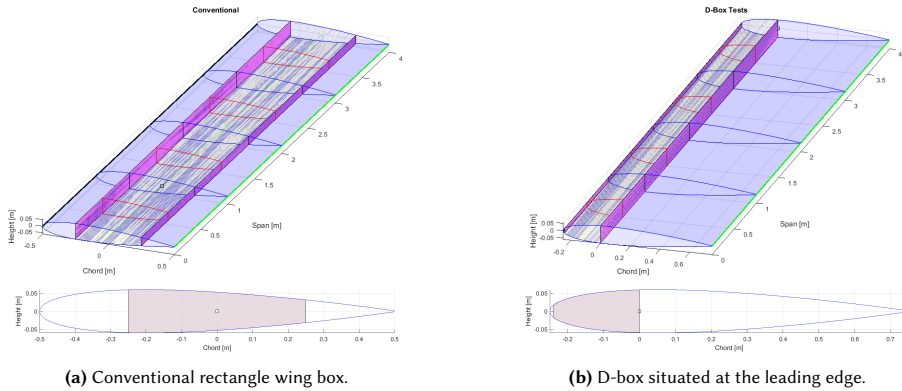


Figure 2.8 | Conventional wing structure with ribs, spars, and stringers compared to a D-box represented with similar structural elements.

A study on the influence of the tether on the structural design of fixed-wing AWE was undertaken on the Makani prototype kites [127]. The studies showed that the positioning of the bridle strongly influenced the structural and aerodynamic response of the wing. Specific to composite rigid kites, Fasel *et al.* utilised a full 3D shell FE model with NASTRAN, exploring morphing wings for AWE [102]. However, it should be noted that such detailed 3D FE analysis, given the computational costs involved, is uncommon in the initial iterative design stage. This is witnessed in this research group’s subsequent work as well, as this detailed model was then utilised to generate a reduced order model (ROM), which has subsequently been widely used in optimisation and controller design studies [128–130].

Synopsis 4 | Structural design of composite wings

Composite structures provide high stiffness-to-weight ratios, allowing for large aspect ratio slender wings that AWEs benefit from. Slender composites witness load deflection couplings arising from material anisotropy, which needs to be modelled with suitable fidelity. Typically, these anisotropic structural models require additional model information, increasing complexity and computational effort. Large deformations, load couplings and anisotropy influences make it imperative to perform the structural sizing early in the system design process. A computational model that balances model fidelity with model complexity and computational costs is desirable for the initial design phases.

2.3.5. Aero-structural domain

The interaction between the aerodynamic and structural domain, particularly the effect of structural deformations on the aerodynamic forces, is known as the phenomenon of aeroelasticity and has been studied for decades [131, 132]. These phenomena are prevalent in slender, large aspect ratio, highly flexible aircraft. Such configurations are typically found on glider and high altitude long endurance (HALE) aircraft configurations. Wherein high aerodynamic efficiency stemming from the design requirement of staying afloat for long durations (i.e. “minimum sink”) motivates aerodynamically efficient wings.

An area of promise emerging from the push of more efficient aircraft is the application of directional stiffness or stiffness-tailored structures. As aptly described by Shirk *et al.*, aeroelastic tailoring is the process by which the directional stiffness is embodied into the structural design process to control aeroelastic deformations (static or dynamic) in a manner that enhances aircraft performance [111]. While this is mainly achieved via anisotropic composites, unconventional stringer, rib orientations, and other atypical structural layouts could also achieve similar results. Given that a different set of fundamental equations governs both the aerodynamic and structural domains, it is common to solve each domain separately, using suitable techniques (commonly called coupling schemes) to transfer the aerodynamic forces to the structural domain and the deformations back to the aerodynamic [132, 133].

For the swept wing geometry in this work, apart from the large aspect ratio, another aspect to consider is the planform geometry. Swept wings demonstrate unique aeroelastic phenomena such as aileron reversal and geometric coupling. Furthermore, the load-deflection coupling in composites can lead to structural failure. An example of such a phenomenon was seen recently in the high aspect ratio swept carbon composite wing - the Aquila 1A unmanned aerial vehicle (UAV). A combination of gusts, upward deflected elevons, and low angle of attack lead to a negative lift component, inducing torsion that further resulted in a downward deformation and ultimately leading to the failure of the wing-box [134].

Particular to fixed-wing AWES, Wijnja *et al.* utilised a non-linear Euler-Bernoulli beam model coupled to a lifting line model via an extended ASWING implementation [127]. The extensions involved adding additional force components from the bridle lines of the wing. Flutter analysis was then performed numerically and experimentally validated via wind tunnel tests. However, given ASWING utilised inviscid aerodynamic approximations, it does not capture near stall region effects [135]. Tests with and without bridles were conducted, with results indicating the strong influence of the position of the tether attachment on the aeroelastic characteristics of the tested wing.

Exploring morphing wings for AWE, Fasel *et al.* coupled a detailed shell FE model implemented in NASTRAN along with an unsteady lifting line method via a two-way explicit coupling scheme [102]. The FE model utilises plate elements for the skin and internal web structures, along with beam and rod elements for the strings and morphing actuators. Symmetric zero displacement boundary condition is enforced at the wing root. The tether is assumed to attach at the wing root, thus no explicit treatment in the FE model is required. The structural model is linearised around a computed static equilibrium point to reduce the computational cost while accounting for large deformations. This linearisation is possible here because the reference wing has relatively high stiffness and hence is less flexible. In subsequent aero-servo-elastic optimisation studies, the authors utilise a ROM using a mode superposition scheme with the first eight modes [128].

Synopsis 5 | Aero-structural design for composite

For tethered, high aspect ratio, anisotropic swept wings considered in this study, the structural deformations could be significant, resulting from interactions between the composite structure, tether, and aerodynamic loads. The structural deformations could be large enough to change the aerodynamic response compared to the undeformed structure. For rigid-wing AWE, the impact of the interaction between aerodynamics, tether, and wing structure requires investigation.

2.4. RESEARCH MOTIVATION AND APPROACH

The design of the airborne subsystem of an **AWES** is governed by requirements determined by system-level design choices. Given the design goal to maximise the power produced, fixed-wing **AWES** that can achieve larger lift-to-drag ratios should be considered as a design solution with high potential. Specifically, a tri-tethered, tailless, swept-wing configuration will form the basis of this thesis. The desire to minimise weight, with the large wing loading (compared to similar size conventional aircraft wings) motivates the use of anisotropic composite materials.

While prior experiences from the wind energy and aerospace sector are vital, they do not encapsulate all aspects of **AWE**. The preceding literature overview outlines the deviations with regards to **AWE**. For complex and novel systems like **AWES**, where experience and expertise are still being accumulated, simulation tools need to operate in a regime where a significant number of parameters are still unknown. Deriving from the spiral systems engineering methodology proposed in Section 2.2.2, for rapid design iteration during the conceptual and preliminary design phases, a balance must be found between the parameter space, model accuracy, and computational cost.

This research aims to develop methods and simulation frameworks for the iterative exploration of the initial design space of fixed-wing **AWES**. Given this focus, high fidelity **CFD** and **FE** simulations and their associated large computational costs are out of the scope of consideration. In addition to computational costs, detailed design parameters required for full anisotropic **FE** models are seldom available early in the design process. This narrows the scope of this research to computationally efficient methods that facilitate iterative design phase(s).

From the literature survey it is found that, in the aerodynamic domain, nonlinear aerodynamic effects arising from operating in the high lift near-stall region require special consideration. Specific to the ground-steered tri-tether swept wing concept, the span and chordwise attachment positions of the bridles with respect to the aerodynamic moment determine both the control authority and the distribution of the forces between the main and the control lines. This combination of nonlinear aerodynamic effects and wing planform design drives the model choices in the aerodynamic domain part of this work.

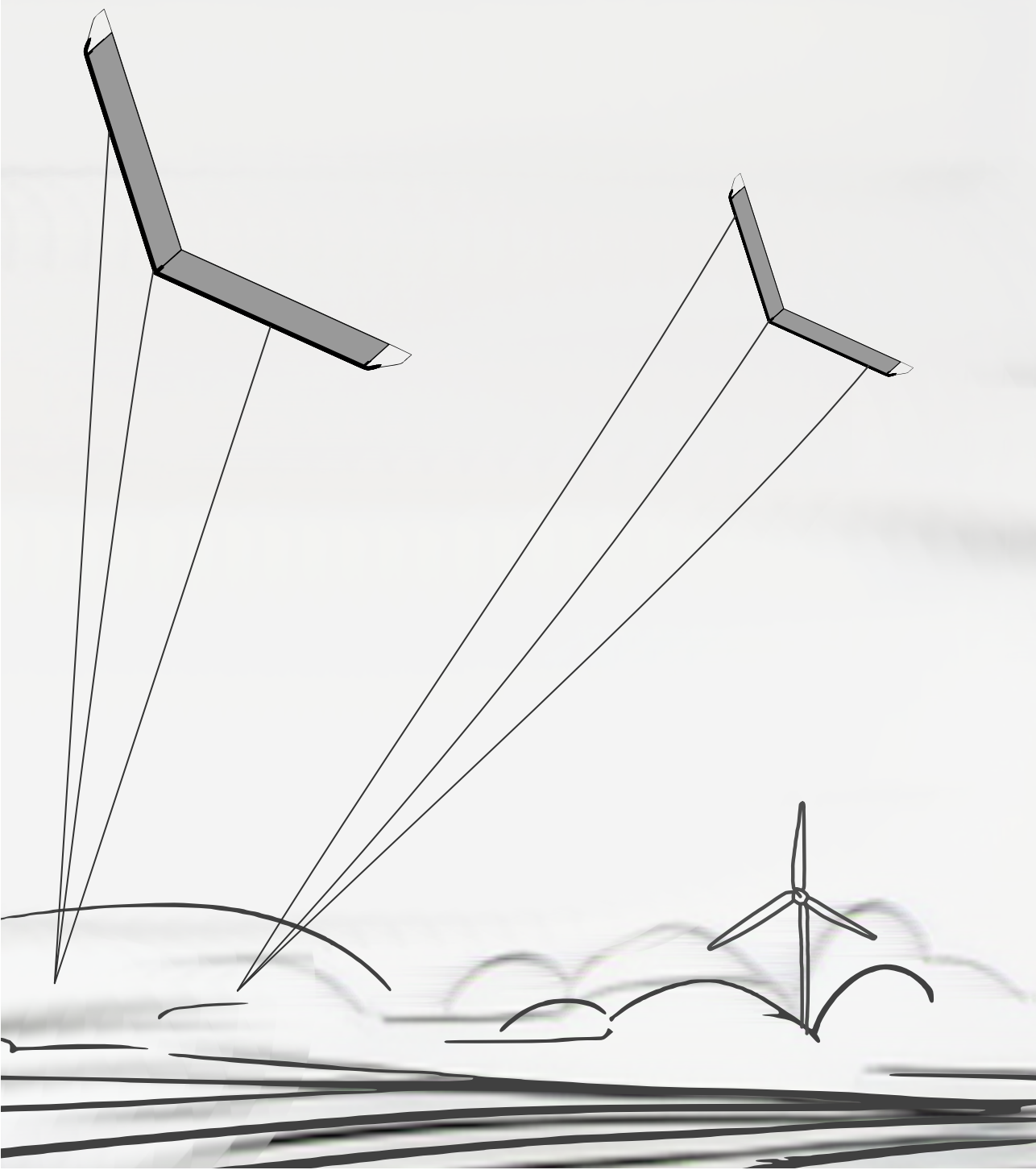
Similarly, the load-deflection coupling phenomenon witnessed in slender anisotropic composite structures can not be neglected in the structural domain. During crosswind manoeuvres, the resultant aerodynamic loads are equivalent in magnitude to the resultant bridle forces acting on the entire wing section at every time instant considered. An aspect that has not been explored fully is the bridle subsystem under the wing. The bridle allows for multiple load transfer points from the tether to the wing structure. This loading could be utilised advantageously by alleviating the bending and torsional forces on the wing by distributing the load introduction points. Hence, a model capturing anisotropic structural effects and allowing for the investigation of bridle system configurations will be developed in this work.

The methodology to be developed here aims to be used for iterative design exploration. The spiral system approach necessitates a multi-level and, thus, multi-fidelity modelling strategy. High-level design requirements for the fixed-wing, tethered airborne subsystem will be derived using a quasi-steady performance model. Planar 3D nonlinear aerodynamic models, in conjunction with anisotropic **FE** beam models, should provide the desired balance between the *trilemma* of model fidelity, computation cost, and parameter knowledge.

2.5. RESEARCH QUESTIONS

Following an examination of the state of the art in the field of **AWES** design, as well as developments in composite wing and blade design in the aerospace and wind turbine industries, the main research may be constructed with a subset of more detailed questions concerning design models and methods posed as follows:

- A. Can a consistent design approach and models be developed for the initial design phases of the airborne subsystem for fixed-wing **AWE**?
 - A.1. What is the minimum fidelity/accuracy required in the initial (conceptual and preliminary) design phase of the airborne subsystem? i.e. what level of detail is needed regarding the aerodynamics, bridle system and composite wing structure design?
 - A.2. How significant are the aeroelastic interaction effects for the airborne subsystem modelling during the initial design phase?
 - A.3. What are the most suited computational models for the initial design phase and how can they be implemented in the spiral system engineering development approach?
 - A.4. Is it necessary to include higher-level fidelity (or more detailed/advanced) tools in the subsequent phase(s) of the design process?
- B. How strong is the interaction between the wing and bridle design, and how should it be incorporated into the design process?
 - B.1. How do the loads introduced at the bridle attachment points affect the design and the aero-structural response of the airborne subsystem?
 - B.2. How do variations of the bridle subsystem affect the wing's aerodynamic and structural design?
 - B.3. Can the bridle subsystem configurations be optimised for system benefits, such as improved performance, controllability and/or reduction of loads?



Chapter 3

Simulation of aerodynamic and bridle loads

If you wish to make an apple pie from scratch, you must first invent the universe

—Carl Sagan

ABSTRACT

This chapter describes the loads witnessed by fixed-wing airborne wind energy (AWE) systems and the assumptions made to model these loads. The complete simulation framework utilised in this work is introduced. Subsequently, the challenges of the simulation of the aerodynamic \mathcal{A} and the bridle \mathcal{B} are covered in detail. The adopted simulation methodologies for these domains are detailed, particularly fast computational models for the analysis and optimisation at the initial (conceptual and preliminary) design phase.

3.1. COMPUTATIONAL OVERVIEW

Computational models for wing design can be broadly classified into characteristic disciplines and constitutive domains, namely the aerodynamic \mathcal{A} , the bridle \mathcal{B} , and the structural \mathcal{S} . The response of these domains can then be described as some output response $\varphi()$ defined by a function of an input $\xi()$. Thus, $\varphi(\mathcal{A}, \mathcal{B}, \mathcal{S}, \dots) = \xi(\mathcal{A}_c, \mathcal{B}_c, \mathcal{S}_c, \dots)$ where the output response is given by a function of system and domain-specific parameters and constants such as the wing geometry, material properties, and external loading inputs among other variables.

3.1.1. Loads on AWE wings

Prior to discussing these domain-specific models, the external loads on an AWE wing are described. They are comprised of the aerodynamic loads and the loads originating from the bridle attached under the wing. Figure 3.1 illustrates the reference tri-tethered swept wing airborne wind energy system(s) (AWES). The bridle system attached at multiple points under the wing is also depicted. The spanwise aerodynamic lift distribution is indicated in blue, and the forces arising from the bridle attachment by red vectors along the bridle lines under the wing. The body-fixed wing reference frame XYZ is also introduced in the figure and originates at the wing's nose, i.e. the leading edge of the root profile.

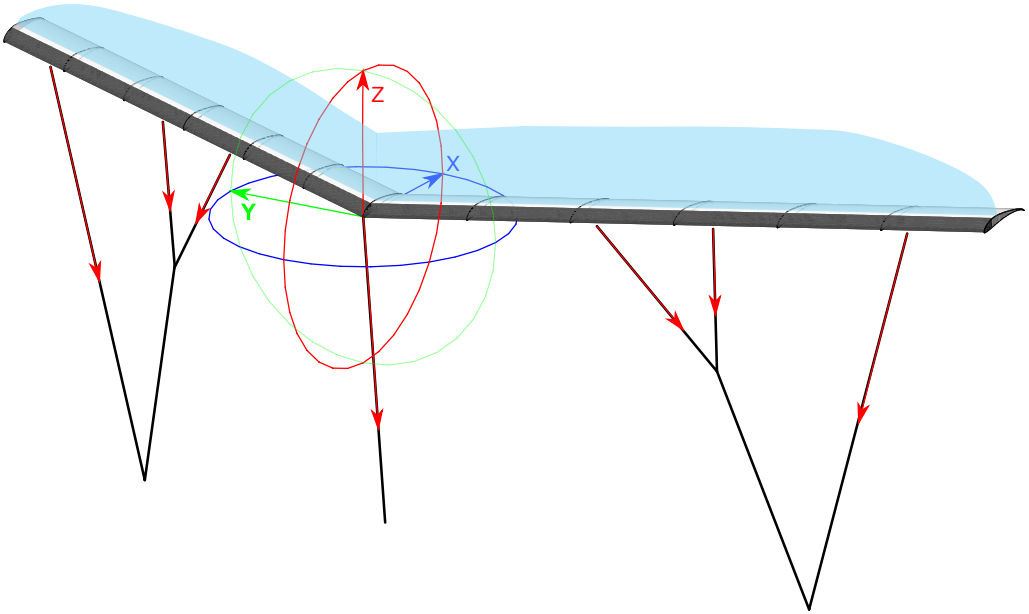


Figure 3.1 | Reference tri-tethered bridled swept wing for AWE, with aerodynamic and bridle loads.

3.1.2. Assumptions and model simplifications

The external loads acting on the equivalent kite structural model during typical operation are illustrated in Figure 3.2. The full 3D aerodynamic pressure distribution is assumed to be distributed as an equivalent vector force acting at the aerodynamic centre along the span. This assumption allows for the complex flow field to be estimated using non computational fluid dynamics (CFD) based methods such as lifting lines and vortex-lattice method (VLM) methods. Thus as depicted in blue in Figure 3.2a, the aerodynamic forces and moments acting on the wing are obtained from the spanwise aerodynamic lift distribution. The specific methodology

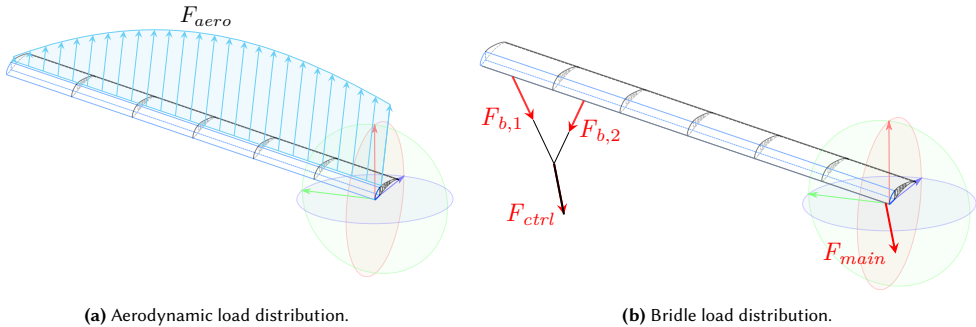


Figure 3.2 | Application of external loads on equivalent kite structural model.

to determine these loads is discussed subsequently in Section 3.2.

Specific to AWE is the additional load resulting from the tethering of the wing, leading to additional load components at the wing's tether(s) attachment points. Moreover, to aid in load distribution, the forces from the tethers are further introduced into the wing structure using a bridle system. The methodology to model the system of pulleys and lines of the bridle is detailed in Section 3.3. Figure 3.2b depicts the bridle forces that are determined from the bridle system and the aerodynamic loads.

The subsequent simplification that the model makes is only to consider the load-bearing member of the wing - the D-box, neglecting stiffness contributions from additional structural members such as the ribs and the textile covering. The external loads are then applied on the D-box as depicted in Figure 3.3. Of note, the chord-wise location of the aerodynamic forces need not coincide with the location of the D-box. The strains and corresponding structural response can then be expressed as a function of the applied loads, cross-section geometry, laminate properties, and composite layup of the D-box.

The 3D slender composite D-box shell structure is further reduced to a 2+1D representation. This is achieved by discretising the D-box into characteristic 2D cross-sections arranged along the wing's span. These 2D cross-sections are used to derive stiffness characteristics that are subsequently utilised with a 1D beam model to capture the 3D structural response of the D-box. The 2+1D reduction of the three-dimensional kite structure, along with other models used for the design of the composite structure of the wing are subsequently detailed in Chapter 4.

3.1.3. Model overview and interfaces

An overview of the various disciplinary modules incorporated into the computational model is provided in Figure 3.4. The inputs and corresponding outputs are outlined, as well as the hierarchy and interdependencies of the modules. A design driver for the computational architecture is to allow for the selection of the desired level of fidelity as required during different stages of the design process.

In this particular work, the design of 2D aerofoils is not considered and assumed to be an available input to the model. The 2D aerofoil polars are thus pre-determined (computed or experimentally) and utilised by the 3D Nonlinear VLM described in Section 3.2 to obtain the

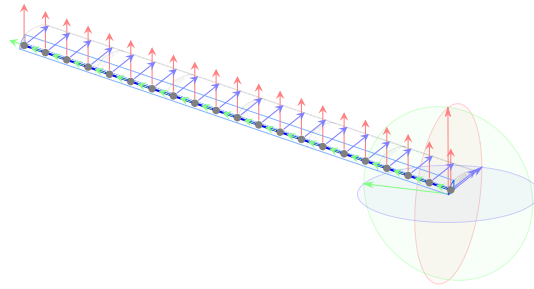


Figure 3.3 | D-box represented as equivalent 1D elements subjected to combined aerodynamic and bridle loads.

spanwise 3D aerodynamic loads for the given aerodynamic profile and wing planform. These aerodynamic loads are combined with the bridle model described in Section 3.3 to determine the bridle loads and thus obtain the external loads acting on the structure. The inputs to the structural model are broadly comprised of wing planform parameters and cross-sectional geometric parameters as covered in Section 4.1.

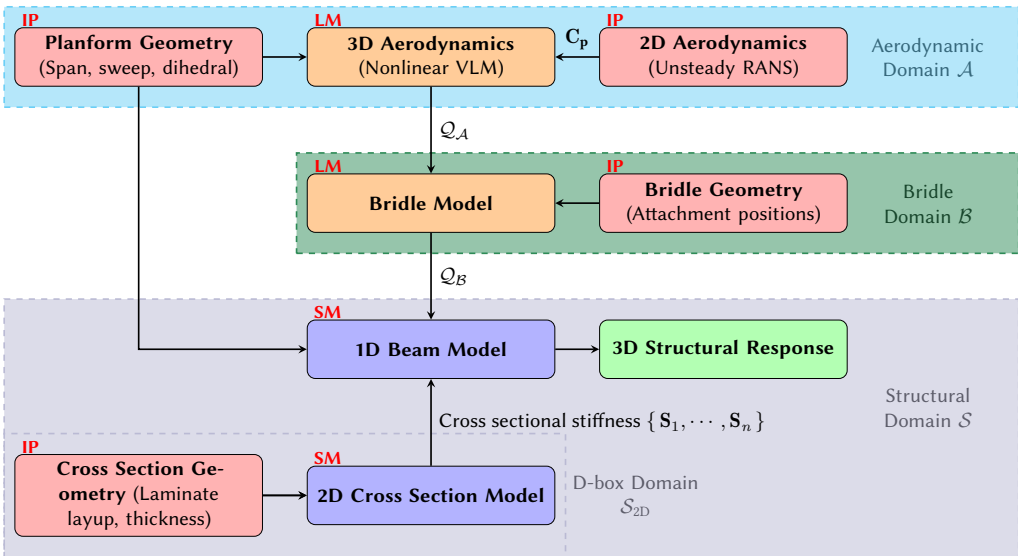


Figure 3.4 | Functional kite structural model overview. All model inputs are indicated in red boxes and shorthand **IP**. External load models by orange boxes and shorthand **LM**, and structural models are indicated in purple boxes and shorthand **SM**.

3.2. AERODYNAMIC DOMAIN

AWE wings constantly operate in a region where inviscid aerodynamic design models have shortcomings (Section 2.3.3). These tools fail to accurately model the decrease in lift slope with the angle of attack, as well as the dramatic increase in drag. To take these viscous effects at high angles of attack into account, either Reynolds averaged Navier-Stokes (RANS) solvers or viscid-inviscid interaction methods need to be employed [99]. Dedicated wind tunnel measurements of aerofoils are also another option. While two-dimensional methods are used routinely in the design and analysis of aerofoils, three-dimensional methods are currently not computationally fast enough to be used in the initial iterative wing design process.

Instead, methods that utilise (extended) lifting line methods that include the nonlinear 2D characteristics are preferred in the initial design phases. Lifting line methods are suitable for unswept, non tapered planar wings. For wings (and lifting bodies) with dihedral, sweep and high aspect ratios, 3D planar lifting surfaces are employed. The extension of the lifting line to incorporate nonlinear sectional lift data dates back to the 1940s [136]. These methods model the lifting line of varying strength with an inviscid assumption, by approximating the vortex sheet with discretised vortices. A subset of these methods is the vortex-step method (VSM), based on Weissinger's method [137]. They use a system of horseshoe vortices of constant strength to model varying strength lifting line. Van Dam *et al.* describes the difficulties and trade-offs that have been made in the past regarding the common methods utilised to design high-lift systems [138]. In addition, van Dam *et al.* also present a method that couples the results of two-dimensional aerodynamic calculations with a single-step VLM [139].

More recently, nonlinear VLM have frequently been proposed for the calculation of the aerodynamic response of kites. Leloup *et al.* present a lifting-line method, which differs from the vortex-lattice methods in placing the collocation points directly on the lifting line [140]. However, no extensive nonlinear aerofoil behaviour is employed in the method besides the evaluation of the drag coefficient due to the effective angle of attack and Reynolds number. This determined C_D is subsequently utilised to derive the glide ratio. Duport *et al.* adapt this method to iteratively solve for the nonlinear aerofoil section lift data as well and compare it with RANS calculations [141]. Gaunaa *et al.* presents a method similar to the one described by van Dam *et al.* [142].

In the above methods employed for AWE, an effective local angle of attack over the wingspan is determined from the flow direction and the downwash of all vortex elements. To account for the reduction in the lift at high angles of attack, a correction is made by modifying the geometric twist such that the local lift from the vortex strength is equivalent to the viscous aerofoil lift at the effective angle of attack. This modification to the twist is subsequently disregarded. These methods are grouped under the term α methods to indicate the effective local angle of attack tailoring over the span [143]. In contrast to these α methods, the term Γ methods is used to describe a set of methods that do not change an effective angle of attack or twist but instead introduce corrections directly to the vortex strength. Compared to the α methods, they are arguably better justified from a fluid-dynamics perspective because they do not make ad-hoc changes to the angles of attack. However, they have been dismissed in the past due to concerns of convergence [143].

The method implemented in this work is a Γ method which employs a fast Newton method to include the fully nonlinear boundary conditions and does not suffer convergence issues. It is based on the generalisation of the VLM boundary conditions, adapted for the nonlinear lift slopes as was initially proposed by Piszkin *et al.* [144]. Complete details of the method can be found in [94]. This method has recently also been adopted by National Renewable Energy Laboratory (NREL)'s AWE simulator KiteAeroDyn [145]. The highlights of the method are briefly outlined in subsequent sections.

3.2.1. Linear boundary conditions

The classic linear vortex step method places horseshoe vortices along the quarter-chord line of the lifting surfaces. These vortices travel along the chord to the trailing edge and are aligned in the direction of the free flow [133]. Every vortex is assumed to be of constant strength, and the individual strength of each vortex is found by calculating the downwash of all vortices onto

central collocation points at $\frac{3}{4}$ -chord in every horseshoe and forcing a parallel flow condition. A schematic of these vortex locations and the discretisation of the wing into equivalent panels is provided in Figure 3.5.

The motivation for this choice comes from the two-dimensional analysis of inviscid flow over parabolic aerofoils. When modelled as a single vortex, the vortex needs to be located at the centre of pressure, which for flat plates and parabolic aerofoils is at quarter-chord. In addition, to arrive at the predefined two-dimensional inviscid lift-slope of 2π , the strength of this vortex must be chosen such that the downwash of the vortex leads to tangential flow at the $\frac{3}{4}$ -chord. This condition is known as the Pistolesis theorem. Enforcing the above boundary conditions of the linear vortex step method is compatible with Pistolesis theorem as for straight wings with an infinite aspect ratio, the wing has a lift-slope of 2π and a centre of pressure located at the quarter-chord.

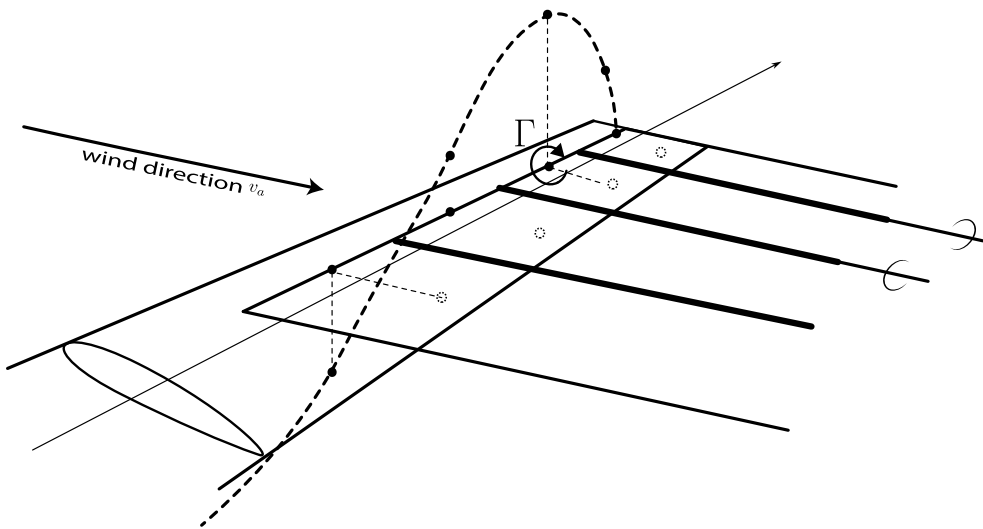


Figure 3.5 | Wing represented by a VLM applied to a lifting line.

3.2.2. Nonlinear conditions

In the nonlinear Weissinger method, the bound vortex strength is instead determined by solving the Kutta-Joukowski law ($L = \rho v_a \Gamma$) along with the sectional lift data, and sufficient boundary conditions. It is commonly stated that the boundary conditions of vortex lattice methods are derived from tangential flow conditions. However, as explained above, the choice of collocation point and vortex position can be extended past the linear airfoil theory. While for a single vortex representation, the choice of location has significance, as the number of vortex lattice elements over the chord increase, the choice of collocation point and vortex position becomes increasingly less important. At every other collocation point, a single vortex will not lead to tangential flow if chosen by the above rule. In order to determine the correct sectional lift parameters, the panel-wise local effective angle of attack ($\alpha_{i,s}$) is determined by computing each panel's downwash velocity. For this, the Biot-Savart law is utilised. To solve for lift using the Kutta-Joukowski law, following Pistolesi's theorem, the tangential flow condition at the $\frac{3}{4}$ -chord is imposed as a boundary condition, and thus determining the strength of the bound vortex.

For an infinite wing with a sweep angle of γ , the lift coefficient can be derived from swept wing theory, as can be seen from Equation 3.1, wherein the effective airspeed's normal component with respect to the nose is reduced by $\cos \gamma$. Additionally, the airspeed v_a is assumed to be the unit vector representing the airspeed direction ($|v_a| = 1$). Hence, for the case of a single vortex path (with strength Γ) at the quarter chord running along the wingspan to infinity, the lift of this wing is given by Equation 3.2.

$$c_l^{2D}(\alpha) = 2\pi(\cos^2 \gamma)\alpha \quad (3.1)$$

$$v_a \times \Gamma = v_a \cos \gamma \Gamma \quad (3.2)$$

These boundary conditions can be rewritten, without using the assumption of swept wing theory for the lift slope (Equation 3.1), but instead using the induced downwash D as given by Biot-Savarts law and the generalised two-dimensional lift as:

$$|v_a \times \Gamma| = c_l^{2D} \left(\alpha - D_{3/4}^{3D} \Gamma + D_{3/4}^{2D} \Gamma \right) \quad (3.3)$$

Thus, we can search for an effective local spanwise angle of attack $\alpha_{i,s}$ such that the resulting vortex strength Γ_{new} is equivalent to the Γ resulting from the sectional lift coefficients prescribed earlier. Given that the induced downwash is the ratio between the induced and free stream velocity, it would be appropriate to express the boundary condition from Equation 3.3 as:

$$v_a \times \Gamma = c_l^{2D} \left(\alpha - \arctan \left(D_{3/4}^{3D} \Gamma + D_{3/4}^{2D} \Gamma \right) \right) \quad (3.4)$$

The implemented solution method solves these nonlinear equations with a damped Newton solver. The static aerodynamic coefficients are determined from the solution to the Kutta-Joukowski law, while the dynamic coefficients and derivatives can be determined without having to solve the nonlinear equations (i.e. downwash, Γ_{new}) again. Instead, it is possible to utilise a linearized form of the angle of attack and sideslip derivatives, and approximate Equation 3.4 around the current Γ and angle of attack to solve for the change in vortex strength $\Delta\Gamma$ for a change in angle of attack $\Delta\alpha$. Thus, with the solution local angle of incidence $\alpha_{i,s}$, the downwash D and the local lift slope $c_l'(\alpha_{i,s})$, $\Delta\Gamma$ is expressed in linear form as:

$$\Delta\alpha_i = \left(\frac{\hat{v}_a \times \hat{\Gamma}}{c_l'(\alpha_{i,s})} + \frac{D}{1 + \alpha_{i,s}^2} \right) \Delta\Gamma \quad (3.5)$$

The linear form of Equation 3.5 can then be utilised to determine dynamic coefficients. For example, considering the non-dimensional roll rate $p = \frac{p_{real}c}{v_\infty}$, the roll damping coefficient can be determined by re-evaluating the Kutta-Joukowski conditions using Finite Differences to determine the new forces and torques:

$$L_p = \frac{L(\alpha, \Gamma) + L(\alpha, \Gamma + \Delta\alpha_p, \Gamma + \Delta\Gamma_p)}{p} \quad (3.6)$$

Thus, using the above aerodynamic analysis methodology, the response of the wing in the aerodynamic domain \mathcal{A} is expressed as a set of aerodynamic coefficients $\{ C_L, C_D, C_M, C_{N_*}, C_{L_*}, \dots \}$,

determined at each panel. These panels are generated from the discretisation of the 3D geometry of the lifting bodies into four node 3D planar VLM panels of zero thickness. Hence, by integrating along the span, the complete spanwise loading of the wing required for the rest of the domain models can be obtained as $\varphi(\mathcal{A}) = \xi(\mathcal{A}_{2D}, \mathcal{A}_{3D})$. This methodology can utilise fast estimates of the aerofoil aerodynamics \mathcal{A}_{2D} during the conceptual phase of design, for example using viscid-inviscid interaction methods [99, 146]. This allows for an initial sizing of the 3D aerodynamic design in typical variables such as sweep, dihedral, aspect ratio, taper, etc. $\langle \mathcal{A}_{3D} \rangle = \{ \gamma, \Gamma_d, \mathcal{R}, \lambda, \dots \}$. Subsequently, during the more detailed phases of design, estimates for the airfoil aerodynamics can be updated for better nonlinear predictions with either experimental data or unsteady Reynolds averaged Navier-Stokes (uRANS).

3.3. BRIDLE DOMAIN

A bridle, in the context of AWE, is the system of tether segments and pulleys under the kite that connects the structure of the wing to the tether(s). The bridles are responsible for distributing and transferring the (aerodynamic) loads on the wing to the tether(s) and, ultimately, the ground station. Tethers for AWE systems are routinely modelled as elastic spring elements [87], while bridles, owing to their much shorter segments, are more commonly modelled as line elements [92, 147]. For systems with a single tether, from the ground to the wing, the bridle configuration typically consists of an “Y” shaped branch with a single pulley [92, 127].

As summarised earlier Section 2.3.2, the bridle configuration plays an important role in the design of AWE, as it influences both the load introduction for the wing structure as well as the stability of the wing. Furthermore, for ground actuated AWES, the controllability of the kite is governed by the bridle system. A suitable configuration, combined with three tethers, results in a favourable load distribution along the span that allows for the control of the wing in both pitch and roll. For such AWES with no control surfaces, the control principle is comparable to aircraft that manoeuvre by relative changes to its centre of gravity, such as hang gliders. With proper design considerations, the bridle potentially allows for the reduction of the wing’s bending moment via favourable load introduction into the wing. An illustrative example of a single pulley “Y” shaped bridle system is shown in Figure 3.6. Three different loading cases are considered, for the same attachment positions, depicting the variation in the directional forces at the attachment positions and the pulley. Such a bridle system will respond differently to a given wing attitude and the resulting aerodynamic forces. Given these force variations, the bridle system configuration is another aspect that can be fine-tuned to obtain potential savings in the structural mass of the wing.

3.3.1. Model assumptions

To determine the structural response of the wing, the resulting forces at the tether positions and attachment points on the wing due to the bridle system needs to be found. For every angle of attack α_a and apparent wind speed v_a , the aeroelastic forces and moments cause a corresponding change in the bridle state to attain an equilibrium. Thus, to attain the forces at the attachment point, the multi-bridle system needs to be solved.

For each bridle loop, the pulley position is constrained by the total length of the tether in the branches. The length of the loop will deform and elongate due to tension in the tether loop, which is in equilibrium with the force in the single tether segment leaving the pulley. When considering the dynamic system, the frictional coefficient of the pulley roller and the velocity of the tether moving the pulley also influence the tension in the branches.

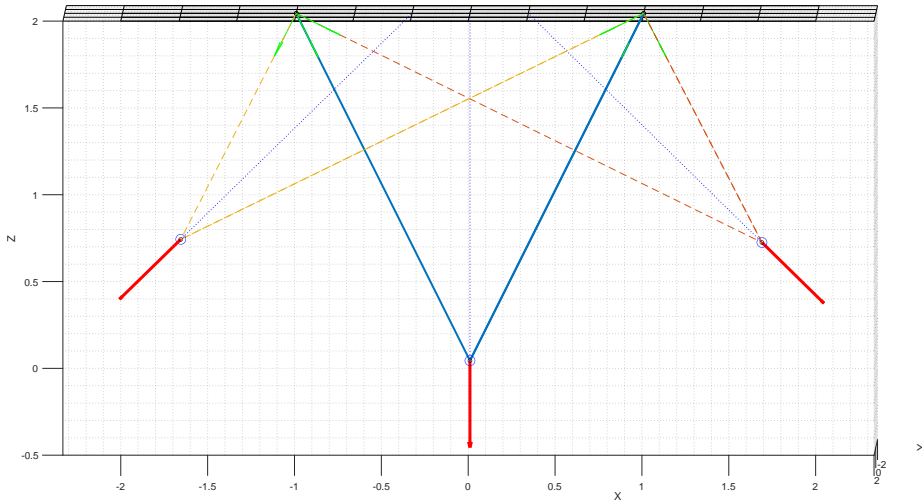


Figure 3.6 | Front view of a simple “Y” bridle system depicting variation in pulley positions and attachment force vectors.

Under nominal loading conditions, there is no sag in the tether segments. Thus, the forces at the two ends of the branch can be determined as a function of the tension in the lines and the position of the pulley. At the current analysis stage, static loads are of interest. Thus, neither dynamic nor frictional effects in the pulley system are currently considered. This simplification allows for the pulleys to be modelled as infinitely small (pulley radius $R_p = 0$) and thus shrinking to a point. Given that the bridle system is in static equilibrium with the aerodynamic forces, the short lengths of tethers in the branches are modelled as rigid, closed tether segments. The effects of the weight of the tethers and pulleys are considered negligible when considering the magnitude of the aerodynamic forces.

3.3.2. Single pulley system

To solve for the complete bridle system state, the attachment point forces that correspond to the particular tether force at the exit of the bridle system need to be determined. Considering a single pulley system defined in $\mathbf{x} \in \mathbb{R}^3$ with two attachment points \mathbf{x}_1 and \mathbf{x}_2 , and the pulley position defined by \mathbf{x}_p as illustrated in Figure 3.7, the forces in the system can be determined as follows. Assuming that the system is in equilibrium, for a given tether force at the pulley \mathbf{F} , the forces in the bridle segments can be obtained by determining the orthogonal projections of the pulley force vector \mathbf{F} on the vector of the pulley segments \mathbf{l}_1 and \mathbf{l}_2 as:

$$\begin{aligned} \mathbf{F}_1 &= \frac{\mathbf{F} \cdot \mathbf{l}_1}{\|\mathbf{l}_1\|} \hat{\mathbf{l}}_1 \\ \mathbf{F}_2 &= \frac{\mathbf{F} \cdot \mathbf{l}_2}{\|\mathbf{l}_2\|} \hat{\mathbf{l}}_2 \end{aligned} \quad (3.7)$$

where

$$\begin{aligned} \mathbf{l}_1 &= \mathbf{x}_1 - \mathbf{x}_p \\ \mathbf{l}_2 &= \mathbf{x}_2 - \mathbf{x}_p \end{aligned} \quad (3.8)$$

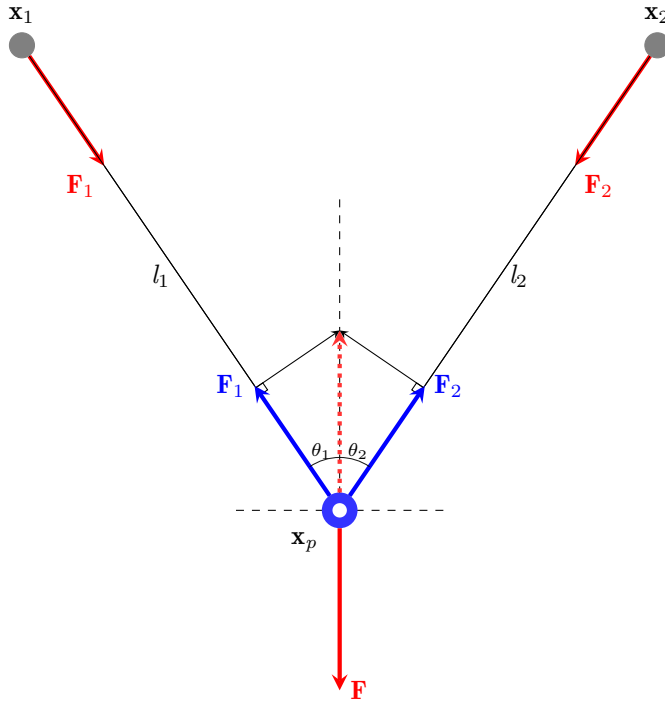


Figure 3.7 | Forces and notation in a single pulley system. Note that $\mathbf{F}, \mathbf{x}_1, \mathbf{x}_2, \mathbf{x}_p \in \mathbb{R}^3$.

Considering an ideal pulley with no friction (where the pulley does not rotate and the rope slides over the pulley), the force in the pulley system is then trivially obtained by solving for the tensions in the tether under equilibrium conditions as:

$$\mathbf{F} = \mathbf{F}_1 + \mathbf{F}_2 \tag{3.9}$$

This equilibrium condition is then utilised to obtain the magnitude of the projections determined from Equation 3.7. Additionally, when considering an infinitely small pulley, a constraint is imposed on the system in terms of the total tether length in the loop. Along with Equations 3.9 and 3.7 boundary constraints on the position of the pulley \mathbf{x}_p are enforced as:

$$l_p = \|\mathbf{l}_1\| + \|\mathbf{l}_2\| \tag{3.10}$$

Hence, for such a single pulley system, this leads to a system of nonlinear equations where the pulley position $\mathbf{x}_p \in \mathbb{R}^3$ and the forces $\mathbf{F}_1, \mathbf{F}_2 \in \mathbb{R}^3$ are unknown. This system is then solved for as a function of the pulley system parameters given by $\mathbf{x}_p = f(\mathbf{x}_1, \mathbf{x}_2, \mathbf{F}, l_p)$. This system can be solved with a numerical method, such as a Levenberg-Marquardt Newton method, as this work implements.

3.3.3. Multi-pulley bridle system

For a more complex system consisting of multiple pulleys, the bridle system can be described by a system of n pulleys \mathbf{P}_i , where the subscript i denotes the index of the particular pulley

system. Each pulley at position \mathbf{x}_{p_i} is subjected to a vector force \mathbf{F}_i that is in equilibrium with the tension force in the branch composed of a tether loop with a length l_{p_i} . The ends of the loop are attached at two points $\mathbf{x}_{1,i}, \mathbf{x}_{2,i}$. A bridle system with a triple ($n = 3$) pulley system $\mathbf{P}_1, \mathbf{P}_2, \mathbf{P}_3$ is depicted in Figure 3.8.

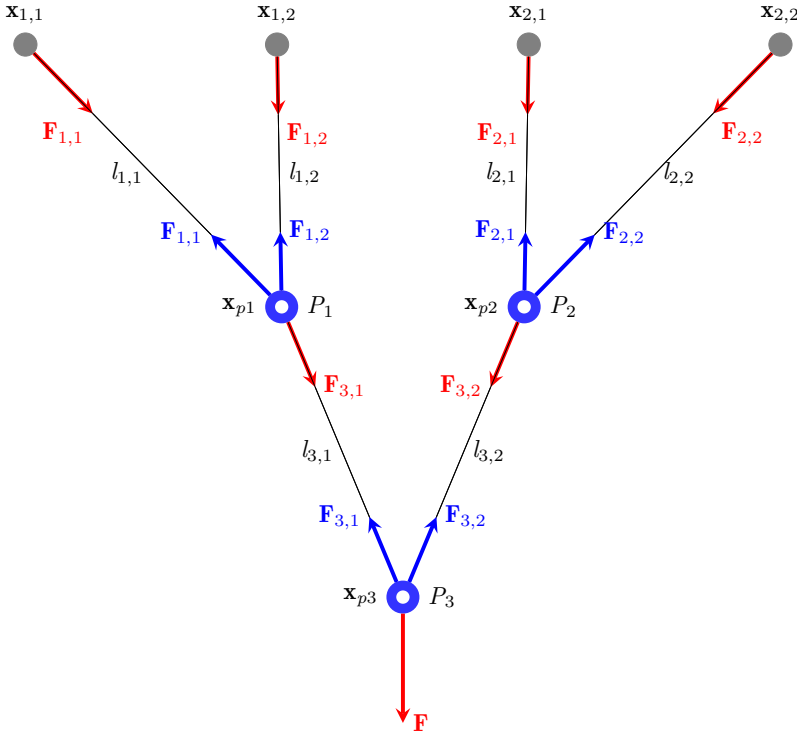


Figure 3.8 | Bridle system model notation, for a system of three pulleys ($\mathbf{P}_1, \mathbf{P}_2, \mathbf{P}_3$), defined by four attachment points $\mathbf{X}_a \in \mathbb{R}^3$.

This bridle system can be considered a nested three-pulley system, where the initial branches are given by two single pulley systems \mathbf{P}_1 (defined by $\mathbf{x}_{1,1}$, $\mathbf{x}_{2,1}$, and l_{p_1}) and \mathbf{P}_2 (defined by $\mathbf{x}_{1,2}$, $\mathbf{x}_{2,2}$, and l_{p_2}). These two systems are further bridged by the \mathbf{P}_3 pulley system, which has branch points defined by the pulley positions (\mathbf{x}_{p_1} and \mathbf{x}_{p_2}) of the previous systems.

The full bridle tree is traversed backwards from the final pulley, assembling the individual tensions $\mathbf{F}_1, \mathbf{F}_2$ and pulley positions \mathbf{X}_p until the fixed points of the system \mathbf{X}_a are reached. The complete nonlinear system of equations for the multi-pulley system is described using the base single pulley relations as defined in Equation 3.7. This leads to a set of generalised nonlinear equations where the unknowns are individual tether branch tensions $\mathbf{F}_{1,2}$ and the pulley positions \mathbf{X}_p are given as:

$$\begin{aligned} \mathbf{X}_p &= \{ \mathbf{x}_{p_1}, \mathbf{x}_{p_2}, \dots, \mathbf{x}_{p_n} \} \\ \mathbf{F}_1 &= \{ \mathbf{F}_{1,1}, \mathbf{F}_{1,2}, \dots, \mathbf{F}_{1,n} \} \\ \mathbf{F}_2 &= \{ \mathbf{F}_{2,1}, \mathbf{F}_{2,2}, \dots, \mathbf{F}_{2,n} \} \end{aligned} \quad (3.11)$$

Where the fixed attachment points \mathbf{X}_a on the wing and the individual pulley tether segment lengths \mathbf{L}_p along with the last external force of the system \mathbf{F} are the known system parameters, and defined as:

$$\begin{aligned}\mathbf{X}_a &= \{ \mathbf{x}_1, \mathbf{x}_2, \dots, \mathbf{x}_n, \mathbf{x}_{n+1} \} \\ \mathbf{L}_p &= \{ l_{p_1}, l_{p_2}, \dots, l_{p_n} \}\end{aligned}\tag{3.12}$$

These relations can be assembled into a system where the nodes are defined by the pulley positions \mathbf{X}_p and fixed attachment points \mathbf{X}_a , while the elements are defined by the individual tether segments \mathbf{L}_p , and wherein the nodal forces \mathbf{F}_1 and \mathbf{F}_2 need to be determined. The resulting set of matrices is solved using a similar Newton method to arrive at the unknown pulley positions \mathbf{X}_p and the forces at each node in the system $\mathbf{F}_{1,2}$ arising from an arbitrary system pulley force \mathbf{F} .

For the tri-tethered system, multiple such multi-pulley bridle systems are situated under the wing (see Figure 3.1). For such setups, there could be multiple solutions of pulley positions that lead to a force equilibrium for a given kite attitude. Thus, to obtain a unique solution for the forces at the bridle attachment points at the wing, an additional assumption ensuring that the three tethers are parallel is prescribed.

Hence, to describe the loading on the wing structure, for each unique aerodynamic state (arising from an angle of attack, sideslip, and apparent wind speed), after calculation of the aerodynamic forces, a solution for the system of nonlinear bridle equations needs to be determined i.e. $\varphi(\mathcal{B}) = \xi(\mathcal{A}, \mathbf{X}_a, \dots)$. Typically where the bridle attachment points $\mathbf{X}_a = f(\mathcal{S})$ are defined as some function of the structural domain. This is done to capture deformation effects from the structural domain, in subsequent higher-fidelity aerostructure models.

3.4. SUMMARY AND CONCLUSIONS

The focus of this research, the design space of the airborne portion of *AWES*, is categorised into three domains – the aerodynamic \mathcal{A} , the bridle system \mathcal{B} and the structural domain \mathcal{S} . Prior to design, methods to determine the loads in these respective domains are required. Models for the aerodynamic load and resulting bridle loads are presented. The implemented models pay special attention to the nonlinear operational regime of fixed-wing *AWE*. Care is taken to ensure the models are computationally efficient enough for typical iterative optimisation in the initial (conceptual and preliminary) design phase. This is achieved by balancing model fidelity, parameter knowledge and computational complexity.

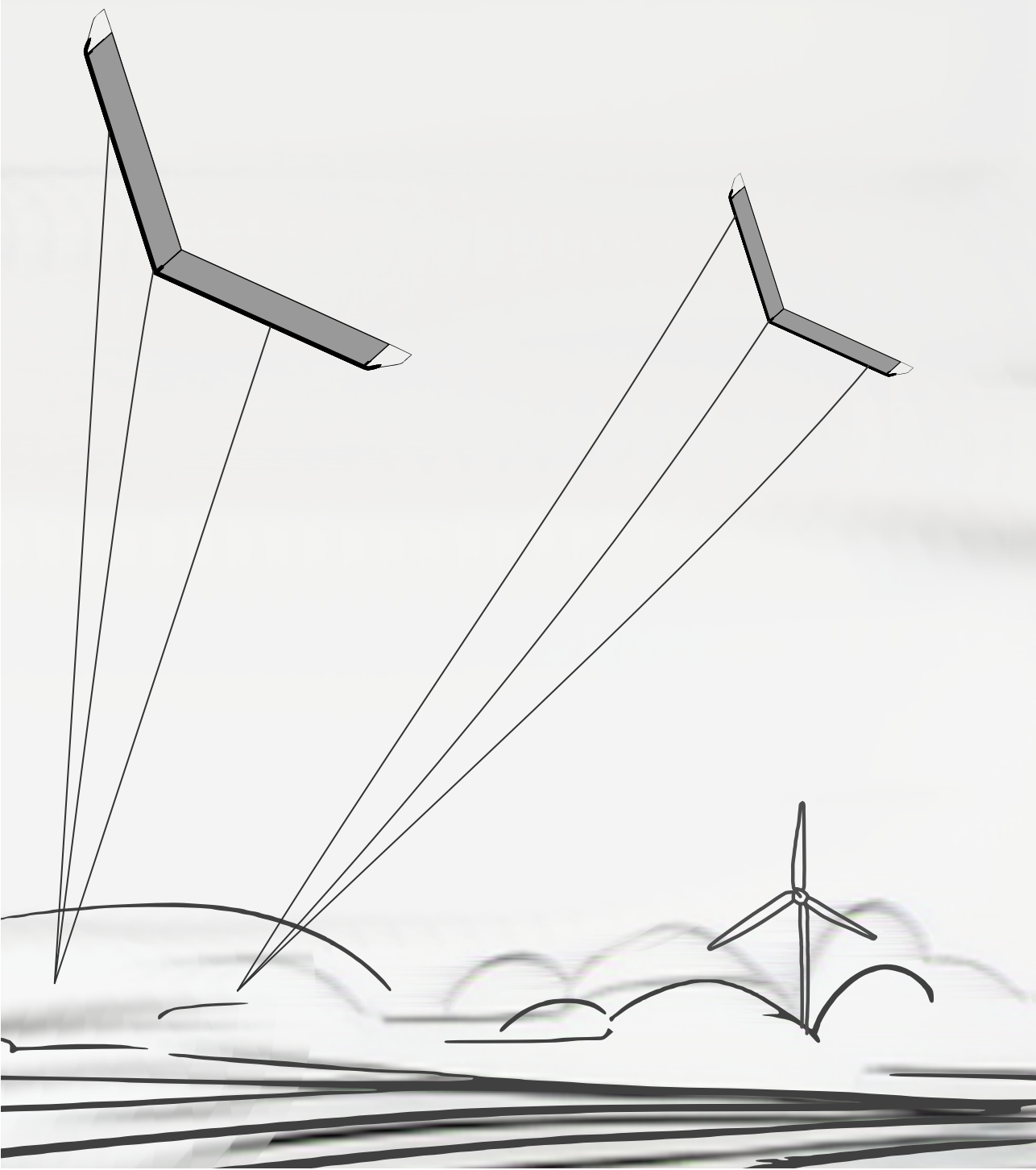
For the aerodynamic domain \mathcal{A} , *AWES* entails operation at high lift, near stall regions that typically display nonlinear effects. Therefore, a single-step nonlinear *VLM* method is employed. Unlike traditional *VLM* methods that add an ad-hoc local angle of attack contribution (α -methods) to match the local lift from the vortex and the viscous 2D airfoil lift, a so-called Γ method is implemented here [94]. In this method, the local angle of attack is not adjusted to match the 2D lift slope but instead expressed using rewritten fully nonlinear boundary conditions. This allows for a computationally fast method to compute the 3D aerodynamic response of the wing, including the large angle of attack (AoA) nonlinearities for initial iterative design.

A unique aspect of *AWE* is the bridle domain \mathcal{B} , consisting of a system of pulleys and tether segments under the wing. The bridle system is the interface that connects the wing structure to the main tether that runs to the ground station. Here, a model is proposed where the sub-

system of tethers and pulleys are modelled in the nominal equilibrium state to determine the force magnitude and direction at each attachment point on the wing. In this loading condition, the segments are under tension and thus can be modelled as straight, inextensible rigid members that extend between points. As the current scope is limited to the static structural response, dynamic effects, pulley mass and friction are neglected, thus allowing for the pulleys to be considered as points. These assumptions facilitate an efficient method to solve the bridle system state for each aerodynamic state of the system, already during the early design phases.

3

With these models, the external loads from the aerodynamic \mathcal{A} and the bridle system \mathcal{B} , required for the design of the wing structure, can thus be calculated. Subsequently, in **Chapter 4**, methods are proposed to couple the structural domain's response by prescribing positions of the aerodynamic and bridle domain ($\mathcal{X}_{\mathcal{A},\mathcal{B}}$) as functions of structural deformation.



Chapter 4

Design and simulation of composite AWE wings

Mathematics is only a tool and one should learn to hold the physical ideas in one's mind without reference to the mathematical form

—P. A. M. Dirac

ABSTRACT

This chapter covers the interactions between the aerodynamic \mathcal{A} , bridle \mathcal{B} and structural \mathcal{S} domains of composite airborne wind energy (AWE) wing design. With the previously covered aerodynamic and bridle model, a multi-level strategy for the anisotropic structural design space is explored here. The structural domain \mathcal{S} is split into a multi-fidelity solution space, starting from the laminate level, followed by 2D cross-sectional models for laminate layup and geometry, and subsequently 1D models for the global wing level deformations. Thus, this strategy allows for the selection of suitable fidelity, depending on which stage of the spiral design strategy one is in. Finally, a coupling strategy is proposed, capturing the aeroelastic response of the wing, while considering effects from \mathcal{A} , \mathcal{B} & \mathcal{S} domains.

4.1. STRUCTURAL DOMAIN

Exploring the structural design domain for composite structures requires a balance of computational cost and model fidelity. It typically is more challenging in comparison to isotropic models as summarised in Section 2.3.4. In this work, a multi-fidelity approach is proposed based on the assumptions described in Section 3.1.2. The structural response of the kite is obtained by simplifying the complex wing skeleton structure, restricting the initial design sizing to only the primary load-bearing structural member, the wing box.

The developed framework approaches the structural domain sizing as a multi-fidelity problem, assembling specific modules for the various elements of the wing box structure as outlined in Figure 4.1. These element-specific models are then integrated into a high-level global response model that utilises computed cross-sectional stiffness models, further employing ply stacking models for detailed sizing and manufacturing.

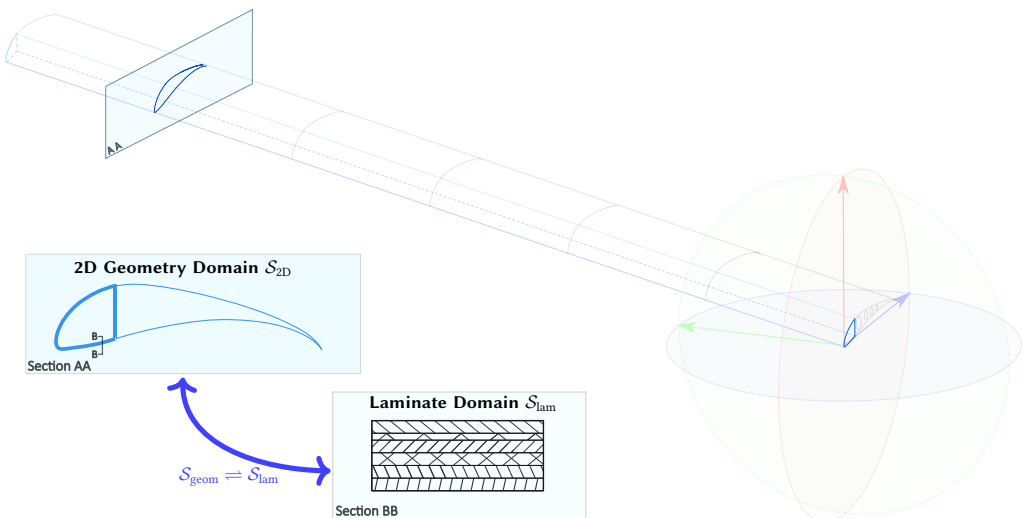


Figure 4.1 | Structural elements and computational domains of an anisotropic composite wing.

4.1.1. Anisotropic laminate structures

The wing box of the airborne wind energy system(s) (AWES) considered here utilises a carbon composite slender shell structure. The walls of this wing box are formed by building up individual layers (laminae) — where each layer (lamina) is a fibre-reinforced composite material that exhibits anisotropic material properties. Typically, each lamina has highly directional carbon fibres embedded into a resin matrix. Varying these lamina properties thus changes the wing box's structural response. Hence, these lamina-level properties also require modelling.

The global structural response $\mathcal{S} = \{\mathcal{S}_{2D}, \mathcal{S}_{1D}\}$ is obtained by breaking down the slender composite 3D shell structure to a 2+1D representation. This is achieved by discretising the D-box into characteristic 2D cross-sections arranged spanwise along the wing. These 2D cross-sections determine the stiffness characteristics given by \mathcal{S}_{2D} that are then utilised in a 1D beam model \mathcal{S}_{1D} to capture the 3D structural response of the D-box. This 2+1D reduction of the three-dimensional kite structure is depicted in Figure 4.2.

Each one-dimensional beam element is hence characterised by its cross-sectional stiffness. This

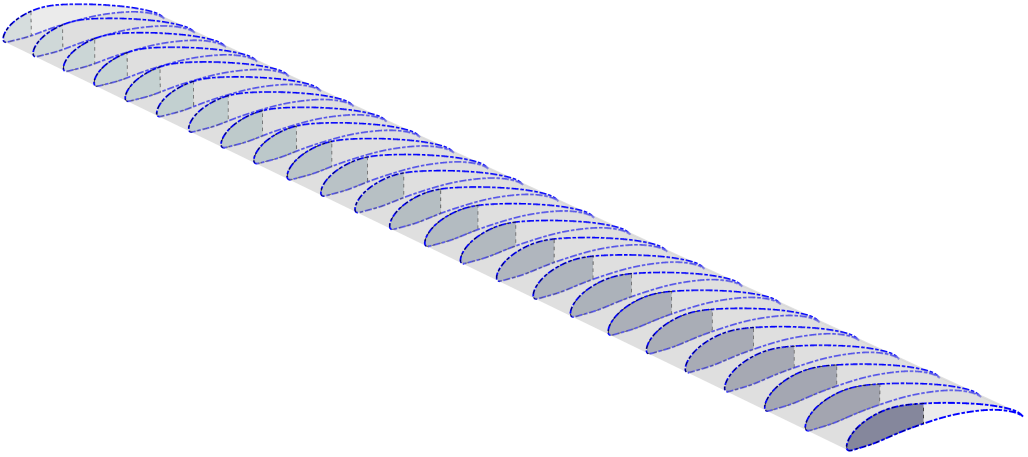


Figure 4.2 | Indicative wing with D-box defined by multiple 2D cross-sections stacked along the span.

stiffness is a function of the two-dimensional cross-sectional geometry, the laminate layup, and internal wall thickness. As illustrated in Figure 4.2 these parameters can be different at each node. Thus, the two-dimensional model captures the geometry and layup of the cross-section, while the one-dimensional model captures the planform geometry of the wing, such as span, sweep, and dihedral.

Asymmetric cross-sections along with varied lamination stacking sequences introduce coupling effects in slender composite structures between extension, bending and torsional stiffness, leading to bend-twist and extension-twist couplings [148]. To account for these, models that consider these anisotropic effects need to be employed. Given the overall goal of the computational framework for use in initial design exploration and optimisation, a trade-off is sought between computational cost, model parameter knowledge, and accuracy. Taking into account these coupling effects during analysis at an early design stage of the wing allows for the exploration of parameters to fine-tune the structural behaviour. Furthermore, it provides the ability to gauge the effects of exploiting these coupling effects for load alleviation and other aeroelastic phenomena such as roll-reversal and flutter [149, 150] already at the early design stages, avoiding expensive redesign cycles later in the design process.

The subsequent sections detail the models, starting with the composite laminate domain \mathcal{S}_{lam} that captures ply-level details that build up the laminate. These laminate level methods \mathcal{S}_{lam} feed into the 2D geometry domain \mathcal{S}_{2D} , which in conjunction with the 1D stiffness domain \mathcal{S}_{1D} describes the full structural domain \mathcal{S} .

4.2. STRUCTURAL LAMINATE DOMAIN \mathcal{S}_{lam}

A common methodology to account for the variations of each lamina layer is classical lamination theory (CLT). The method allows for the determination of the in-plane, out-of-plane and coupling stiffness parameters for the laminate stack. The resulting stiffness matrix \mathbf{ABD} is a symmetric 6×6 matrix that relates the applied loads to the associated strains in the laminate. The notation \mathbf{A} is used for the in-plane component, \mathbf{D} for the out-of-plane component and \mathbf{B} for the coupling parameters. Hence, to model the overall structural response of the wing structure (built up of multiple layers), it is vital to take into account the variation of the laminate's

stiffness as a function of the number and orientations of the layers of fibres.

4.2.1. Classical Laminate Theory

CLT provides a methodology to determine smeared stiffness properties for a laminate layup based on individual lamina properties. Some important assumptions made by this methodology are:

1. Each lamina layer is dominated by planar dimensions in comparison to the thickness dimension.
2. There is an infinitesimally thin layer of ideal adhesive that bonds each individual lamina layer together.
3. Kirchhoff-Love hypothesis enforces the assumption that the each ply remains plane during bending, while the shear deformation is linearly varying along the thickness of the laminate.

Considering each segment, composed of individual ply layers with unidirectional fibres, a ply level coordinate system is defined, where x_1 is aligned with the axis of the fibre, and x_2 is orthogonal to this axis as depicted in Figure 4.3a. The angle θ_{ply} is the angle between the ply axis and the global coordinate system.

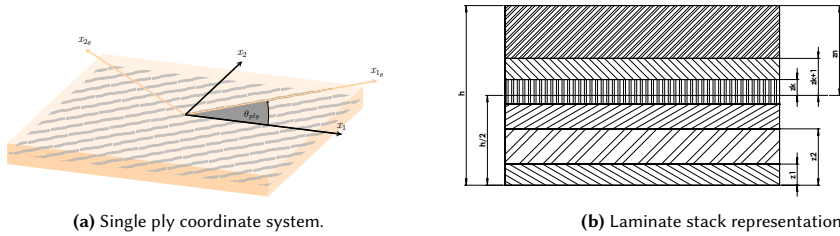


Figure 4.3 | Composite laminate notation for CLT.

Since the thickness of the ply is small compared to other dimensions, the assumption of plane stress reduces the stress-strain relationship in the material coordinate system to:

$$\begin{bmatrix} \epsilon_1 \\ \epsilon_2 \\ \gamma_{12} \end{bmatrix} = \begin{bmatrix} \frac{1}{E_{11}} & -\frac{\nu_{12}}{E_{11}} & 0 \\ -\frac{\nu_{21}}{E_{22}} & \frac{1}{E_{22}} & 0 \\ 0 & 0 & \frac{1}{G_{12}} \end{bmatrix} \begin{bmatrix} \sigma_1 \\ \sigma_2 \\ \tau_{12} \end{bmatrix} \quad (4.1)$$

Or expressed in the inverted form in terms of the reduced stiffness matrix \mathbf{Q} as:

$$\sigma_i = \mathbf{Q}_{ij} \epsilon_j \quad (4.2)$$

where

$$\mathbf{Q}_{ij} = \begin{bmatrix} Q_{11} & Q_{12} & 0 \\ Q_{21} & Q_{22} & 0 \\ 0 & 0 & Q_{66} \end{bmatrix} \quad (4.3)$$

The non-zero reduced stiffness matrix elements are expressed in terms of ply engineering constants as:

$$\begin{aligned}
 Q_{11} &= \frac{E_{11}}{1 - \nu_{12}\nu_{21}} \\
 Q_{22} &= \frac{E_{22}}{1 - \nu_{12}\nu_{21}} \\
 Q_{12} &= \frac{\nu_{21}E_{11}}{1 - \nu_{12}\nu_{21}} = \frac{\nu_{12}E_{22}}{1 - \nu_{12}\nu_{21}} = Q_{21} \\
 Q_{66} &= G_{66}
 \end{aligned} \tag{4.4}$$

Where E_{11} and E_{22} are the ply longitudinal and transverse Young's modulus respectively. G_{12} is the in-plane shear modulus while ν_{12} is the Poisson's ratio. To express the material coordinate stress strain relation in the global coordinate axis, Equation 4.3 can be reformed with the transformed reduced stiffness matrix $\bar{\mathbf{Q}}$ as:

$$\sigma_i = \bar{Q}_{ij}\epsilon_j \tag{4.5}$$

Where the transformation is a function of the ply rotation angle θ_{ply} and is given by:

$$\bar{\mathbf{Q}} = \mathbf{T}^{-1}\mathbf{Q}\mathbf{R}\mathbf{T}\mathbf{R}^{-1} \tag{4.6}$$

wherein

$$\mathbf{T} = \begin{bmatrix} \cos^2 \theta_{ply} & \sin^2 \theta_{ply} & 2 \cos \theta_{ply} \sin \theta_{ply} \\ \sin^2 \theta_{ply} & \cos^2 \theta_{ply} & -2 \cos \theta_{ply} \sin \theta_{ply} \\ -\cos \theta_{ply} \sin \theta_{ply} & \cos \theta_{ply} \sin \theta_{ply} & \cos^2 \theta_{ply} - \sin^2 \theta_{ply} \end{bmatrix} \tag{4.7}$$

$$\mathbf{R} = \begin{bmatrix} 1 & 0 & 0 \\ 0 & 1 & 0 \\ 0 & 0 & 2 \end{bmatrix} \tag{4.8}$$

Here, \mathbf{T} is the transformation matrix, and the matrix \mathbf{R} accounts for the usage of the engineering strain γ_{12} instead of the tensor strain ϵ_{12} . The stress strain relation from Equation 4.5 is expressed in the global coordinate system now as:

$$\begin{bmatrix} \sigma_x \\ \sigma_y \\ \tau_{xy} \end{bmatrix} = \bar{\mathbf{Q}} \begin{bmatrix} \epsilon_x \\ \epsilon_y \\ \gamma_{xy} \end{bmatrix} \tag{4.9}$$

When considering the stiffness of the complete laminate, the Kirchhoff-Love hypothesis which enforces the assumption that each ply remains planar during bending, while the shear deformation is linearly varying along the thickness of the laminate is imposed. Furthermore, given the Kirchhoff-Love hypothesis the strain variation is continuous though the laminate and is linearised around the mid ply strains (ϵ^0) and curvatures (κ) to result in the constituent relations for each ply k to be expressed as:

$$\begin{bmatrix} \sigma_x \\ \sigma_y \\ \tau_{xy} \end{bmatrix}_k = \bar{\mathbf{Q}}_k \left\{ \begin{bmatrix} \epsilon_x^0 \\ \epsilon_y^0 \\ \gamma_{xy}^0 \end{bmatrix} + z \begin{bmatrix} \kappa_x \\ \kappa_y \\ \kappa_{xy} \end{bmatrix} \right\} \tag{4.10}$$

Where $\bar{\mathbf{Q}}_k$ is the reduced stiffness matrix for the k^{th} ply in the laminate, and z is the thickness coordinate. For a general laminate consisting of n layers with arbitrary ply angles θ_{ply} at

each layer, the stress and moment results are determined by integrating through the thickness direction, leading to:

$$\begin{aligned} \begin{bmatrix} N_x \\ N_y \\ N_{xy} \end{bmatrix} &= \sum_{k=1}^n \int_{z_{k-1}}^{z_k} \left\{ \bar{\mathbf{Q}}_k \begin{bmatrix} \epsilon_x^0 \\ \epsilon_y^0 \\ \gamma_{xy}^0 \end{bmatrix} + z \bar{\mathbf{Q}}_k \begin{bmatrix} \kappa_x \\ \kappa_y \\ \kappa_{xy} \end{bmatrix} \right\} dz \\ \begin{bmatrix} M_x \\ M_y \\ M_{xy} \end{bmatrix} &= \sum_{k=1}^n \int_{z_{k-1}}^{z_k} \left\{ z \bar{\mathbf{Q}}_k \begin{bmatrix} \epsilon_x^0 \\ \epsilon_y^0 \\ \gamma_{xy}^0 \end{bmatrix} + z^2 \bar{\mathbf{Q}}_k \begin{bmatrix} \kappa_x \\ \kappa_y \\ \kappa_{xy} \end{bmatrix} \right\} dz \end{aligned} \quad (4.11)$$

Given that the midplane strains ϵ^0 and curvatures κ are independent of the laminate thickness, the stresses of a single layer are a simple integration, following which the stresses in each ply are summed. This allows Equation 4.11 to be expressed in matrix form as:

$$\begin{bmatrix} N_x \\ N_y \\ N_{xy} \end{bmatrix} = \mathbf{A} \begin{bmatrix} \epsilon_x^0 \\ \epsilon_y^0 \\ \gamma_{xy}^0 \end{bmatrix} + \mathbf{B} \begin{bmatrix} \kappa_x \\ \kappa_y \\ \kappa_{xy} \end{bmatrix} \quad (4.12)$$

$$\begin{bmatrix} M_x \\ M_y \\ M_{xy} \end{bmatrix} = \mathbf{B} \begin{bmatrix} \epsilon_x^0 \\ \epsilon_y^0 \\ \gamma_{xy}^0 \end{bmatrix} + \mathbf{D} \begin{bmatrix} \kappa_x \\ \kappa_y \\ \kappa_{xy} \end{bmatrix} \quad (4.13)$$

Where the \mathbf{A} , \mathbf{B} , \mathbf{D} are the laminate extension stiffness, coupling stiffness, and bending stiffness matrices respectively and are defined as:

$$\mathbf{A} = \sum_{k=1}^n \bar{\mathbf{Q}}(h_k - h_{k-1}) \quad (4.14)$$

$$\mathbf{B} = \frac{1}{2} \sum_{k=1}^n \bar{\mathbf{Q}}(h_k^2 - h_{k-1}^2) \quad (4.15)$$

$$\mathbf{D} = \frac{1}{3} \sum_{k=1}^n \bar{\mathbf{Q}}(h_k^3 - h_{k-1}^3) \quad (4.16)$$

Thus, the constituent stress strain relations for an arbitrary layup laminate can be concisely expressed in matrix form as:

$$\begin{Bmatrix} N \\ M \end{Bmatrix} = \begin{Bmatrix} \mathbf{A} & \mathbf{B} \\ \mathbf{B} & \mathbf{D} \end{Bmatrix} \begin{Bmatrix} \epsilon \\ \kappa \end{Bmatrix} \quad (4.17)$$

The equivalent laminate engineering constants can be determined using the stress and strain constituent relations from Equation 4.17, by individually setting each load component and determining the resulting relationship between the components. For example, to determine the equivalent Young's modulus of the laminate in the x direction, E_x Equation 4.17 is expanded

into the full matrix form to obtain:

$$\begin{bmatrix} N_x \\ 0 \\ 0 \\ 0 \\ 0 \\ 0 \end{bmatrix} = \begin{bmatrix} A_{11} & A_{12} & A_{16} & B_{11} & B_{12} & B_{16} \\ A_{21} & A_{22} & A_{26} & B_{21} & B_{22} & B_{26} \\ A_{61} & A_{62} & A_{66} & B_{61} & B_{62} & B_{66} \\ B_{11} & B_{12} & B_{16} & D_{11} & D_{12} & D_{16} \\ B_{21} & B_{22} & B_{26} & D_{21} & D_{22} & D_{26} \\ B_{61} & B_{62} & B_{66} & D_{61} & D_{62} & D_{66} \end{bmatrix} \begin{bmatrix} \epsilon_x^0 \\ \epsilon_y^0 \\ \gamma_{xy}^0 \\ \kappa_x \\ \kappa_y \\ \kappa_{xy} \end{bmatrix} \quad (4.18)$$

Equation 4.18 after solving and simplifying yields the expression for the laminates equivalent Young's modulus E_x as:

$$E_x = \frac{N_x/h}{\epsilon_x} = \frac{1}{h} \left\{ \begin{array}{c} \mathbf{A} \quad \mathbf{B} \\ \mathbf{B} \quad \mathbf{D} \end{array} \middle/ \begin{array}{c} A_{22} \quad A_{26} \quad B_{21} \quad B_{22} \quad B_{26} \\ A_{62} \quad A_{66} \quad B_{61} \quad B_{62} \quad B_{66} \\ B_{12} \quad B_{16} \quad D_{11} \quad D_{12} \quad D_{16} \\ B_{22} \quad B_{26} \quad D_{21} \quad D_{22} \quad D_{26} \\ B_{62} \quad B_{66} \quad D_{61} \quad D_{62} \quad D_{66} \end{array} \right\} \quad (4.19)$$

The other laminate engineering constants (E_y, ν_{xy}, ν_{yx} and G_{xy}) are calculated similarly and for the sake of brevity are not described.

4.2.2. Lamination parameters

CLT allows for the determination of the laminate stiffness matrix $ABD = f(\mathbf{Q}_k(\theta_{ply}), t_{ply}, \dots)$. This essentially mandates that for each stiffness required from the laminate domain $\varphi(\mathcal{S}_{lam})$, knowledge of individual fibre orientation details at the ply level is required. Considering a typical D-box (Figure 4.1) has multiple cross-sections, and each of these cross-sections is discretised into multiple such \mathcal{S}_{lam} elements, the complexity and number of design variables rapidly explode.

Here, instead, a method is utilised that abstracts one level of complexity, arising from the fibre orientation θ_{ply} namely lamination parameters. This is done by decomposing the stiffness of laminate as a function of material-dependent properties $\mathbf{\Gamma} = f(t_{ply}, \mathbf{U})$, and the individual fibre orientations of each lamina $\xi = f(\theta_{ply})$. This decoupling allows for the expression of the laminate stiffness explicitly using lamination parameters. Thus facilitating expressing the stiffness in terms of material invariants and layup sequences $\mathbf{ABD} = f(\mathbf{\Gamma}, \xi^{A,B,D})$.

The material invariants \mathbf{U} as the name suggests, consider the material properties of the laminate and are expressed as a function of the reduced stiffness matrix [151] of the unidirectional lamina \mathbf{Q}_{ij} :

$$\begin{aligned} U_1 &= (3Q_{11} + 3Q_{22} + 2Q_{12} + 4Q_{66})/8 \\ U_2 &= (Q_{11} - Q_{12})/2 \\ U_3 &= (Q_{11} + Q_{22} - 2Q_{12} - 4Q_{66})/8 \\ U_4 &= (Q_{11} + Q_{22} + 6Q_{12} - 4Q_{66})/8 \\ U_5 &= (Q_{11} + Q_{22} - 2Q_{12} + 4Q_{66})/8 \end{aligned} \quad (4.20)$$

These invariants can be more conveniently expressed in tensor form $\Gamma_{0\dots 4}$ as:

$$\begin{aligned} \Gamma_0 &= \begin{bmatrix} U_1 & U_2 & 0 \\ U_4 & U_1 & 0 \\ 0 & 0 & U_5 \end{bmatrix}, & \Gamma_1 &= \begin{bmatrix} U_2 & 0 & 0 \\ 0 & -U_2 & 0 \\ 0 & 0 & 0 \end{bmatrix}, \\ \Gamma_2 &= \frac{1}{2} \begin{bmatrix} 0 & 0 & U_2 \\ 0 & 0 & U_2 \\ U_2 & U_2 & 0 \end{bmatrix}, & \Gamma_3 &= \begin{bmatrix} U_3 & -U_3 & 0 \\ -U_3 & U_3 & 0 \\ 0 & 0 & -U_3 \end{bmatrix}, & \Gamma_4 &= \begin{bmatrix} 0 & 0 & U_3 \\ 0 & 0 & -U_3 \\ U_3 & -U_3 & 0 \end{bmatrix} \end{aligned} \quad (4.21)$$

Similarly, the effects of the laminate layup sequence are captured by the lamination parameters. The in-plane lamination parameters ξ^A , out-of-plane parameter ξ^D and coupling parameter ξ^B are then determined by:

$$\begin{aligned} \xi_{[1,2,3,4]}^A &= \frac{1}{2} \int_{-1}^1 [\cos 2\theta(\bar{z}) \quad \sin 2\theta(\bar{z}) \quad \cos 4\theta(\bar{z}) \quad \sin 4\theta(\bar{z})] d\bar{z} \\ \xi_{[1,2,3,4]}^B &= \int_{-1}^1 [\cos 2\theta(\bar{z}) \quad \sin 2\theta(\bar{z}) \quad \cos 4\theta(\bar{z}) \quad \sin 4\theta(\bar{z})] \bar{z} d\bar{z} \\ \xi_{[1,2,3,4]}^D &= \frac{3}{2} \int_{-1}^1 [\cos 2\theta(\bar{z}) \quad \sin 2\theta(\bar{z}) \quad \cos 4\theta(\bar{z}) \quad \sin 4\theta(\bar{z})] \bar{z}^2 d\bar{z} \end{aligned} \quad (4.22)$$

Where $\theta(\bar{z})$ is the laminate orientation distribution expressed as a function of the thickness normalised height $\bar{z} = (2/h)z$. Subsequently, the bending, extension and coupling laminate stiffness tensors \mathbf{A} , \mathbf{B} and \mathbf{D} are expressed as a linear combination of the material invariants $\Gamma_{0\dots 4}$ and the lamination parameters $\xi^{A,B,D}$ just defined as:

$$\begin{aligned} \mathbf{A} &= h(\Gamma_0 + \Gamma_1 \xi_1^A + \Gamma_2 \xi_2^A + \Gamma_3 \xi_3^A + \Gamma_4 \xi_4^A) \\ \mathbf{B} &= \frac{h^2}{4} (\Gamma_1 \xi_1^B + \Gamma_2 \xi_2^B + \Gamma_3 \xi_3^B + \Gamma_4 \xi_4^B) \\ \mathbf{D} &= \frac{h^3}{12} (\Gamma_0 + \Gamma_1 \xi_1^D + \Gamma_2 \xi_2^D + \Gamma_3 \xi_3^D + \Gamma_4 \xi_4^D) \end{aligned} \quad (4.23)$$

Modelling the laminate stiffness using lamination parameters aids in the subsequent optimisation performed using the overall computational framework. By decoupling the laminate stiffness from fibre orientation, lamination parameters efficiently define the stiffness of a laminate. Thus, a laminate with an arbitrary number of plies and any arbitrary stacking sequence can be described by the material invariants Γ and twelve lamination parameters. Furthermore, detailed stacking sequences are not required when finding a viable solution in the lamination parameter domain during initial topology optimisation. This allows for the solution of laminate stiffness-based objective functions directly $J = f(\xi^{A,B,D}, \dots)$. The subsequent step of solving for the particular stacking sequence(s) that result in these parameters can be solved as a separate optimisation problem, typically prior to manufacturing design stages.

Of note, from the perspective of the cross-sectional modeller, the methodology to determine the laminate stiffness is insignificant. The motivation for employing lamination parameters here is from the spiral systems model, allowing for cross-section topology design optimisation early in the design cycle. Some examples of such topology optimisation exercises are formulated in subsequent Chapters.

4.3. STRUCTURAL GEOMETRIC DOMAIN S_{2D}

Prior to determining the global structural response of the wing in terms of deflections and rotations, a method to determine the stiffness of the wing section is required. As detailed earlier, the primary loadbearing structure of the wing, the so-called “wing box” must withstand the loads that arise from the aerodynamic and bridle forces.

Unlike the conventional rectangular wing box section found in most traditional aircraft, the wing boxes for the wing considered here are located in the leading edge section, leading to a characteristic “D” shape - hence the name D-box as pictured in Figure 4.4. This poses a design challenge, as unlike the rectangular wing box that is symmetric, the analysis of the D-box should consider the asymmetric geometry, over and above the usual thickness variation. Considerations and the final modelling strategy utilised in this work are detailed subsequently.

4



Figure 4.4 | Early prototype wing box formed by atypical D-box positioned at the leading edge (circa 2016, image courtesy of EnerKite).

Methodology

Determination characteristic cross-sectional stiffness properties for wing sections can be broken down into the following steps:

1. Discretise the cross-section into a representative number of elements.
2. Determine equivalent geometrical and stiffness parameters for each discretised element.
3. Determine the stiffness tensor for the entire cross-section based on the contribution of these elements.

4.3.1. Cross-section topology parametrisation and discretisation

The D-box is a fibre reinforced composite structure that is built up from multiple plies — where each lamina could theoretically be of different material and/or fibre orientations and thus, as

a whole, exhibits anisotropic material properties. A typical cross-section with the individual layers of the leading edge portion of the D-box is visualised in Figure 4.5b. Here the individual lamina is depicted in different colours to indicate that each could have a combination of different thicknesses, fibre orientations, and material properties.

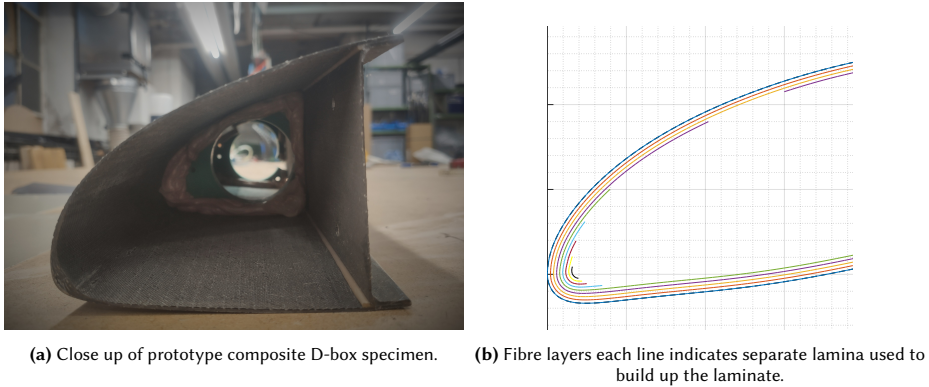


Figure 4.5 | Capturing geometry, laminate layup, and thickness from the 2D D-box cross-section.

As seen from Figure 4.5b, the interior thickness of this shell is not constant. When considering this from an optimisation point of view, the outer geometric manifold is determined by the aerodynamic domain $\mathcal{A}_{profile}$. Thus, from a strictly structural perspective, the outer boundary of the problem is defined, leaving an internal volume where structural reinforcements need to be placed. For conventional wings and wind turbine blades, these would be skins, spars and stringers. However, in the current D-box, these functions of such reinforcements are provided directly by shell members. These shell members are idealised by layer lines in each cross-section of the D-box.

Topology parameterisation strategies broadly consist of solid isotropic materials with penalization (SIMP), which utilises a penalisation function to either allow or deny material placement on a grid discretisation of the topology. The other class employs boundary-based methods, where the boundary manifolds are determined by some implicit function, which can implicitly or explicitly be used to perturb these boundaries. In this work, to be optimisation friendly enough for the initial design stage, a robust strategy utilising splines and Dirichlet tessellation meshes is developed, allowing for the variation of the internal geometry of the D-box. This strategy is briefly described subsequently. The nuances of converting the spline discretisation to equivalent laminate domain \mathcal{S}_{lam} parameters are detailed in Section 5.1.2.

Typically, the D-shaped wing box (or D-box) consists of a shell that follows the aerodynamic profile near the leading edge and a vertical web reinforcement further aft at some chordwise location. As described previously in Figure 4.5b, the composition of these sections is built up with an arbitrary number of layers of varying ply materials and ply orientations.

A methodology to account for the geometry and thickness parameters using a spline-based discretisation of the internal geometric profile of the D-box is explored. By altering the path of this spline, the thickness of the internal material can be perturbed smoothly to allow for varying thickness distribution along the internal profile. This allows for the inclusion of locally reinforced regions by increasing material thickness. This is performed near the leading edge, for example, as can be seen from a typical internal D-box geometry shown in Figure 4.5b.

The methodology for the spline parameterisation builds upon the class shape transformation (CST) approximation method that is commonly used in aerofoil and wing optimisation [152]. The CST approximation utilises a combination of class functions and shape parameters to describe the spline control points. As the name suggests, the class function defines a base class of a specific shape, while the shape function then describes perturbations of this class shape. Thus, defining features of a particular class like a rounded leading edge and sharp trailing edge can be described by the class function. When the rough domain is known, such as for the aerofoils here, the class function can be fixed. Thereby reducing the optimisation variables to only the shape function. Compared to traditional Bezier splines, this reduces the number of design variables required to describe the aerofoil's geometry. Using this methodology, a generalised shape can be described using the relation:

$$\zeta(\Psi) = \underbrace{C_{N_2}^{N_1}(\Psi)}_{\text{Class function}} \cdot \underbrace{\sum_{i=0}^n B_i S_i(\Psi)}_{\text{Shape function}} \quad (4.24)$$

where, $\Psi = x/c$ is the non-dimensional position along the chord, and $\zeta = y/c$ is the non-dimensional position in the thickness axis. $N_{1,2}$ are the characteristic class coefficients, and B_i is the shape coefficient vector. For typical NACA style aerofoil with blunt leading edges, the class coefficients are given by $N_1 = 0.5$, $N_2 = 1.0$. Thus, polynomial weights \mathcal{A} for the shape function are then the design parameters utilised to describe the airfoil. In Kulfan's original work, she suggests Bernstein polynomials for the shape function [152].

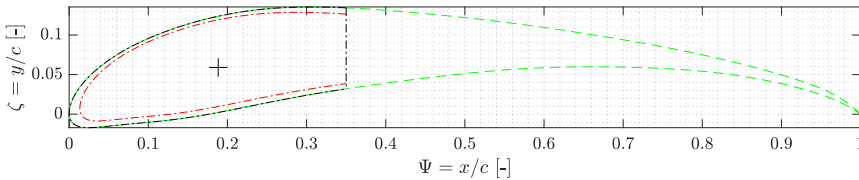


Figure 4.6 | Internal D-box geometry parameterisation. External aerofoil is depicted by dashed green lines. The location of the D-box is shown in black, and the internal C-shell thickness bounded by spline is shown in red.

This spline-based discretisation approach yields an efficient methodology to describe the internal geometry with a relatively low number of design parameters. The internal D-box geometries depicted in Figure 4.8 are obtained using a spline with an order of 9 for each of the upper and lower surfaces (i.e. $n_o = n_l = 9$). This allows the complete internal geometry to be described using only 20 design variables for this particular aerofoil. Hence, by varying the spline parameters, the shape of the internal geometry can be manipulated.

However, the classical CST parametrisation has a limit when it comes to capturing smaller local perturbations in the geometry. This becomes an area of interest when considering certain aspects, for example, prescribing local boundary thickness constraints in the C-shell for improved load transfer from bridle attachment fixtures. An example of classical CST parametrisation's

inability to deal with local geometrical changes are illustrated in Figure 4.7. Splines of increasing order are required to capture local shape change accurately. By sufficiently increasing the Bernstein polynomial order, $n_o = 20$ in this example, the local perturbation is approximated relatively well — however this leads to instabilities near the straight sections leading to the dip, as seen by the oscillatory behaviour.

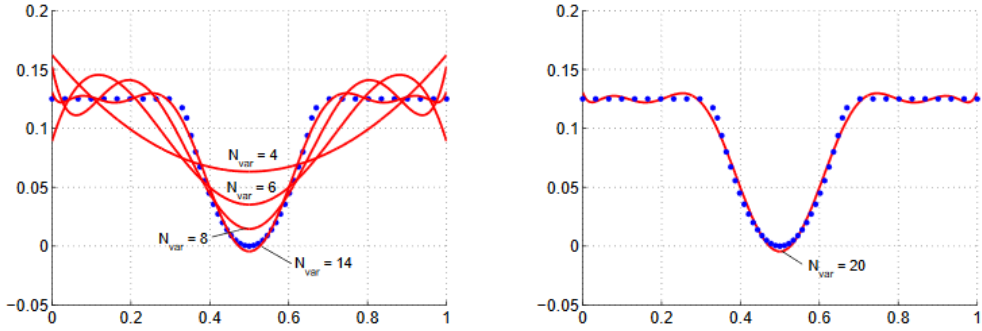


Figure 4.7 | Limitation of CST approximations for local deformations [153].

In this work, an extension to the CST that replaces the Bernstein polynomial representation with a Bezier spline is employed [153]. This methodology allows for local refinements while maintaining a relatively low number of overall design variables. Hence the thickness of the internal geometry along the profile can be locally varied to introduce specific reinforcements directly in the spline domain.

One such example would be additional thickening at the leading edge of the profile, as depicted in Figure 4.8a. It can be observed that there is an asymmetric thickness distribution, where the upper profile has a distinctly lower thickness than the lower surface. This would be another example of local refinement. This reinforcement is due to the bridle attachment points located on the lower surface, resulting in a localised force introduction region. This is compensated for by a gradual local thickening of the lower surface around the chordwise location of the attachment point. Furthermore, with the parametrisation implemented, constraints on the thickness can be easily introduced. An exaggerated example of thickening only the upper surface of the C-shell after 5% of the chord is shown in Figure 4.8b. An additional benefit of this methodology is that it leads to a smooth increase in the thickness with no local step changes.

The implemented spline-based geometry parametrisation allows for an efficient description of the geometric domain available for structural reinforcement as some function of these splines. Hence, for a given D-box $\mathcal{S}_{geom} = f(\zeta_{Dbox}, \dots)$, where, for n cross-sections in the D-box, $\zeta_{Dbox} = \{\zeta_1, \zeta_2, \dots, \zeta_n\}$. A detailed description of the implementation of the transformation of these smooth continuous splines into discretised thicknesses required for optimisation is found in Section 5.1.2 of Chapter 5.

4.3.2. Stiffness parameters - analytical approach

With the geometry described and discretised as $\mathcal{S}_{geom} = \varphi(\zeta_{Dbox}, \dots)$, the next step is to determine a characteristic stiffness for the full cross-section as a function of this geometry and laminate stiffness parameters, essentially $\mathcal{S}_{2D} = f(\mathcal{S}_{geom}, \varphi(\mathcal{S}_{lam}), \dots)$. A naïve analytical

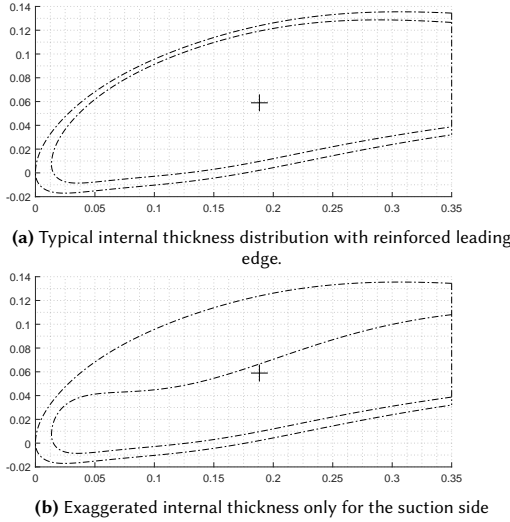


Figure 4.8 | Internal thickness distribution of the D-box discretised by splines.

approach dubbed the Segmented Cross Section Modeller (SCSM) is outlined first, followed by a finite element (FE) method.

From continuum mechanics, the stress strain relations can be simplified into the contracted form as:

$$\epsilon = \frac{1}{2} [\nabla \mathbf{u} + \nabla \mathbf{u}^T] \quad (4.25)$$

$$\sigma_i = \mathbf{C}_{ij} \epsilon_j \quad (4.26)$$

The stress-strain relation for any thin walled composite beam with an arbitrary cross-section and ply layup neglecting the traverse shear warping can be expanded as [154]:

$$\begin{bmatrix} N_x \\ M_y \\ M_z \\ \tau \end{bmatrix} = \begin{bmatrix} C_{11} & C_{12} & C_{13} & C_{14} \\ C_{21} & C_{22} & C_{23} & C_{24} \\ C_{31} & C_{32} & C_{33} & C_{34} \\ C_{41} & C_{42} & C_{43} & C_{44} \end{bmatrix} \begin{bmatrix} \epsilon_x \\ \kappa_y \\ \kappa_z \\ \beta \end{bmatrix} \quad (4.27)$$

Where N and M are the force and moment components in their respective axis, τ is the torque, ϵ is the normal strain, κ the curvatures of the beam, and β is the first derivative of the twist along the axial (spanwise) axis.

When considering an uncoupled cross-section, the stiffness tensor in Equation 4.27 can be expressed utilising the Euler-Bernoulli relations as:

$$\mathbf{C}_{ij} \approx \begin{bmatrix} EA & ES_z & ES_y & 0 \\ ES_z & EI_y & EI_{yz} & 0 \\ ES_y & EI_{yz} & EI_z & 0 \\ 0 & 0 & 0 & GJ \end{bmatrix} \quad (4.28)$$

The uncoupling is at best an approximation, but allows for the application of 2D CLT to determine the equivalent stiffness parameters of the composite laminate cross-section. How-

ever, this method does not capture all the deformation couplings that are inherent to slender composite beam structures [155]. While this method is limited within the bounds of these assumptions, it provides a simple first order estimation of the stiffness parameters of a composite cross-section with symmetrical geometry. Thus, to estimate the engineering parameters of the overall cross-section $[\bullet]^{sec}$, while allowing for varying laminate materials, the equivalent laminate stiffness properties of each segment $[\bullet]^{seg}$ is integrated across the cross-section to obtain the smeared cross-sectional stiffness:

$$\begin{bmatrix} EA \\ EI \\ ES_- \end{bmatrix}^{sec} \approx \int_S \begin{bmatrix} EA \\ EI \\ ES_- \end{bmatrix}^{seg} \approx \sum_{s=1}^M \begin{bmatrix} EA \\ EI \\ ES_- \end{bmatrix}_s^{seg} \quad (4.29)$$

Where M is the number of discretised sections and the subscript s indicates the index of the segment.

Segment Stiffness Parameters

To obtain the overall cross-section stiffness, equivalent geometric and laminate stiffness properties are required for each discretised segment in the cross-section. The areas and moment of inertias for each segment are calculated by simple integrations, assuming that the planar region has a uniform density [156]. Hence, for each segment with region S enclosed by the boundary, the areas and moments are given trivially by:

$$\begin{aligned} A &= \int \int_S dx dy \\ I_{xx} &= \int \int_S y^2 dx dy \\ I_{yy} &= \int \int_S x^2 dx dy \end{aligned} \quad (4.30)$$

Any method to determine laminate stiffness parameters \mathcal{S}_{lam} as described previously in Section 4.2 can be utilised to arrive at the equivalent segment stiffness properties $\{E_x, E_y, \nu_{xy}, \nu_{yx}, G_{xy}\}^{seg}$. Subsequently, the contribution of individual segment stiffness parameters towards the overall cross-section can be calculated using the smeared approach from Equation 4.29.

Cross-Section Stiffness

With the individual segment engineering constants and geometrical parameters known, the axial stiffness parameters can be determined by a simple integration about the domain, considering that the moments are already transferred to the respective global coordinate system. The torsional stiffness of the cross-section is calculated using the Bredt shear flow theory [157]. For a closed contour s , applied torque T is given by:

$$T = \oint_s pq ds \quad (4.31)$$

Given the thin-walled nature of the problem, the torsional stress τ in the section is assumed to be distributed evenly across the contour and is given by:

$$\tau = \frac{q}{t(s)} = \frac{T}{2t(s)A_e} \quad (4.32)$$

Where q is the shear flow, t is the thickness of contour, that can vary along the contour s , and A_e is the enclosed area by the contour middle line. The constituent stress-strain relations from Equation 4.27 are utilised to determine the torsional stiffness as:

$$\beta = \frac{d\phi}{dx} = \frac{q}{2A_e} \oint_s \frac{ds}{Gt} \quad (4.33)$$

Substituting Equation 4.32 into the above, the torsional stiffness can be solved for as:

$$GJ = \frac{4A_e^2}{\oint_s \frac{ds}{Gt}} \quad (4.34)$$

Hence, the cross-section's torsional stiffness is determined using each segment's thickness and in-plane shear modulus. Finally, collecting the stiffness terms from Equation 4.29, the required approximations of the cross-section stiffness matrix can be determined.

4.3.3. Stiffness parameters - FE approach

The previously outlined analytical method has limitations concerning neglecting particular shear and coupling effects. To obtain the fully coupled cross-sectional stiffness properties of the 3D structure, an anisotropic thin-walled cross-section modeller developed by Ferede *et al.* [158] is utilised.

The 2D finite element model builds upon the geometrically exact shell theory from Simo *et al.* [159] and is based on additional assumptions of small displacements and rotations. The FE implementation uses linear Hermitian elements to discretise the cross-section, where each element takes into account the equivalent laminate geometry and stiffness parameters S_{lam} as outlined in Section 4.2. This is done by decomposing the shell displacement components into beam displacement and solving for the warping functions using a variational asymptotic approach by minimising the strain energy per unit length. As this is essentially the St. Venant solution to the shell problem, usual assumptions of the cross-section being far away from the boundary and load introduction must be observed. Thus, the modeller can calculate the fully populated 6×6 Timoshenko S and additionally provides the reduced 4×4 Euler-Bernoulli stiffness matrix. A schematic of the reduction of the shell problem to a prismatic beam, along with relevant notation, is given in Figure 4.9. The reader is recommended to consult the original paper for implementation details [158]. Unlike the previous analytical approach, the FE solver is cross-section agnostic and can be utilised with arbitrary geometry in conjunction with open, closed, single-cell, and multi-cell composite sections.

4.3.4. Numerical case studies

The performance of the Segmented Cross Section Modeller (SCSM) is evaluated for a few representative cross-sections, and the results are compared to Euler-Bernoulli stiffness that can also be calculated by the described 2D FE composite cross-section modeller (DCAT) [158]. The simulations were carried out on an AS4/3501-6 composite and the engineering constants used are listed in Table 4.1.

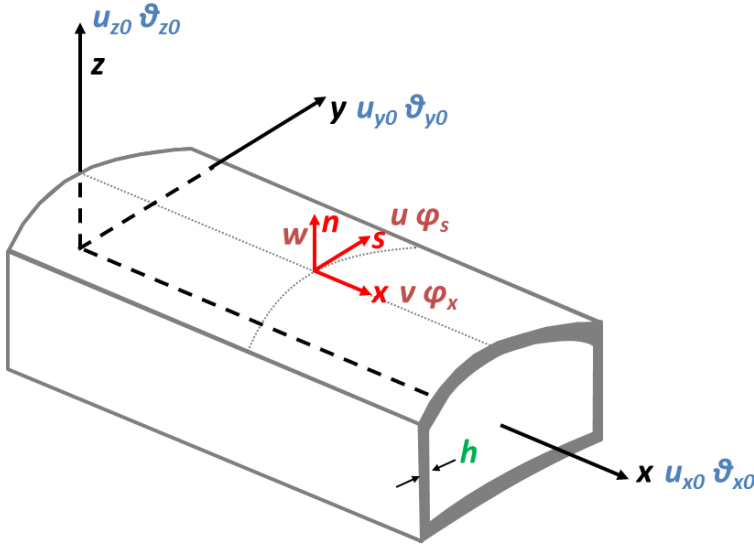


Figure 4.9 | 2D FE solver based on the assumption that cross-section can be modelled as a prismatic slender shell structure [158].

Table 4.1 | Engineering constants for AS4/3501-6 carbon epoxy composite [160].

Longitudinal modulus	E_{11}	148	GPa
Transverse modulus	E_{22}	10.5	GPa
In-plane shear modulus	G_{12}	5.61	GPa
Poisson's ratio	ν_{12}	0.28	–
Density	ρ	1.449×10^3	kg/m ³

Box Cross Section

A simple rectangular box section with a quasi-isotropic $[\pm 45, 0, 90]_s$ layup is first analysed. To evaluate the relative performance of these models, the finite element mesh utilises the same number of nodes as the number of segments in the SCSM method, as shown in Figure 4.10. Moreover, the relative percentage error is shown in the figure, along with the absolute stiffness parameter values. For the comparisons carried out, only the diagonal elements are considered, neglecting the off-diagonal coupling elements of the stiffness tensor. Thus, this leads to an infinite relative error for specific terms of the stiffness tensor. While there is an agreement in the axial stiffness parameters, the torsional stiffness is significantly under predicted.

Circular Cross Section

For the circular cross-section, the same ply layup $[\pm 45, 0, 90]_s$ is utilised, increasing the number of segments to 100. The increase in the number of elements leads to an agreement of $\approx 1\%$ to DCAT as seen in Figure 4.11. The torsional stiffness is again drastically under predicted by SCSM.

Box Section

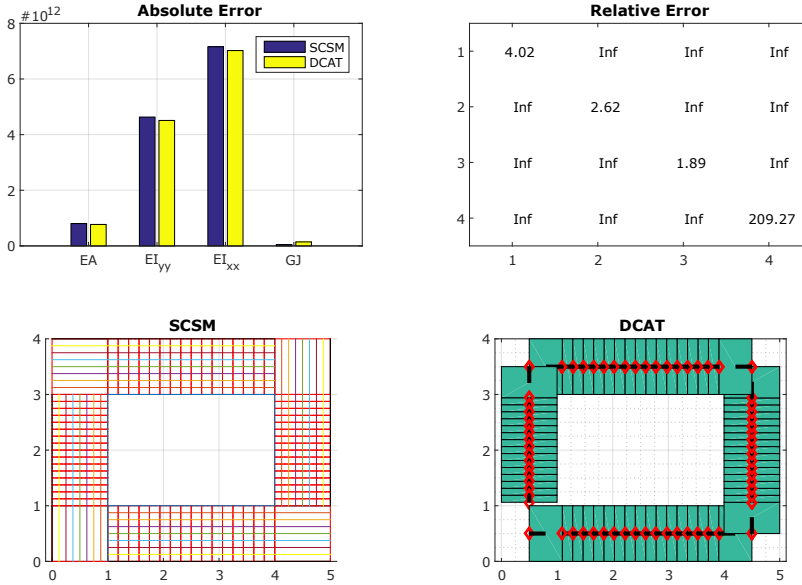


Figure 4.10 | Rectangular box section - comparison between SCSM and DCAT.

Dbox Cross Section

A characteristic Dbox cross-section is simulated. All the test cases presented above featured a uniform cross-section thickness. However, this aerofoil cross-section features a non-uniform thickness profile. To facilitate modelling the laminate stacking sequence in the profile, each segment utilises a master ply layup template to determine the relevant ply angles for each discretised segment. However, since both models utilise the same number of elements, the input to the models $\{S_{lam}\}$ remains the same. The results are seen in Figure 4.12.

Yet again, while there is an excellent agreement in the axial stiffness components ($\leq 0.30\%$ relative error), the torsional stiffness is significantly under predicted and needs further investigation.

To conclude, for the considered test cases with typical cross-sections, the analytical method displays good agreement in predicting the axial stiffness components when compared to the FE method. However, SCSM grossly under predicts the torsional stiffness parameter. This is attributed to the inability of SCSM to predict the shear flow and shear centre. There are analytical methods for predicting shear flow in symmetrically balanced ply laminate cross-sections [161]. Nevertheless, an extension for the prediction of torsional stiffness for an arbitrary cross-section and ply-layup is disregarded at this stage. This is motivated by the larger computational cost arising from the calculation for each nodal ABD stiffness (S_{lam}) as compared to the determination of the cross-sectional stiffness. This is described in further detail subsequently.

Circle Section

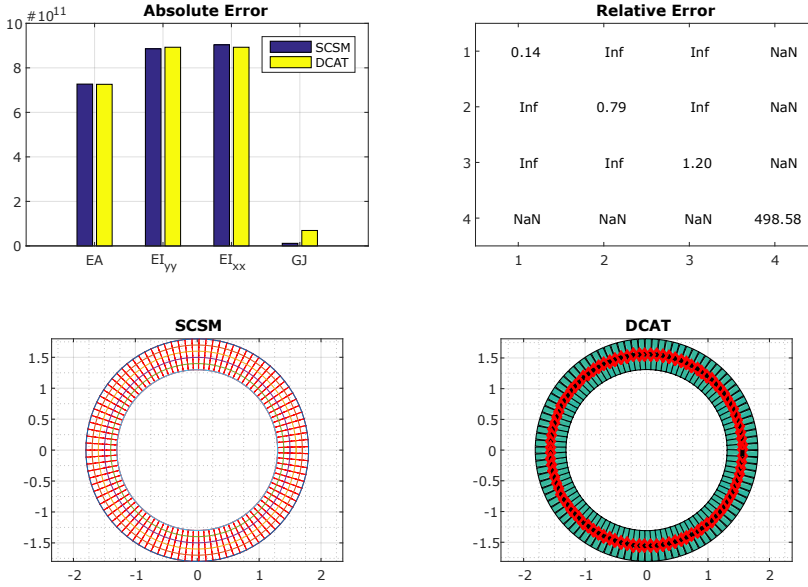


Figure 4.11 | Circular tube section - comparison between SCSM and DCAT.

4.3.5. Multi-fidelity expression of \mathcal{S}_{2D}

Recall that the cross-sectional stiffness is essentially given by both the geometry and laminate stiffness domains $\mathcal{S}_{2D} = f(\mathcal{S}_{\text{geom}}, \varphi(\mathcal{S}_{\text{lam}}), \dots)$. A more precise formulation (from Section 4.2) for a n element discretisation of $\mathcal{S}_{\text{geom}}$ would be:

$$\mathcal{S}_{2D} = f(\mathcal{S}_{\text{geom}}, \varphi(\mathcal{S}_{\text{lam}}), \dots)$$

where

$$\varphi(\mathcal{S}_{\text{lam}}) = \{ \varphi(\mathbf{\Gamma}(\mathcal{S}_{\text{geom}}), \boldsymbol{\xi}^{A,B,D})_1, \dots, \varphi(\mathbf{\Gamma}(\mathcal{S}_{\text{geom}}), \boldsymbol{\xi}^{A,B,D})_n \} \quad (4.35)$$

Hence, for a given internal profile geometry parameterised by $\mathcal{S}_{\text{geom}}$, a (relatively) significant computation effort is spent calculating the n laminate stiffness to determine $\varphi(\mathcal{S}_{\text{lam}})$ for $\mathcal{S}_{\text{geom}}$. When processing these sequentially, this dominates the \mathcal{S}_{2D} computation time and therefore, the analytical method quickly loses favour. It should be noted though, that $\varphi(\mathcal{S}_{\text{lam}}(\mathcal{S}_{\text{geom}}))$ is most often a so-called *embarrassingly parallel* problem, and computations can be trivially batch processed across the complete $\mathcal{S}_{\text{geom}}$ domain.

For the cross-sectional mass matrix, the laminate mass of unit spanwise length is considered, while mass moments are calculated as outlined in Equation 4.30. As the computational time for the elemental laminate stiffness is the same regardless of which of the two cross-sectional modellers are used, DCAT becomes the logical choice with its ability to calculate the fully populated 6×6 cross-sectional stiffness tensor. Furthermore, there is no requirement to pre-determine the bending axis for the cross-section, allowing the stiffness tensor \mathbf{S} to be calculated about any

Airfoil Section

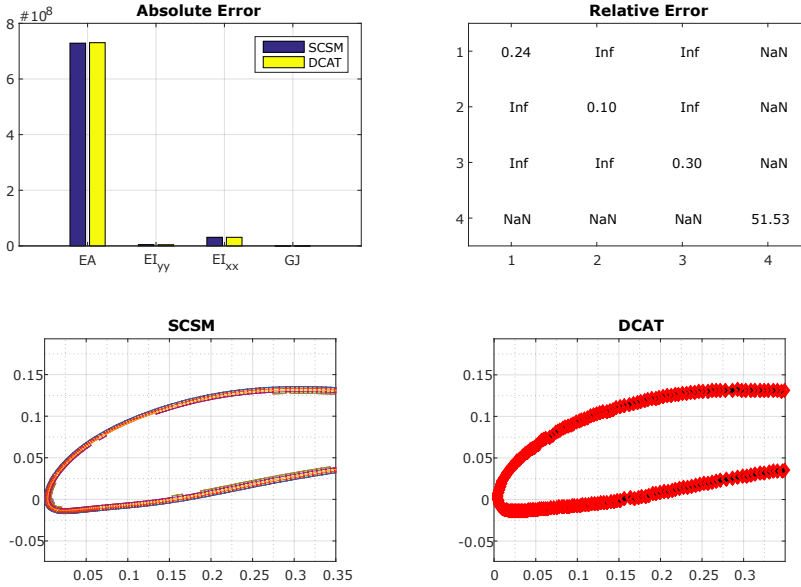


Figure 4.12 | Dbox section - comparison between SCSM and DCAT.

arbitrary axis, making it more optimisation friendly. For more details, refer to Section 5.1. Finally, as a second phase, the modeller can be run using a known \mathcal{S}_{1D} solution to recover the shell strains, including the second-order free warping solution. This enables typical laminate failure criteria to be used as problem constraints during optimisation.

4.4. STRUCTURAL STIFFNESS DOMAIN \mathcal{S}_{1D}

Moving from the cross-section domain \mathcal{S}_{2D} to the 3D structural response requires the process outlined in Section 4.3 to be repeated for each characteristic cross-section in the structure. Thus, considering a typical wing with a multiple D-box sections as depicted in Figure 4.13, the structural geometric domain is given as $\varphi(\mathcal{S}_{2D}) = \{\mathcal{S}_{2D1}, \mathcal{S}_{2D2}, \dots, \mathcal{S}_{2Dn}\}$ where n are the total number of unique sections. A beam reference frame xyz is introduced that has its origin at the root of the beam. The y -axis of this frame is aligned along the axis of the beam. Here, L is the length of the one-dimensional beam, and l is the length of each one-dimensional element.

Depending on the modelling methodology chosen, $\varphi(\mathcal{S}_{2D})$ could either be the second order fully populated 6×6 Timoshenko stiffness tensor \mathbf{S} as determined using the FE solver or a reduced 4×4 approximated Euler stiffness tensor \mathbf{C} utilising the analytical method. However, as motivated previously, the fully populated Timoshenko stiffness tensor is preferred and hence utilised to determine the \mathcal{S}_{1D} structural response. This stiffness tensor \mathbf{S} relates the one-dimensional forces and moments acting on the equivalent beam to the experienced strains and curvatures as:

$$\mathbf{F} = \mathbf{S} \cdot \boldsymbol{\epsilon} \quad (4.36)$$

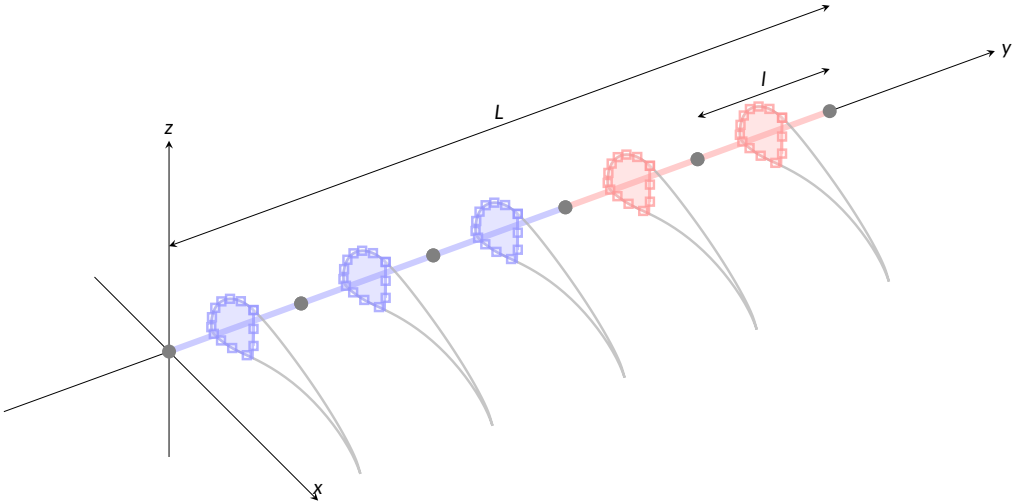


Figure 4.13 | 2+1D representation of the kite structure.

where the stiffness tensor in expanded notation is:

$$\mathbf{S} = \begin{bmatrix} S_{11} & S_{12} & S_{13} & S_{14} & S_{15} & S_{16} \\ S_{21} & S_{22} & S_{23} & S_{24} & S_{25} & S_{26} \\ S_{31} & S_{32} & S_{33} & S_{34} & S_{35} & S_{36} \\ S_{41} & S_{42} & S_{43} & S_{44} & S_{45} & S_{46} \\ S_{51} & S_{52} & S_{53} & S_{54} & S_{55} & S_{56} \\ S_{61} & S_{62} & S_{63} & S_{64} & S_{65} & S_{66} \end{bmatrix} \quad (4.37)$$

and \mathbf{F} is the cross-sectional load vector that comprises the forces and moments defined as:

$$\mathbf{F} = \{F_x, F_y, F_z, M_x, M_y, M_z\}^\top \quad (4.38)$$

and the cross-sectional strain vector ϵ that similarly groups the strains and curvatures are defined as:

$$\epsilon = \{\epsilon_x, \epsilon_y, \epsilon_z, \kappa_x, \kappa_y, \kappa_z\}^\top \quad (4.39)$$

To complement the implemented cross-sectional modeller (described in Section 4.3), a one-dimensional beam model is required. As introduced previously, composite materials, by nature of their anisotropy, tend to have a lower ratio of shear to extension modulus when compared to isotropic materials. Thus, in the analysis of slender composite structures, it is critical to capture shear deformation effects — as compared to a geometrical equivalent isotropic beam.

From beam elements that include shear effects in literature, different methods have been utilised to consider the effects of material anisotropy. Stemple and Lee developed an element that directly utilises the laminate stiffness tensor \mathbf{ABD} determined by S_{lam} as described in Section 4.2.1. Their method incorporates shear effects by prescribing warping displacements parallel to the deformed axis that are then superimposed over the cross-section [162]. Saravanos *et al.* formulate a shear beam element for hollow, closed cross-sections with an arbitrary

skin laminate layup, with an additional focus on capturing the damping effects of the composite layup [163]. Kim *et al.* formulated an element with an arbitrary higher order polynomial displacement assumption, followed by minimising the elastic energy of the entire beam to obtain a solution [164]. Other elements consider 2D section parameters of \mathcal{S}_{2D} directly in the formulation of the beam element. Kennedy *et al.* use a homogenisation-based theory that expresses the stress and strains as a linear combination of the solution of pre-chosen solutions shapes, along with the contribution from the strain residual that accounts for the solution parts not captured by the fundamental solution [117]. In addition, there are other higher order beam models based on the variational asymptotic method (VAM) [165] and unified Carrera one-dimensional formulation [166, 167], that utilise higher order shear deformation theory.

Compared to the well-known Euler-Bernoulli beam model, the Timoshenko beam model is based upon first-order shear deformation theory and includes transverse shear effects but neglects the effects of cross-sectional warping and transverse normal strains. Hence, given the use of asymmetric geometry, composite material, and to capture the tension-shear coupling, this work employs a Timoshenko based beam element to model the structural 3D planform aspects of the wing as 1D beam elements. An added advantage is the ability to calculate the Timoshenko stiffness tensor from \mathcal{S}_{2D} about an arbitrary reference point, thus avoiding the requirement of determining the shear centre explicitly for each optimisation iteration.

In this work, a two node linear Timoshenko beam element with 12 (6 translations and 6 rotations) degrees of freedom is formulated using the following relations. The described beam element considers the anisotropic material effects by utilising a fully populated 6×6 sectional stiffness tensor for each element. Furthermore, care is taken to include the coupling effects that are commonly lost in standard Timoshenko beam elements that consider simplified flexural rigidity and torsional rigidity for a predefined cross-section. Thus, an anisotropic composite or non-homogeneous slender structure can be modelled while imposing the constraint that the cross-section is constant for each node in the 1D analysis. At this juncture, only small deformations and strains are considered in a linear element formulation. The coordinate system utilised in the formulation of the element is shown in Figure 4.14a, where each element e has a characteristic stiffness tensor \mathbf{S}_e and an element length l , and the overall length of the beam is defined as L in the beam reference frame.

Common Timoshenko isotropic elements simplify the stiffness tensor \mathbf{S} (Equation 4.37) to its diagonal representation. This is commonly done by formulating the beam element around the shear and elastic axis, orienting the principle axes resulting in diminishing $EI_{\bullet\bullet}$ terms that describe the bending couplings. Similarly, with the shear centre assumption, the torsional coupling terms can also be significantly reduced. However, this mandates that the reference beam axis will gyrate about changing 2D sectional geometry $\mathcal{S}_{\text{geom}}$ when considering a topology optimisation using methods described in Section 4.3.1. To avoid such complications, the beam element is formulated with no such diagonal-dominated tensor assumptions, allowing for both material anisotropy and asymmetric geometric coupling effects to be accounted for in the model.

4.4.1. Constitutive equations and displacement field

The displacement field \mathbf{u} for each node can be expressed in terms of three translations (u_x, u_y, u_z) and three rotations ($\theta_x, \theta_y, \theta_z$) as illustrated in Figure 4.14b. The displacement field \mathbf{u} can thus

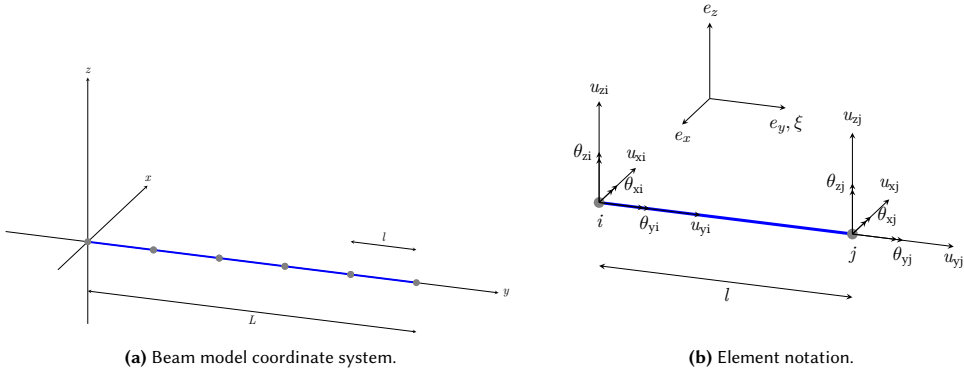


Figure 4.14 | Beam model notation.

be expressed as:

$$\mathbf{u} = \{u_x, u_y, u_z, \theta_x, \theta_y, \theta_z\}^T \quad (4.40)$$

Similar to Equation 4.36, for each node, the generalised Timoshenko strain vector ϵ that incorporates the effects of transverse shear can be expressed in terms of the elements of displacement field \mathbf{u} as:

$$\epsilon = \{\dot{u}_x - \theta_z, \dot{u}_y, \dot{u}_y + \theta_x, \dot{\theta}_x, \dot{\theta}_y, \dot{\theta}_z\}^T \quad (4.41)$$

Consecutively, from the Timoshenko relations, the translations are decomposed into the effects arising from shear stress and those stemming from the bending moment and are expressed as:

$$\begin{aligned} \frac{\partial u_x}{\partial y} &= \theta_z + \epsilon_{yx} \\ \frac{\partial u_z}{\partial y} &= -\theta_x + \epsilon_{yz} \end{aligned} \quad (4.42)$$

Where ϵ_{yx} and ϵ_{yz} are the shear strains in the yx and yz planes, respectively.

4.4.2. Equilibrium and compatibility equations

For a cross-sectional applied load vector \mathbf{F} , the equilibrium conditions for the shear stress and bending moment relations are given by:

$$\begin{aligned} \frac{\partial M_x}{\partial y} - F_z &= 0 \\ \frac{\partial M_z}{\partial y} + F_x &= 0 \end{aligned} \quad (4.43)$$

From the principle of virtual work, the potential energy Π of a system can be defined as the sum of the strain energy \mathbf{U} and work done by the external forces \mathbf{V} . This is expressed as:

$$\Pi = \mathbf{U} + \mathbf{V} \quad (4.44)$$

where

$$\mathbf{U} = \frac{1}{2} \int_V \mathbf{F} \cdot \epsilon dV \quad (4.45)$$

Thus, to attain equilibrium, the strain energy is minimised - i.e.:

$$\frac{\partial U}{\partial \mathbf{u}} = 0 \quad (4.46)$$

4.4.3. Finite element implementation

For the FE implementation, a two node element is considered as described previously, with its reference frame as defined in Figure 4.14a. Each element has an elemental length l , depicted in Figure 4.14b. The displacement field for each of the two nodes is expressed as three translations and three rotations as similarly defined previously in Equation 4.40. Thus, the elemental displacement vector $\mathbf{u}(\xi)$, defined using the normalised element coordinate $\xi = y/l$, is given by:

$$\mathbf{u}(\xi) = \mathcal{N}(\xi)\mathbf{u}_l \quad (4.47)$$

where $\mathcal{N}(\xi)$ is the element shape function matrix and where the nodal displacement field \mathbf{u}_l is given for the element's i, j nodes by:

$$\mathbf{u}_l = \{u_{xi}, u_{yi}, u_{zi}, \theta_{xi}, \theta_{yi}, \theta_{zi}, u_{xj}, u_{yj}, u_{zj}, \theta_{xj}, \theta_{yj}, \theta_{zj}\}^T \quad (4.48)$$

In order to approximate the translations in the displacement field \mathbf{u} , following the kinematics of a beam undergoing bending [168], a linear shape function is chosen for the axial displacement u_y while cubic shape functions are chosen for the cross-sectional planar displacements u_x and u_z . For the rotations in the displacement field, a linear shape function is assumed for the torsional rotation along the beam axis θ_y , and following the Timoshenko assumptions of Equation 4.42, the cross-sectional rotations are expressed as derivatives of the cross-sectional planar displacements (u_x and u_z) along with an additional unknown each, to account for the shear deformation contributions ϵ_{yx} and ϵ_{yz} . This ultimately leads to fourteen unknown coefficients for the beam element, which is expressed as the polynomial matrix \mathbf{A} presented in Equation 4.50.

Subsequently, the shape function matrix $\mathcal{N}(\xi)$ is built up from these displacement assumptions along with the compatibility and equilibrium conditions as:

$$\mathcal{N}(\xi) = \mathbf{A}(\xi)\mathbf{E}(\xi)^{-1}\mathbf{T} \quad (4.49)$$

where $\mathbf{A}(\xi)$ is the polynomial coefficient matrix consisting of the fourteen unknowns from the displacement assumptions outlined previously and is given by:

$$\mathbf{A}(\xi) = \begin{bmatrix} \xi^3 & \xi^2 & \xi & 1 & 0 & 0 & 0 & 0 & 0 & 0 & 0 & 0 & 0 & 0 \\ 0 & 0 & 0 & 0 & \xi & 1 & 0 & 0 & 0 & 0 & 0 & 0 & 0 & 0 \\ 0 & 0 & 0 & 0 & 0 & 0 & \xi^3 & \xi^2 & \xi & 1 & 0 & 0 & 0 & 0 \\ 0 & 0 & 0 & 0 & 0 & 0 & -3\xi^2 & -2\xi & -1 & 0 & 1 & 0 & 0 & 0 \\ 0 & 0 & 0 & 0 & 0 & 0 & 0 & 0 & 0 & 0 & \xi & 1 & 0 & 0 \\ 3\xi^2 & 2\xi & 1 & 0 & 0 & 0 & 0 & 0 & 0 & 0 & 0 & 0 & 0 & -1 \end{bmatrix} \quad (4.50)$$

The equilibrium and compatibility equations, as outlined in Section 4.4.2 are then expressed as the coefficient matrix $\mathbf{E}(\xi)$ and are cast in the form of the element equilibrium coefficients that are dependent on the normalised element coordinate $\mathbf{E}_1(\xi)$ and the boundary displacement

compatibility conditions \mathbf{E}_2 , that are only dependent on the element length l . The matrix \mathbf{T} in Equation 4.49 is a transformation matrix that accounts for the boundary compatibility conditions, i.e.:

$$\mathbf{E}(\xi) = \begin{Bmatrix} \mathbf{E}_1(\xi) \\ \mathbf{E}_2 \end{Bmatrix} \quad (4.51)$$

where

$$\mathbf{E}_2 = \begin{Bmatrix} \mathbf{A}(0) \\ \mathbf{A}(l) \end{Bmatrix} \quad (4.52)$$

The matrix \mathbf{E}_1 is obtained by utilising the coefficient of the equilibrium relations from Equation 4.43 and is expressed by casting the cross-sectional load vector \mathbf{F} components in terms of the elemental cross-sectional stiffness tensors \mathbf{S} (expressed in matrix notation), along with the nodal strain vector ϵ from Equation 4.41. However, the strain vector ϵ is cast in the normalised element coordinate ξ using the displacement approximations from Equation 4.50, to yield:

$$\mathbf{E}_1 = \begin{bmatrix} 6S_{46} - 6S_{36}\xi & -2S_{36} & 0 & 0 & -S_{23} & 0 & 6S_{34}\xi - 6S_{44} & 2S_{34} & 0 & 0 & -S_{33} & -S_{35} & 0 & -S_{13} \\ 6S_{66} + 6S_{16}\xi & 2S_{16} & 0 & 0 & S_{12} & 0 & -6S_{46} - 6S_{14}\xi & -2S_{14} & 0 & 0 & S_{13} & S_{15} & 0 & S_{11} \end{bmatrix} \quad (4.53)$$

Note the inclusion of off-diagonal coupling terms of the stiffness tensor \mathbf{S} to include both geometric and material coupling effects in the beam element formulation. The strain displacement matrix is then obtained from the shape function matrix $\mathcal{N}(\xi)$ defined in Equation 4.49 and can be separated into a displacement component and its derivative term as:

$$\mathbf{B}(\xi) = \mathbf{B}_0 \mathcal{N}(\xi) + \frac{\partial \mathcal{N}(\xi)}{\partial \xi} \quad (4.54)$$

where \mathbf{B}_0 is a transformation matrix to account for the Timoshenko strains as defined in Equation 4.41.

From the displacement field, the strain field is expressed in terms of the strain displacement matrix $\mathbf{B}(\xi)$ and the nodal displacements \mathbf{u}_l as:

$$\epsilon = \mathbf{B}(\xi)\mathbf{u}_l \quad (4.55)$$

Thus, the element stiffness tensor \mathbf{K}_e is obtained by expressing Equation 4.45 with Equation 4.55 and numerically integrating along the element length l to get:

$$\mathbf{K}_e = \int_0^l \mathbf{B}(\xi)^\top \mathbf{C} \mathbf{B}(\xi) d\xi \quad (4.56)$$

Special care is taken to alleviate shear locking by choosing the appropriate number of integration points along the elemental length. This implemented one-dimensional composite Timoshenko beam element is coupled with the cross-sectional stiffness tensor obtained as described in Section 4.3 to complete the structural model of the kite. Hence, utilising this model, the structural response of the wing can be determined by incorporating the external loads on the wing as described in Section 3.1.1.

4.4.4. Framework specific implementation details

For a two node element, the stiffness matrix can be different at each node. In such cases, a simple linear interpolation between the nodes can be applied $\mathbf{S}_e = (1 - \xi)\mathbf{S}_i + \xi\mathbf{S}_j$. However, this would require a nodal level stiffness mapping during the problem definition. Instead, in the implemented framework, an assumption is made that the elemental length l is sufficiently short, and thus an elemental level stiffness is utilised. In the case of varying stiffness at the nodes, an average elemental stiffness is prescribed in the problem definition instead as $\mathbf{S}_e = \frac{1}{2}(\mathbf{S}_i + \mathbf{S}_j)$.

Geometric nonlinearities

As with any Timoshenko/Euler beam theory, the developed element does not capture all the nonlinear kinematics, such as torsional warping and transverse shear deformations inherent to 3D slender shell structures. Furthermore, the assumption of the relations for the cross-section geometry to the axis of the beam could also break down as materials with large out-of-plane warping are used. However, for typical wing box-like structures, there are other engineering and design constraints (such as fatigue life) that the structure is subjected. This makes it a valid assumption that the employed materials are still in their linear elastic domain. This small strain theory is also utilised in the described beam element.

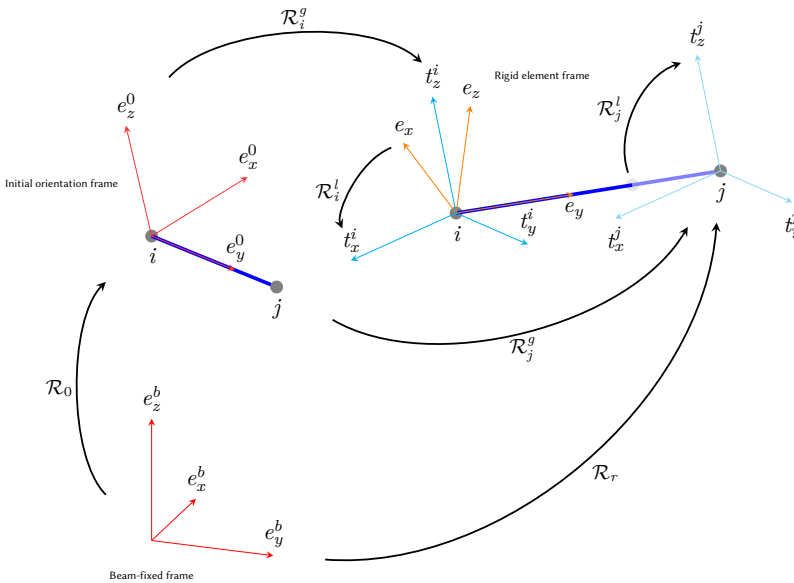


Figure 4.15 | Schematic overview of beam kinematics and frames in the co-rotation implementation.

While strain nonlinearities can be ignored for typical wing box and beam structures, geometric nonlinearities arising from large deformations and rotations can be a cause of concern, especially for semi-rigid and flexible wings. An alternative to a geometrically exact beam theory is a co-rotational framework [169]. This framework sub-divides the 1D beam deflection domain $\langle \mathbf{u} \rangle$ into local elastic deformations $\langle \mathbf{u} \rangle_{lf}$ in the element and large rigid body kinematics for the beam elements $\langle \mathbf{u} \rangle_{rb}$. This is achieved via a rotation matrix for the displacements from the local element frame to the rigid body element frame, as seen in Figure 4.15. In this manner, a

linear element, such as the previously developed Timoshenko element, can account for large deformations and rotations. In this work, the method of Battini *et al.* is employed [170]. One should note that the co-rotational framework is not limited to linear elements, and the small strain assumption is an artefact of the current problem and not the co-rotational framework's capabilities.

Spanwise nonlinearities

For D-boxes with varying cross-sectional geometry across the span, it is critical to discretise the span sections with sufficient resolution. For most cases, the D-box sectional geometry varies linearly across the span, providing a larger bending moment at the root of the wing in comparison to the tip as seen in Figure 4.16.

In particular scenarios where the laminate plan is maintained constant across multiple sections, and only the sectional geometry changes linearly, it could be possible to speed up computations by utilising an interpolation scheme in conjunction with lookups from previous calculations. This idea is briefly explored in [Chapter 7](#).

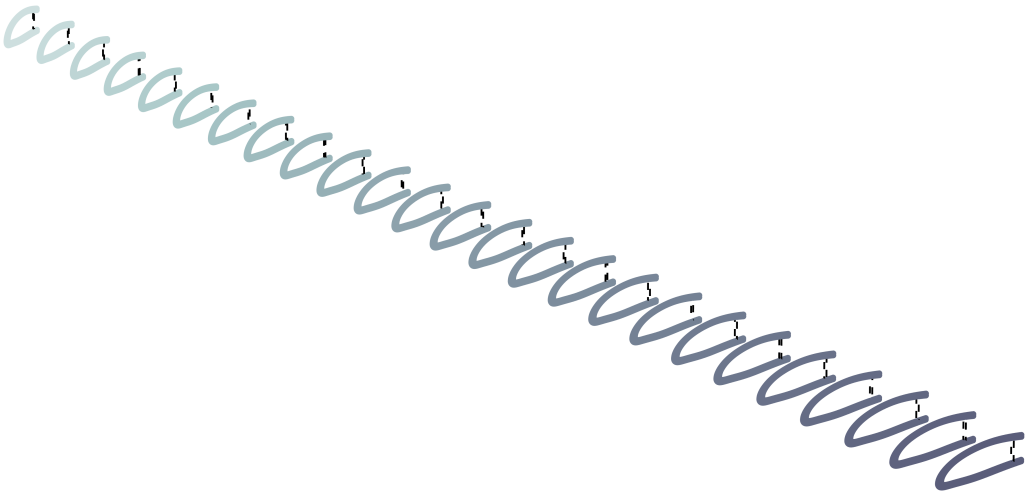


Figure 4.16 | Cross-sections discretisation of a tapered D-box.

4.5. COUPLED AERO STRUCTURAL SOLVER

Methods to define the response of the wing in the individual domains of aerodynamic \mathcal{A} , bridle \mathcal{B} & structural \mathcal{S} are outlined above. Methods to couple the responses from these domains in the global simulation framework are now explored. The overall wing response can be expressed as $\mathcal{F}(\mathcal{A}, \mathcal{B}, \mathcal{S})$, where $\mathcal{F}()$ is defined as some function that yields the domain's response space. Furthermore, multiple methods to determine this response can be used in the implemented framework depending on the phase of design or fidelity required.

The simplest methodology is the so-called *one-way coupled* solution, where each domain transfers solutions only in a single direction. Thus, a static solution can be obtained where each domain feeds into the next. i.e. $\mathcal{F}(\mathcal{A}, \mathcal{B}, \mathcal{S}) = \mathcal{A} \rightarrow \mathcal{B} \rightarrow \mathcal{S}$. In contrast, a *two-way coupled* solution shares information both ways, such that $\mathcal{F}(\mathcal{A}, \mathcal{B}, \mathcal{S}) = \mathcal{A} \rightleftharpoons \mathcal{B} \rightleftharpoons \mathcal{S}$.

The *two-way coupling* allows for the incorporation of the interdependent effects of the aerodynamic, bridle and structural domains on each other to obtain the wing's response. Chapter 5 utilises the *one-way coupled* response, whereas Chapter 7 explores the *two-way coupled* response of the wing. Synopsis 5 outlines motivations for exploring this coupled response as early in the design process as feasible.

Simulation methodology for *two-way coupling* is mainly composed of two categories, the monolithic and the partitioned approach. In the monolithic approach, the governing equations of the different domains are framed together and solved simultaneously. For typical fluid structure interaction (FSI) problems, this would be the combination of the fluid \mathcal{A} and the structural \mathcal{S} equations. Additionally, in the case of AWE wings, the tether and bridle governing equations would also require to be considered at the same time. Instead, in this work, the alternative partitioned approach is utilised. In this approach, each domain $\mathcal{A}, \mathcal{B}, \mathcal{S}$ and its constituent equations are solved separately, and a suitable scheme is utilised to transfer the response from each domain. A schematic representation of this is depicted in Figure 4.17.

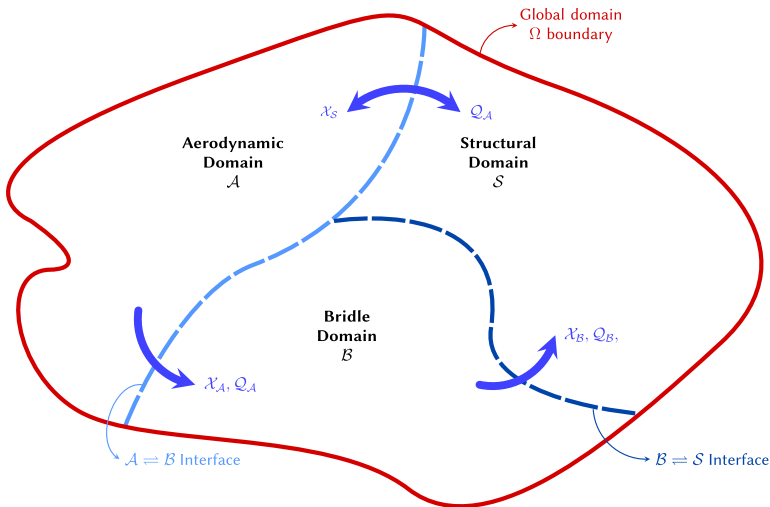


Figure 4.17 | Partitioned approach and information exchange for coupling of the different $\mathcal{A} = \mathcal{B} = \mathcal{S}$ AWE domains.

4.5.1. Coupling methodology

In the realm of partitioned coupling methods, there are two main schemes, explicit (loosely coupled) and implicit (strongly coupled) methods. Hybrid and semi-explicit schemes also exist, but these are not detailed here. For coupling problems, the fundamental strategy is to solve for the converged response state $\mathcal{F}(\dots)$ across the domains in an iterative manner, where each new state $\mathcal{F}(\dots)_i$ is some function of the previous state. Each domain solver then assumes that the solution from other domains remains fixed during each solution step. For the AWE problem in consideration here, this can be expressed as:

$$\mathcal{F}(\mathcal{A}, \mathcal{B}, \mathcal{S})_i = f(\varphi(\mathcal{A}, \mathcal{B}, \mathcal{S})_{i-1}, \dots) \quad (4.57)$$

This problem is then iteratively solved until a converged solution of the response of all domains $\mathcal{F}(\mathcal{A}, \mathcal{B}, \mathcal{S})$ is found and where the convergence is given by:

$$\mathcal{F}() \rightarrow \mathcal{C}(\mathcal{F}()_i, \mathcal{F}()_{i-1}) \leq \epsilon_{\text{tol}} \quad (4.58)$$

Where $\mathcal{C}(\dots)$ is some convergence function, and ϵ_{tol} is the allowed tolerance that defines a converged solution. In the simplest form, the convergence function could be enforcing that the positions of the solution grid \mathcal{X} of the fluid and structural domain are the same at the domain interface for the converged time step t :

$$\mathcal{C}(\mathcal{A}, \mathcal{B}, \mathcal{S}) \equiv \mathcal{X}_{\mathcal{A}}(t) = \mathcal{X}_{\mathcal{B}}(t) = \mathcal{X}_{\mathcal{S}}(t) \quad (4.59)$$

With an explicit coupling scheme, each iteration step can be performed with only the information from the previous iteration, and the solver then marches along the interface until the convergence criteria are fulfilled. Furthermore, for each iteration step i , only a single exchange of information across the interface domain is performed. Hence, in cases where each domain solver uses a different iteration step size, the coupling step is performed only when all solvers are at the same state in time. An explicit coupling scheme can fundamentally be considered an extrapolation scheme that utilises the previous iteration.

In contrast, an implicit scheme utilises additional conditioning, such as to minimise the convergence function $\mathcal{C}()$. Thus, for a displacement-based convergence expressed in the position space \mathcal{X} , this could be solved by a fixed-point iterative method, such as a Newton method.

Considering the response state $\mathcal{F}()_i$ at an iteration step i , the relations between each domain can be expressed neglecting all parameters that are fixed for each iteration as:

$$\begin{aligned} \mathcal{F}(\mathcal{A})_i &= \varphi(\mathcal{A}(\mathcal{F}(\mathcal{S})))_i \\ \mathcal{F}(\mathcal{B})_i &= \varphi(\mathcal{B}(\mathcal{F}(\mathcal{A})))_i \\ \mathcal{F}(\mathcal{S})_i &= \varphi(\mathcal{S}(\mathcal{F}(\mathcal{A}, \mathcal{B})))_i \end{aligned} \quad (4.60)$$

Where the aerodynamic response $\mathcal{F}(\mathcal{A})$ is given by the resulting forces in the domain $\mathcal{Q}_{\mathcal{A}}$, determined by the solver function $\varphi(\mathcal{A}())$. Consecutively, the bridge space response $\mathcal{F}(\mathcal{B})$ is determined from the aerodynamic response. Finally, the structural response $\mathcal{F}(\mathcal{S})$ is given by the deformed structure described in the kinematic space $\mathcal{X}_{\mathcal{S}}$. Thus, we can reframe Equation 4.60 in the force and position domains $\langle \mathcal{Q}, \mathcal{X} \rangle$ instead as:

$$\begin{aligned} \mathcal{F}(\mathcal{A})_i &= \langle \mathcal{Q}_{\mathcal{A}} \rangle_i = \varphi(\mathcal{A}(\mathcal{X}_{\mathcal{S}}))_i \\ \mathcal{F}(\mathcal{B})_i &= \langle \mathcal{Q}_{\mathcal{B}} \rangle_i = \varphi(\mathcal{B}(\mathcal{Q}_{\mathcal{A}}, \mathcal{X}_{\mathcal{S}}))_i \\ \mathcal{F}(\mathcal{S})_i &= \langle \mathcal{X}_{\mathcal{S}} \rangle_i = \varphi(\mathcal{S}(\mathcal{Q}_{\mathcal{A}}, \mathcal{Q}_{\mathcal{B}}))_i \end{aligned} \quad (4.61)$$

The $\langle \rangle$ notation is used to indicate that there might be multiple bodies contained in the domain. The above set of relations for each domain can be further combined and expressed as a fixed-point iteration of the kinematic space expressed $\mathcal{X}_{\mathcal{S}}$ as:

$$\langle \mathcal{X}_{\mathcal{S}} \rangle_i^{j+1} \equiv \langle \mathcal{N}(\mathcal{X}_{\mathcal{S}}) \rangle_i^j \quad (4.62)$$

Where i is the solution step, j is the iteration for the particular solution step, and \mathcal{N} is the solver space of all problem domains and is given by:

$$\mathcal{N}(\mathcal{X}_S) = \mathcal{S}(\mathcal{Q}_A(\mathcal{X}_S), \mathcal{Q}_B(\mathcal{X}_S)) \quad (4.63)$$

$$= \mathcal{S}(\mathcal{A}(\mathcal{X}_S), \mathcal{B}(\mathcal{X}_S)) \quad (4.64)$$

By reframing the problem as some function of the kinematic space $\mathcal{N}(\mathcal{X}_S)$, Newton or modified Newton methods can be implemented to solve the problem more efficiently than with an explicit scheme (Equation 4.59). While requiring fewer iterations than an explicit scheme, conventional fixed-point typically display linear convergence. However, the number of iterations can be further reduced by utilising convergence acceleration schemes such as the common Anderson acceleration method [171].

4

In this work, only the static equilibrium state of the wing is considered. Thus, the solution for the coupled response is determined for a pseudo-time step, with either an implicit or explicit method to perform the iterations required to determine this equilibrium state. This allows for the expression of the kinematic space \mathcal{X}_S directly in the deformation position field $\langle \mathbf{u} \rangle$, neglecting dynamic inertial contributions. For the implicit scheme, a Newton method is implemented to couple the three domains.

4.5.2. Dynamic load stepping

In Section 4.4.2 the finite element method (FEM) implementation of the developed method presents that for a given applied force vector \mathbf{F} , and the strain energy \mathbf{U} is minimised. This is done by framing the problem in terms of residuals \mathcal{R} of the difference between these applied forces and the internal forces, which are minimised at each iteration of the numerical method:

$$\mathcal{R}(\mathbf{u}) = \mathbf{F}_{int}(\mathbf{u}) + \mathbf{F}_{ext}(\mathbf{u}) = 0 \quad (4.65)$$

When considering a typical D-box, the wing response comparing the coupled to an uncoupled solution is seen in Figure 4.18a. For this example case, there is a significant change in the tip deflections normalised by the span.

However, when considering a highly loaded D-box as seen in Figure 4.18, there can be a significant order of magnitude of deflections. In such cases, additional conditioning needs to be implemented in the FE method to aid in the solver's convergence. In the developed framework, a dynamic load-stepping scheme is implemented and is achieved by reframing the previous equation as:

$$\mathcal{R} = \mathbf{F}_{int}(\mathbf{u}) + \lambda \mathbf{F}_{ext}(\mathbf{u}) \quad (4.66)$$

Where λ is a scaling factor that provides a means to adjust the applied load. By incorporating a dynamic scaling based on the Newton iteration of the solver, the applied load can be incremented to aid in convergence, especially in cases of nonlinear responses. Thus, the incremental load step can be defined in terms of the load step iterations $i_{\mathcal{R}}$ and the step limit $N_{\mathcal{R}}$ as:

$$\lambda \in [0, 1] = f(i_{\mathcal{R}}, N_{\mathcal{R}}, \dots) \quad (4.67)$$

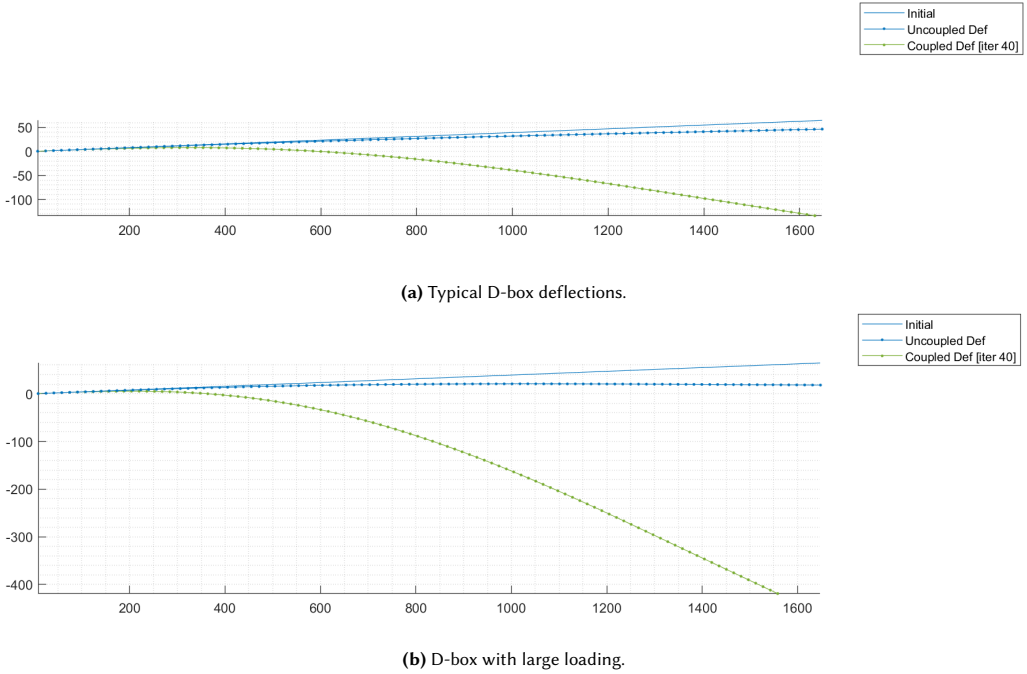


Figure 4.18 | Comparison of static to aero-structural coupled solver.

By tracking the number of iterations taken in the previous load step $N_{\mathcal{R}_{i-1}}$, and comparing it to the allocated number of steps $N_{\mathcal{R}}$, the load scaling factor can be used to increase or decrease the load step, depending on the convergence history. The current implementation utilises the following formulation for the scaling factor:

$$\lambda_i = \lambda_{i-1} + \frac{N_{\mathcal{R}}}{N_{\mathcal{R}_{i-1}}} (\lambda_{i-1} - \lambda_{i-2}) \quad (4.68)$$

When utilising a Newton method to solve Equation 4.66, for each load step i , the equation can be expressed in terms of the Newton iteration index j as:

$$\mathcal{R}_i^j = \mathbf{F}_{int}(\mathbf{u})^j + \lambda_i \mathbf{F}_{ext}(\mathbf{u})^j \quad (4.69)$$

4.5.3. Interface mapping $\mathcal{A} \rightleftharpoons \mathcal{S}$

As described previously in Section 4.5.1, the response space of the structural domain \mathcal{S} is given by $\mathcal{F}(\mathcal{S}) = \{ \mathcal{X}_{\mathcal{S}}, \mathcal{Q}_{\mathcal{S}} \}$. In the implemented framework, this position space $\mathcal{X}_{\mathcal{S}}$ is defined by the 3D deformation position field $\langle \mathbf{u} \rangle \in \mathbb{R}^3$, which essentially describes a segmented line in 3D space, along with rotations at each nodal point.

Hence, at each coupling step this deformation information $\langle \mathbf{u} \rangle$ is relayed back into the aerodynamic domain \mathcal{A} , and is used to update its position space $\mathcal{X}_{\mathcal{A}}$:

$$\mathcal{X}_A = f(\mathcal{X}_S) = f(\mathbf{u}) \quad (4.70)$$

However, as the position space of the aerodynamic domain \mathcal{X}_A is described by quad node 3D planar elements with zero thickness, this requires a mapping between the two position spaces.

To aid in the parameterised variation of the 3D geometry of the wing for use in design optimisation, the 3D discretisation of the wing $\langle \mathcal{A}_{3D} \rangle = \{ \gamma, \Gamma_d, \mathcal{R}, \lambda, \dots \}$ is expressed in typical variables such as sweep, dihedral, aspect ratio, etc. to define the initial wing geometry. Additionally, this allows for the wing to be described as a superposition of some 1D line geometry $\langle \mathcal{A}_{1D} \rangle = \{ \gamma, \Gamma_d, \dots \}$ in conjunction with other planform parameters as $\mathcal{A}_{3D} = \{ \mathcal{A}_{1D}, \mathcal{R}, \lambda, \Omega, \dots \}$.

4

This combination of base 1D line elements and the derived quad node planar discretisation for a typical multi-surface aircraft configuration is illustrated in Figure 4.19.

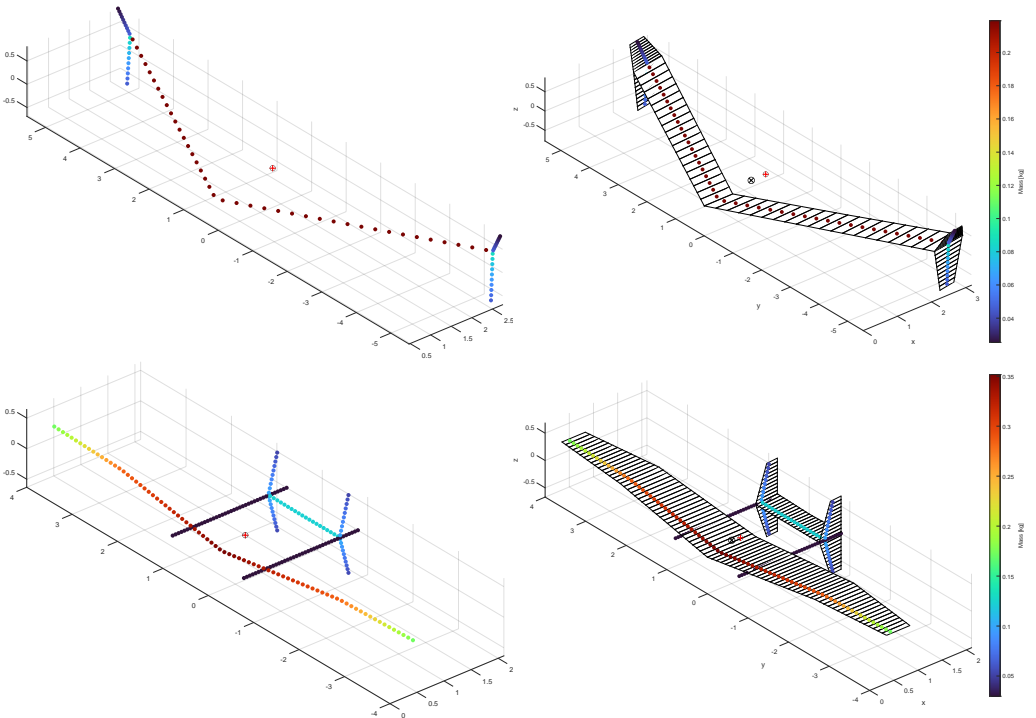


Figure 4.19 | Approximation of the 3D wing geometry using 1D line elements in conjunction with 3D planar panels.

The mapping methodology currently implemented is to express \mathcal{X}_A as:

$$\begin{aligned} \mathcal{X}_A(\mathcal{X}_S) &= f(\mathcal{A}_{3D}(\mathcal{X}_S)) \\ \text{where} \\ \langle \mathcal{A}_{3D} \rangle &= \langle \{ \mathcal{A}_{1D}(\mathbf{u}), \mathcal{A}_{2D}(\mathbf{u}) \} \rangle \end{aligned} \quad (4.71)$$

Which can be expressed in terms of wing geometry parameters \mathcal{A}_p as:

$$\begin{aligned}\langle \mathcal{A}_{1D}(\mathbf{u}) \rangle &= \langle \mathcal{T}(\mathbf{u}, \mathcal{A}_{p1D}) : \mathcal{A}_{p1D} \in \{ \gamma, \Gamma_d, \dots \} \rangle \\ \langle \mathcal{A}_{2D}(\mathbf{u}) \rangle &= \langle \mathcal{T}(\mathbf{u}, \mathcal{A}_{p2D}) : \mathcal{A}_{p2D} \in \{ \mathcal{R}, \lambda, \Omega, \dots \} \rangle\end{aligned}\quad (4.72)$$

Where \mathcal{T} is a transfer function that maps both the displacements and rotations from the structural domain $\langle \mathbf{u} \rangle$ to the 3D planar representation of the aerodynamic domain as:

$$\mathcal{T}(\mathbf{u}, \mathcal{X}_A) : \mathbb{R}^6 \mapsto \mathbb{R}^3 \quad (4.73)$$

Furthermore, the transfer function also accommodates the difference in the number of nodal points in \mathcal{X}_S and \mathcal{X}_A . In this work, \mathcal{T} is formulated using a spline-based interpolation scheme. Thereby, for multi-lifting element aircraft configuration such as in Figure 4.19, different interpolation functions can be chosen to suit each type of body in the configuration.

4.6. SUMMARY AND CONCLUSIONS

For the response of the structural design space, a methodology to model the structure of typical composite structures of rigid and semi-rigid wings is proposed. The main load-bearing wing component is a “D” shaped wing-box, which is represented as a slender carbon composite shell and further idealised as a stack of two-dimensional cross-section models arranged along an anisotropic one-dimensional beam model.

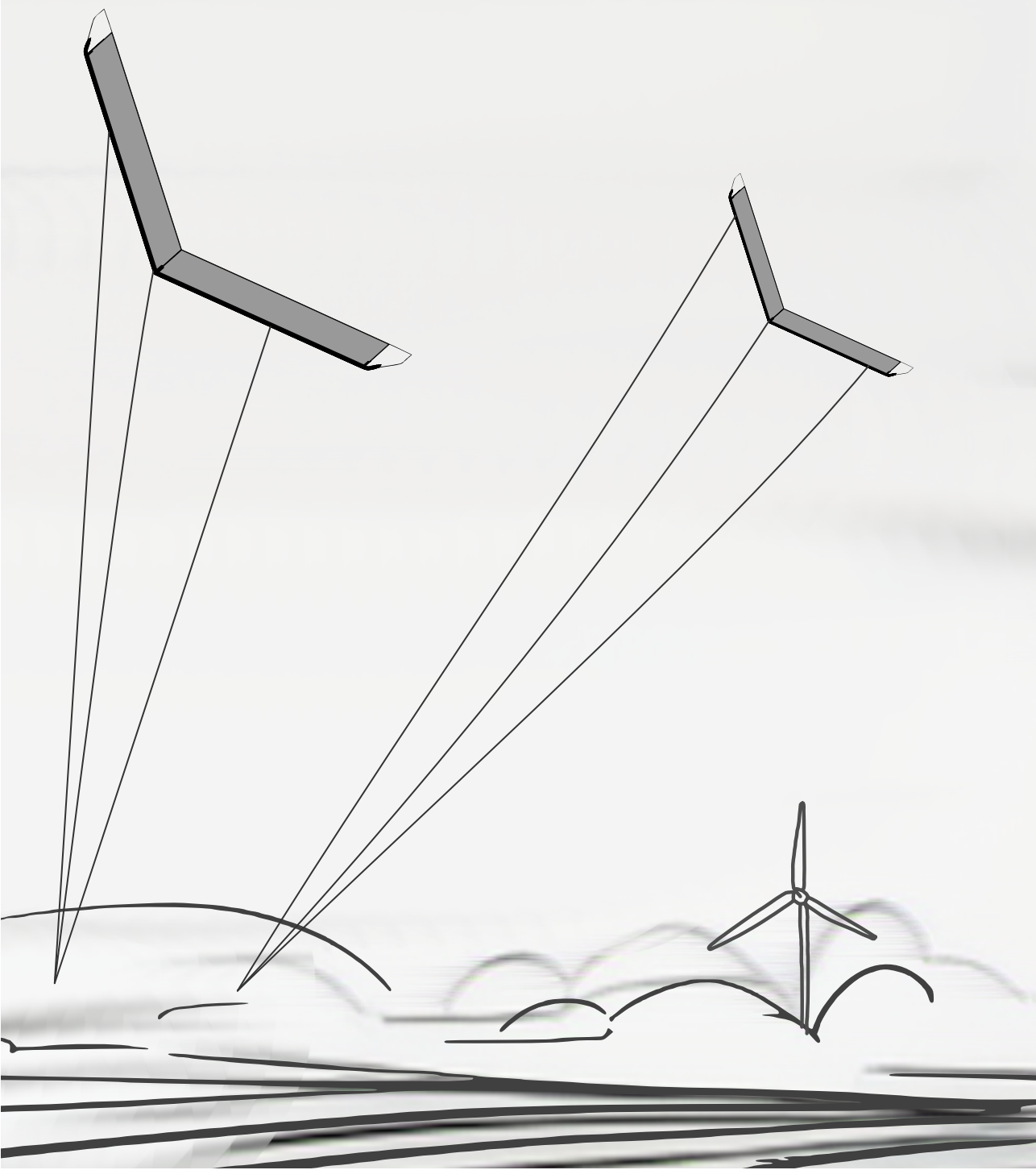
To capture the effects of the internal geometry of the wing-box, laminate layup sequence, and material anisotropy influences, 2D cross-sectional models are utilised. At the laminate stiffness domain \mathcal{S}_{lam} level, a spline-based scheme to parametrise the internal geometry is introduced. This discretised geometry is then used with CLT to determine the equivalent laminate stiffness from either a ply layup sequence or lamination parameters. The cross-sectional model is maintained agnostic to how the layer level laminate stiffness is determined.

These laminate stiffnesses are then propagated to a FE cross-section model that uses linear Hermitian elements to calculate the complete 6×6 second order Timoshenko stiffness tensor (\mathbf{S}) of the cross-section. The implemented method solves the variational asymptotic representations of the Saint Venant solutions. In addition, a complimentary 1D model that captures coupling effects witnessed in slender composites based on Timoshenko theory is developed. This model utilises first-order shear deformation theory and includes effects of transverse shear in the formulation but neglects cross-sectional warping effects and transverse normal strains. In the structural models, the stiffness tensor (\mathbf{S}) for each unique cross-section in the wing can be calculated about an arbitrary reference axis — negating the requirement of the determination of the shear centre and neutral axis a priori, which is critical for any iterative design.

In the scope of the overall simulation framework, the aerodynamic and bridle domains are initially treated as input variables for the structural domain. i.e. $\mathcal{S} = f(\varphi(\mathcal{A}, \mathcal{B}), \dots)$. Subsequently, an approach to determine the coupled aero-structural-bridle response is detailed. A partitioned approach is proposed with multiple coupling schemes. An explicit approach, as well as, a more efficient implicit coupling scheme are applied.

The multi-fidelity approach to solving the composite structural domain is a large aspect of the proposed framework. The implementation allows for results in either the stiffness domain \mathcal{S}_{1D} , or the more involved topology level 2D geometry domain \mathcal{S}_{2D} . Furthermore, at the most

detailed level, manufacturing level ply stacking sequences can be obtained in the laminate level domain \mathcal{S}_{lam} . This multi-fidelity approach thus allows for a suitable solution fidelity to be chosen, providing appropriate domain solutions depending on the particular stage of the design processes. Subsequent chapters explore the capabilities of the developed framework, using different analyses and optimisation case studies.



Chapter 5

Structural design space

अधहिसुतदरुशन इवसु जातुनुधः

—आदशरुकराचारु, भाषु, ॡ.१ॢ.१

That is like blind people, describing an elephant by touch.

—Ādi Śaṅkarācāryaḥ, *Bhāṣya, Chāndogyopaniṣad* 5.18.1

Adapted from:
Structural Analysis and Optimization of a Tethered Swept Wing for Airborne Wind Energy Generation
Wind Energy, 23(4), 1006-1025 (2020)

ABSTRACT

This chapter explores the structural design space of carbon composite wings, considering a purely static problem with constant pre-computed external loading. No aeroelastic coupling is considered at this stage, and changes in loading due to structural deformations will be covered in Chapter 7.

In the first step, the wing box design's effect on the wing's static structural response is explored. The external wing sectional geometry is pre-determined based on chosen 2D aerofoil profiles. Hence, the investigation is limited to the wing cross-sections' internal geometry and composite layup sequence. Initially, the internal geometry and layup of the cross-section are optimised by considering a reference cross-sectional stiffness tensor \mathbf{S} as a target criterion while minimising the sectional mass. Subsequently, a more detailed optimisation that accounts for multiple varied 2D wing box sections and the resulting 1D wing box deflections is undertaken. In both mass optimisations described, internal cross-sectional geometry and laminate layup influences are considered but at varying levels of fidelity.

Prior to any design exploration, it is crucial to determine the design load case(s) for the wing. Considering the flight envelope of a pumping cycle airborne wind energy (AWE) wing, there are multiple critical design load cases to account for — not limited to typical reel-out, transition and other manoeuvre loads. A detailed discussion on the selection of design load cases for airborne wind energy system(s) (AWES) is a vast topic and is not considered here. This design exercise uses static load cases derived from the power generation phase during a typical crosswind flight manoeuvre at nominal design wind speed as the design load case(s).

For the aerodynamics, the aerofoils along the wing sections are obtained by an optimisation procedure that maximises lift over drag while also considering the stability criteria required for the swept wing during both traction and retraction as described in Section 2.3.2. The resulting 2D aerodynamic characteristics utilised are determined using viscid-inviscid interaction methods during conceptual design, and typically refined using unsteady Reynolds averaged Navier-Stokes (uRANS) simulations for later the design phases. For the wing planform, the 3D aerodynamic loads are derived by the non-linear vortex-lattice method (VLM) method described in Section 3.2.

In this chapter, only the static response of the wing structure for a fixed planform geometry is investigated. Thus, all studies are carried out using the reference wing geometry introduced Section 2.1. Therefore, all 3D aerodynamic design variables \mathcal{A}_{3D} such as span, aspect ratio, sweep, dihedral, etc. are pre-determined and remain constant for a particular analysis. This results in a purely structural design exercise and is not coupled with the aerodynamics as is done subsequently in Chapter 7.

Furthermore, the aerofoil sections of the wing are also pre-selected. The corresponding aerofoil aerodynamics \mathcal{A}_{2D} are then pre-computed for the entire operational range of angles of attack and hashed to a lookup table. Thus, both the 2D and 3D aerodynamic parameters are pre-determined at this initial design stage, resulting in static aerodynamic loads that can be applied to the structural model, allowing for the structural design space of the wing to be explored in isolation. The portion of the computational model in focus for this chapter is visualised in Figure 5.1. Thus, to reiterate, the computational model utilises the spanwise 3D aerodynamic loads for the given aerodynamic profile and wing planform strictly as inputs (i.e. $\mathcal{F}(\mathcal{A}, \mathcal{B}, \mathcal{S}) = \mathcal{A} \rightarrow \mathcal{B} \rightarrow \mathcal{S}$), neglecting the effects of the resulting structural deformations on the aerodynamic response. Such a static analysis facilitates the conceptual phase of design, where a large number of design candidates are typically considered.

With the aerodynamic domain \mathcal{A} considered fixed during the analysis, the remaining parameter space for the static structural design of the wing can be parametrised by two main factors:

1. Wing box cross-section geometry and material properties (\mathcal{S})
2. Bridle line configuration (\mathcal{B})

A typical design process that explores these two parameter spaces in detail, with the static structural tool chain developed in this work, is described in subsequent discussions.

5.0.1. The D-box — an atypical wing box

Compared to conventional aircraft wings and wind turbine blades, the reference wings are composed of slender sections and thus require a different structural reinforcement concept.

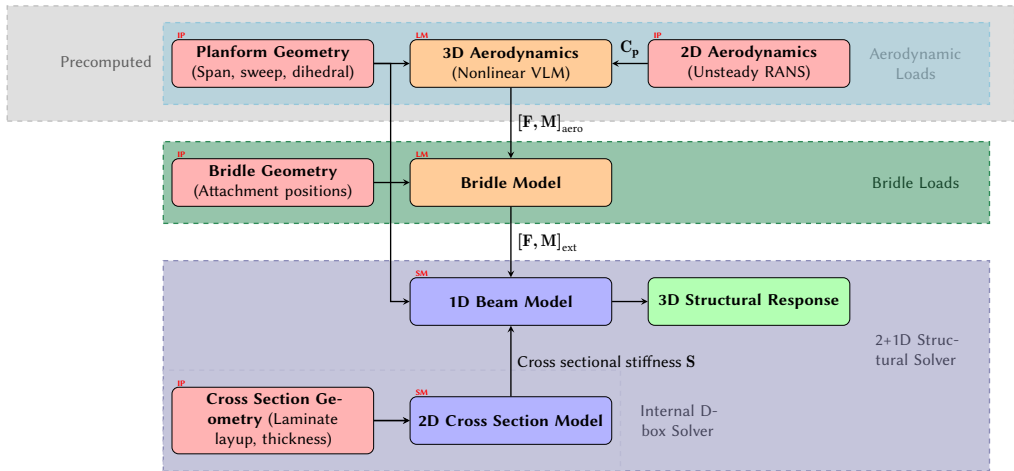


Figure 5.1 | Overview of the static portions of the full computational framework (Figure 3.4) utilised in this Chapter. Aerodynamic loads are maintained fixed for a particular analysis case. Inputs (IP) are shown in red. Models that determine loads (LM) are indicated in orange, and structural models (SM) are indicated in purple.

5

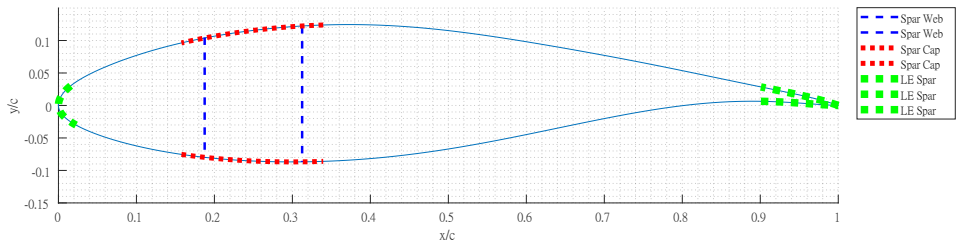
Using the example of the Makani M600 energy kit [172], the base aerofoil of the wing has been reconstructed and illustrated in Figure 5.2b. Similar to conventional aircraft wings, a rectangular spar box is found near the quarter chord that serves as the main structural member of the wing. A typical aerofoil of the 5 MW NREL reference wind turbine is illustrated in Figure 5.2a as another comparison point. A cross-sectional profile from a blade section from about $\approx 66\%$ of the span is depicted.

The characteristic spar web and spar caps of the blade section are seen, in addition to skin stiffeners at the leading and trailing edge reinforcements. The reference swept wing section is depicted for comparison in Figure 5.2c. The starkly thinner profile has a limited cross-sectional area to accommodate the typical rectangular wing box located around the quarter chord. Furthermore, considering the high wing loading requirements in conjunction with the slender profiles, a typical spar box would require considerable laminate thickness to achieve the desired stiffness requirements.

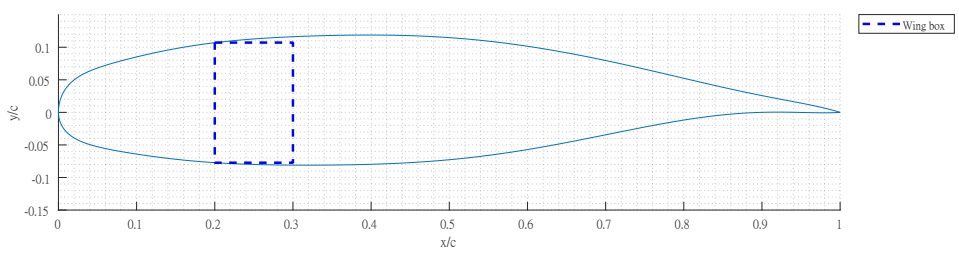
As a result, the wing structure in the reference wings does not have a typical rectangular wing box located near the quarter chord. Instead, an atypical wing box is used that incorporates the leading edge of the profile into the wing box — referred to as a D-box given its particular geometry. This hybrid spar box structure reinforces the leading edge geometry of the profile, similar to the reinforced front section of wind turbine blades.

The atypical wing box location is also motivated by the attachment of the bridle lines to the wing. The positions of the attachment points are governed by the target load distribution desired in the three tethers and the required steerability of the wing. The swept planform makes both these effects a function of the spanwise as well as the chord-wise location of the attachment points.

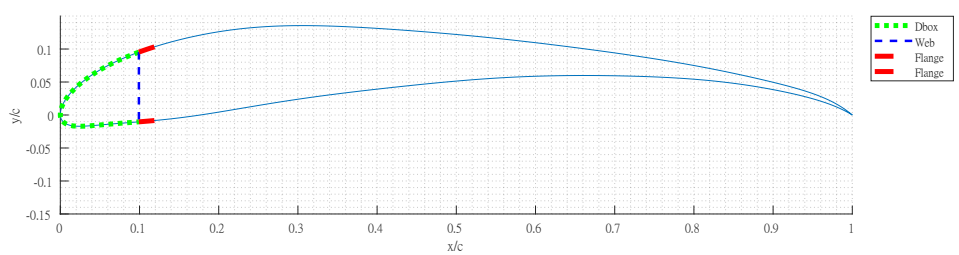
Given these load distribution and steerability criteria, the bridle attachment points on the reference wing are situated towards the leading edge. If a standard wing box (centred on the quarter chord) were used instead, additional structural components would be required to transfer the



(a) Conventional wind turbine aerofoil and internal structural reinforcements (DU21_A17 profile from NREL 5MW reference wind turbine).



(b) Makani M600 Energy Kite profile and wingbox structure.



(c) Reference profile and reinforcements.

Figure 5.2 | Comparison of aerofoils and internal wing box structural reinforcements for wind turbine blades, the Makani energy kite and the reference wing.

forces and resultant moments from the attachment sites at the leading edge into the wing box. Given the carbon skeleton and fabric-covered construction of the reference wings, this would lead to significant additional structural reinforcements and the associated undesired increase in mass.

Another element to consider is the leading edge auxiliary high-lift devices employed (further details in A.2.2). Given their aspect ratio and slenderness, these high-lift devices require sufficient support along the span to prevent buckling. With a spar box and rib construction of the wing, the auxiliary devices commonly require a denser rib spacing compared to the main wing section. With a conventional wing box, this leads to additional considerations and complexity for the rib design, especially given that the skin is fabric and not a sheet/panel structure as is customary for aircraft wing structures.

All these design requirements lead to a unique D-box design. To achieve the target stiffness and

mass target, this wing box serves multiple purposes. It is the structural load-bearing member for the aerodynamic and inertial forces. The wing box also gives sufficient structural support for the force transfer via the bridle line system attached to the wing. Additionally, it provides suitable mounting positions for the leading edge high lift device. By combining all these functions, additional structural members for these purposes along the chord to the wing box are avoided, simplifying both the rib design and over-all-wing design. This, however, comes at the cost of additional requirements for the design of the D-box. The multiple load introduction points and corresponding load transfer in the D-box require consideration. At this initial stage of design, best practices based on prior experience are employed such as local thickening at the bridle attachment positions. Detailed examination of the load transfer effects necessitates a more precise 3D finite element (FE) model, normally employed during the detailed design stage and is not discussed in this work.

5.1. WING BOX INTERNAL GEOMETRY AND STRUCTURAL OPTIMISATION

5

The reference wing is made up of two distinctive “Root” and “Tip” sections as illustrated in Figure 2.2, using two characteristic 2D cross-sections. The exact details of the aerofoil design are not strictly relevant to the current structural discussion and as previously stated, aerofoil aerodynamics \mathcal{A}_{2D} are precomputed. As a result, the aerofoil profile geometry serves as a boundary for the interior structural design. For this discussion, the aerofoils for the “Root” and “Tip” sections are selected from similar aerofoil families and thus have comparable profile geometry.

As described earlier, every 2D cross-sectional geometry has fixed outer profiles determined a priori from the aerofoil shapes, which are in turn derived from the aerodynamic requirements. Thus, this leaves the internal structural geometry $\mathcal{S}_{\text{geom}}$, consisting of laminate material, thicknesses and laminate layup \mathcal{S}_{lam} , as variables in the \mathcal{S} design space. A mass minimisation design optimisation is carried out, with the reference design being a traditional classical lamination theory (CLT) based initial design.

5.1.1. Laminate layup tailoring

The goal of this design study is to analyse the implications of individual ply level effects on the global structural response in the implemented structural analysis framework detailed in Chapter 3 and Chapter 4. The motivation for this has been mentioned briefly in Section 2.3.5, outlining the desire to impart desired, defined deflections for a given loading condition. These deflections, in turn, give rise to desired aerodynamic response and can hence be used towards passive load alleviation capabilities in such composite structures.

To illustrate the effects of varying the laminate on the structural response, a cantilever box beam is considered, where each side is built up with six layers of an AS4/3501-6 graphite-epoxy composite. In Figure 5.3, three variations to the stacking sequence for these six layer laminates are depicted. These variations, depending on the fibre orientation of the ply, lead to varying degrees of bend-twist coupling for the pure bending load that the structure is subjected to. As the mass of the laminates in these three cases is the same, one can begin to see the advantages swapping or “tailoring” of the laminates can achieve towards load alleviation. By exploiting similar bend-twist coupling effects in a wing, local angle of attack such as washout can be incorporated into the wing, thus tailoring the spanwise loading of the wing in response to

particular load cases. Thereby, the structural response could be tailored such that, for instance, increasing bending loads from guests could automatically induce a pitch-down effect on the wing. This would, in turn, reduce the aerodynamic loads. This idea of tailoring is further explored in [Chapter 7](#), where the coupled aero-structural response of the wing is considered.

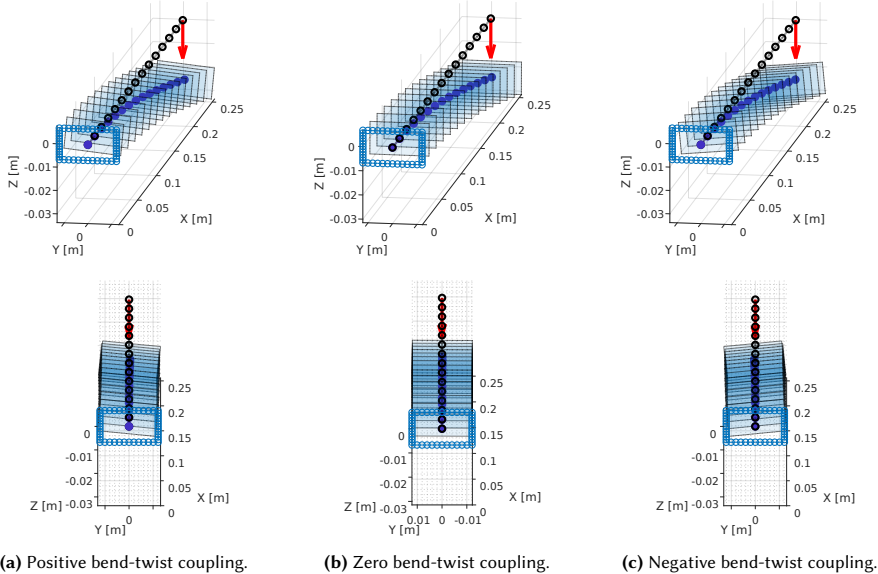


Figure 5.3 | Cantilever box beam that is subjected to a pure bending load displaying varying levels of bend twist coupling. The variation in these cases is only in the ply stacking sequence of the laminates of the beam shell.

In the current optimisation, the static response is first considered. The objective is to tailor the internal D-box geometry (laminate material, layer thicknesses and fibre orientations) for a chosen wing configuration (airfoil, planform and bridle geometry). The laminate material is pre-selected to limit the parameter space based on available manufacturing infrastructure. This constrains the design space to the layer thicknesses $\mathcal{S}_{\text{geom}}$ and fibre orientation of the laminate \mathcal{S}_{lam} . The optimisation is undertaken for a fixed design load case. The details of the load case are derived from nominal reel-out loads arising from crosswind operation. Hence, the structural mass of the D-box is minimised by varying the thicknesses and fibre orientations while maintaining a reference target stiffness that is prescribed by imposing a constraint on the allowable deflection of the structure to match the reference design.

5.1.2. Laminate thickness parameterisation

From a design perspective, the external shape of the D-box is constrained by the airfoil profile on the exterior, while the internal geometry and laminate details are considered a part of the optimisation domain (i.e. $\mathcal{S}_{2D} = f(\mathcal{S}_{\text{geom}}, \varphi(\mathcal{S}_{\text{lam}}), \dots)$). Hence the parameters in this domain include the internal geometry, laminate thickness, laminate layup, and material properties of the laminates. The topology discretisation of this outer geometry boundary is done using the spline-based methods described previously in [Section 4.3.1](#).

Following the geometric parameterisation, the next step is to derive the laminate thicknesses, which are then used along with material properties to determine the stiffness of the laminate layup. These laminate stiffnesses are utilised to determine the cross-sectional stiffnesses of the

geometry described by a given spline parametrisation. This is achieved by applying the cross-sectional modelling methodology detailed in Section 4.3 of Chapter 4. Hence, a method is required to convert the spline-based parametrisation used to describe the limits of the internal geometry into the required laminate stiffness parameters for the cross-sectional solver.

Since the internal geometry and, therefore, the thicknesses can change at each optimisation step, a methodology that can cope with the changing internal geometry is desired. A naïve implementation of traversing along the chord would soon result in geometric anomalies at the inflexion points. Hence, a more robust methodology is sought and developed here. This methodology is based on the knowledge that in each iteration of the internal stiffness optimisation loop, the outer domain of the geometry does not change, whereas only the interior geometry is perturbed at each optimisation iteration.

To accomplish this, the exterior aerofoil profile is first represented using a similar spline-based approximation as the internal geometry spline. This external spline would thus remain constant for the subsequent inner geometry perturbations. A fixed set of reference points in the section $\mathbf{P}_{sp} \in \mathbb{R}^2$ is generated by traversing along the spline coordinates of the aerofoil. A cosine distribution is used for typical aerofoils in this application, emphasising additional details at the leading edge. Thus, for a fixed external profile geometry spline, a unique set of reference points are generated. The 2D region bounded by the profile is subdivided into a tessellation of polygons, where the number of polygons is determined by the cardinality $n(\mathbf{P}_{sp})$ of the set of reference points on the bounding spline. As a 2D metric space describes the profile plane, the Euclidean norm is used as the distance function to calculate a Dirichlet tessellation in this 2D aerofoil plane [173]. This discretisation results in a set of polygons, where each polygon contains only a single reference point, and all points in the polygon are closer to the contained reference points than any of the other points in \mathbf{P}_{sp} . The resulting set of Thiessen polygons obtained is constant for a given exterior aerofoil geometry described by \mathbf{P}_{sp} , as illustrated in Figure 5.4.

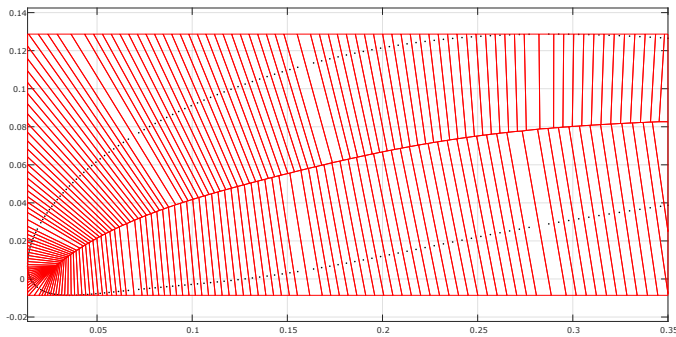


Figure 5.4 | Discretisation of the spline using Thiessen polygons.

From the intersection points of the resulting Thiessen polygons and the spline geometry, a subset of polygons is obtained that is bounded by the external and internal spline geometry. This results in a segmentation strategy that allows for the conversion of the spline-based parametrisation into a thickness profile described by the spline. Therefore, this allows for the mapping from the 2D topology to \mathcal{S}_{lam} . The resulting thickness profile is thus a function of the

internal spline, evaluated at points from \mathbf{P}_{sp} that are fixed in the external aerofoil spline coordinate system. Hence, this enforces that the number of segments used in the calculations of the stiffness parameters remains constant, even for varying internal spline thicknesses. Using the example of the same reference aerofoil, a typical resulting segmentation strategy is visualised in Figure 5.5.

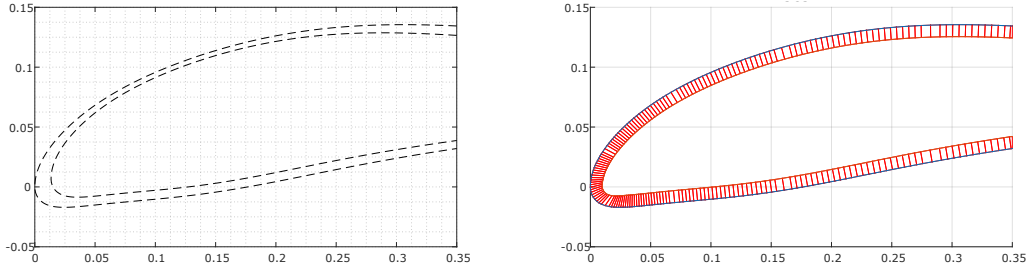


Figure 5.5 | Conversion of the spline-based discretisation to laminate segments for a typical aerofoil profile.

When considering the aim of local geometric perturbations in the thickness profile, the segmentation method is still found to be sufficiently capable. Local changes in the shell thickness prescribed by the spline can be captured in the segmentation with a moderate outer aerofoil segmentation distribution. A more involved spline segmentation is shown in Figure 5.6, where the local reinforcements at the leading edge are also captured by using a cosine distribution. Furthermore, the figure illustrates the ability of the method to sufficiently capture the local reduction of shell thickness as witnessed on the suction side. The robustness of the methodology developed here is not thoroughly tested but was found to be sufficient for the scope of the typical geometries encountered during the internal geometry optimisation.

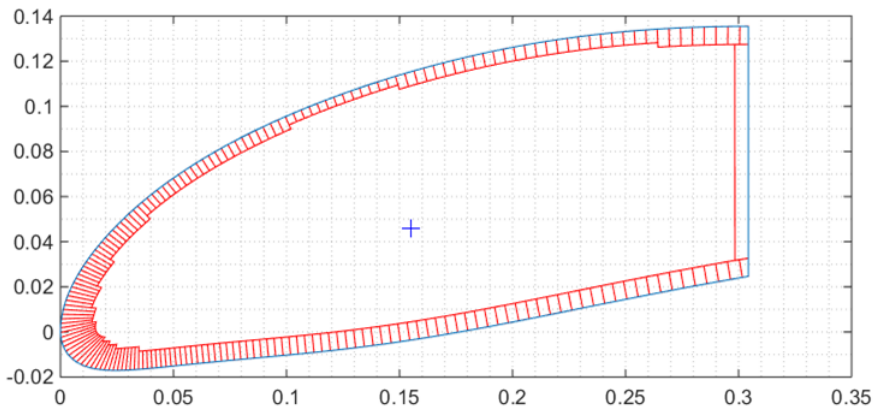


Figure 5.6 | Segmentations strategy applied to D-box spline discretisation consisting of local regions of varying thickness.

A manufacturing aspect that had to be considered in the discretisation process is that the shell layup comprises individual carbon fibre fabric sheets that are layered into the mould to build up the material thickness. A physical constraint arises from the manufacturing technique employed, as the carbon fibre fabric is available in standard thicknesses, as illustrated

earlier in Figure 4.5b. However, the spline parameterisation methodology results in a continuous thickness distribution along the spline and does not account for the discrete thickness steps associated with each fibre layer. Hence, during the intersection computations of the interior spline with the polygon boundaries, a predetermined material thickness database is used to calculate and impose the physical thickness based on the criteria for minimal layer height. This is illustrated in Figure 5.7. In the figure, the internal spline is plotted at discrete chordwise locations using triangle markers. The resulting segment geometry accounting for the material thickness and minimal length l_{mat} is visualised. Additional criteria are imposed to ensure that each adjacent segment is comprised of the same base layers. Thus, in Figure 5.7, each layer in the laminate is visualised by a line of a different colour. Hence it is possible to set up zones based on manufacturing capabilities to ensure that all segments in that zone have a homogenous base layer of material.

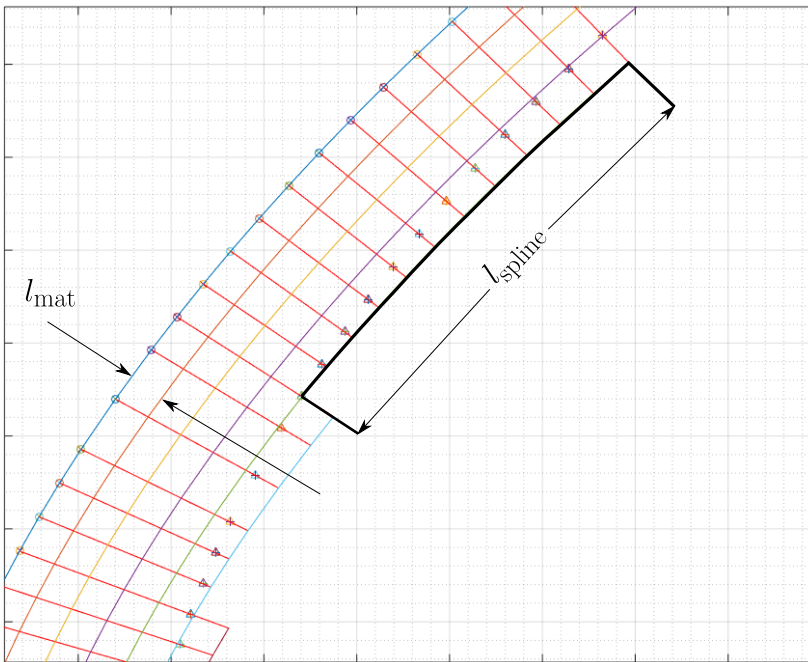


Figure 5.7 | A highlighted cross-section view of the shell section of the profile. Spline location is visualised by triangle markers, while individual coloured lines visualise material layers. Red lines mark the bounds of the discretisation domain. The segmentation is adjusted using a material length, l_{spline} and ply material thickness l_{mat} to take into account discrete ply thickness steps.

5.2. CASE STUDY: CROSS-SECTIONAL TOPOLOGY OPTIMISATION

Initial trials with this approach are carried out, parametrising the number of segments to which the same laminate stack is restricted. This is done by dividing the external aerofoil spline into several n_{spline} sections. Then, criteria for the thickness profile of the internal geometry along the length l_{spline} of each spline segment is prescribed in terms of the material length l_{mat} as seen from the annotations in Figure 5.7. While these length parameters could also be added as a design variable in the optimisation, a more pragmatic approach would be to keep them fixed. As material length parameters are dictated by material availability and manufacturing process capabilities, per-material lengths are utilised from a preselected database of materials suitable

for the manufacturing capabilities and costs. Similarly, the spline length l_{spline} parameter is determined from the discretisation of the external aerofoil spline and is derived from the manufacturing tolerances for material placement. Hence, this leaves the stacking sequence and the spline thickness parameters as free variables for the mass minimisation problem.

To evaluate this methodology, a 2D cross-sectional mass minimisation is carried out, where only the 2D cross-sectional stiffness \mathcal{S}_{2D} is considered. This is accomplished by setting constraints for the problem such that the optimised cross-section has the same stiffness (within a tolerance) as a reference section. The stiffness of the reference section \mathbf{S}_{ref} can be obtained from any suitable methodology, ranging from full 3D shell element based finite element method (FEM), or as in this case, using the full 2+1D model, with the desired deflection criteria.

The problem can be formulated in terms of the cross-sectional laminate thickness profile $\mathbf{h} = h_1, h_2, \dots, h_{n_{spline}}$ determined from the spline parameterisation parameters defined by $\mathbf{X} \in \mathbb{R}^{2(n_o+1)}$. Where n_o is the order of the spline polynomial chosen. A pre-selected material database is utilised, from which materials are chosen in order to create the stacking sequence for each of the n_{spline} segments in the cross-section. The minimisation problem can thus be defined as:

$$\begin{aligned}
 & \underset{\mathbf{X}}{\text{minimize}} && \sum_{i=0}^{n_{spline}} h_i(\mathbf{X}) \\
 & \text{subject to} && \xi_i^{A,B,D}(\mathbf{X}) \\
 & && |\mathbf{S}(\mathbf{X}) - \mathbf{S}_{ref}| \leq S_{tol}
 \end{aligned} \tag{5.1}$$

Initial optimisation results show that the local increase or decrease of the shell thickness only start to manifest at larger physical D-box scales. For the scale of the reference wing's D-box, some results of this approach are presented in Figure 5.8. These results show that for the evaluated load cases and current geometric scale of the D-box, the shell thickness converges to a uniform value along the spline, thus not warranting such a detailed geometric parameterisation of the cross-section. This is a function of the aspect ratio of the considered cross-section — the geometrical scale of the section is only a few orders of magnitude larger than the shell thickness. As the geometric scale of the cross-section increases with respect to the shell thicknesses, this detailed shell parameterisation method should prove helpful.

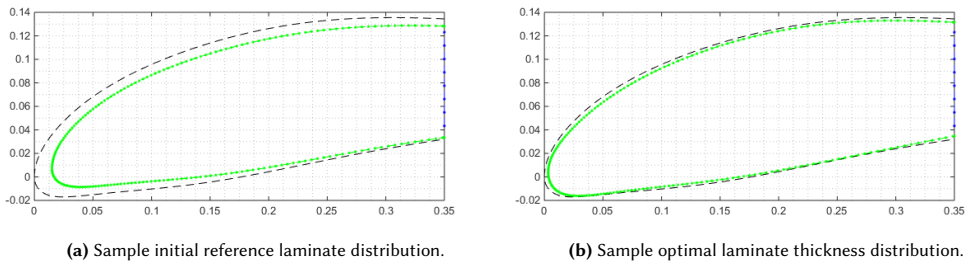


Figure 5.8 | Initial results based on a spline-based internal geometry optimisation.

5.3. CASE STUDY: CROSS-SECTIONAL LAMINATE LAYUP OPTIMISATION

Given the spline parameterisation's convergence to predominantly uniform laminate thicknesses along the shell, it was decided to simplify greatly the internal D-box geometry parameterisation. Additionally, accounting for the typical manufacturing processes utilised in the prototype phase limits the focus of the optimisation to layups that can be manufactured in-house. Thus, the internal geometry of the D-box cross-section is deconstructed into fewer distinct geometrical groups. In this case, the internal geometry is broken down into a "C-Beam", and an aerofoil-shaped shell "D-Shell" as illustrated in Figure 5.9a. The "C-Beam" geometry is further composed of a single web and two flanges at the top and bottom.

Following the spiral system development process (see Section 2.2.2), fast design-build-fly times are desired. Hence, in compliance with the manufacturing process available, each of these three geometric groups are composed of characteristic laminate layups, i.e. the fibre orientations and the number of layers for every node in one of these geometric groups are maintained the same. This allows for a constrained design space in compliance with the manufacturing process utilised (during prototyping). Thus, for the optimisation considered, all two-dimensional elements in one geometric group are assigned the same thickness and characteristic stiffness properties. The characteristic stiffness for the laminate, as indicated in Section 4.3, is a function of the material properties, as well as the fibre orientation in each layer of the laminate.

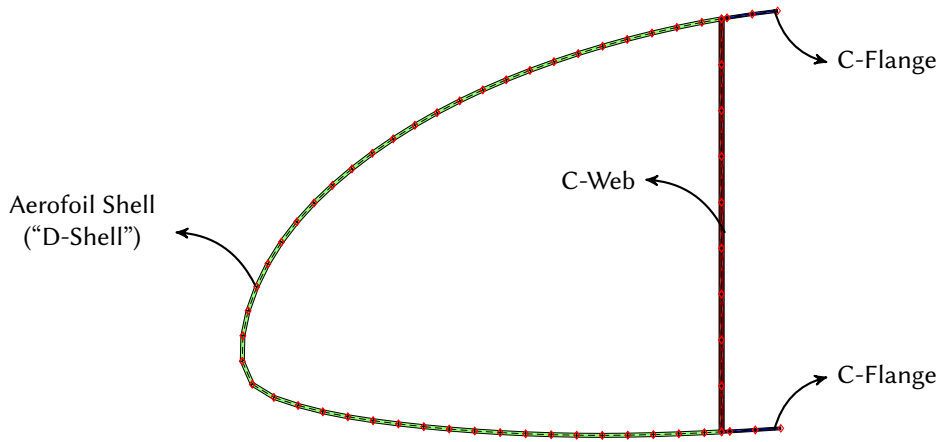
5

Lamination parameters

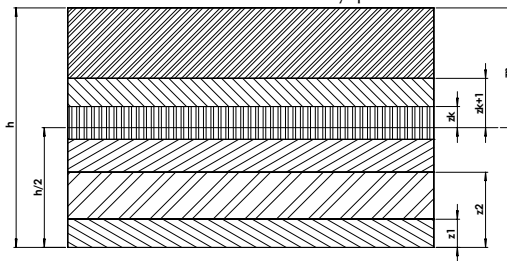
For each 2D node in the cross-section solver, a characteristic stiffness parameter is required. For composite laminates, this is traditionally determined by CLT as touched upon in Section 4.3. Based on manufacturing requirements and availability criteria, a selection of materials is pre-chosen for the ply layers of the laminate, for the current cross-section discretisation. This simplification reduces the degrees of freedom for the optimisation problem to the overall thickness and fibre orientations for the layers in each geometric group in the cross-section discretisation. Hence, for every characteristic cross-section in the wing, each distinct 2D geometric group will have a laminate stacking sequence and thickness as a variable for the optimisation.

In order to uncouple the dependency of the fibre angle orientation on the characteristic stiffness (ABD) of each 2D laminate node, lamination parameters are chosen over traditional CLT based ABD stiffness parameters, as detailed in Section 5.3. With lamination parameters, an arbitrary stacking sequence, with an arbitrary number of plies, can be described by material invariants and 12 lamination parameters.

The utilisation of lamination parameters significantly reduces the number of design variables of the optimisation problem, making the problem independent of the plies at each two-dimensional node. The second major advantage is that, unlike the irregular, discrete ply angle design space of this manufacturing process, the lamination parameters design space is bounded and shown to be convex [174]. Closed form expressions exist for in-plane, out-of-plane and bending expressions for cases where they vary independently [175]. However, closed form solutions that completely constrain the entire feasible design space are still a topic of active research. To the best of the author's knowledge, no closed form expressions are available for problems that are not strictly dependent on either in-plane or out-of-plane stiffness exclusively.



(a) Discretised D-box cross-section where each of the distinct geometric groups (D-Shell, C-Web, and C-Flange) have their characteristic laminate layups.



(b) Sample laminate layup at one distinct geometric group.

Figure 5.9 | Typical cross-section geometry utilised along the span of the beam.

To determine a design space using in-plane, out-of-plane, and coupling stiffness parameters, the feasible region can be obtained by successive convex hull approximations leading to a large set of linear constraints (i.e. 37126 for the fully coupled case) [176]. For the current optimisation problem, the feasible region is determined from the convex hull for a set of ply angles chosen a priori following the methodology of Bloomfield *et al.* [177], to suit the current manufacturing requirements, reducing the total number of constraints.

Optimisation problem formulation

The optimisation problem aims to minimise the mass of the D-box, whilst satisfying predefined deflection criteria. In the problem, a baseline initial design is chosen from traditional CLT based approximations. The mass of the D-box can be expressed as a function of the individual thickness of each element in each spanwise 2D cross-section. As described in Section 5.3, each spanwise 2D cross-section is broken down into three unique geometric groups - the D-Shell, C-Web and C-Flange. Thus, for each 2D cross-section, the elemental mass can be expressed as a function of the material density of the laminate, and the thickness profile of each of the three geometric element groups collected into the vector $\mathbf{h}_i = [h_{shell}, h_{web}, h_{flange}]$. Here, the

subscript i denotes the index of the 2D cross-section in consideration.

Thus, the mass is computed as a function of the thickness profile of all 2D nodes, for all the 2D cross-sections considered and is represented by the vector $\mathbf{h} = \mathbf{h}_1, \mathbf{h}_2, \dots, \mathbf{h}_n$, where n is the number of elements in the 1D model. The dimension of \mathbf{h} is thus the summation of all the 2D nodes for all the cross-sections stacked along the span. Constraints on the maximum allowed deflections, laminate thickness, and feasible design space for the lamination parameters are defined as follows:

$$\begin{aligned} & \underset{\mathbf{h}}{\text{minimize}} && \sum_{i=1}^n M_i(\mathbf{h}_i) \\ & \text{subject to} && \mathbf{U}(\mathbf{h}) \leq \mathbf{U}(\mathbf{h})_{ref} \\ & && \mathbf{h}_{min} \leq \mathbf{h} \\ & && f(\boldsymbol{\xi}^A, \boldsymbol{\xi}^B, \boldsymbol{\xi}^D) \leq 0 \end{aligned} \quad (5.2)$$

where \mathbf{h} is a vector of the laminate heights of the shell, web and flange for all spanwise, two-dimensional sections just described, and \mathbf{U} is the deflection of the D-box. For each two-dimensional geometric group, the design vector consists of 12 lamination parameters to account for the stacking sequence of the laminate and one parameter for the laminate height h as described in Table 5.1. This leads to 39 variables for each 2D section, consisting of 3 characteristic geometric groups (D-Shell, C-Web, and C-Flange) described in Figure 5.9a.

For the current optimisation, the wing span is discretised into two distinct 2D cross-sections - the root and the tip 2D sections. Around 40% of the beam span is assumed to be composed of a cross-section equal to the root section, and the rest utilises the tip section, similar to Section 6.1. This leads to an overall design vector of 78 variables. A gradient based interior point algorithm is utilised to solve the problem defined in Equation 5.2.

Table 5.1 | Optimisation variables for each of the three (D-Shell, C-Web, and C-Flange) two-dimensional element groups, leading to 39 variables for each characteristic two-dimensional cross-section, and thus 78 variables in total for the two unique cross-sections considered in the current optimisation.

Stacking Sequence	$\boldsymbol{\xi}_{[1,2,3,4]}^A$	[-]
	$\boldsymbol{\xi}_{[1,2,3,4]}^B$	[-]
	$\boldsymbol{\xi}_{[1,2,3,4]}^C$	[-]
Laminate thickness	h	[mm]

Results and discussion

Solutions of the described minimisation for an example problem consisting of two cross-sections are visualised in Figure 5.10 for the root, and in Figure 5.11 for the tip cross-section. In both figures, all thicknesses are plotted to scale and are normalised to the initial reference design. Both sections are normalised to the thickness of the reference root section. This normalisation is done to reduce the effects of variation of the initial reference design in the reported results. This factor is important as the savings in the weight achieved are highly dependent on the initial reference design and the proximity of the initial reference design to the cost function's minima.

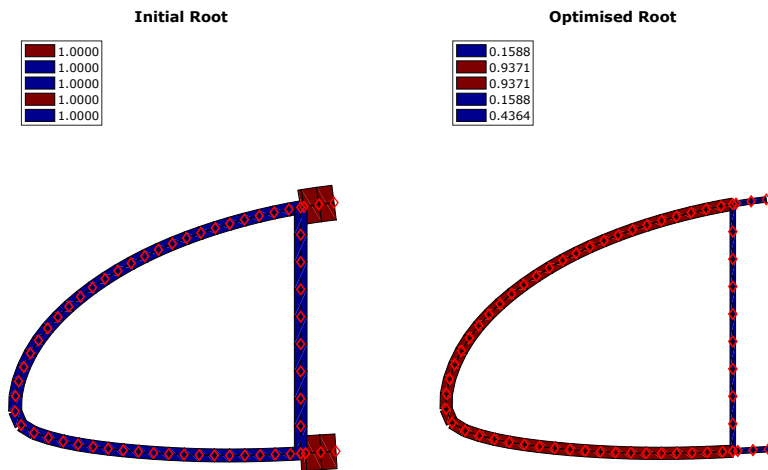


Figure 5.10 | Comparison of optimisation results for the root cross-section. Note: the element thicknesses illustrated are scaled to the actual laminate thickness.

The initial cross-section reference layup and thickness for the optimisation problem is determined utilising the calculation methodology typically employed during initial design stages. The “C-Web” and “C-Flange” sections are sized using the critical forces and moments in the D-box. Classical laminated plate theory is then applied to size the corresponding thickness and layup for these sections along with the Tsai-Wu failure criteria [178].

The results obtained demonstrate the benefits of utilising a more comprehensive design methodology right from the initial design stage. For the given laminate properties used in this analysis, the optimised laminate layups lead to $\approx 20\%$ reduction in mass as compared to the initial reference cross-section geometry. What is apparent from the results is that the optimised profiles consider the contribution of the asymmetric aerofoil shell towards the stiffness of the D-box. Furthermore, in both the root and tip profiles, the layup in the “C-Web” and “C-Flange” sections is constrained to the minimum prescribed thickness defined in the problem definition. For layups in the tip section, an increase in the thickness of “D-Shell” is also witnessed. Given the deflection constraints imposed in the problem definition (Equation 5.2), the optimised cross-section profiles and laminate layups show that it is possible to achieve similar overall torsional and edgewise stiffness with a lower mass penalty from the optimised layup of the “D-Shell” as compared to initial thicker “C-Beam” sections, given the scale of the geometry considered.

5.4. SUMMARY AND CONCLUSIONS

Building upon the methodology to parametrise and model the wing structure of typical composite rigid and semi-rigid AWE from Chapter 4, the 2D structural domain \mathcal{S}_{2D} is explored in this chapter. A computationally inexpensive structural model that includes the effects of load-deflection couplings and other shear deformation effects experienced by slender composite structures is used here. In all subsequent studies, the primary load-bearing member of the composite kite is modelled with a 2+1D finite element approach. The results show that the developed structural model has sufficient fidelity to perform mass minimisation by optimising both the ply layup and topology in the laminate design space (\mathcal{S}_{lam}) and cross-sectional geometry (\mathcal{S}_{geom}) that together comprises the 2D structural domain \mathcal{S}_{2D} . While the methods utilised here also apply to conventional turbine blades and aircraft-type AWE structures, the

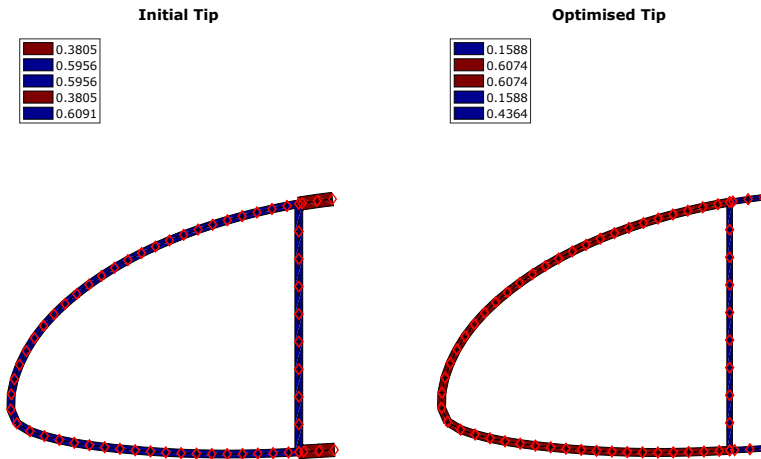


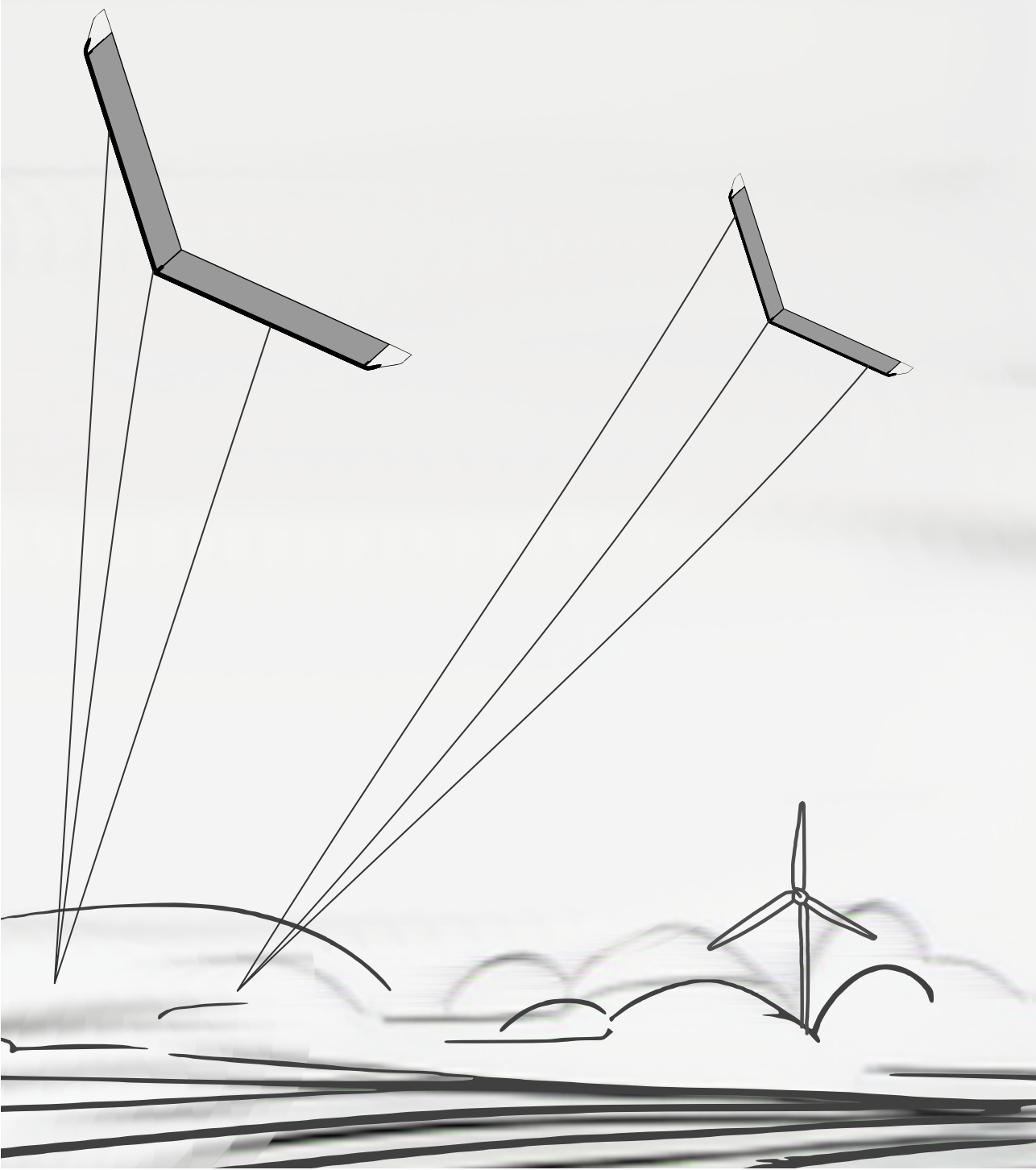
Figure 5.11 | Comparison of optimisation results for the tip cross-section. Note: the element thicknesses illustrated are scaled to the actual laminate thickness.

5

particular design challenges of the reference wing are explicitly explored.

The wing-box in the considered case is an atypical D-box of the composite swept reference wing. It is modelled by considering individual characteristic 2D cross-sections stacked along the span of an anisotropic 1D beam model. The external loads on the beam are determined using a nonlinear **VLM** for the 3D aerodynamic loads, coupled with a bridle model that determines the forces resulting from the bridle-pulley system at equilibrium conditions. The methodology developed allows for the computationally fast and inexpensive exploration of initial design space for rigid kites for **AWES** applications. The model has multiple levels of fidelity, providing capabilities such as optimisation of the 2D cross-sectional geometry in isolation. This is particularly useful when detailed laminate stacking sequences are unknown or not required, such as for initial mass estimation for wing sizing studies.

A 2D cross-sectional geometric and layup optimisation was done by setting a target stiffness for the cross-section while minimising the mass. This methodology was not pursued further, as the additional complexity and computational time yielded little benefits, especially given the geometric scale of the D-box that was considered and the particular composite manufacturing capabilities available at the time. Thus, a simplification was made in the 2D cross-sectional geometry, grouping distinctive geometric elements (web, flange and shell in this case). The reduced computational cost allows for multiple cross-sections to be considered in the complete 2+1D framework, with which an optimisation of the internal geometry of a root and a tip section of the reference swept rigid wing is carried out to minimise mass while meeting target deflection criteria. The resulting solution yields an optimised laminate layup and thickness that, for the typical load case evaluated, leads to an overall weight savings of $\approx 20\%$ compared to the initial reference design.



Chapter 6

Bridle design space

*The existence of the nightmare abyss is not a reason to fear,
its an invitation to go skinny dipping.*

—HP Lovelace

Adapted from:
Structural Analysis and Optimization of a Tethered Swept Wing for Airborne Wind Energy Generation
Wind Energy, 23(4), 1006-1025 (2020)

ABSTRACT

This chapter explores the influence of the bridle domain \mathcal{B} on the structural response of the wing. The significance of the load introduction from the bridle configuration is outlined. The relation between the wing's stability and control criteria and bridle system design is examined. Subsequently, a case study with multiple bridle system configurations is carried out to analyse the impact of the bridle configuration on the structural domain's \mathcal{S} response.

6.1. BRIDLE CONFIGURATION DESIGN

The computational model developed allows for the fast evaluation of various wing geometry and bridle configurations, allowing for the exploration of different bridle configurations on the structural response of the wing. As described previously in Section 2.3.2, the bridle subsystem design plays a vital role in the flight dynamics of the wing since it determines both the stability and steerability of the kite from the ground. These flight mechanical criteria determine the requirements for the location of the bridle to tether interface. However, these criteria are not elaborated in detail to limit the scope of discussion and are instead treated as positional constraints for the interface in the problem formulation. Furthermore, the bridle configuration also provides an opportunity to change the load distribution along the wing's span, which is the focus of this section i.e. $\varphi(\mathcal{S}) = f(\xi(\mathcal{B}))$.

6.2. IMPACT OF BRIDLE DESIGN ON LOAD INTRODUCTION

As touched upon in Section 3.3 and in Figure 3.6, the bridle domain \mathcal{B} provides a unique opportunity in the design of composite wings for airborne wind energy (AWE). To explore the change in the load introduction arising from the bridle configuration, an illustrative case is considered for two bridle systems ("A" and "B") with a fixed external tether force vector \mathbf{F} . This tether force is applied at the final pulley of the system. A further assumption is made that the wing is undergoing no sideslip. This results in a tether force vector with force components only along the Z and X axis, with no force components along the span (Y axis). These components can be visualised by the force vector at the final pulley, as depicted in Figure 6.1.

Two bridle configurations are seen in Figure 6.1, a single pulley configuration ("A") is depicted by the system with dashed lines and a triple pulley system ("B") with dotted lines. The lengths of the bridle segments are tuned such that both systems have their final pulleys at the same position, thus resulting in the same tether force vector \mathbf{F} being applied to both systems. Thus, the physical difference in the two bridle systems depicted is the additional two branches in the bridle system "B" compared to "A". This leads to two additional attachment positions on the wing, depicted by black markers (\otimes) in the figure, along with the corresponding extra two pulleys to make up the branch.

Considering the case of the same tether force \mathbf{F} at the final pulley for both configurations, the resulting force vectors at the attachment points are solved for and visualised in bold in Figure 6.1. The force vectors depicted are uniformly scaled with respect to their magnitude. The additional attachment points and a pulley in the second system make it immediately apparent that the forces' magnitude and direction are different for these two systems. By increasing the number of bridle segments, leading to more attachment points along the wing, the magnitude of force at each attachment position is naturally reduced as the total $\|\mathbf{F}\|$ is distributed linearly across the attachment points. By distributing these attachment positions along the wing's span, the wing's bending moments can be tailored, reducing the wing's stiffness requirements. This allows for a much lighter wing for given deflection criteria. However, as with all engineering designs, a trade-off must be achieved at the system design level. The negative impact on the energy harvesting capabilities of the kite arising from the increased system drag from additional bridle segments needs to be balanced against the beneficial structural tailoring.

The direction of force introduction by the bridles at the attachment points is an interesting factor to consider, especially given the anisotropic composite structures and the various load

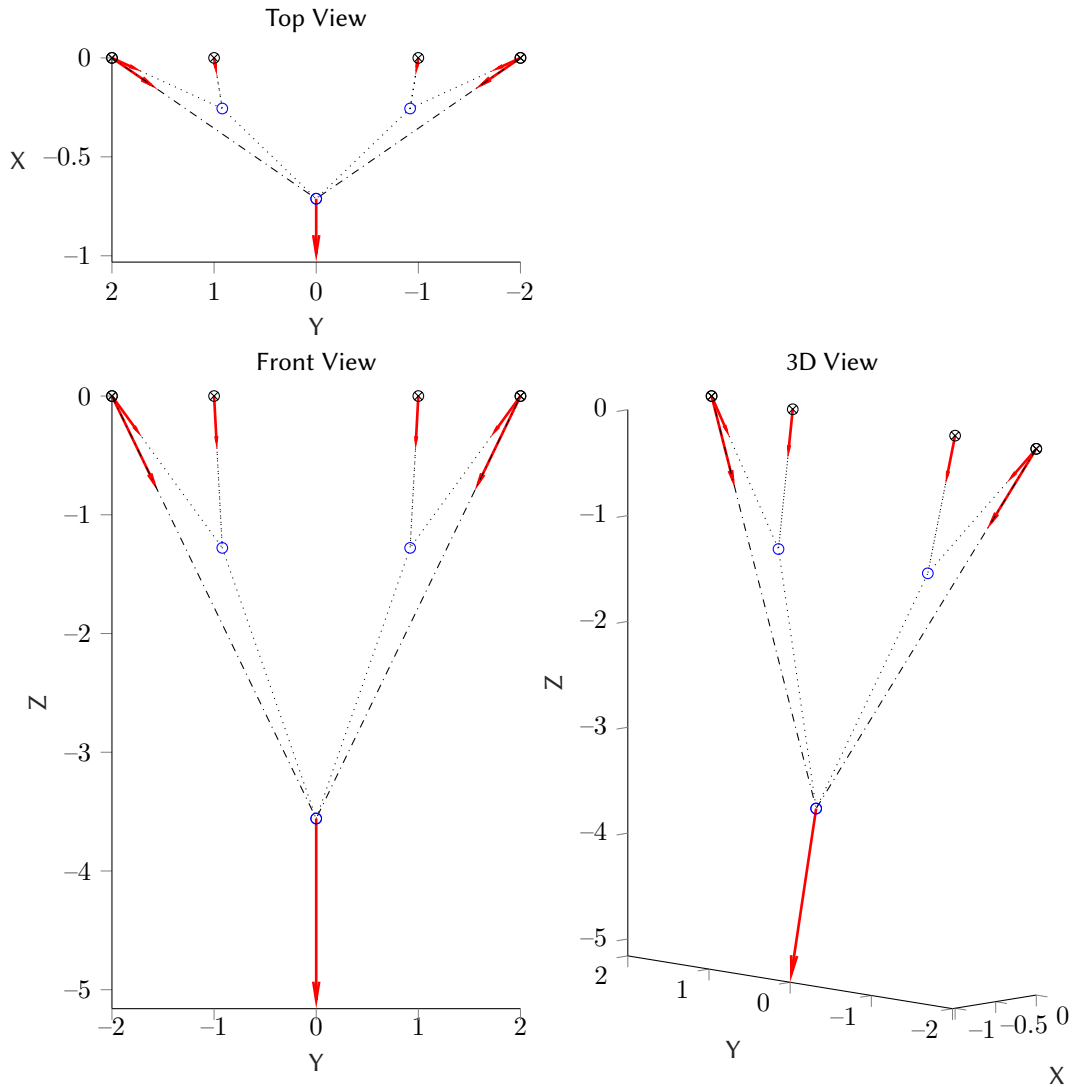


Figure 6.1 | Comparing the influence of bridle and pulley configurations. Two bridle systems are considered, a single pulley system (dashed lines) and a triple pulley system (dotted lines). Both systems have their final pulley at the same location. For the same tether force vector F , acting at the final pulley, the forces at the attachment points are visualised.

deformation couplings experienced by them (see Section 5.1.1). Although two bridle configurations might have a similar magnitude of forces at the attachment positions, a change in the direction of force can lead to a change in the structural response of the wing. This change in direction is seen in Figure 6.1 at the first attachment position. The material parameters, along with the laminate layup along the wing, define the magnitude of load deflections coupling the particular wing section experiences. This makes it extremely critical to consider the bridle design already during initial design stages rather than designing the wing structure in isola-

tion and adding the bridle in later design phases. These factors make the bridle configuration even more critical when considering the coupled aero-structural response of the wing as seen subsequently in **Chapter 7**.

From the system perspective, the ratio of the forces on the main line to those on the control lines is a key parameter that influences the steerability of the kite. This force ratio also plays a role in energy harvesting. As such tri-tethered systems commonly have the electrical machine used for power generation coupled only to the main drum and not the steering drum. However, this can be alleviated using a mechanical link between the three electrical machines, such as the EnerDrive [179].

6.2.1. Bridle and wing design

From the perspective of wing design, the design space needs to be constrained depending on the level of fidelity required. When examining the bridle design from a performance and energy harvesting lens, it is sufficient to constrain bridle design to maintain the force balance ratio required between the main and the control lines, allowing sufficient control authority and power harvesting capacity on the main line. However, when considering the stability and steerability of the wing, the vector force in the steering line plays a significant role. As a preliminary design exercise, multiple bridle configurations are simulated (depicted in Figure 6.2) that would all lead to the same steerability of the kite as both the vector and magnitude of the steering tether force \mathbf{F}_c would be maintained the same for all four cases. This is because the forces in the tethers are in equilibrium with the aerodynamic forces in the system and are a function of the pulley position as described in Section 3.3. In the scenario depicted, the force at the pulley is the same for all the bridle configurations depicted, given the same aerodynamic forces. This is because the final pulley where the tether attaches to the bridle system is kept at a constant position. Considering the level of fidelity of the static structural models, these bridle configurations would lead to a varied structural response that is further explored.

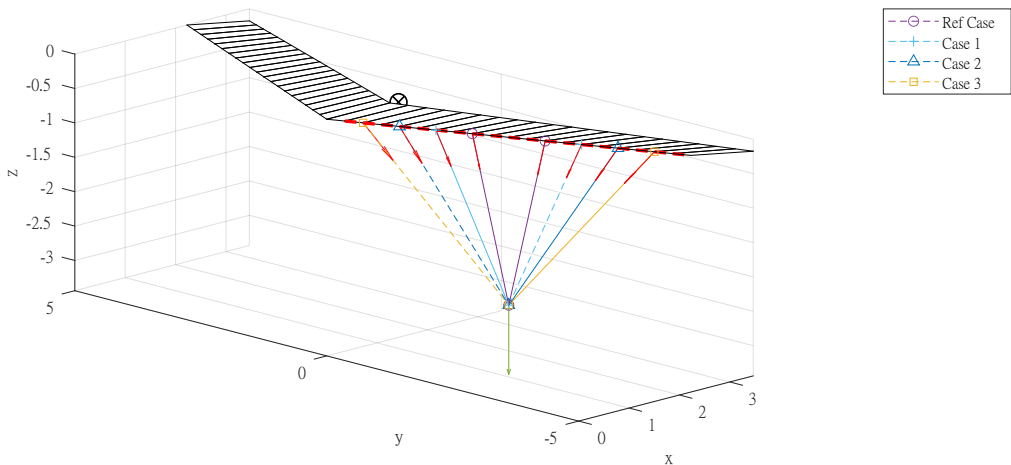


Figure 6.2 | Comparing the influence of bridle attachment positions. Multiple bridle systems that lead to the same tether force vector \mathbf{F} acting at the final pulley, but leading to varied force introduction into the structure.

6.2.2. Power generation with multiple tethers

For multi-tethered AWE systems, the ratio of the force distribution across the tethers that run to the ground is a design space to explore. For a typical tri-tethered system, this would be split into a single “main” line and two “steering” lines. When considering this design space from the perspective of power harvesting, the constraint of the location of the pulley can be relaxed, taking into account only the force ratio.

Three example attachment positions that maintain the same force ratio between the main and control line are explored, as depicted in Figure 6.3. The configurations are viewed from the top for a typical load case of a reel-out manoeuvre, but with no sideslip considered. Thus, the tether forces have both X and Z components but no Y component. This can be seen from the figure by the offset X position of the control line pulleys compared to the attachment positions on the wing. Here, configuration “A” (Figure 6.3a) consists of a more inward location of the control line pulley at around 62% of the total wing span, while configuration “B” (Figure 6.3b) and “C” (Figure 6.3c) both have the control line pulley at the same point at roughly 70% of the span.

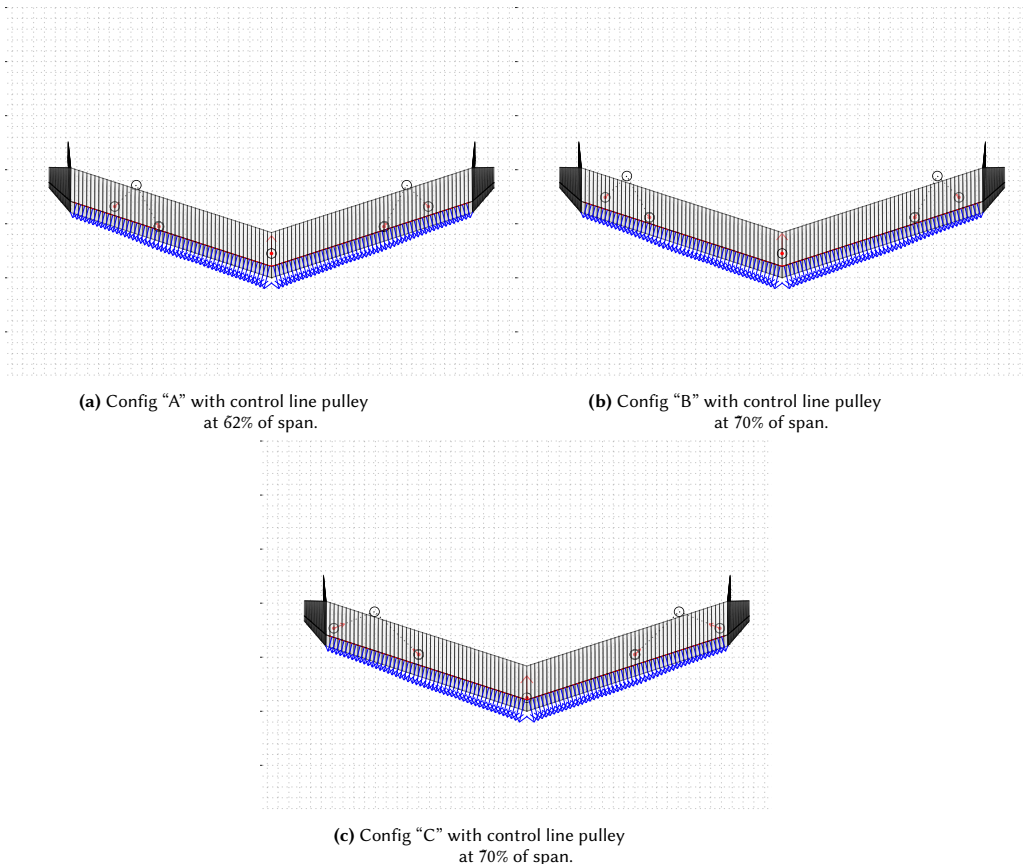


Figure 6.3 | Varying bridle attachment position along the wing span while maintaining a similar force balance ratio between main and control tethers.

These three designs would have different discipline biases from the system design perspective.

Configuration “A” with the control closer to the root would result in a lower root bending moment for the same force distribution and thus would require a less stiff D-box, which could result in a lighter wing. However, this would be offset by the steerability of the kite, especially when it comes to roll authority as a function of control line tether length. As discussed earlier, from the control perspective, the magnitude and direction of the force at the final pulley to which the tether is attached is critical.

Configurations “B” and “C” have the same control force in both cases, as both configurations have the final control line pulley at the exact location for a given aerodynamic load case. Thus, when comparing these two configurations, the design considerations are mainly driven by the structural domain, especially considering the variation of the force introduction angles at the attachment points, as well as the location of these attachment points. Therefore, for a fixed exit tether force of the bridle system, the wing attachment points and pulley positions are an additional design space that influences the structural response of the wing. This bridle configuration space can be beneficially exploited in satisfying deflection and mass criteria for wing design.

6.3. CASE STUDY: BRIDLE INFLUENCE ON STRUCTURAL RESPONSE

To assess the influence of the bridle domain \mathcal{B} on the structural response of the wing, some typical bridle configurations typically explored in the concept phase are visualised in Figure 6.4. In the figure, the red force vectors indicate the force distribution at the attachment points along the wing structure. These examples were obtained by varying the attachment positions and bridle configuration while maintaining the design goal of the force distribution between the main and the control line within the desired range.

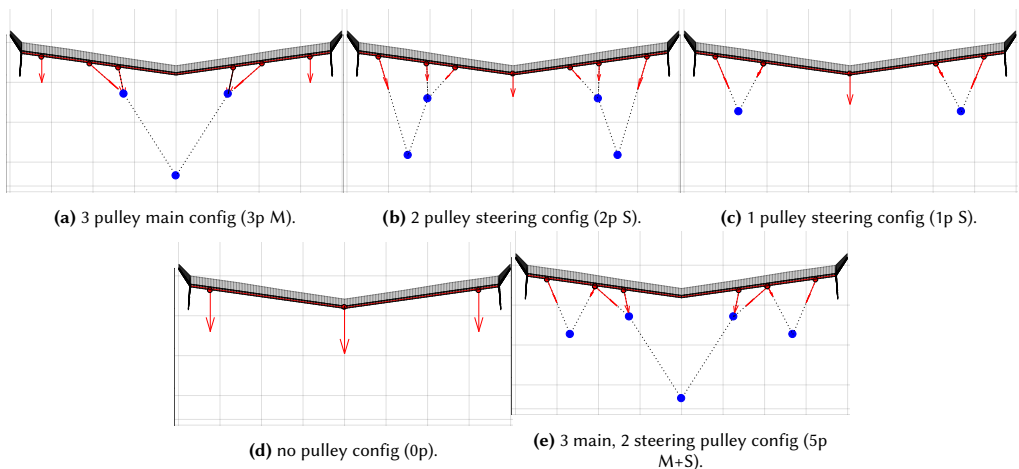


Figure 6.4 | Five typical bridle configurations depicting the variation of bridle force distribution for same nominal cross wind operation design point.

In this design study, five bridle designs are considered. The bridle configurations all use three main tethers to connect to the ground but vary in the number of attachment points along the wing and the number of pulleys utilised. Configuration “A” (Figure 6.4a) utilises a system of

three pulleys for the main tether. Configuration B (Figure 6.4b) consists of a two-pulley system, while configuration “C” (Figure 6.4c) utilises a single pulley system for each control tether. In configurations “B” and “C”, the main line is attached directly to the main attachment point with no pulleys. Similarly, configuration “D” (Figure 6.4d) consists of no pulleys, with direct tether connections to the attachment points on the wing, while configuration “E” (Figure 6.4e) is a combination of configuration “A” and configuration “C”.

6.3.1. Structural deflection response

The significance of the bridle configuration is further explored by analysing the structural response in the stiffness domain \mathcal{S}_{1D} for these five bridle configurations “A” to “E” as illustrated in Figure 6.4. To isolate and quantify the influence of the bridle configuration better, the wing planform and the 2D cross-section geometry are fixed for these analysis cases. This is done by assigning a reference stiffness tensor \mathbf{S}_e for every element in the 1D model, based on reference D-box geometry and material layup. This allows for a relative comparison of these different bridle configurations, at the conceptual design stage without having to completely detail the laminate stacking sequence and layout for the 2D cross-sections of the wing. At a later design stage, the design of the cross-sections can be carried using the methodology covered in Section 5.1.

For this case study, two unique sections were considered along the span of the wing, wherein two-thirds of the half span is composed of typical 2D sections described as root sections, and the rest consists of 2D tip sections. These two sections were thus kept constant across all the bridle configurations considered in this analysis fidelity. Utilising the structural model, the resulting deflections are depicted in Figure 6.5.

The deflections in the figure are plotted in the beam reference frame xyz as introduced in Figure 3.1 that originates at the half-wing beam reference axis. While differences in deflections are expected due to varying load distributions caused by different bridle configurations, the analysis methodology captures and quantifies these effects. Comparing the magnitudes of deflection, the tip deflection is most prominent in the z axis, with the maximum deflection of $\approx 5\%$ of the span as compared to $\approx 1\%$ in the chordwise x axis and $\approx 0.5\%$ for spanwise y axis.

For deflections in the z axis, compared to traditional wings, the AWE D-box experiences downward wing tip deflections due to the bridling. More bridle attachment points reduce the root bending moment, which results in lower z deflections for the configurations with more pulleys. It should be noted that from the structural point of view, more attachment points allow better load introduction along the span and, thus, lighter wings. However, as mentioned previously, the increase in the overall system drag is also an aspect that needs to be considered from the system perspective.

6.4. SUMMARY AND CONCLUSIONS

The bridle design space \mathcal{B} plays a significant role in the load introduction into the wing structure. Compared to a single tether, the bridle distributes the load across multiple points into the wing structure. Changes in load introduction could also lead to a different structural response, given the change in load deflection couplings in the wing structure. This coupling phenomenon makes the wing’s structural response sensitive to the bridle attachment forces’ location, magnitude and direction. This is important, as the total magnitude of force for differ-

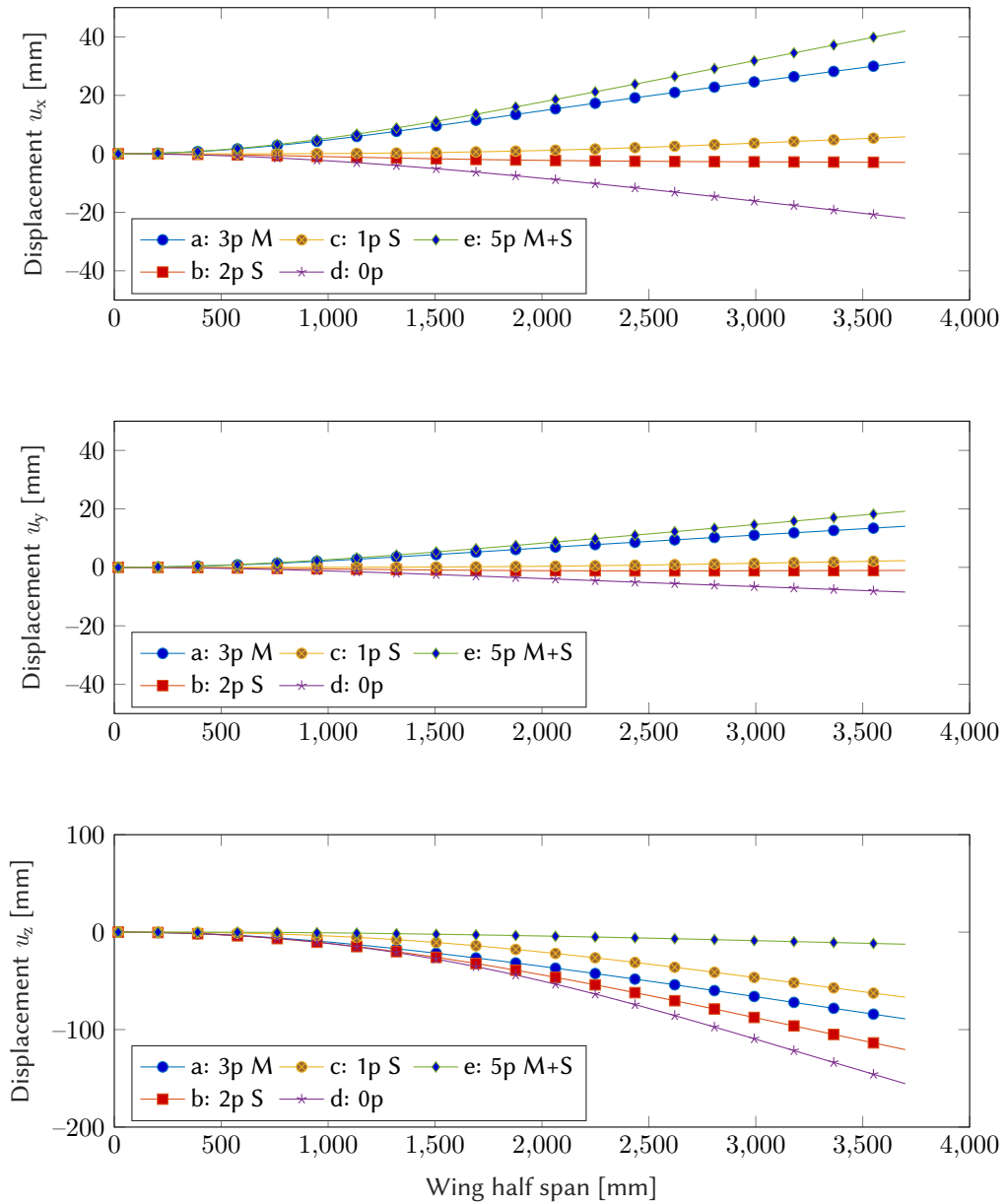
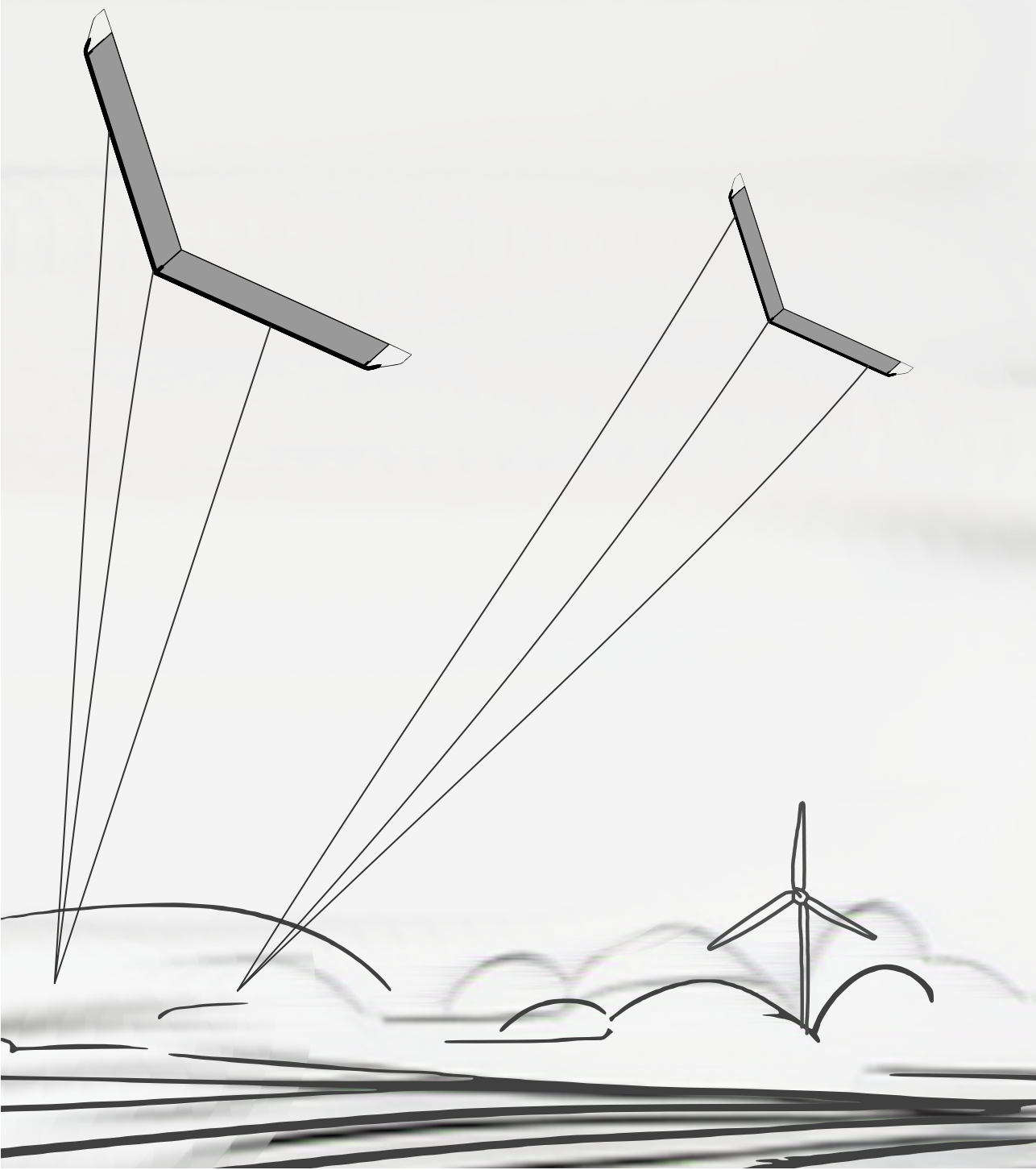


Figure 6.5 | Influence of bridle configurations on the structural response of typical wing box design. Note that the plot axes are not equal and are scaled.

ent bridle configurations can be designed to remain the same but could result in a very different structural response given the change in the direction of the force vectors at the attachment positions. Hence, a well-designed bridle could allow for a lighter wing by reducing the bending moments that the wing is subjected to, thus reducing the overall mass of the wing.

From the results of the case studies in this chapter, optimising the bridle configuration provides a significant opportunity for mass reduction without requiring a relatively computationally expensive D-box laminate layup optimisation exercise (as carried out in [Chapter 5](#)). However, care should be taken while changing the bridle configuration for the same reason of changing load introduction. Furthermore, these analyses are all carried out for a static load case. These varying loads could be potentially detrimental when considering the coupled aero-structural response as explored further in [Chapter 7](#).

Based on these results, it is recommended to incorporate the bridle configuration already in the conceptual design phases rather than sizing the wing structure first and then incorporating the bridle later in the design process. The fast computational speed of the model should allow for a rigorous multidisciplinary optimisation (MDO) of both the bridle domain \mathcal{B} and the structural domain \mathcal{S} in the future.



Chapter 7

Aero-structural design space

In theory there is no difference between theory and practice. In practice there is.

—Benjamin Brewster

Adapted from:
Aero-structural Design of Composite Wings for Airborne Wind Energy Applications
TORQUE (2020), J. Phys.: Conf. Ser. 1618 032016

ABSTRACT

This chapter explores the bridle and structural design space for composite kites, utilising a two-way coupled aero-structural-bridle framework. Design studies in the bridle configurations, their effects on wing deformations, and the resulting change in the aerodynamic force distribution are performed. The developed coupling strategy builds upon the 2+1D structural model used for static analysis from [Chapter 5](#) that captures the complex composite coupling effects witnessed in slender composite structures. The structural model is coupled to the aerodynamic and bridle models to obtain the kite's equilibrium aero-structural-bridle state. A design exploration using the complete computational model is performed to assess the effects of varied load introduction to the wing structure and effects on the aerodynamics. This is done through two case studies. The first, in which different bridle configurations and their effect on the wing loading is explored and a second case in which a tailored D-box is examined for the same loading case. Additionally, a partitioned multi-fidelity approach is explored by dividing the structural domain S into the stiffness domain S_{1D} and the geometric domain S_{2D} . This allows for the design exploration to be carried out in the lower fidelity stiffness domain, and once a feasible design is found, to detail it further in the geometric domain.

7.1. INTRODUCTION

The structural analysis carried out previously in [Chapter 5](#) considers a precomputed aerodynamic load case, neglecting changes in the aerodynamic loads arising from structural deformations of the wing. As explored in detail in [Section 6.1](#), the bridle geometry is another factor influencing the structural response. The geometry of the bridle attachment points, along with the pulley positions and the aerodynamic loads, determine the load transfer path into the structure. Moreover, the analysis of the bridle configurations in [Chapter 6](#), was a one-way coupled and did not consider further phenomena arising from the structural deformations.

The work presented in this chapter explores the aerodynamic, bridle and structural design space for bridled composite wings. The methodology here accounts for the changes in the aerodynamic domain \mathcal{A} and bridle domain \mathcal{B} caused by the deformations of the wing structure. The structural deformations are used to update and recompute the aerodynamic and bridle forces to determine the coupled aeroelastic response of the wing.

The static kinematic equilibrium for the system is determined using a coupling strategy as discussed in [Section 7.2](#). This methodology is used to capture and quantify the aero-structural-bridle coupling effects on the structural response of the wing using the previously described aerodynamic, bridle and structural solvers from [Chapter 3](#) and [Chapter 4](#). An overview of the modules of the computational framework in focus for the studies presented here is visualised in [Figure 7.1](#). In this work as well, the 2D aerodynamics is precomputed and still considered an input to the model.

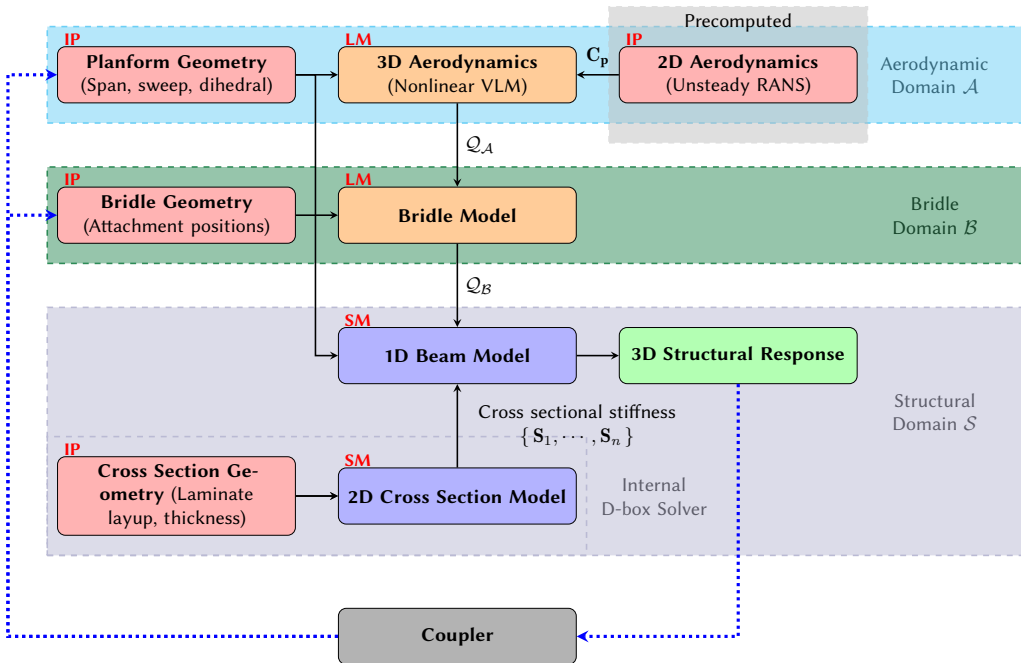


Figure 7.1 | Overview of the coupling between the computational framework modules (introduced in [Figure 3.4](#)). Inputs (IP) are shown in red. Models that determine loads (LM) are indicated in orange, and structural models (SM) are indicated in purple. Blue dotted lines illustrate the coupling information flow.

Similar to prior design studies, these studies utilise the reference tri-tether swept wing platform

introduced in Section 2.1. This work explores the influence of bridle configurations on the design in greater fidelity, highlighting the need to consider the aero-structural-bridle coupling effects already during the early design stages.

The aero-structural response of the wing is predominantly a function of the wing-box stiffness and load-deflection couplings that arise from the composite layup. However, it is further affected by the bridle system and the corresponding load introductions at the bridle attachment points, and thus the bridle configuration also needs to be considered. Section 7.3 recaps the design drivers for the different bridle configurations and highlights the motivation of switching bridle configurations during the prototyping phase to tune the wing's controllability and steering response. From results in Chapter 6, it is known that a change in the attachment point of the tether influences the structural response of the wing by changing the load introduction path into the structure.

The objective of this work is dual-fold. The first is to perform a bridle configuration design space exploration to highlight the perils of aeroelastic effects that might not be apparent from uncoupled static simulations. The second objective is to find a suitable aero-structural-bridle design for the airborne wind energy (AWE) wing considered. Section 7.4 describes the aero-structural-bridle response for two typical bridle configurations. For this study, all other parameters such as wing planform, aerofoils, D-box design, and aerodynamic operational conditions are maintained the same.

The described analysis methodology highlighted in Figure 7.1 is then used to tailor the stiffness of the wing-box for a given bridle configuration as described in Section 7.5. This is achieved by dividing the analysis into its constitutive domains - the structural \mathcal{S} , aerodynamic \mathcal{A} and the bridle \mathcal{B} domains. For the structural design of the D-box, the problem can be formulated as a multilevel optimisation problem in the structure domain that sequentially solves the design problem in the stiffness domain \mathcal{S}_{1D} and the geometry domain \mathcal{S}_{2D} . This problem formulation results in a relatively fast and computationally efficient method to design a suitable D-box while considering these aero-structural-bridle coupling effects.

7.2. AERO-STRUCTURAL-BRIDLE COUPLING STRATEGY

The simulation methodology utilised here builds upon the previously described 2+1D structural model (Section 4.1), the nonlinear vortex-lattice method (VLM) for the aerodynamic loads (Section 3.2), and complemented by the bridle model (Section 3.3). This aero-structural computational framework can model effects of detailed structural parameters (internal wing-box geometry, composite ply layup sequence, material anisotropy effects, etc.), as well as more general wing details (planform, span, sweep, dihedral, bridle geometry, etc.).

Given the nature of this work, and the focus on fast computational models that can be exploited for iterative design early in the design process, a complete high fidelity fluid structure interaction (FSI) simulation is out of the scope. A conventional monolithic approach where the governing equations for fluid and structure problems are solved simultaneously is not considered at this stage. Instead, a partitioned approach is employed in this work. Thus, the aerodynamic, bridle and structural models are solved in isolation, with a mesh mapping strategy to transfer the loads and deformations between the models at each coupling iteration step.

An explicit two-way coupling is implemented here, solving for the kinematic steady-state solution. Dynamics and other effects in the time domain are neglected at this juncture. Starting

with the undeformed wing shape, the aerodynamic model solves for the spanwise aerodynamic loading to determine the initial load profile. The resulting bridle forces for the aerodynamic forces are then solved, and the resulting structural response for both these loads is determined. All the individual domain's non-linear problems are solved sequentially, and coupling is implemented with a Newton-Raphson method, linearising each step as a Newton iteration. A solution is found when the changes in the structural response of each Newton step converge to its steady-state value.

The coupling strategy is thus used to determine the static kinematic equilibrium response of the structure for a given load case. Similar to previous studies in [Chapter 5](#), the aerofoil design is not considered here, and in this work, aerofoils are selected a priori, and the profile aerodynamics are precomputed. Therefore, the load case for a particular wing is given as a function of the angle of attack α , wind speed v_a , and other such operational parameters. A schematic of the coupled computational model is depicted in [Figure 7.1](#). The dotted blue arrows depict the information flow from the structural domain to the aerodynamic and bridle domains in the schematic.

Given the low fidelity of the models, mesh mapping is not as involved as higher fidelity models with more complex unstructured meshes. Here, the translations and rotations determined from the structural module are used to update the location of the collocation points of the aerodynamic model. The change in the local angle of attack is then determined as a function of the structural rotational deformations. An interpolation scheme is utilised to account for different mesh densities of the structural and aerodynamic models. The deformed structure and corresponding new aerodynamic loads lead to a different state for the bridle subsystem, which is then subsequently updated and solved to determine the corresponding structural loading for the next step. In order to aid in the convergence of the entire aero-structural-bridle system, dynamic load stepping and relaxation are also implemented.

7.3. DESIGN DRIVERS

The computation model described above and visualised in [Figure 7.1](#) is utilised to analyse the representative tri-tethered swept wing configuration introduced in [Section 2.1](#). Considering the non-actuated wing and fully ground-controlled concept, the bridle geometry is vital, providing a suitable distribution of forces between the three tethers. This allows for roll and pitch control by differential force components as illustrated previously in [Figure 2.5](#).

Similar to the static analysis in [Chapter 5](#), the reference wing considered here has pre-chosen aerofoils, so for a given operational condition, the aero-structural-bridle response of the wing can be parametrised by the following factors:

1. Wing planform ($\mathcal{A}_{3D}, \mathcal{S}_{1D}$)
2. Bridle line configuration (\mathcal{B})
3. Wing box cross-section geometry and material properties (\mathcal{S}_{2D})

The wing planform design is driven by aerodynamics requirements and consists of typical parameters like span, sweep, aspect ratio, etc.. $\langle \mathcal{A}_{3D} \rangle = \{ \gamma, \Gamma_d, \mathbb{R}, \lambda, \dots \}$. The planform directly impacts the structural domain, as bending moments are a function of the wing span (and related geometry). Furthermore, for swept wing designs, geometric coupling is also witnessed.

Given the bridle attachment points are determined from the wing geometry, the response of the wing in all \mathcal{A} , \mathcal{B} and \mathcal{S} are influenced by the wing planform geometry.

As previously described, the bridle configuration also plays a vital role in the control of tether-steered kites (both airborne and ground-based steering). For tether-steered fixed-wing AWE, steering is achieved by a change in the magnitude of the main \mathbf{F}_m and control forces \mathbf{F}_c as depicted in Figure 2.5. The spanwise and chordwise attachment positions of the bridle, along with the aerodynamic centre of pressure, lead to a force equilibrium for the system and, thus, an equilibrium state of the kite. Hence, in order to steer the kite, a differential force on the tethers is utilised to shift the kite into a new equilibrium attitude and position.

Similar to the pitching case, differential actuation on the two steering lines leads to a rolling moment and, subsequently, a new position of the kite. Hence, with the tri-tether system, it is possible to control both the kite's pitch and roll with no direct yaw control. Yaw is achieved by adverse yaw generated from the roll actuation. Hence, the amount of steering force required and the kite's stability motivates the search for different bridle configurations that could provide adequate controllability, along with multiple load introduction points into the wing, serving as a means of structural load alleviation.

Therefore any change in the location, magnitude, and direction of the main \mathbf{F}_m or control forces \mathbf{F}_c would change the flight dynamics and steering characteristics of the kite. During the initial flight testing and prototyping phases of wing design, this proves to be a rapid way to test new control strategies and tune the wing's flight dynamics and stability characteristics. Given the use of a passive airborne wing concept with no control surfaces, this commonly results in the requirement of a given prototype wing to be suitable for multiple bridle configurations.

7

Given the significance of the bridle configuration on the wing deformations determined previously (6, [80]), in the case study presented in Section 7.4, the structural and aerodynamic configuration of the wing system is kept constant, and only the bridle configuration is modified. Here, two bridle configurations are further analysed to assess their impact on the aero-structural response of the airborne system. Subsequently, in Section 7.5 a design exercise is carried out in the structural stiffness \mathcal{S} domain, and a suitable wing-box is tailored for a particular bridle configuration.

7.4. CASE STUDY: BRIDLE CONFIGURATIONS

Two characteristic bridle configurations are chosen for this case study. Depicted in Figure 7.2, bridle configuration “2PS” consists of two pulleys with three attachment points at the wing (Figure 7.2a). In contrast, bridle “1PS” utilises a single pulley with two attachment points (Figure 7.2b).

These particular bridles were chosen based on their steerability and flight mechanical stability criteria that they impart to the system. From Figure 7.2, it can be seen that the different positions of the final pulley in the bridle and thus the control force vector \mathbf{F}_c for the two bridles change. Although the spanwise location of the pulleys is not significantly different, there is a difference in their position under the wing, which plays a role in the lateral stability of the kite. The flight mechanical aspects of such ground-controlled wings are an interesting field of study, especially regarding system design, but are not covered in depth in this body of work. Two representative bridles are hence chosen based on desired flight characteristics for the kite that are not discussed here. It is of note that both the selected bridle configurations show

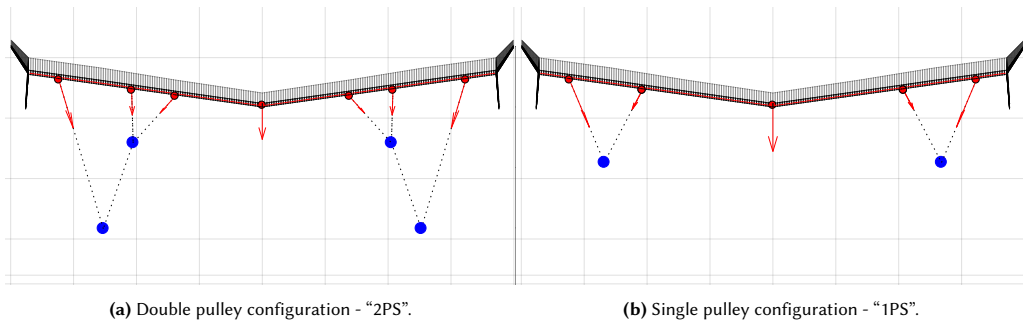


Figure 7.2 | Bridle variations considered in this study. Red circles illustrate bridle attachment points, and force components in the bridle are depicted in red. Blue circles illustrate pulleys. Adapted from [80].

satisfactory structural response and meet deflection criteria during static analysis, such as the previous analysis in Section 6.1.

Using the coupled framework, aero-structural deformation results are presented in Figures 7.3 and 7.4, comparing two bridle configurations for a given wing planform and internal D-box geometry. Three increasing load cases are considered by increasing the angle of attack ($\alpha = 5, 10$ and 20°) while maintaining the same operational wind conditions. In both figures, the bridle force vectors are depicted in red and the spanwise aerodynamic load profile is depicted in blue. The motivation of this case study is to examine the aeroelastic effects that arise from the variation in the load transfer from the wing-box. Thus as mentioned previously, all other parameters between the cases are maintained the same, and only effects stemming from the two bridle configurations are compared in this case study.

As seen from Figures 7.3 and 7.4, the aerodynamic load distribution of the initial state depicted in the top row is the same for both bridle cases. The aerodynamic analysis depends only on the wing planform geometry and aerofoil characteristics and does not consider any structural deformation effects at the initial stage. Hence, this leads to an initial aerodynamic load profile that is agnostic to the bridle configurations. Thus, taking the example of load case 2 ($\alpha = 5$) presented in Figures 7.3b and 7.4b, all operational conditions are maintained the same with the only change being the bridle configuration, resulting in a different aerodynamic response of the wing.

The coupled aero-structural simulations, as expected, result in a different spanwise aerodynamic load distribution compared to the initial non-deformed wing. The deformations and rotations of the wing-box lead to changes in the position of the lifting surface of the wing, along with changes in the local spanwise angle of attack. As seen in Figure 7.3a, in the case considered, this effect results in larger aerodynamic forces at the wing tips. This change in aerodynamic loading compared to the static analysis has repercussions, impacting the controllability of the kite. The variation in spanwise loading changes the load balance between the main and control lines. Depending on the magnitude and particular bridle configuration, this change influences the control and stability of the kite and after a limit, leads to an unstable and non-controllable system.

In addition to the changes in the flight dynamics of the wing, there are more fundamental structural implications which can be seen from the increasing load cases in Figures 7.3b and 7.3c. The larger aerodynamic loads towards the wing tips cause an increase in the bridle forces,

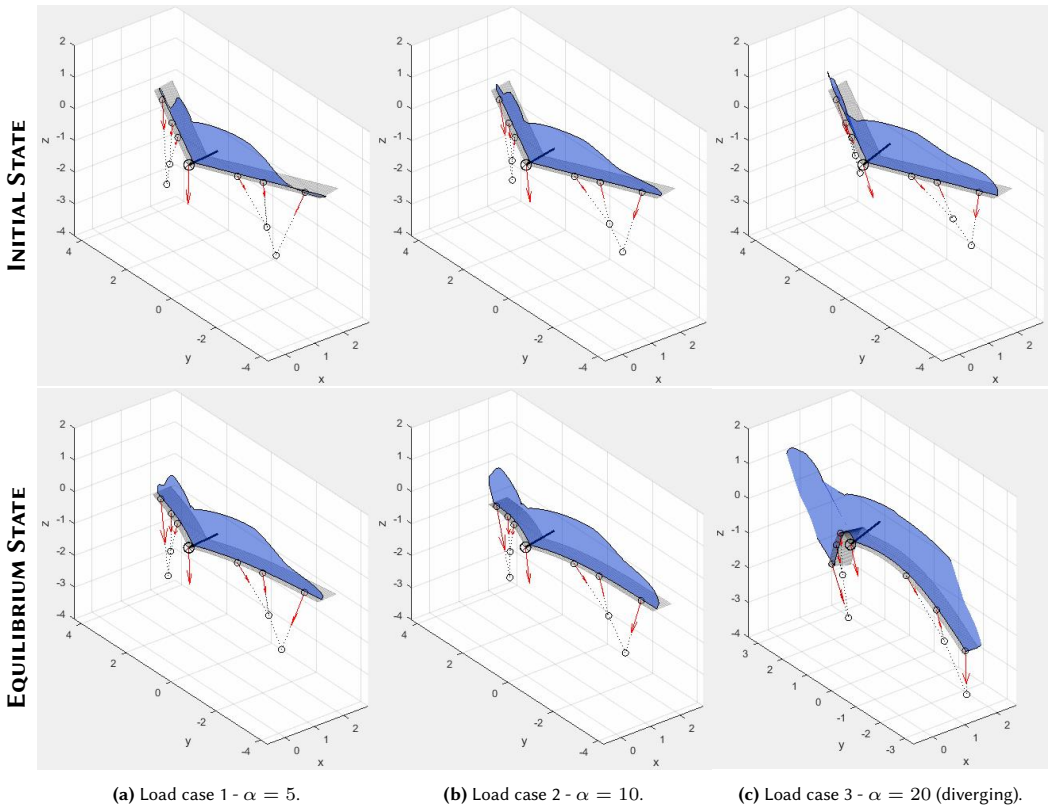


Figure 7.3 | Aero-structural response for bridle configuration “2PS”, with increasing load cases (angle of attack α) at operational wind conditions. Aerodynamic loads are visualised in blue, with bridle segment loads visualised in red.

leading to an increased local spanwise twist, resulting again in an increase in the aerodynamic load. As seen in Figure 7.3c this leads to aeroelastic divergence, with the local angle of attack at the tip sections continuing to increase until ultimately resulting in structural failure.

In the carbon composite wing-box considered here, this effect is further aggravated by the bending-twist and tension-twist coupling modes of slender composite structures. The increasing aerodynamic loads lead to increased bending loads on the structure, which due to the bend-twist coupling, leads to a rotational twist deformation of the wing-box. Moreover, when looking at Figure 7.2a, it can be seen that the innermost attachment points of the bridle will lead to a significant axial force component along the beam axis which contributes further to the tension-twist coupling.

Using the same load cases of $\alpha = 5, 10$ and 20° , results for the “1PS” bridle configuration are illustrated in Figure 7.4. The change in the bridle configuration leads to an alternative load transfer path, given the same initial aerodynamic load profile. Similar effects of increasing aerodynamic loads towards the wing tips are witnessed. However, the magnitude of this effect is significantly lower. With fewer attachment points, the force component on the outermost bridle segment is higher than for the “2PS” configuration (Figure 7.4), leading to larger bending forces and thus more significant deflections in the z axis.

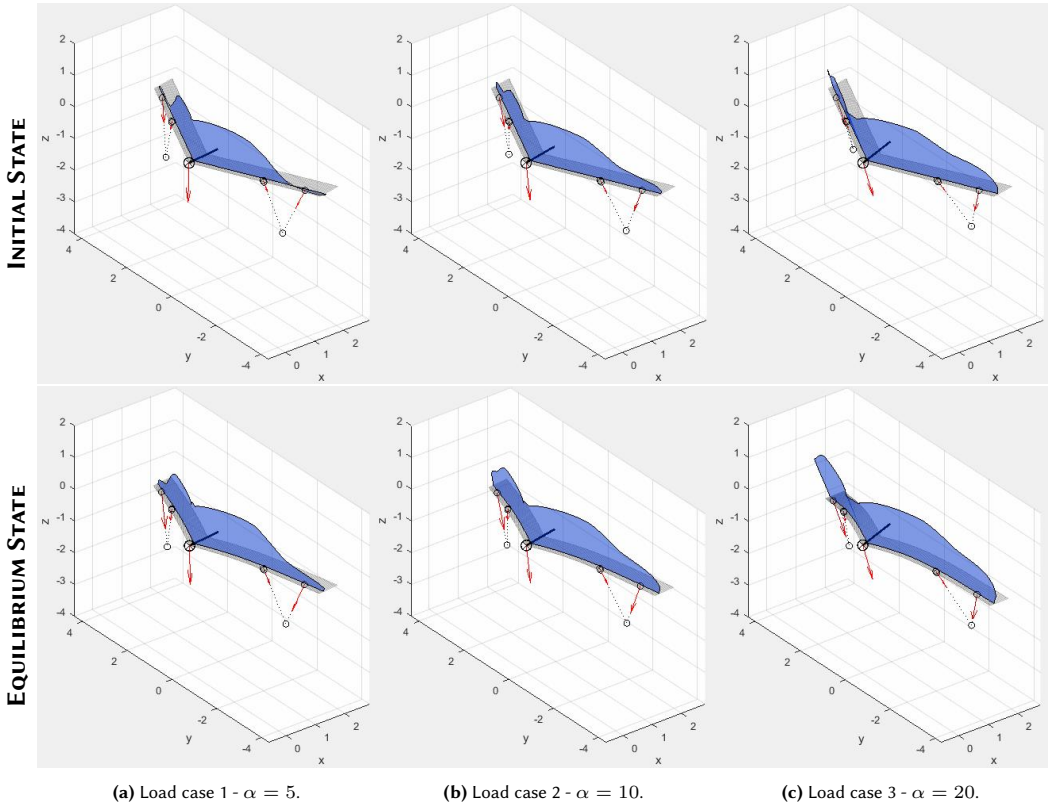


Figure 7.4 | Aero-structural response for bridle configuration “1PS”, with increasing load cases (angle of attack α) at operational wind conditions, same as in Figure 7.3.

The deformations for the two bridles cases for a single load case are further compared in Figure 7.5. The change in the initial state to the final equilibrium state for the axial displacement along the wing span axis and the change in the local spanwise angle of attack are both plotted against the non-dimension wing span. For the “1PS” bridle, due to the configuration of the inner bridle attachment points, a lower axial force component leads to lower axial displacements as seen in Figure 7.5a in comparison to the “2PS” configuration. The axial deformations are in the order of magnitude of $\lesssim 0.1\%$ of the wing span for both cases.

However, these axial loads, in turn, lead to a change in the local angle of attack $\Delta\alpha$ along the span as seen in Figure 7.5b. This change is due to the tension-twist coupling effects of the composite D-box layout. For the given load case, this leads to an almost halving of the deformed local angle of attack for the “2PS” in comparison to the “1PS” bridle, especially towards the tip regions. Due to this effect, for the same load case 3 of $\alpha = 20^\circ$, the “1PS” bridle configuration has a suitable aerodynamic response (Figure 7.3c) in comparison to the diverging nature of bridle “2PS” (Figure 7.4c). Thus, for the same D-box geometry and the same initial aerodynamic load conditions (α and apparent wind velocity), the resulting structural response for different bridle configurations can be drastically different from the uncoupled initial static analysis. Such effects further motivate considering the coupled aero-structural-bridle response for the system already in initial design studies.

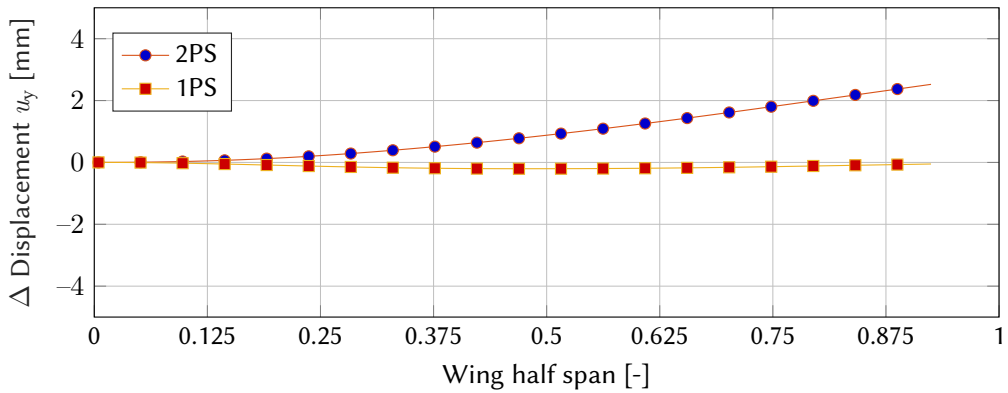
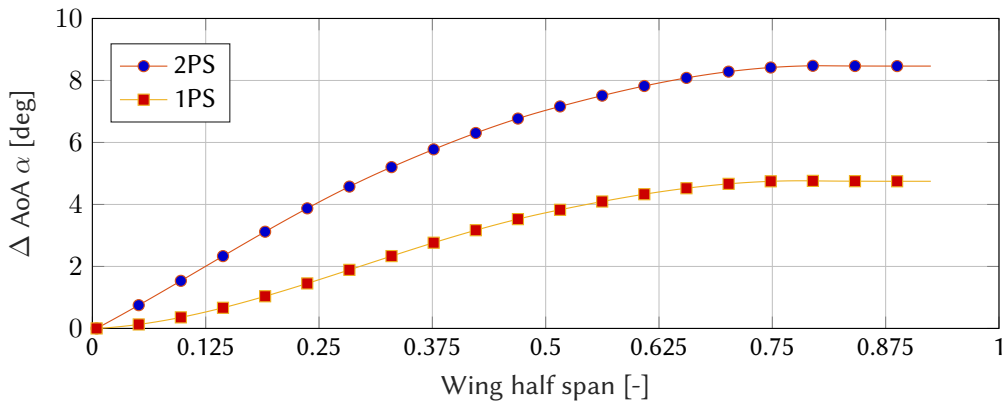
(a) Axial displacements Δu_y .(b) Local Angle of Attack (α_a) $\Delta \alpha$.

Figure 7.5 | Change (*equilibrium – initial*) of state for “2PS” and “1PS” bridle configurations, plotted against the non-dimensional wing half span for load case 2. Note that the plot axes are not equal and are scaled.

7.5. CASE STUDY: D-BOX STIFFNESS

Thus far, the analysis described focuses on comparing different bridle configurations for a fixed wing and D-box. Once a bridle configuration is determined that has suitable flight dynamics and steerability, improvements can be achieved by designing a specific D-box for the particular wing and bridle configuration. An approach would be to modify the D-box in order to achieve a suitable aero-structural-bridle response for a given bridle configuration.

This work explicitly tailored a new D-box for the “2PS” bridle configuration using the coupled solver and a multilevel optimisation strategy. Considering the critical diverging load case of $\alpha = 20^\circ$ previously depicted in Figure 7.3c, the newly modified D-box (dubbed “B”) can withstand this load case as seen in Figure 7.6.

7.5.1. Stiffness domain S_{1D}

The D-box design is derived using the described load cases to determine the required stiffness for the new D-box “B”, such that it has a favourable aero-structural-bridle response. It is important to note that this optimisation is conducted for only a subset of load cases. Thus,

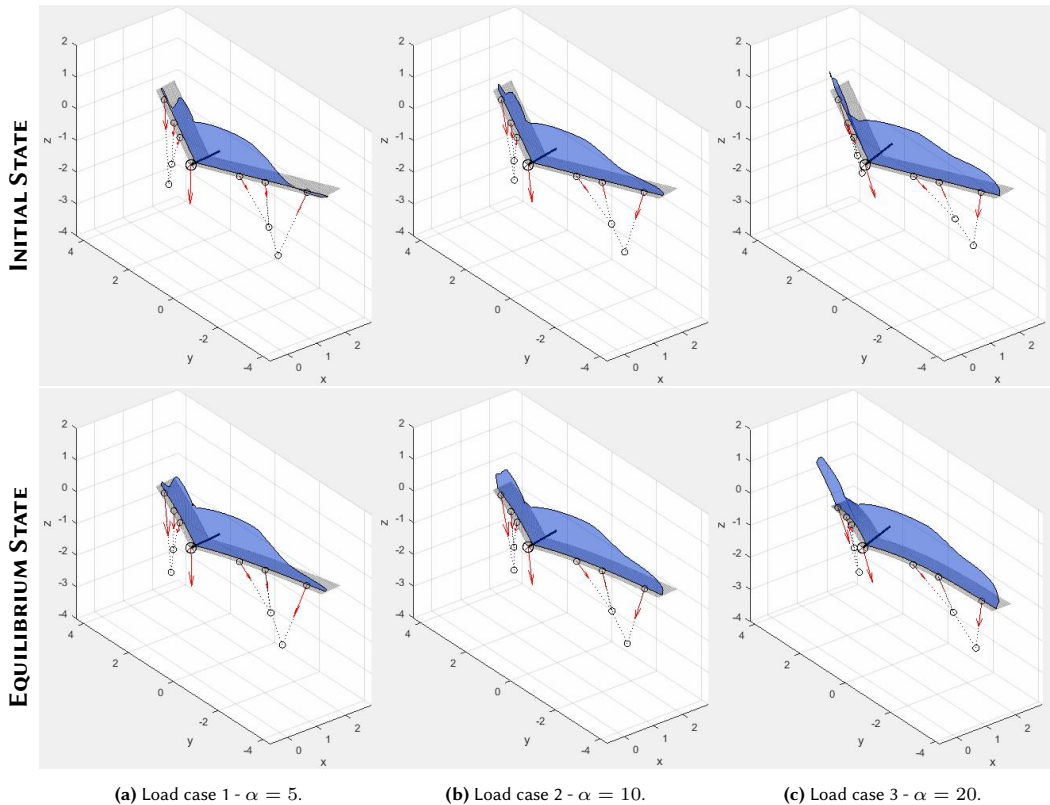


Figure 7.6 | Aero-structural response for bridle configuration “2PS” and tailored D-box “B”, with increasing load cases (angle of attack α) at operational wind conditions, same as in Figure 7.3.

these results are tuned specifically to the given load cases, wing, and bridle configuration. A more robust design would have to consider more load cases, including gusts and other operational load cases. This case study serves as a preliminary exploration of the methodology’s capabilities and highlights the potential of utilising such methods early in the design phase.

A multilevel optimisation strategy that abstracts away details of the geometry and layout of the D-box in the first stage is employed here. A schematic overview of the coupling and information exchange is depicted in Figure 7.7. This strategy allows for the optimisation to be carried out directly in the stiffness domain based on some target stiffness criteria. Thus, the relatively computationally expensive detailed laminate level optimisation is carried out only once a suitable solution is found in the stiffness domain and not at every optimisation iteration step during the coupled analysis.

Considering the wing structural design, the different design domains can be segregated broadly into the structural domain \mathcal{S} , aerodynamics \mathcal{A} and the bridle space \mathcal{B} . In this optimisation exercise, the structural domain is focused on, with the bridle and aerodynamic domains forming passive components. Thus, all parameters in the \mathcal{A} and \mathcal{B} domains are pre-selected such that the response of both domains $\varphi(\mathcal{A}, \mathcal{B})$ can be expressed as a function of some preselected inputs to the model $\xi(\mathcal{A}, \mathcal{B})$, and the response of the structural domain $\varphi(\mathcal{S})$ as:

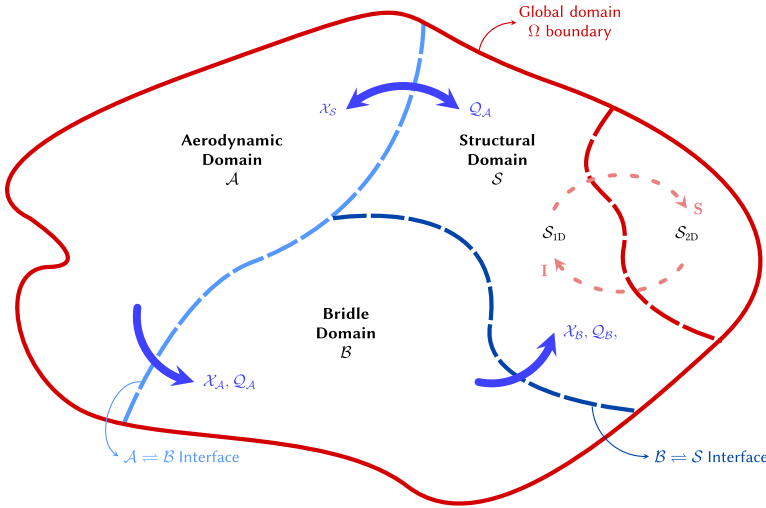


Figure 7.7 | Partitioned approach and information exchange $\mathcal{A} \rightleftharpoons \mathcal{B} \rightleftharpoons \mathcal{S}_{1D}$ domains.

$$\begin{aligned}\varphi(\mathcal{A}) &= f(\xi(\mathcal{A}_c), \varphi(\mathcal{S})) \\ \varphi(\mathcal{B}) &= f(\xi(\mathcal{B}_c), \varphi(\mathcal{S}))\end{aligned}\quad (7.1)$$

where $\mathcal{A}_c = \{\gamma, \Gamma_d, \mathbb{R}, \lambda, \dots\}$ and $\mathcal{B}_c = \{\{\mathbf{x}_p\}, \{\mathbf{x}_i\}, \{L_b\}, \dots\}$ are a set of pre-selected constant input parameters for the individual aerodynamic and bridle domain solvers.

Stiffness domain \mathcal{S}_{1D} optimisation

The structural domain \mathcal{S} can be further expressed in terms of the stiffness domain $\mathcal{S}_{\text{stiffness}}$ and the geometry domain $\mathcal{S}_{\text{geom}}$. This is possible, as recalling from Equation 4.36, the 1D beam model parametrises the stiffness of the D-box using the stiffness tensor \mathbf{S} , which is determined for each characteristic cross-section in the wing. Considering the same operational aerodynamic environment (α, v_a, \dots) , and a fixed bridle configuration described by \mathcal{B}_c , the aero-structural-bridle response of the wing can be expressed purely in the structural stiffness domain $\mathcal{S}_{\text{stiffness}}$, as a function of the cross-sectional stiffness's $f(\mathbf{S}_1, \mathbf{S}_2 \dots, \mathbf{S}_{n_{sec}})$, where the subscript n_{sec} denotes the number of unique cross-sections in the wing-box.

While the individual cross-sectional stiffnesses are a function of geometry and layup, the current stiffness domain is described completely by the individual stiffness tensors in conjunction with the 1D structural model. Hence the structure stiffness domain is referred to as \mathcal{S}_{1D} . Thus, in the stiffness domain \mathcal{S}_{1D} , the structural response $\varphi(\mathcal{S}_{1D})$ can be expressed by $\xi(\mathcal{S}_{1D}) \in \mathbb{R}^{21(n_{sec})}$. Furthermore, although the stiffness tensor is given by $\mathbf{S} \in \mathbb{R}^{6 \times 6}$, being symmetric it can be expressed as $\mathbf{S} \in \mathbb{R}^{21}$.

By expressing the response of structural domain \mathcal{S} in terms of \mathcal{S}_{1D} and \mathcal{S}_{2D} , this methodology thus allows for the wing-box optimisation to be split into multiple subproblems that can then be solved sequentially. An overview of this hierarchical scheme is given in Figure 7.8.

For this case study, the reference wing described in Section 2.1 is utilised. Thus, this exercise

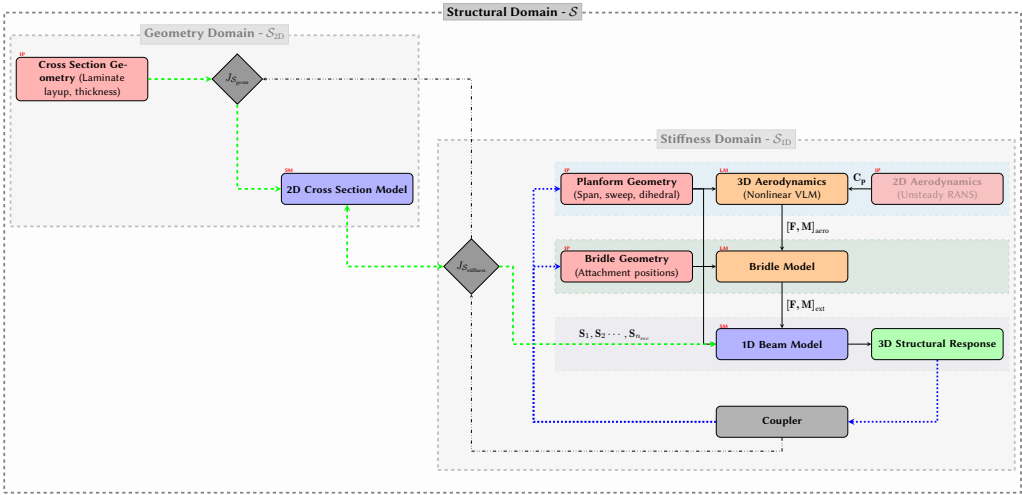


Figure 7.8 | Multilevel optimisation strategy for D-box design using the aero-structural-bridle framework.

limits $n_{sec} = 2$ for the two “root” and “tip” sections in the wing. A stiffness optimisation is carried out by minimising the required stiffness for given deflection criteria, using the stiffness domain optimisation portion of the framework depicted in Figure 7.8. The problem in S_{1D} can be formulated to minimise the stiffness tensor elements while constrained by deflection targets and stiffness limits. The optimisation cost function $J_{S_{stiffness}}$ is thus given as:

$$\begin{aligned}
 & \underset{\mathbf{X}}{\text{minimize}} && \sum_{i=0}^{n_{sec}} \|\mathbf{S}(\mathbf{X})_i\| \\
 & \text{subject to} && \mathbf{f}(\mathbf{u}) \leq \mathbf{u}_{\text{target}} \\
 & && \mathbf{S}_{\text{max}} - \mathbf{S}(\mathbf{X}) \leq \mathbf{S}_{\text{tol}}
 \end{aligned} \tag{7.2}$$

For this case study, the deflection constraints were defined using the displacement field \mathbf{u} with a trivial tip deflection target defined as:

$$\mathbf{f}(\mathbf{u}) \leq \mathbf{u}_{\text{target}} \Rightarrow \|\mathbf{u}_{\text{tip}}\| \leq l_t \tag{7.3}$$

where \mathbf{u}_{tip} is the tip translation defined in Euclidean norm space, and the deflection tip length limit $l_t = f(b)$ is defined as some function of wing span b .

The resulting optimised D-box “B” is suitable for the “2PS” bridle configuration, as seen from the analysis results in Figure 7.3. Where the original D-box had a diverging response for load case 3 of $\alpha = 20^\circ$, the optimised D-box has a converged result that satisfies the deformation constraint criteria applied in the problem. Looking at the individual stiffness tensor \mathbf{S} components in comparison to the original case in Figure 7.9, the optimised stiffness tensor has drastically reduced the coupling stiffness while compensating with increased bending stiffness seen in the diagonal terms.

7.5.2. Geometry domain S_{2D}

The cost function $J_{S_{stiffness}}$ described here is a trivial formulation used for this case study. A more detailed formulation could improve it, for example, by adding weightage for the coupling terms

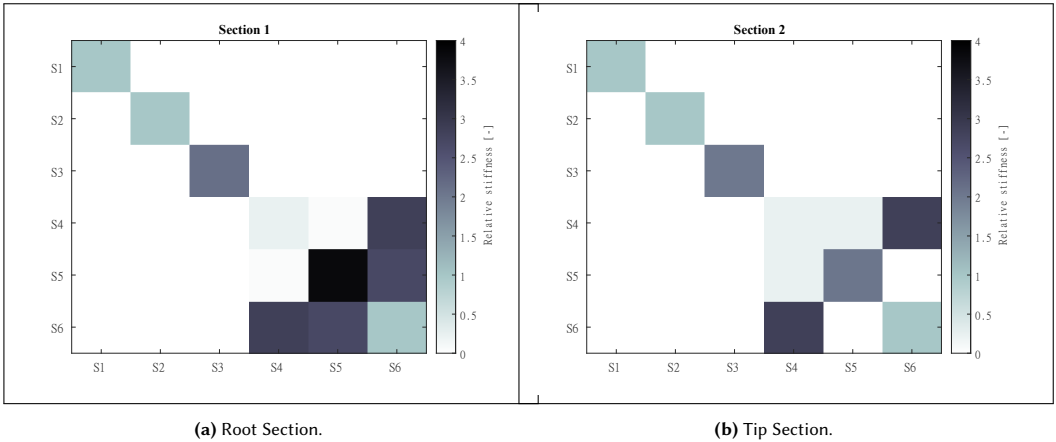


Figure 7.9 | Comparison of the stiffness tensor \mathbf{S} components for the optimised D-box “B” (results in Figure 7.6) normalised by the initial D-box (results in Figure 7.3).

in the stiffness tensor \mathbf{S} in order to achieve more fine-grained control of the aero-structural-bridle response. The problem formulation can also be extended to include constraints from the aerodynamic domain \mathcal{A} to ensure that the pre-deflection static spanwise aerodynamic lift is still achieved through favourable deflections. However, given that the current optimisation is purely in the structural stiffness domain $\mathcal{S}_{\text{stiffness}}$, if a constraint is placed to achieve the same aerodynamic spanwise profile as the undeflected static case, this will tend towards extremely stiff wings, limited by prescribed maximum feasible stiffness \mathbf{S}_{max} . Rather than performing this aeroelastic tailoring purely in the stiffness domain, it would instead be advisable to include planform parameters ($\{\gamma, \Gamma_d, \mathcal{R}, \lambda, \dots\}$) in the optimisation to ensure that the deformed aerodynamic profile satisfies requirements. This optimisation problem could then be formulated as a more rigorous multidisciplinary optimisation (MDO) problem, which could be solved more efficiently by introducing coupling variables.

Once a suitable solution is found in the $\mathcal{S}_{\text{stiffness}}$ domain for this coupled problem, the underlying geometry and laminate layup required to satisfy the cross-sectional stiffness can be determined. This partitioning allows for problems in $\mathcal{S}_{\text{stiffness}}$ to be shifted into the structural geometry domain $\mathcal{S}_{\text{geom}}$ in order to carry out a mass minimisation. This reformulation allows for the laminate layup and geometry constraints to be solved using an optimisation strategy similar to previously described ones in Section 5.1, and hence not repeated here. This overall process is represented in Algorithm 1.

Stiffness \mathcal{S}_{1D} to geometry \mathcal{S}_{2D} domain mapping

To probe design space, the steps in Algorithm 1 would require to be processed for multiple design candidates and load cases. In this case study, these criteria are represented as a set of deflection constraint criteria $\{\mathbf{u}_{\text{target}_1}, \dots, \mathbf{u}_{\text{target}_n}\}$. Thus, by performing the coupled multi-hierarchy optimisation for these multiple deflection constraint criteria, an optimum design front of feasible results in the structural domain \mathcal{S} for D-box designs can be generated for a particular study. Typically, this would be limited to a given planform design. Thus, a set of candidate solutions in \mathcal{S}_{1D} can be generated for a particular case study as depicted in Figure 7.10, where each solution is derived from a deflection constraint.

```

Result: Optimised D-box  $\in \varphi(\mathcal{A}, \mathcal{B}, \mathcal{S})$ 
Init:  $\{\mathcal{A}, \mathcal{B}, \mathcal{S}\}_c$ 
while  $\min_{\mathbf{X}_{2D}} J_{\mathcal{S}_{2D}}$  do //  $\mathcal{S}_{2D}$  optimisation
  while  $\min_{\mathbf{X}_{1D}} J_{\mathcal{S}_{1D}}$  do //  $\mathcal{S}_{1D}$  optimisation
     $\mathbf{S}_n \leftarrow \mathbf{S}(\mathbf{X}_{1D})_n \in \{n \leq n_{sec}\}$ 
    while  $\text{newton}_{\varepsilon_s} \varphi(\mathcal{S}_{1D}, \mathcal{A}, \mathcal{B}) \vee z \leq z_{max}$  do // Coupling solver
       $\mathcal{S}_{1D} \iff \mathcal{A}, \mathcal{B}$  // mesh mapping
       $\mathcal{C}_z \leftarrow f(\mathcal{S}_{1D}, \mathcal{A}, \mathcal{B})_z$  // load stepping, relaxation
      while  $\text{newton}_{\varepsilon_A} \varphi(\mathcal{A}) \vee i \leq i_{max}$  do // Aero solver
        Solve:  $\mathcal{A}(\mathcal{C}_z, \dots)_i$ 
         $\varphi(\mathcal{A}) \leftarrow \mathcal{A}(\dots)_i$ 
      end
      while  $\text{newton}_{\varepsilon_B} \varphi(\mathcal{B}) \vee j \leq j_{max}$  do // Bridle solver
        Solve:  $\mathcal{B}(\mathcal{C}_z, \dots)_j$ 
         $\varphi(\mathcal{B}) \leftarrow \mathcal{B}(\dots)_j$ 
      end
      while  $\text{newton}_{\varepsilon_{\mathcal{S}_{1D}}} \varphi(\mathcal{S}_{1D}) \vee k \leq k_{max}$  do // 1D Structural solver
        Solve:  $\mathcal{S}_{1D}(\mathcal{C}_z, \dots)_k$ 
         $\varphi(\mathcal{S}_{1D}) \leftarrow \varphi(\mathcal{S}_{1D})_k$ 
      end
       $\varphi(\mathcal{S}_{1D}, \mathcal{A}, \mathcal{B}) \leftarrow \varphi(\mathcal{S}_{1D}(\dots), \mathcal{A}(\dots), \mathcal{B}(\dots))_z$ 
    end
  end
  while  $\text{newton}_{\varepsilon_{\mathcal{S}_{2D}}} \varphi(\mathcal{S}_{2D}) \vee l \leq l_{max}$  do // 2D Structural solver
    Solve:  $\mathcal{S}_{2D}(\mathcal{S}_{1D}(\min \mathbf{X}_{1D}), \dots)_k$ 
     $\varphi(\mathcal{S}_{2D}) \leftarrow \varphi(\mathcal{S}_{2D})_k$ 
  end
end

```

Algorithm 1 | Multi-fidelity D-box optimisation overview.

The first method explored is by using the solution space $\varphi(\mathcal{S}_{1D})$ to subsequently solve for the resulting D-box geometry. Thus, by repeating the complete D-box optimisation process ($J_{\mathcal{S}_{2D}}$) from Algorithm 1 for multiple deflection criteria set in Equation 7.3, an optimum front of D-box geometry solutions can be generated. Thereby, the geometry and laminate layup $\varphi(\mathcal{S}_{2D})$ that results in the required stiffness $\varphi(\mathcal{S}_{1D})$ are determined by solving multiple topology optimisation problems with the stiffness criteria i.e. $\varphi(\mathcal{S}_{2D}) \Rightarrow J_{\mathcal{S}_{2D}} = f(\varphi(\mathcal{S}_{1D}))$. This, however, is a relatively involved process, as recalling from Equation 4.35, the solution requires the discretised geometry \mathcal{S}_{geom} as well as corresponding stiffness for the laminates $\mathcal{S}_{lam}(\mathcal{S}_{geom})$ i.e.:

$$\mathcal{S}_{2D} = f(\mathcal{S}_{geom}, \{ \varphi(\mathbf{\Gamma}(\mathcal{S}_{geom}), \xi^{A,B,D})_1, \dots, \varphi(\mathbf{\Gamma}(\mathcal{S}_{geom}), \xi^{A,B,D})_n \}) \quad (7.4)$$

An alternative method would be to determine a mapping between $\varphi(\mathcal{S}_{1D})$ and parameters of interest in \mathcal{S}_{2D} , avoiding the relatively expensive topology optimisation step for each scenario.

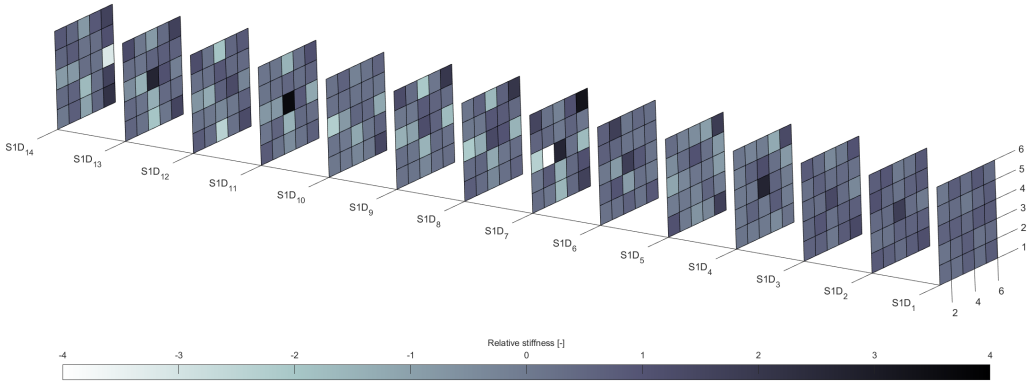


Figure 7.10 | Sample candidate solution space of the structural stiffness domain S_{1D} .

During the conceptual stages of design, a common goal is to determine the structure's mass while meeting the design constraints. Thus, for a given planform and bridle design, this mapping \mathcal{M} could be expressed as:

$$\mathcal{M}(S_{2D}, \dots) : \|\mathbf{u}_{\text{target}}\| \mapsto \mathbf{M}$$

where

$$\mathbf{M} = f(\varphi(S_{2D}), \dots, \xi(\mathcal{A}_c), \xi(\mathcal{B}_c)) \quad (7.5)$$

7

In this work, the mapping function \mathcal{M} is implemented as a lookup table that is constantly updated with new solutions from the topology optimisations ($J_{S_{2D}}$). This strategy thus leads to an optimum design front of D-box topology for given deflection constraints in the stiffness domain. For the reference wing utilised in this design study, this leads to an unsurprising result of increasing structural mass to achieve lower deflections as seen in Figure 7.11.

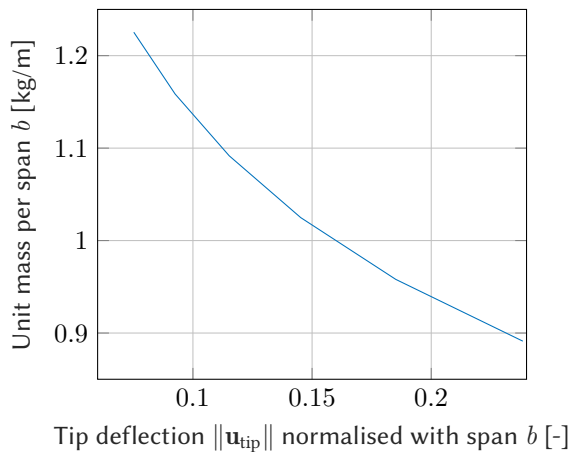


Figure 7.11 | Optimum design front of D-box mass determined in the structural geometry domain $\varphi(S_{2D})$ for given deflection limit criteria l_t subjected to the solution space of the structural stiffness domain S_{1D} .

This methodology thus allows for an engineering choice to be made with respect to the mass penalty for increased stiffness and lower deformations. An indicative solution space is plotted in Figure 7.11 for the D-box mass per unit span — determined from the $\varphi(\mathcal{S}_{2D})$ response, against the tip deflection criteria l_t applied in the \mathcal{S}_{1D} space. Here, l_t is expressed in non-dimensionalised percentage of wingspan b . It should be noted that such a feasible solution space is particularly specific to the given inputs and constraints placed on the optimisation problem and hence requires consideration before extrapolating engineering conclusions for other wing-box designs. However, these models' relatively low computational costs allow for such studies to be performed already in the initial design phases.

7.6. SUMMARY AND CONCLUSIONS

The motivation for the work presented here on the coupled aero-structural-bridle analysis for composite kites is driven by the large wing loading and low mass requirements on AWE systems. Utilising slender composite structures for their high stiffness-to-mass ratio leads to load-deflection coupling effects that need to be accounted for right from the initial design stage. An explicit two-way coupling between the aerodynamic \mathcal{A} , bridle \mathcal{B} , and the structural \mathcal{S} domain to solve for the steady-state kinematic solution between these three domains is performed in this chapter. The developed methodology allows for evaluating the coupled aero-structural-bridle response of the wing and bridle system.

For non-actuated passive systems that cannot tune the wing's characteristics via onboard actuators, the bridle configuration provides a method to adjust the wing's flight dynamics, stability and steerability. This is extremely useful during the initial prototyping and flight testing phase, providing a method to modify the wing characteristics without a complete redesign and rebuild cycle. Previous results in Chapter 6 show that changing bridle configurations leads to a varied static structural response of the wing with the same D-box design. Here, the analysis is extended to evaluate the aero-structural-bridle response of the reference wing with two bridle configurations, with all other parameters remaining frozen.

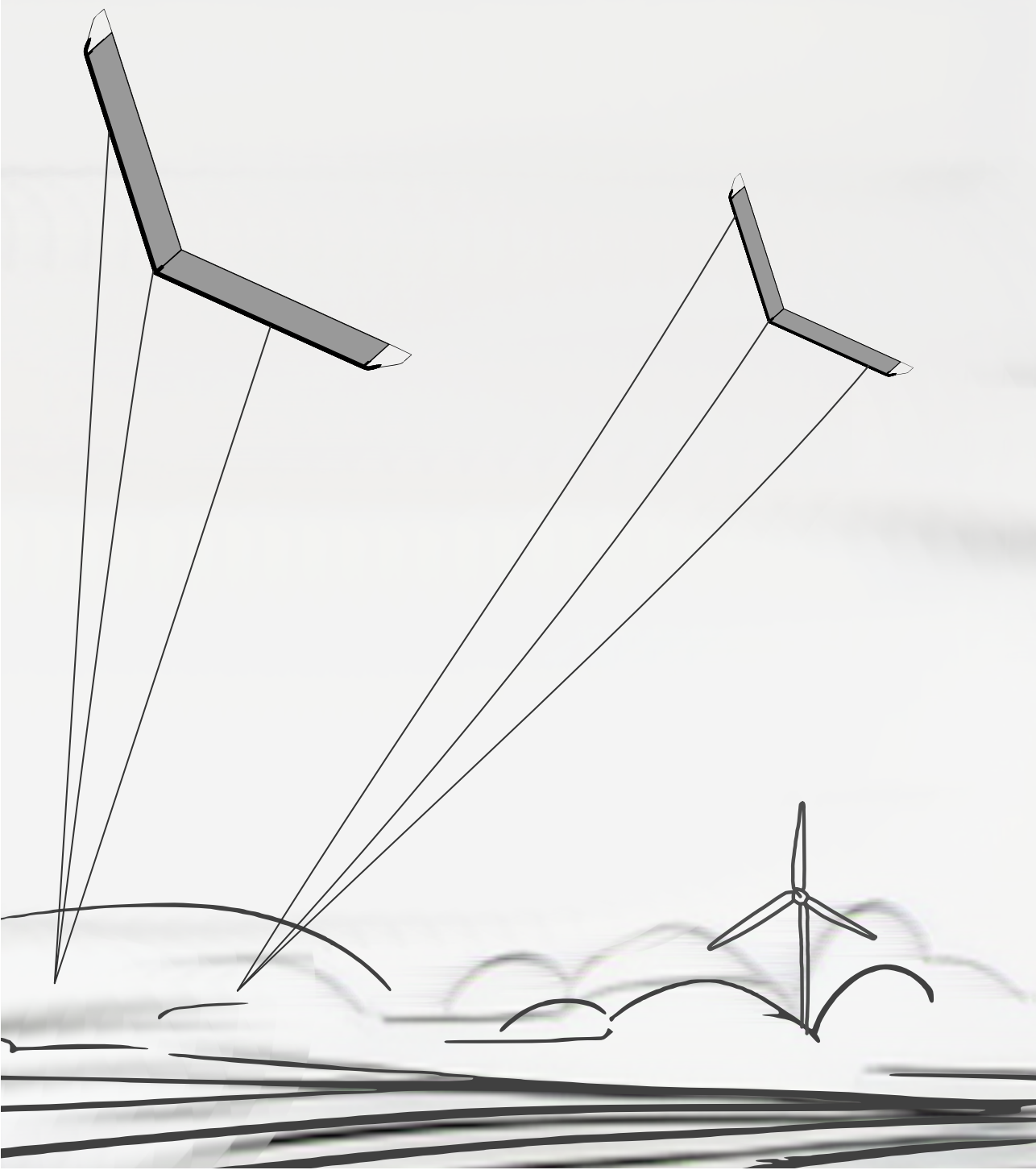
Design studies of different aerodynamic load cases for bridle configurations reveal that when considering the load-deflection phenomenon, the wing structure's deformation can significantly affect the aerodynamic spanwise load profile. This change in aerodynamics, in turn, results in a different bridle response than in the static case. In the first design study in Section 7.4, the structural parameters of the D-box are maintained the same to isolate the effects of the bridle on the aeroelastic response of the kite. The influence of the bridle geometry and attachment point locations is significant. Although the initial aerodynamic loading profile is the same for both considered cases, the different bridle configuration changes the load introduction into the D-box structure, altering the structural response after the first iteration. For the bridle configurations considered here, for increasing load cases, bridle configuration "2PS" with its increased axial force component undergoes aeroelastic divergence. In comparison, bridle configuration "1PS" alters the axial force component in the structure, and thus the tension-twist coupling in the D-box, resulting in a stable equilibrium state for the same load condition.

This leads to the conclusion that such wings with composite structures undergoing load-deflection couplings require investigation prior to changing load introduction, such as by modifying bridle configurations. Furthermore, a static analysis might not be sufficient when considering the aeroelastic effects of such lightweight, slender structures subjected to large deformations.

Section 7.5 presents a multi-hierarchy optimisation scheme that sequentially solves for an optimum D-box design in the structural stiffness \mathcal{S}_{1D} and the geometry \mathcal{S}_{2D} domain. Using this methodology, a new D-box “B” design is tailored that has a favourable response for the same diverging load case with bridle configuration “2PS”.

By abstracting away the detailed geometry and laminate layup parameters, the scheme solves for feasible designs during the initial design phase that satisfies the aero-structural-bridle response criteria. The results from the stiffness domain $\varphi(\mathcal{S}_{1D})$ can be subsequently utilised to generate feasible designs in the geometry domain \mathcal{S}_{2D} , allowing for design trade studies and providing a path towards comprehensive system design. A method to map the solutions from the stiffness domain to structural mass is explored, which shows initially promising results. Ideally, a more robust data-driven approach would be better suited than the simple lookup table currently implemented and is left as an avenue of future exploration.

In conclusion, the computational model developed and utilised here is sufficiently computationally fast to be used in the initial design stage. This allows for a holistic design process considering the coupled aerodynamic, bridle and structural response. Furthermore, the modular framework provides a platform to perform design studies of suitable fidelity for varied bridle configurations and wing and wing-box geometries to explore further the design space of AWE systems.



Chapter 8

Conclusions and discussion

Man muss immer umkehren

—Carl Gustav Jacob Jacobi

8.1. CONCLUSIONS

A multi-disciplinary simulation framework for the design of tethered composite aircraft has been presented in this thesis. The research focuses on exploring the design space for fixed-wing airborne wind energy (AWE) wings, specifically during the initial (conceptual and preliminary) design phases. Subsequently, case studies have been conducted at varying fidelities to examine the interaction of the aerodynamic \mathcal{A} , bridle \mathcal{B} , and structural \mathcal{S} domains. The research questions stated in Section 2.5 are answered based on these results. For clarity, the research questions are recapitulated below.

A. Can a consistent design approach and models be developed for the initial design phases of the airborne subsystem for fixed-wing AWE?

The methods in the proposed framework have been explicitly chosen for their low computational cost and complexity. The aerodynamic and structural domains are divided into 2D and 1D models that are combined to determine the 3D response of the wing. These methods provide a good balance between model accuracy, number of parameters and computational effort.

A1. What is the minimum fidelity/accuracy required in the initial (conceptual and preliminary) design phase of the airborne subsystem? i.e. what level of detail is needed regarding the aerodynamics, bridle system and composite wing structure design?

From the case studies presented in Chapter 5 and Chapter 6, it can be concluded that the developed 2+1D method for the structural domain \mathcal{S} has sufficient fidelity to incorporate the composite load-deflection coupling effects. The bridle and pulley system solver also captures the force introduction from the bridle configuration \mathcal{B} . Case studies from Chapter 7 reveal that a static aero-structural-bridle coupling based on vortex-lattice method (VLM) 1D aerodynamics and 2+1D structural model is sufficient to capture load-deflection effects. As seen from case studies in Chapter 7, the resulting deformations can be considerable enough to change the aerodynamic response and thereby the bridle and structural response.

A2. How significant are the aeroelastic interaction effects for the airborne subsystem modelling during the initial design phase?

Comparing the static case studies from Chapter 5 and Chapter 6 to the coupled aero-structural-bridle methods utilised in Chapter 7, it is seen that the interaction between the three (aerodynamic \mathcal{A} , bridle \mathcal{B} and structural \mathcal{S}) domains causes a significant change in the response of the wing. Furthermore, particular combinations of bridle configurations and wing designs (Section 7.4) could lead to adverse load introduction, and ultimately to aeroelastic divergence and structural failure. For the bridle configuration considered, increasing angle of attack α_a causes a larger axial loading component at the attachment point, which due to the axial-twist coupling leads to a structural deformation that further increases the angle of attack. The static models from Chapters 5 and 6 would not capture such failures. Therefore, the coupled aero-structural-bridle response of the wing should already be examined at the initial design stages to prevent expensive redesigns later in the engineering process.

The results from Chapter 7 reveal that a one-way coupled analysis can mask diverging aero-structural-bridle load deflection couplings that lead to structural failures. Albeit, this conclusion is not broadly applicable, as the presented analyses are particular to the reference swept, large aspect-ratio wing considered in this work. For typical rectangular wings with higher structural stiffness, the deformations may not be significant enough to cause a substantial

change in the coupled aerodynamic response of the wing.

Moreover, the coupled aero-structural-bridle framework entails additional computational cost. Therefore, the decision of when to employ it during the initial design process is not straightforward. Drawing from the experience gained through this work using the spiral systems engineering approach for rapid prototype iteration (Section 2.2.2), it is recommended to include coupling effects already at the initial design space exploration when designing high aspect ratio semi-rigid bridled wings for AWE.

A3. What are the most suited computational models for the initial design phase and how can they be implemented in the spiral system engineering development approach?

The static models cannot accurately capture failures arising from the coupling between the aerodynamics, bridle and structural domains. To avoid failure/redesigns at a later design stage, a multi-fidelity modelling approach is suggested to include the coupling while abstracting the composite ply level details in the design exploration. At the conceptual stages, exploring the design space in the stiffness domain \mathcal{S}_{1D} is sufficient. Once a feasible concept design is identified, the cross-section geometry and laminate stiffness (\mathcal{S}_{2D}) that satisfies these stiffness requirements can be determined at the next design stage. Subsequently, detailed manufacturing constraints can be incorporated when solving for a ply-layup plan that satisfies the laminate stiffness domain (\mathcal{S}_{lam}). In this manner, the proposed framework facilitates the addition of more parameters to the analysis as the design phases mature. Thus, formulating the structural domain as the stiffness \mathcal{S}_{1D} , geometric \mathcal{S}_{2D} , and the laminate \mathcal{S}_{lam} domains allows for an expanding spiral, iterative design approach.

A4. Is it necessary to include higher-level fidelity (or more detailed/advanced) tools in the subsequent phase(s) of the design process?

The proposed framework is explicitly developed for iterative design exploration. This necessitates multiple simplifications in the aerodynamic, bridle and structural domain models. As outlined, the current level of fidelity already captures cases of structural failures that would have been neglected in the one-way coupled models. However, while the results show the framework has sufficient fidelity for the initial design phases, there are multiple aspects where higher fidelity tools would be required for a detailed design. These topics are further elaborated in Section 8.2.

B. How strong is the interaction between the wing and bridle design, and how should it be incorporated into the design process?

Case studies in Chapter 6 expose the risks of developing a bridle system isolated from the structural design of the wing. The load introduced into the wing structure can significantly vary when the bridle attachment points are altered. Multiple load-deflection coupling from these bridle attachment points leads to a varied structural response for composite high aspect ratio swept wings. Furthermore, while several bridle arrangements can be designed for the same overall force magnitude, the structural reactions can differ substantially. This component becomes more critical when examining the combined aero-structural-bridle response because large deformations can modify the aerodynamic reaction, changing the bridle response significantly.

B1. How do the loads introduced at the bridle attachment points affect the design and the aero-structural response of the airborne subsystem?

For the non-trivial multi-pulley bridles configurations employed in this work, it has been shown in **Chapter 6** that the load introduced at the bridle attachment points can significantly change depending on the aerodynamic response of the wing. Response in this domain is, as expected, a function of the orientation and attitude of the wing. Thus, introduction of the aerodynamically coupled bridle load motivates probing the design space of the wing early in the design phases to ensure a critical load case is not dismissed prematurely.

Furthermore, the importance of considering the combined aero-structural-bridle response is evident from case studies presented in **Chapter 7**. The load-deflection couplings significantly vary the aerodynamic response compared to the static studies. Additionally, depending on the design and load cases, the coupling can result in a different spanwise lift distribution and thus different flight dynamics. In some extreme cases, the change in the lift can also lead to divergence and eventual structural failure.

B2. How do variations of the bridle subsystem affect the wing's aerodynamic and structural design?

The aerodynamic response of the wing drives the direction and magnitude of the forces in the bridle system. Hence, the bridle response is strictly a function of the aerodynamic load and the bridle geometry. In the implemented model, the bridle configuration is determined by the pulley positions and the attachment points. Given the use of a static aerodynamic model in this work, the impact of the bridle system on the wing aerodynamics is thus not considered directly. Instead, the bridle configuration effects on the structural domain \mathcal{S} are explored. The bridle configuration is responsible for the tether load introduction into the wing structure. Thus, the locations of the attachment points and the orientation of the tether with respect to the wing at these points significantly impact the structural deformations and therefore the aerodynamic response.

B3. Can the bridle subsystem configurations be optimised for system benefits, such as improved performance, controllability and/or reduction of loads?

The significance of bridle subsystem of airborne wind energy system(s) (AWES) spreads across multiple disciplines. For the ground-steered concept, the bridle configuration is coupled with the flight dynamics of the wing. Thus, a suitable design is required to ensure the controllability of the system. As shown in **Chapter 6**, the controllability (within the scope of this work) is determined essentially by the interface between the tether and the bridle subsystem, typically at the last pulley branch in the system.

The studies presented in **Chapter 6** demonstrate that the bridle configuration provides an extra means to tune the structural response of the wing in the stiffness domain \mathcal{S} . Using a favourable load introduction distribution along the wing's span, the bridles can also be exploited for load alleviation by beneficially utilising the load-deflection couplings. However, this requires rigorous knowledge of the entire load envelope. Lastly, for the aerodynamic domain \mathcal{A} , the extra drag from the bridle system must be balanced with the beneficial structural response with increasing load introduction points. In this work, the drag is superficially penalized by constraining the segment length constraints during the bridle configuration design.

8.2. FUTURE RECOMMENDATIONS

A general conclusion can be made regarding the structural domain beyond the proposed research questions' purview. Engineering intuition would suggest reinforcing the torsional stiffness of the D-box to avoid a large change in the twist of the wing. However, experience shows this is more complex when considering the changing load introduction from the bridles. Increasing axial or bending load from particular bridle configurations and load cases could lead to other bend-twist and extension-twist couplings that significantly change the aerodynamic response.

The developed models, methodologies, and knowledge gained from this work are currently being utilised at EnerKite to develop next-generation composite AWE wings. As with any continuously evolving technology, insights spark ideas for improvement. In this regard, some of these idea are presented here

8.2.1. Aerodynamic domain

Based on the iterative nature of the design stage this framework has been developed for, recommendations are made to increase the level of fidelity of the aerodynamic model in two aspects:

Panel methods

By utilising a panel method, a higher fidelity pressure field can be calculated (as compared to an equivalent force from a VLM method). Incorporating the pressure distribution would allow for further optimisation of the structural topology, especially in the chord-wise distribution that has only been rudimentarily considered in the D-box topology. Additionally, in the case of the membrane-covered semi-rigid EnerKite wing concept, the influence of the aerodynamic pressure distribution on the membrane would be an interesting area to explore.

8

Unsteady effects

To improve the aeroelasticity capabilities of the framework, incorporating unsteady effects would add significant insight into the aero-structural-bridle response of the system. This could be achieved, for example, by introducing a non-planar wake model. This would allow for the incorporation of structural dynamics into the aerodynamic response. However, both these aspects have their own set of challenges. Both panel and unsteady vortex-lattice method (uVLM) typically do not account for nonlinear viscous effects in the operating regime of AWE. They might significantly overestimate the lift by neglecting flow separation from high angle of attack α_a and near-stall regions.

Finally, the importance of experimental data must be considered. Flight data from operations in real-world conditions provide a qualitative understanding of the flow phenomenon. Hence, correlating this data with high fidelity computational fluid dynamics (CFD) and control experiments from wind tunnel studies are crucial for developing new aerodynamic simulation tools.

8.2.2. Bridle domain

The current model proposed for the bridle focuses on determining the load introduction vectors into the structure for varying aerodynamic loading. However, the model is purely a static

representation of the equilibrium and does not consider any dynamic effects. Moreover, the model does not consider the elasticity of the bridle lines and subsequent dynamics of the load introduction from the bridle. Thus, adding these effects to the bridle model aligns with the overall theme of enhancing the framework to investigate dynamic effects.

As for the bridle configuration design and optimisation, the currently studied configurations were manually determined and not optimised for the structural response. Therefore, an interesting exercise would be to determine bridle configurations that, while maintaining a constant tether force vector (critical for the steerability of ground controller AWE), vary the effective attachment positions, thereby optimising the structural response of the wing.

8.2.3. Structural domain

At the most general level, the 2+1D model could be replaced by a full 3D shell model at the cost of increased computational time and model complexity. This would allow for the inclusion of some non-trivial phenomena currently neglected in the proposed model. The most critical of which is buckling. Besides this, general recommendations are also provided in two main categories.

Structural dynamics

Extending the structural model to account for structural dynamics arising from inertial effects is recommended. Furthermore, as the load-deflection couplings in composites have a frequency aspect, the inclusion of these effects would be paramount for improving the capabilities of the coupled aero-structural-bridle framework.

Failure modes

One aspect to consider is the accelerated fatigue resulting from the nature of the pumping cycle and the associated alternating high and low loading cycles experienced by the wing. Thus, fatigue and associated damage are critical criteria when designing AWE wings for long, maintenance-free continuous operation as with modern wind turbine blades.

8.2.4. Flight dynamics of bridled wings

The current work treats the wing's flight dynamics as a requirement, that is enforced via constraints in the bridle configuration and wing planform. However, it is prudent to include the flight dynamics model in the framework to analyse and trade the controllability of the wing with other design aspects. This would allow propagation of the dynamics of the wing response into the flight dynamics model to further investigate undesired coupling states.

8.2.5. Design load cases

One of the stark differences between AWE and the conventional wind and aerospace sectors is the absence of design load cases (DLC). Determining realistic load cases for AWE is a significant undertaking that requires long-term operational data. Additionally, identifying and determining critical load cases arising from off-design situations such as partial system failures would be crucial for AWE to achieve certification-driven practices similar to the other sectors.

A recommended first step towards this is the collection of flight telemetric data already during the testing phase of AWE. Onboard structural health monitoring (SHM) and other condition monitoring systems would provide vital insights at this testing phase. Realistic DLC are often

the missing link in the optimisation of AWE. Regardless of the methodology and fidelity of the models employed, results from unrealistic load cases would lead to optimistic but unfounded results.

8.3. LESSONS LEARNT

Based on this work's specific experiences and insights, a few opinionated ideas on the general field of AWE design are presented encouraging readers to contemplate upon them. The first would be to embrace the Pareto principle via multi-fidelity modelling. The Pareto distribution (or more commonly the Pareto principle/80-20 rule) is a probability distribution that states that 20% of causes control 80% of the outcomes. Similarly, in engineering design, this principle is commonly paraphrased into determining the 20% of the effort that achieves 80% of the goals.

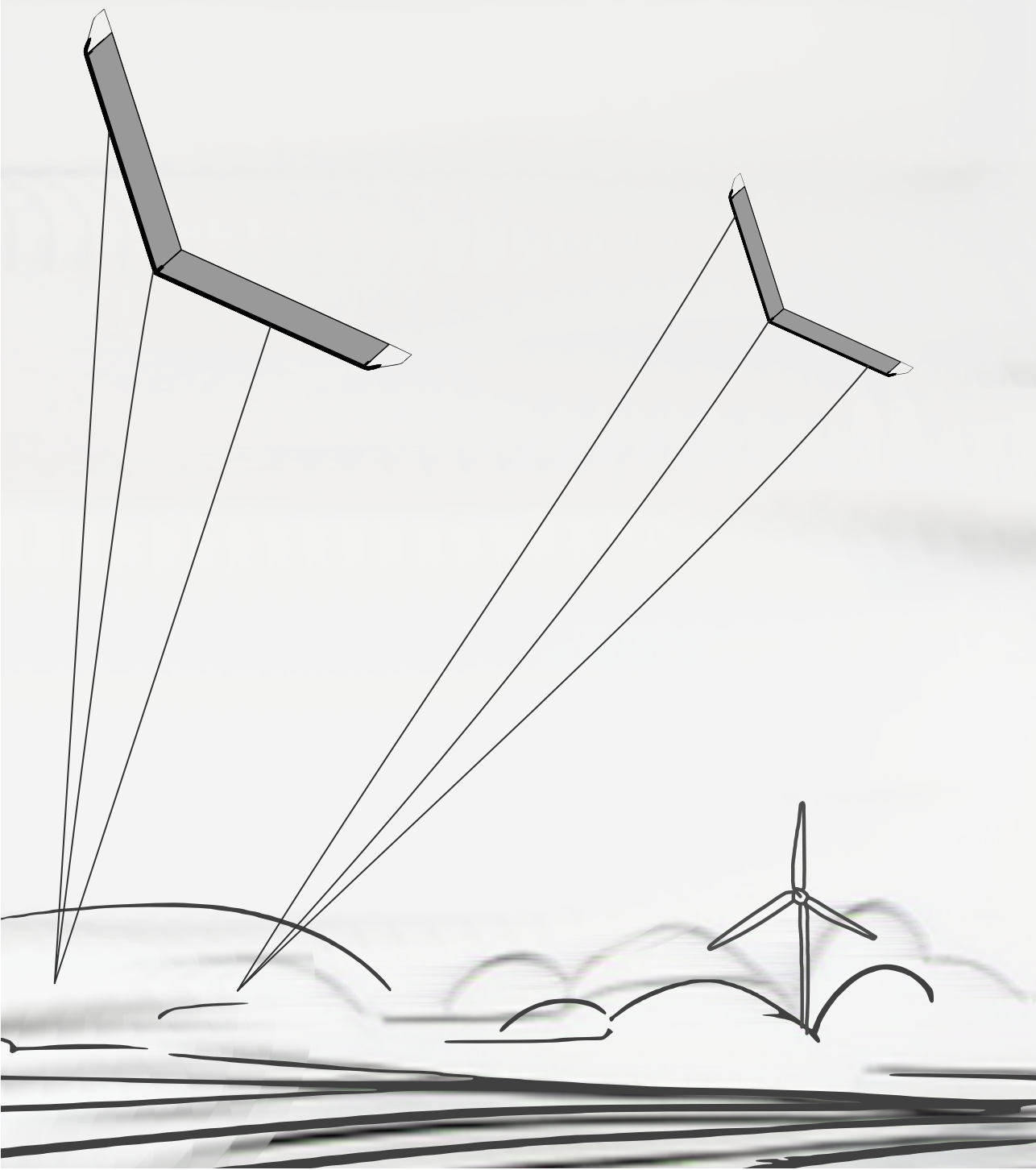
Within the scope of this thesis, multiple analogous low-hanging fruits can be identified.

- Segregate and recompose domains into subdomains (multi-disciplinary)
- Solve only what is required for the particular design phase (multi-fidelity)
- Optimise the bridles domain for structural mass minimisation

The second is to start early. The sooner a phenomenon can be quantified in the design process, the faster the design candidates can be screened. Based on this work, an example would be the coupled aero-structural-bridle effects that were initially neglected during the first phases of prototype design. Once the significance of aeroelasticity was identified, the design toolchain was adapted to include these effects for subsequent prototype wing designs. However, care should be taken to remain within the model's assumptions.

Finally, would be to not re-invent the wheel — while AWE has unique aspects, it also has many attributes that have already been solved in the wind and aerospace sectors. Embracing the knowledge and methods from these well-established fields is critical to increasing the pace of commercialisation of AWE. The $\approx 30+$ years it took to mature commercial wind turbines is time the AWE sector does not have.

The insights from leveraging data from increasing flight hours, knowledge of load cases, and operational limitations specific to AWES can be combined to formulate structured probing of the design space using the presented framework, enabling the systematic design exploration and facilitating the realisation of utility-scale AWES.



Appendix A

The EnerKite system

Innovation at its core is solving a problem without conventional bias.

—William Otto

This appendix provides a brief history of the evolution of the EnerKite system into the current tri-tethered swept wing design. The system design is driven by the predetermined trifecta of the goals that pertain to organisations (business case), use case and functional principles that have been made specifically for this system. The system thus combines aspects from soft-wing kites, such as tether-based steering, and rigid composite structures of more aircraft-like systems, leading to a distinctive high aspect ratio fixed-wing airborne wind energy system(s) (AWES).

A.1. EARLY GENERATION KITES

The EnerKite team have been designing, building, and autonomously flying kites and tethered crafts for over a decade. Initially, the team focused on soft-wing kites. Unlike other soft-wing kites that use a pod under the kite for steering, the ram-air kites were steered by multiple lines leading from the kite to the base station. In collaboration with Festo for the *CyberKite* project, some of the earliest generations of kites that would later inspire and evolve into the current system were flown. Multiple kites were built in the project, ranging from 6 to 24 m². Some of these quad-tether kite wings are pictured in Figure A.1. The quad-lines were further connected to a system of bridles used to deform the wing tips to steer the kite [180, 181].



Figure A.1 | Early generation quad-tether ram-air kites developed in collaboration with FESTO (circa 2010) [181].

The *CyberKite* project proved the feasibility of autonomous tethered flight. Post this; the focus shifted to the power generation aspect of such systems. This led to the development of the *EK30* technology demonstrator. The first generation system used soft-wing ram-air kites steered entirely from the ground with three tethers. The system consisted of a mobile 30 kW base station and completed its maiden flight back in March 2012 [74]. Ever since extensive test campaigns have been carried out with multiple airborne platforms across numerous test sites using this mobile research platform.

A critical feat for the system was a successful endurance test that spanned over 72 hours [70, 74, 182]. In this extended test campaign, over 40 hours were flown entirely autonomously with no manual pilot input. While this comprehensive operational test was carried out at the test field at Pritzwalk, Germany, the mobile *EK30* unit also conducted operations at other sites in Germany, Belgium and The Netherlands. Typical tether lengths of 300 to 600 m were maintained during these campaigns. Pictured in Figure A.2 is the *EK30* mobile technology demonstrator with an early generation ram-air kite. Details of the mobile ground station are given in Table A.2, and that of the earlier generation soft-wing kites are listed in Table A.1.

These early-generation kites focused on validating the ground-controlled concept for power generation using the pumping cycle with kites in a repeatable and reliable manner. However, after over 100 hours of operation, there were concerns about the concept, particularly concerning the lifetime of the kites and the power output of such a tri-tether soft-wing kite system.

Table A.1 | Details of the early generation ram-air kites [74].

Generation 1 Ram-air		
Area	15.0 m ²	Flat
Area	12.8 m ²	Projected
Wing span	12.8 m	Flat
Mass	4.2 kg	Kite only
Generation 2 Ram-air		
Area	21.0 m ²	Flat
Area	17.9 m ²	Projected
Wing span	17.9 m	Flat
Mass	5.8 kg	Kite only

With the base concept proven successful, the following design iteration concentrated on improving the system's power output.



Figure A.2 | The EK30 mobile technology demonstrator in operation with the early generation soft-wing kites (circa 2013, image courtesy of EnerKite).

Table A.2 | Details of the Gen01 *EK30* mobile technology demonstrator [74].

Ground station (mechanical)		
Tether force (main line)	8.2 kN	RMS
Tether force (main line) peak	16 kN	Peak
Collective line speed	26 m/s	Max
Relative control line speed	3.2 m/s	Max
Collective line acceleration	26 m/s ²	Max
Control line acceleration	20 m/s ²	Max
Winch rotational speed	20 rpm	Max
Winch rotational acceleration	20 m/s ²	Max
Drum tether capacity	1200 m	
Ground station (electrical)		
Regenerative power	57 kW	Peak
Regenerative power	30 kW	Nominal
Storage capacity	50 kWh	
Grid connection	1×230,3×400 V	
Ground station (footprint w/o vehicle)		
Height	0.75 m	
Diameter	2.10 m	
Weight (including storage)	4100 kg	

A.1.1. Improving power generation

From the test campaigns and data gathered from the early-generation soft-wing kites, it was clear that a significant amount of power generated during the pumping cycle was reinvested into the system during the retraction phase. The early generation ram-air kites produced ≈ 5 kW of measured peak power output per cycle [71]. Further refinements of the earlier generation ram-air system theoretically could yield about 4 kW/m² of power by maintaining appropriate tether forces and control torques at nominal wind speeds of 7.5 m/s [70]. Given the tri-tether system and the associated drag, the soft-wing system did not have a sufficiently high lift-to-drag ratio, thus yielding low peak power output. Furthermore, the system required a significant portion of the harvested power to retract the kite.

Soft-wing kites have typical lift-to-drag ratios of ≈ 6 . The founding team had significant expertise with lighter-than-air soft kites before creating the *EK30* concept [180, 181, 183, 184]. Based on these experiences, it was concluded that improvements to the lift-to-drag ratio had reached a threshold with the technology available in the field of soft-wing kites. Additional concerns about the lifetime of such fabric kites were also considered at this stage.

The primary motivation for a new concept was the retraction phase. For soft-wing kites, the retraction method is to reduce the aerodynamic forces on the kite and reel in the kite while maintaining minimal tension on the tether(s). This was initially achieved by flying outside the wind window, allowing for retraction at lower wind speeds. Alternatively, a reduction in force can also be achieved by increasing the elevation angle to an almost vertical azimuth position

and then retracting the kite at lower tether tension. Other less common methods include flying upwind behind the ground station and retracting the kite with the wind, as was explored by EnerKite to extract maximum power from the early generation kites. All these strategies, however, require that a minimum tension always be maintained in the tethers. This is driven by the minimum angle of attack (AoA) α_a needed to maintain the leading edge shape of the ram-air kite. Multiple retraction strategies were investigated during the early days for the soft-wing kites, but in the end, the energy lost during these maneuvers was considered insurmountable. Thus, a design that allowed for a more efficient retraction method that resulted in lower power losses during the retraction phase was envisioned.

An alternative approach would be to reduce the aerodynamic forces during retraction by decreasing the angle of attack, or so-called “de-powering”. This approach would allow the kite to be retracted directly by pitching down to fly against the wind while reeling in. Soft-wing kites such as ram-air wings are prone to collapsing at lower angles of attack, and thus an alternative wing design was required.

There are two contradictory requirements when considering the design goals for this new wing. A high lift-to-drag ratio is desired during the traction phase to maximise the power output. In conventional aircraft, a similar design goal is commonly found in designs optimising for endurance, where the sink rate $\frac{C_D}{C_L^{3/2}}$ is minimised. In the case of airborne wind energy (AWE), C_D should correspond to the system drag, consisting of the wing and the tethers, necessitating further higher C_L for optimal power generation. During the retraction phase, contrary to the traction phase, a lower lift-to-drag ratio is required to minimise the aerodynamic forces generated by the kite during reeling in, thus minimising the power invested in the pumping cycle. These two operational points are quite significantly apart and require changing the wing’s aerodynamic properties for these phases. The soft-wing kite designs could no longer achieve these distinct system states for harvest and retraction and the desire for higher power harvesting factors, resulting in higher lift coefficients C_L requirements during harvest. Thus, the development of an alternative wing design embarked.

The obvious way to achieve the different states required for harvest and retraction would be to employ actuators similar to conventional aircraft that modify the system configuration for take-off, cruise, and landing — different operation phases. Conventional aircraft typically endure minimal operational time in the take-off and landing phase and significantly longer durations at cruise. Hence, it is common to prioritise the system goals for the cruise phase and maintain additional auxiliary devices to aid in the take-off and landing phases.

For the [AWES](#) in consideration, these two different system states for efficient retraction could be achieved by either onboard actuation with traditional control surfaces or more exotic methods, such as morphing wings that modify the aerodynamic profile of the wing. Another effective retraction alternative would be changing the centre of mass as done with hang gliders. Deriving from this idea, an approach explored by the EnerKite design is to exploit a tri-tethered system to change the apparent centre of mass of the wing. Steering is thus achievable by manipulating the force ratio between the three lines, by a combination of controller force demand from the ground station, and suitable aerodynamic centre of pressure C_p movement to the angle of attack i.e. suitable pitching moment of the wing C_M . These changes allow for the kite’s pitch angle, and thus via the change in AoA, the lift generated, and consequently forces in the tethers to be modified, allowing for a direct-retractable wing.

A.1.2. Pursuing light-weight wings for AWE

Systematic design parameter sensitivity studies using power prediction models reveal that the airborne system mass was a critical design parameter [71]. The lighter the airborne system is, the lower the minimum wind speed (called the cut-in wind speed) at which the system can operate, increasing the influence of the airborne mass on site-specific yield — especially in low-wind operating conditions. Considering wind is a stochastic property and varies in magnitude and direction, a lower cut-in wind speed increases the annual yield, as it reduces the required number of landings and re-launches of the wing, further influencing the site-specific leveled cost of electricity (LCOE) of the system [71, 185].

The relation between the airborne mass of the kite and the generated power capacity can be seen from the results of performance studies in Figure A.3. A lower aerial mass allows the system to begin generating power at a lower wind speed. For AWES, the take-off wind speed of the system is thus analogous to the cut-in wind of traditional wind turbines and represents the wind speed from which the system can generate power.

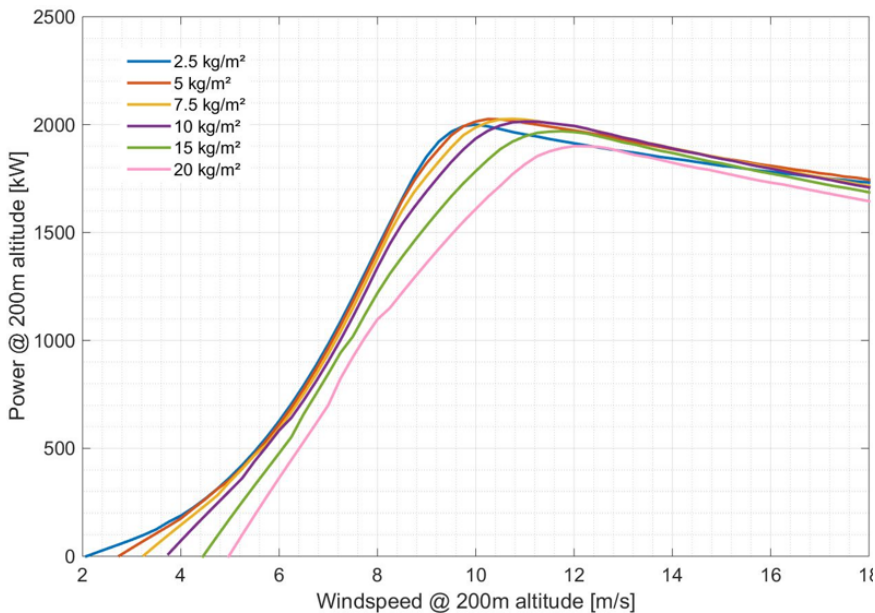


Figure A.3 | Power curves for typical EnerKite systems illustrating the influence of airborne mass on cut in wind speed.

Such high-level design sensitivity studies emphasise the low mass required to achieve the desired capacity factors at the nominal design wind speeds based on typical on-shore site-specific speeds at 200 m. When considering the twin system design goals of high capacity factors and operation at low wind off-shore conditions, it becomes apparent that the longer the kite can stay in the air, the more power is produced. Hence, additional weightage in the system design is designated for low wind conditions, which results in requirements on both the system's mass and the launching capabilities.

A new system design was conceived, with the plateau being reached with soft-wing kites. This system maintained the core design philosophies from the soft-wing kites, such as ground steering and no single point of failure by redundant tethers. Additionally, the system aimed

to provide much higher lift-to-drag ratios and allow for a more efficient retraction method. These requirements had to be met while satisfying the stringent mass requirements that were found to be critical to system yield from performance estimation studies [71]. Thus, the system design decisions result in the airborne mass of the wing being a driving factor in the airborne system concept. This influence of this low-mass target can be seen in both the wing structural concept and the system's launching and landing methodology, described subsequently.

A.1.3. Launching and landing system

A robust and reliable method to autonomously land and launch the airborne system is critical for the commercial success of AWE. Surveying the current ecosystem of rigid wings, a convergence of technology towards conventional drone-like propulsion systems in the form of vertical take-off and landing (VTOL) solutions is found [32]. Other alternatives include a ground-based launching system such as mast and winch assisted, catapult drives, or rotational drives [186].

The focus on minimising airborne mass for the system influences the design space to centre on ground-based concepts. While launching typically occurs in ideal wind conditions, the landing has additional requirements to operate in varying weather conditions. A trade study utilising a high-level set of requirements was undertaken on VTOL, catapult assisted, and a rotating arm-based launching and landing concepts visualised in Figure A.4. The outcome of this analysis prompted the rotating mast landing and launching concept for the EnerKite system [187].

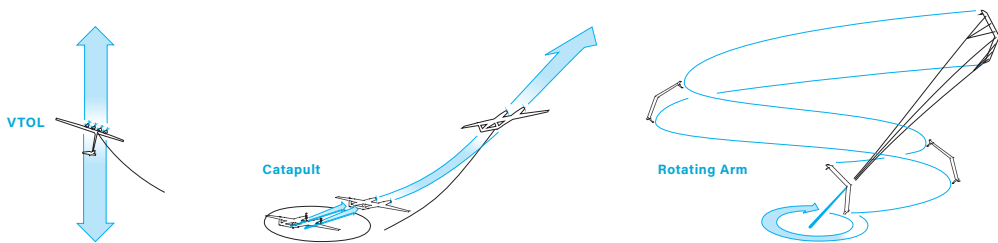


Figure A.4 | Ground assisted launching and landing concepts considered [187].

The study calculates the masses and power capacities required onboard the wing and in the ground station. Scaling effects with different power ratings, wing sizes and masses, in conjunction with economic and safety aspects, determined the rotating arm as the most suitable. The rotating arm benefits from a lower airborne mass and complexity, which has better safety aspects in case of airborne component failures. However, the reduced aerial mass is traded with an increased complexity of the ground station, mast actuation system, and wing control strategy. This becomes even more crucial when the wing is near the ground. Given the apparent airspeed and resulting low tether forces, control authority is typically limited at shorter tether lengths. Wind turbulence at these speeds tends to dominate, leading to sudden loss of tension in the tethers from wind gusts. These phenomena, coupled with a lower recovery margin given the ground proximity, lead to challenging controller design. Moreover, with the ground-actuated three-line concept, there is no direct yaw control, with only pitch and roll control authority. This aspect of the system is further discussed in Section 2.3.2.

Considering the operation of the system, there are distinct phases — start up, intermediate flight on short line length (rotating), transition to and from crosswind flight, and landing. These phases require varied wing attitudes and aerodynamic states, all controlled via the three

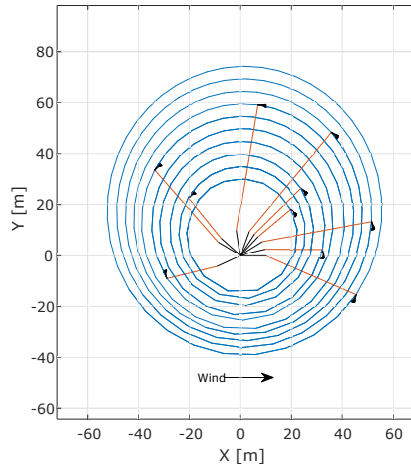


Figure A.5 | Periodic paths for launching and landing, with elongated paths to counter the wind direction [187].

tethers. The lift the wing generates is controlled via the pitch and roll of the wing, while yawing is achieved by adverse yaw. For launching, the mast is sped up until the centripetal and lift forces from the wing are sufficient to support the mass of the wing. At this point, the wing detaches from the mast. The mast then tows the wing to maintain periodic elliptical trajectories as the tether is reeled in and out to compensate for wind speed variations. The wing's path continues spirally until it reaches a target azimuth elevation angle and line length. At this stage, the system tracks the wind window, and once the kite enters the wind window, a transition manoeuvre is undertaken, commencing the crosswind pumping cycle. Throughout these rotational phases, the tether length and arm rotational speed are varied as a function of the rotational angle, compensating for the variation of wind direction, tracking the wind window and compensating for gusts and other disturbances, similar to example trajectories illustrated in Figure A.5.

A.2. THE ENERKITE SYSTEM CONCEPT

The culmination of all prior developments, system use cases, and business case choices lead to a system concept as depicted in Figure A.6. The system consists of a ground station that, at the current scale, fits in a standard shipping container. The motivation for this choice is to aid in the transportation and deployment of the system, which would not require custom solutions, leveraging established flatbed infrastructure. The ground station encloses actuator drives, control systems, and energy storage with battery banks. The drives and the drums for the tether are attached to a rotating base that further houses the landing and launching mast. The mast tip contains the docking mechanism to securely constrain the wing until it is ready to be deployed and launched. The same docking mechanism affixes the wing during the landing phase of operations.

A.2.1. Technical demonstrator

With a focus on rapid testing and flexible operations, the mobile ground station utilised with soft kites was retrofitted with the rotating launching and landing mast. These platform upgrades allowed the reuse of the proven technology and experience gained during the soft-wing development phase. The drive units, control systems and other tether hardware were

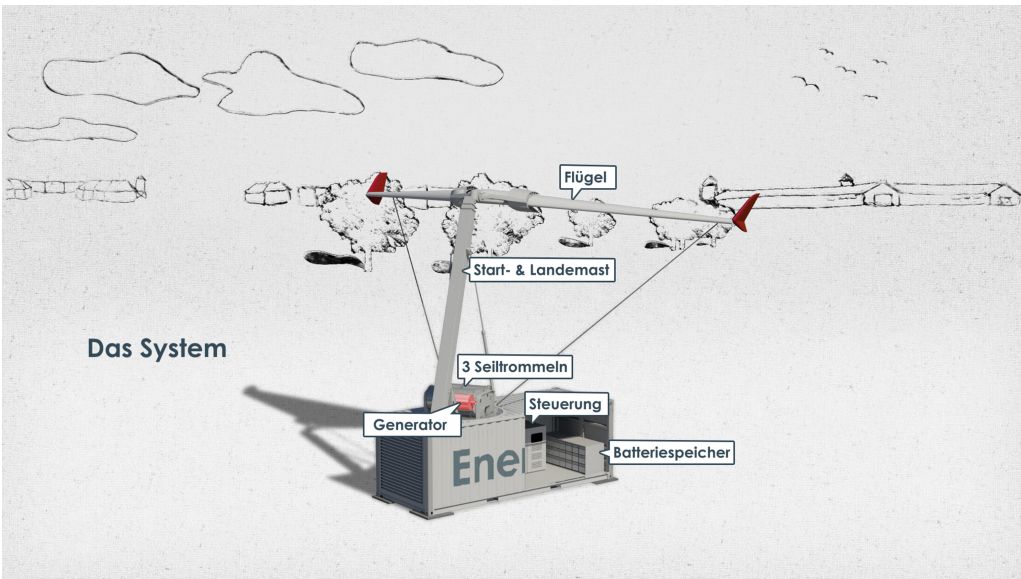


Figure A.6 | EnerKite container system concept.

retrofitted to a new rotary table. Hence, this meant the original rated capacity of 30 kW was still maintained.

Auxiliary drive systems for the mast were added to achieve actuation for rotation, elevation and extension degrees of freedom. An adaptive mast-head subsystem that tracks the wing's attitude and guides the main and control ropes was also developed. This mast-head subsystem also serves as the docking interface between the ground-fixed portion of the system and the airborne wing. This upgraded technical demonstrator is pictured during a typical rotatory launching maneuverer with an early prototype rigid wing in Figure A.7.



Figure A.7 | EnerKite technical demonstrator system comprising a mobile base station with a rotational landing and launching mast, pictured during a launching operation with a prototype wing [80].

A.2.2. Airborne subsystem

As covered in Section 1.3.1, the requirements for the airborne system are unique, combining characteristics common in soft-wing kites, such as passive steering via tether-based actuation. These requirements are contrasted by features common to “aircraft” like AWES, such as rigid

structural members and aerofoils with high lift coefficients C_L . This leads to a concept design that, by virtue, captures the benefits of both “kite” and “aircraft” like concepts.

The motivation of lower nominal wind speeds and high capacity factors drive the design towards a design goal of minimising airborne mass. Further design requirements, such as high aerodynamic lift and low drag, combined with conceptual choices such as tether-based steering, culminated in the selection of a tailless swept wing for the planform. Eliminating the fuselage and conventional empennage provides lower pressure and parasitic drag, lower structural mass and more straightforward construction. Given the high lift and low drag requirement, a wing planform minimising the induced drag was a natural choice. Prandtl’s work from the early 1920s on lifting lines shows that minimal induced drag for a given span is achieved by an elliptical span loading [106, 188]. However, a genuinely elliptical planform is uncommon in aircraft designs owing to the structural complexities stemming from bending moments and manufacturing constraints. Instead, tailoring the span aero loading using varying sweep and chord allows a conventional rectangular wing to achieve a near elliptical span loading. In a subsequent paper in 1933 [107], Prandtl introduces an optimal span loading considering the wing’s structural weight. A few years later, in 1935, Reimar Horten proposed an approximately equivalent “bell” shaped spanwise load profile. Horten also suggested that the bell distribution increased lateral stability by providing proverse yaw [189].

While tailless aircraft provide elegant, minimal wings, they pose a challenge from the flight dynamics, with low lateral and longitudinal stability. Considering that the system is passively steering from the ground, this research area is active at EnerKite. An envelope of coefficients that provide the desired flight characteristics is utilised to determine the required spanwise loading. By adequate tailoring of the aerofoil and twist distribution along the span and other constraints, such as structural considerations, a swept tailless planform was chosen as the airborne development platform for the *EK30* technical demonstrator [70].

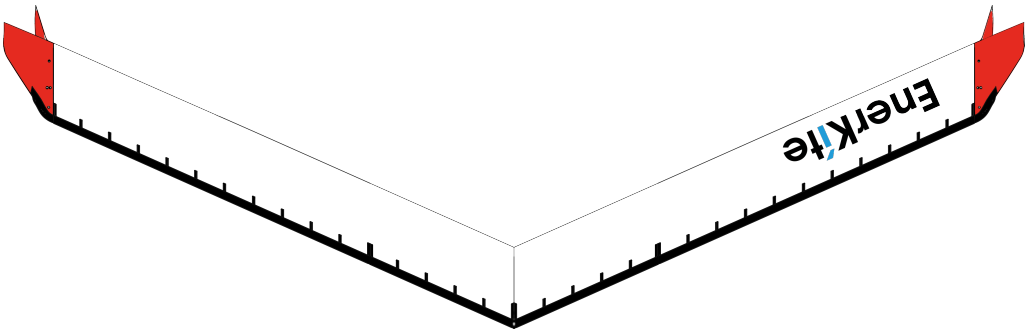


Figure A.8 | Early generation swept wing planform, with winglets and leading edge high lift devices.

Figure A.8 shows a planform view of the wing. The early generation swept wings consist of varying aerofoil sections along the span but with a constant chord (unit taper ratio λ). Also seen are the integrated winglets that provide lateral stability and function as additional lifting surfaces during the rotatory launching phase. When it comes to aerofoil design, multiple aspects require consideration. The quest for high C_L leads to multi-element aerofoil designs, as seen in Figure A.9a, where a leading edge slat is incorporated into the wing. Figure A.8 also depicts the leading edge high lift device that runs along the entire wing span. Flight mechanic stability is another aspect that is accounted for in the aerofoil design. Care must be taken to

achieve a suitable pitching moment C_M to ensure longitudinal stability of the wing by adjusting the profile pitching moment and planform parameters such as profile location, sweep and twist.

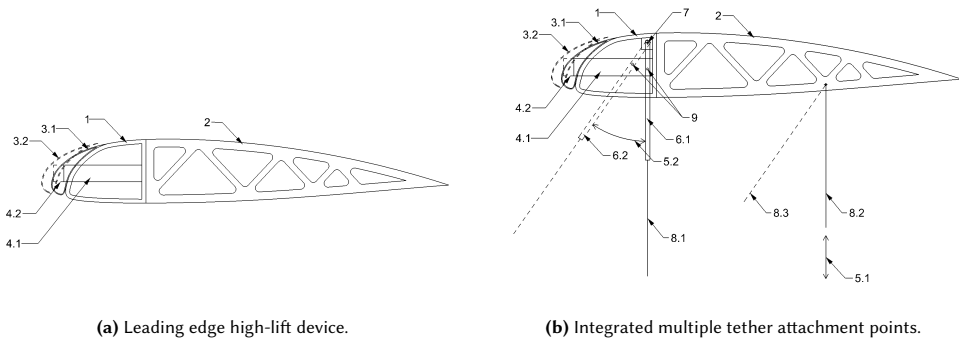


Figure A.9 | EnerKite wing concept sectional details [190].

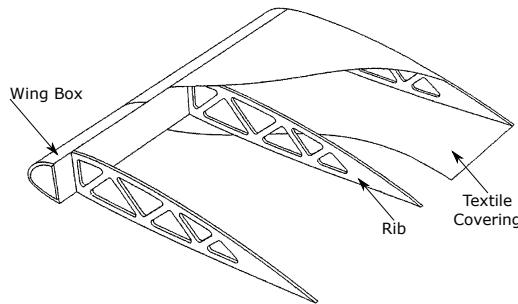


Figure A.10 | Schematic fixed-wing kite structure illustrating the D-box, ribs, and textile covering [80].

In addition to tailless designs, the wings employ several ways to reduce airborne mass. Unlike traditional fixed-wing with spars, ribs, stringers, and skin structural parts, the wing has a carbon composite skeleton with a textile polymer covering. The structure combines aspects typical to “soft” along with “aircraft” type AWES. The hybrid wing allows for a low mass for a given surface area by replacing conventional aluminium or composite skin with a polymer textile. This technique is similar to early-generation doped cotton aircraft construction. Under the skin, the carbon skeleton provides the structural rigidity and strength required to withstand crosswind loads. Typical operational design points require the wing to provide a traction force of well over 100 kg/m^2 while maintaining a structural wing mass of $\leq 5 \text{ kg/m}^2$. Figure A.11 illustrates the 30 kW prototype wing during assembly in the workshop.

Unlike traditional aircraft wings and wind turbine blades that utilise a rectangular torsion box at quarter-chord, the kite structure under consideration uses an atypical “D” shaped wing-box, henceforth referred to as the D-box, as seen in Figure A.8 and detailed further in Figure A.10.

The D-box comprises an aerofoil-shaped “C” shell section and a vertical web and flange section. The increased weight penalty from utilising a rectangular torsion box and additional reinforcements at the leading edge for the high-lift devices and tether attachments motivate this atypical wing-box shape. The lightweight construction uses the wing-box, composite ribs,



Figure A.11 | Prototype rigid wing skeleton pictured during assembly [80, 191].

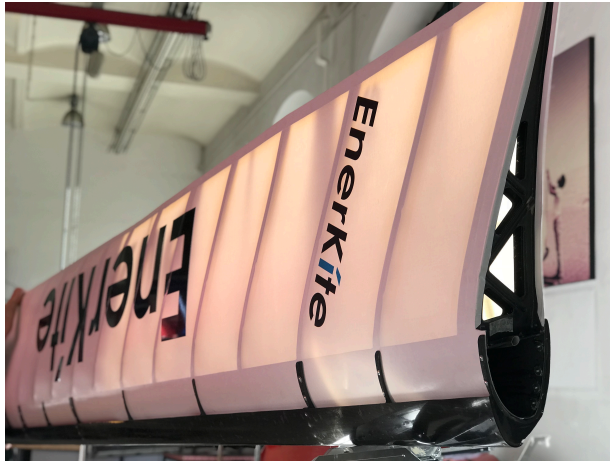


Figure A.12 | Prototype fixed-wing kite structure with carbon skeleton and textile covering (image courtesy EnerKite).

and a textile covering to maintain the aerodynamic shape of the wing. A section of a constructed prototype wing can be seen in Figure A.12. The D-box, the integrated high lift device, the rib skeleton, and the polymer covering can be seen here.

The atypical wing construction proposed by EnerKite has unique aspects that lead to a large design space in the geometric and material domains. The location of the wing-box and rib distribution is one such geometric concern. The polymer fabric coating is borrowed from the aerospace domain but still requires investigation in the field of lifetime and high cycle fatigue. Carbon fibre composite is an anisotropic material that witnesses varying load deflection couplings based on fibre orientation.

Bibliography

1. Masson-Delmotte, V., Zhai, P., Pörtner, H.-O., et al.: Global warming of 1.5 C. An IPCC Special Report on the impacts of global warming of 1(5) (2018)
2. Shukla, P. R., Skea, J., Calvo Buendia, E., et al.: IPCC, 2019: Climate Change and Land: an IPCC special report on climate change, desertification, land degradation, sustainable land management, food security, and greenhouse gas fluxes in terrestrial ecosystems. (2019)
3. Roberts, D. C., Masson-Delmotte, V., Zhai, P., et al.: IPCC, 2019: IPCC Special Report on the Ocean and Cryosphere in a Changing Climate. (2019)
4. Global Energy Review 2021. International Energy Agency (2021)
5. World Energy Outlook 2022. International Energy Agency (2022)
6. World Resources Institute: Climate Watch Historical Country Greenhouse Gas Emissions Data. World Resources Institute. <https://www.climatewatchdata.org/ghg-emissions> (2022). Accessed 01/19/2022
7. Renewable Power Generation Costs in 2019. International Renewable Energy Agency (2019)
8. Candade, A. A., Ranneberg, M., Schmehl, R.: Development of a Toolchain for Aero-structural Design of Composite AWE Kites. In: Abstract from AWEC 2019: 8th international Airborne Wind Energy, Glasgow, United Kingdom, Oct 2019. doi: [10.4233/uuid:57fd203c-e069-11e9-9fcb-441ea15f7c9c](https://doi.org/10.4233/uuid:57fd203c-e069-11e9-9fcb-441ea15f7c9c)
9. Burton, T., Sharpe, D., Jenkins, N., Bossanyi, E.: Wind Energy Handbook. John Wiley & Sons, Ltd, Chichester (2001). doi: [10.1002/0470846062](https://doi.org/10.1002/0470846062)
10. Ramirez, L., Fraile, D., Brindley, G.: Offshore Wind in Europe: Key Trends and Statistics 2018. Published February (2018)
11. Ramirez, L., Fraile, D., Brindley, G.: Wind energy in Europe in 2018 - Trends and statistics. 32 (2019). doi: [10.13140/RG.2.2.12678.63049](https://doi.org/10.13140/RG.2.2.12678.63049)
12. Ramirez, L., Fraile, D., Brindley, G.: Offshore wind in Europe: Key trends and statistics 2020. (2020)
13. Ramirez, L., Fraile, D., Brindley, G.: Wind energy in Europe: 2020 Statistics and the outlook for 2021-2025. (2020)
14. Siemens Gamesa: Powered by change: Siemens Gamesa launches 14 MW offshore Direct Drive turbine with 222-meter rotor. Siemens Gamesa. <https://www.siemensgamesa.com/en-int/-/media/siemensgamesa/downloads/en/newsroom/2020/05/siemens-gamesa-press-release-turbine-14-222-dd-en.pdf> (2020). Accessed 12/15/2020
15. Kristian Holmelund Jakobsen: Vestas launches the V236-15.0 MW to set new industry benchmark and take next step towards leadership in offshore wind. Vestas. <https://mb.cision.com/Public/18886/3283489/a42e3f67f111dd1e.pdf> (2021). Accessed 03/02/2022
16. Burton, T., Jenkins, N., Sharpe, D., Bossanyi, E.: Wind Energy Handbook. 2nd ed. John Wiley & Sons, Ltd, Chichester (2011). doi: [10.1002/9781119992714](https://doi.org/10.1002/9781119992714)
17. Gaertner, E., Rinker, J., Sethuraman, L., et al.: Definition of the IEA 15-Megawatt Offshore Reference Wind Turbine, International Energy Agency, 2020
18. Allen, C., Viselli, A., Dagher, H., et al.: Definition of the UMaine VoltturnUS-S Reference Platform Developed for the IEA Wind 15-Megawatt Offshore Reference Wind Turbine, International Energy Agency
19. Peeringa, J. M., Brood, R., Ceyhan, O., Engels, W., De Winkel, G.: Upwind 20 MW wind turbine pre-design. Petten: ECN (2011)
20. Ashuri, T., Martins, J. R. R. A., Zaaier, M. B., Kuik, G. A. M. van, Bussel, G. J. W. van: Aeroservoelastic design definition of a 20 MW common research wind turbine model. Wind Energy **19**(11), 2071–2087 (2016)
21. Sartori, L., Bellini, F., Croce, A., Bottasso, C. L.: Preliminary design and optimization of a 20MW reference wind turbine. In: Journal of Physics: Conference Series, vol. 1037, 4, p. 042003, IOP Publishing, (2018)
22. Nijssen R Lahuerta, F. W. W. N. A. I. L. B. R. L. S. N. F. A. K. M. K. M. S. R. K. D. F. T., Tiedemann, S.: Innovations on component level for coming 20MW turbines. **308974**(308974), 1–79 (2017)
23. Schmidt, W., Anderson, W.: Kites: Pioneers of Atmospheric Research. In: Ahrens, U., Diehl, M., Schmehl, R. (eds.) Airborne Wind Energy, Green Energy and Technology, Chap. 6, pp. 95–116. Springer, Berlin Heidelberg (2013). doi: [10.1007/978-3-642-39965-7_6](https://doi.org/10.1007/978-3-642-39965-7_6)
24. Oberth, H.: Das Drachenkraftwerk. Uni Verlag, Dr. Roth-Oberth, Feucht, Germany (1977)

-
25. Roberts, B. W., Blackler, J.: Various Systems for Generation of Electricity Using Upper Atmospheric Winds. In: Proceedings of the 2nd Wind Energy Innovation Systems Conference, pp. 67–80, Solar Energy Research Institute, Colorado Springs, CO, USA, Dec 3–5, 1980
 26. Loyd, M. L.: Crosswind kite power. *Journal of Energy* 4(3), 106–111 (1980). doi: [10.2514/3.48021](https://doi.org/10.2514/3.48021)
 27. Loyd, M. L.: Wind driven apparatus for power generation. US Patent 4,251,040, Dec 1978
 28. Loyd, M. L.: Foreword. In: Ahrens, U., Diehl, M., Schmehl, R. (eds.) *Airborne Wind Energy, Green Energy and Technology*. Springer, Berlin Heidelberg (2013). doi: [10.1007/978-3-642-39965-7](https://doi.org/10.1007/978-3-642-39965-7)
 29. Kristian Petrick and Stefanie Thoms: Introduction Airborne Wind Energy: Airborne Wind Energy – an emerging renewable technology. Airborne Wind Europe. https://airbornewindeurope.org/wp-content/uploads/2022/02/Airborne-Wind-Europe_Introduction-to-Airborne-Wind-Energy.pdf (2022). Accessed 03/02/2022
 30. Ahrens, U., Diehl, M., Schmehl, R. (eds.): *Airborne Wind Energy*. Green Energy and Technology, pp. 23–45. Springer, Berlin Heidelberg (2013). doi: [10.1007/978-3-642-39965-7](https://doi.org/10.1007/978-3-642-39965-7)
 31. Roland Schmehl: Introduction Airborne Wind Energy: Airborne Wind Energy – an emerging renewable technology. AWESCO. <http://www.awesco.eu/awe-explained/> (2019). Accessed 03/02/2022
 32. Cherubini, A., Papini, A., Vertechy, R., Fontana, M.: Airborne Wind Energy Systems: A review of the technologies. *Renewable and Sustainable Energy Reviews* 51, 1461–1476 (2015). doi: [10.1016/j.rser.2015.07.053](https://doi.org/10.1016/j.rser.2015.07.053)
 33. Schmehl, R. (ed.): *Airborne Wind Energy – Advances in Technology Development and Research*. Green Energy and Technology. Springer, Singapore (2018), 754 pp. doi: [10.1007/978-981-10-1947-0](https://doi.org/10.1007/978-981-10-1947-0)
 34. Cherubini, A., Fontana, M.: Modelling and Design of Off-Shore Floating Platform for High Altitude Wind Energy Converters. In: Schmehl, R. (ed.). *Book of Abstracts of the International Airborne Wind Energy Conference 2015*, p. 42, Delft, The Netherlands, June 15–16, 2015. doi: [10.4233/uuid:7df59b79-2c6b-4e30-bd58-8454f493bb09](https://doi.org/10.4233/uuid:7df59b79-2c6b-4e30-bd58-8454f493bb09). Presentation video recording available from: <https://collegerama.tudelft.nl/Mediasite/Play/d16d2d1661af47e88f6e13fb8255e2341d>
 35. Bechtle, P., Gehrmann, T., Sieg, C., Zillmann, U.: AWESome: An open-source test platform for airborne wind energy systems. (2017). doi: [10.48550/arXiv.1704.08695](https://doi.org/10.48550/arXiv.1704.08695)
 36. Malz, E. C., Koenemann, J., Sieberling, S., Gros, S.: A reference model for airborne wind energy systems for optimization and control. *Renewable Energy* 140, 1004–1011 (2019). doi: [10.1016/j.renene.2019.03.111](https://doi.org/10.1016/j.renene.2019.03.111)
 37. Stiesdal, H.: Airborne Wind Energy – Challenges and Opportunities Based on Experiences From the Conventional Wind Industry. In: Diehl, M., Leuthold, R., Schmehl, R. (eds.). *Book of Abstracts of the Airborne Wind Energy Conference 2017*, p. 13, Freiburg, Germany (2017). doi: [10.4233/uuid:4c361ef1-d2d2-4d14-9868-16541f60edc7](https://doi.org/10.4233/uuid:4c361ef1-d2d2-4d14-9868-16541f60edc7). Presentation video recording available from: www.awec2017.com
 38. Papakostas, N., Papachatzakis, P., Xanthakis, V., Mourtzis, D., Chryssoulouris, G.: An approach to operational aircraft maintenance planning. *Decision support systems* 48(4), 604–612 (2010)
 39. Kroes, M. J., Sterkenburg, R.: *Aircraft Maintenance & Repair*. McGraw-Hill Education (2013)
 40. Van den Bergh, J., De Bruecker, P., Beliën, J., Peeters, J.: *Aircraft maintenance operations: state of the art*. HUB Research Paper 2013/09 (2013)
 41. Andrawus, J. A., Watson, J., Kishk, M., Gordon, H.: Optimisation of wind turbine inspection intervals. *Wind Engineering* 32(5), 477–490 (2008)
 42. Fischer, K., Besnard, F., Bertling, L.: Reliability-centered maintenance for wind turbines based on statistical analysis and practical experience. *IEEE Transactions on Energy Conversion* 27(1), 184–195 (2011)
 43. Shafiee, M., Sørensen, J. D.: Maintenance optimization and inspection planning of wind energy assets: Models, methods and strategies. *Reliability Engineering & System Safety* 192, 105993 (2019)
 44. Walker, H., Lockhart, E., Desai, J., et al.: *Model of Operation-and-Maintenance Costs for Photovoltaic Systems*, National Renewable Energy Lab.(NREL), Golden, CO (United States), 2020
 45. Murdock, S.: The longest flight : Yuma’s quest for the future. Longest Flight LLC, Roll, AZ (1999)
 46. release, A. P.: Zephyr S set to break aircraft world endurance record. <https://www.airbus.com/newsroom/press-releases/en/2018/07/Zephyr-S-set-to-break-aircraft-world-endurance-record.html>. Accessed: 2020-08-20, 2018
 47. Grantz, A.: X-37B Orbital Test Vehicle and Derivatives. In: AIAA SPACE 2011 Conference & Exposition, September, pp. 1–14, Reston, Virginia, June 2011. doi: [10.2514/6.2011-7315](https://doi.org/10.2514/6.2011-7315)
 48. Raymer, D.: *Aircraft Design: A Conceptual Approach*, Sixth Edition, p. 745. American Institute of Aeronautics and Astronautics, Inc., Washington, DC (2018). doi: [10.2514/4.104909](https://doi.org/10.2514/4.104909)
 49. Anderson, J. D.: *Fundamentals of Aerodynamics*, 5th ed. McGraw-Hill (2014)
 50. Agency, E. A. S.: *Certification Specifications for Normal Utility, Aerobatic, and Commuter Category Aeroplanes CS-23*, 2017
 51. Agency, E. A. S.: *Certification Specifications and Acceptable Means of Compliance for Large Aeroplanes CS-25*, 2019
 52. Agency, E. A. S.: *Certification Specifications and Acceptable Means of Compliance for Sailplanes and Powered Sailplanes CS-22*, 2021

53. Group, I. 6.-1. W. et al.: Wind energy generation systems - Part 1: Design requirements, Edition 4.0. Final Draft International Standard (FDIS) (2019)
54. Salma, V., Ruiterkamp, R., Kruijff, M., Paassen, M. M. R. v., Schmehl, R.: Current and Expected Airspace Regulations for Airborne Wind Energy Systems. In: Schmehl, R. (ed.) *Airborne Wind Energy – Advances in Technology Development and Research*, Green Energy and Technology, Chap. 29, pp. 703–725. Springer, Singapore (2018). doi: [10.1007/978-981-10-1947-0_29](https://doi.org/10.1007/978-981-10-1947-0_29)
55. Salma, V., Friedl, F., Schmehl, R.: Improving reliability and safety of airborne wind energy systems. *Wind Energy* **23**(2), 340–356 (2020). doi: [10.1002/we.2433](https://doi.org/10.1002/we.2433)
56. Weiss, P.: Airborne Wind Energy Prepares for Take Off. *Engineering* **6**(2), 107–109 (2020). doi: [10.1016/j.eng.2019.12.002](https://doi.org/10.1016/j.eng.2019.12.002)
57. Weiss, P.: After Highflyer Crashes, Airborne Wind Energy Regroups. *Engineering* **7**(3), 277–279 (2021). doi: [10.1016/j.eng.2021.01.004](https://doi.org/10.1016/j.eng.2021.01.004)
58. Kaa, G. van de, Kamp, L.: Exploring design dominance in early stages of the dominance process: The case of airborne wind energy. *Journal of Cleaner Production* **321**(March), 128918 (2021). doi: [10.1016/j.jclepro.2021.128918](https://doi.org/10.1016/j.jclepro.2021.128918)
59. Boehm, B. W.: A spiral model of software development and enhancement. *Computer* **21**(5), 61–72 (1988). doi: [10.1109/2.59](https://doi.org/10.1109/2.59)
60. Argatov, I., Rautakorpi, P., Silvennoinen, R.: Estimation of the mechanical energy output of the kite wind generator. *Renewable Energy* **34**(6), 1525–1532 (2009). doi: [10.1016/j.renene.2008.11.001](https://doi.org/10.1016/j.renene.2008.11.001)
61. Luchsinger, R. H.: Pumping Cycle Kite Power. In: Ahrens, U., Diehl, M., Schmehl, R. (eds.) *Airborne Wind Energy, Green Energy and Technology*, Chap. 3, pp. 47–64. Springer, Berlin Heidelberg (2013). doi: [10.1007/978-3-642-39965-7_3](https://doi.org/10.1007/978-3-642-39965-7_3)
62. Schmehl, R., Noom, M., Vlugt, R. van der: Traction Power Generation with Tethered Wings. In: Ahrens, U., Diehl, M., Schmehl, R. (eds.) *Airborne Wind Energy, Green Energy and Technology*, Chap. 2, pp. 23–45. Springer, Berlin Heidelberg (2013). doi: [10.1007/978-3-642-39965-7_2](https://doi.org/10.1007/978-3-642-39965-7_2)
63. Williams, P.: Optimal wind power extraction with a tethered kite. AIAA Paper 2006-6193. In: *Proceedings of the AIAA Guidance, Navigation, and Control Conference and Exhibit*, Keystone, CO, USA, Aug 21–24, 2006. doi: [10.2514/6.2006-6193](https://doi.org/10.2514/6.2006-6193)
64. Williams, P., Lansdorp, B., Ockels, W.: Optimal Crosswind Towing and Power Generation with Tethered Kites. *AIAA Journal of Guidance, Control, and Dynamics* **31**(1), 81–93 (2008). doi: [10.2514/1.30089](https://doi.org/10.2514/1.30089)
65. Horn, G., Gros, S., Diehl, M.: Numerical Trajectory Optimization for Airborne Wind Energy Systems Described by High Fidelity Aircraft Models. In: Ahrens, U., Diehl, M., Schmehl, R. (eds.) *Airborne Wind Energy, Green Energy and Technology*, Chap. 11, pp. 205–218. Springer, Berlin Heidelberg (2013). doi: [10.1007/978-3-642-39965-7_11](https://doi.org/10.1007/978-3-642-39965-7_11)
66. Gros, S., Zanon, M., Diehl, M.: Control of Airborne Wind Energy Systems Based on Nonlinear Model Predictive Control & Moving Horizon Estimation. In: *Proceedings of the European Control Conference (ECC13)*, Zurich, Switzerland, July 17–19, 2013
67. Rapp, S., Schmehl, R., Oland, E., et al.: A Modular Control Architecture for Airborne Wind Energy Systems. In: *AIAA Scitech 2019 Forum*, Reston, Virginia, Jan 2019. doi: [10.2514/6.2019-1419](https://doi.org/10.2514/6.2019-1419)
68. Erhard, M., Horn, G., Diehl, M.: A quaternion-based model for optimal control of the SkySails airborne wind energy system. *ZAMM – Journal of Applied Mathematics and Mechanics* (2016). doi: [10.1002/zamm.201500180](https://doi.org/10.1002/zamm.201500180)
69. De Schutter, J., Leuthold, R., Bronnenmeyer, T., Paelinck, R., Diehl, M.: Optimal control of stacked multi-kite systems for utility-scale airborne wind energy. *Proceedings of the IEEE Conference on Decision and Control 2019-December*(Cdc), 4865–4870 (2019). doi: [10.1109/CDC40024.2019.9030026](https://doi.org/10.1109/CDC40024.2019.9030026)
70. Ranneberg, M., Bormann, A.: Estimation, Optimisation and Validation of Power Curves for Airborne Wind Energy. In: Schmehl, R. (ed.) *Book of Abstracts of the International Airborne Wind Energy Conference 2015*, pp. 50–51, Delft, The Netherlands, June 15–16, 2015. doi: [10.4233/uuid:7df59b79-2c6b-4e30-bd58-8454f493bb09](https://doi.org/10.4233/uuid:7df59b79-2c6b-4e30-bd58-8454f493bb09). Presentation video recording available from: <https://collegerama.tudelft.nl/Mediasite/Play/a5fcb164487546849230da29a8a81f421d>
71. Ranneberg, M., Brandt, D., Bormann, A., et al.: Fast Power Curve and Yield Estimation of Yo-Yo Airborne Wind Energy Systems. In: Schmehl, R. (ed.) *Airborne Wind Energy – Advances in Technology Development and Research*, Green Energy and Technology, Chap. 25, pp. 77–95. Springer, Singapore (2018). doi: [10.1007/978-981-10-1947-0_25](https://doi.org/10.1007/978-981-10-1947-0_25)
72. Vlugt, R. van der, Bley, A., Schmehl, R., Noom, M.: Quasi-Steady Model of a Pumping Kite Power System. *Renewable Energy* **131**, 83–99 (2019). doi: [10.1016/j.renene.2018.07.023](https://doi.org/10.1016/j.renene.2018.07.023)
73. Rushdi, M. A., Rushdi, A. A., Dief, T. N., et al.: Power prediction of airborne wind energy systems using multivariate machine learning. *Energies* **13**(9), 1–23 (2020). doi: [10.3390/en13092367](https://doi.org/10.3390/en13092367)
74. Bormann, A., Ranneberg, M., Kövesdi, P., Gebhardt, C., Skutnik, S.: Development of a Three-Line Ground-Actuated Airborne Wind Energy Converter. In: Ahrens, U., Diehl, M., Schmehl, R. (eds.) *Airborne Wind Energy*,

-
- Green Energy and Technology, Chap. 24, pp. 427–437. Springer, Berlin Heidelberg (2013). doi: [10.1007/978-3-642-39965-7_24](https://doi.org/10.1007/978-3-642-39965-7_24)
75. Paulig, X., Bungart, M., Specht, B.: Conceptual Design of Textile Kites Considering Overall System Performance. In: Ahrens, U., Diehl, M., Schmehl, R. (eds.) *Airborne Wind Energy*, Green Energy and Technology, Chap. 32, pp. 547–562. Springer, Berlin Heidelberg (2013). doi: [10.1007/978-3-642-39965-7_32](https://doi.org/10.1007/978-3-642-39965-7_32)
 76. Vlugt, R. van der, Peschel, J., Schmehl, R.: Design and Experimental Characterization of a Pumping Kite Power System. In: Ahrens, U., Diehl, M., Schmehl, R. (eds.) *Airborne Wind Energy*, Green Energy and Technology, Chap. 23, pp. 403–425. Springer, Berlin Heidelberg (2013). doi: [10.1007/978-3-642-39965-7_23](https://doi.org/10.1007/978-3-642-39965-7_23)
 77. Vander Lind, D.: Analysis and Flight Test Validation of High Performance Airborne Wind Turbines. In: Ahrens, U., Diehl, M., Schmehl, R. (eds.) *Airborne Wind Energy*, Green Energy and Technology, Chap. 28, pp. 473–490. Springer, Berlin Heidelberg (2013). doi: [10.1007/978-3-642-39965-7_28](https://doi.org/10.1007/978-3-642-39965-7_28)
 78. Luchsinger, R., Aregger, D., Bezar, F., et al.: Pumping Cycle Kite Power with Twings. In: Schmehl, R. (ed.) *Airborne Wind Energy – Advances in Technology Development and Research*, Green Energy and Technology, pp. 603–621. Springer (2018). doi: [10.1007/978-981-10-1947-0_24](https://doi.org/10.1007/978-981-10-1947-0_24)
 79. TwingTec AG.: Twingtec – Wind Energy 2.0. <https://twingtec.ch/>. Accessed 03/17/2020
 80. Candade, A. A., Ranneberg, M., Schmehl, R.: Structural analysis and optimization of a tethered swept wing for airborne wind energy generation. *Wind Energy* **23**(November 2019), we.2469 (2020). doi: [10.1002/we.2469](https://doi.org/10.1002/we.2469)
 81. Diehl, M., Magni, L., Nicolao, G. D.: Efficient NMPC of unstable periodic systems using approximate infinite horizon closed loop costing. *Annual Reviews in Control* **28**(1), 37–45 (2004). doi: [10.1016/j.arcontrol.2004.01.011](https://doi.org/10.1016/j.arcontrol.2004.01.011)
 82. Erhard, M., Strauch, H.: Flight control of tethered kites in autonomous pumping cycles for airborne wind energy. *Control Engineering Practice* **40**, 13–26 (2015). doi: [10.1016/j.conengprac.2015.03.001](https://doi.org/10.1016/j.conengprac.2015.03.001)
 83. Fagiano, L., Zraggen, A. U., Morari, M., Khammash, M.: Automatic control of tethered wings for airborne wind energy: design and experimental results. In: *Proceedings of the European Control Conference (ECC13)*, Zurich, Switzerland, July 17–19, 2013
 84. Fagiano, L., Zraggen, A. U., Morari, M., Khammash, M.: Automatic crosswind flight of tethered wings for airborne wind energy: modeling, control design and experimental results. *IEEE Transactions on Control Systems Technology* **22**(4), 1433–1447 (2014). doi: [10.1109/TCST.2013.2279592](https://doi.org/10.1109/TCST.2013.2279592)
 85. Zraggen, A. U., Fagiano, L., Morari, M.: Automatic Retraction and Full-Cycle Operation for a Class of Airborne Wind Energy Generators. *IEEE Transactions on Control Systems Technology* **24**(2), 594–608 (2015). doi: [10.1109/TCST.2015.2452230](https://doi.org/10.1109/TCST.2015.2452230)
 86. Rapp, S., Schmehl, R.: Vertical Takeoff and Landing of Flexible Wing Kite Power Systems. *Journal of Guidance, Control, and Dynamics* **41**(11), 2386–2400 (2018). doi: [10.2514/1.G003535](https://doi.org/10.2514/1.G003535)
 87. Fechner, U., Vlugt, R. van der, Schreuder, E., Schmehl, R.: Dynamic Model of a Pumping Kite Power System. *Renewable Energy* **83**, 705–716 (2015). doi: [10.1016/j.renene.2015.04.028](https://doi.org/10.1016/j.renene.2015.04.028)
 88. Canale, M., Fagiano, L., Milanese, M.: Power kites for wind energy generation - fast predictive control of tethered airfoils. *IEEE Control Systems Magazine* **27**(6), 25–38 (2007). doi: [10.1109/MCS.2007.909465](https://doi.org/10.1109/MCS.2007.909465)
 89. Williams, P., Lansdorp, B., Ockels, W. J.: Modeling and Control of a Kite on a Variable Length Flexible Inelastic Tether. *AIAA Paper 2007-6705*. In: *Proceedings of the AIAA Modeling and Simulation Technologies Conference and Exhibit*, Hilton Head, SC, USA, Aug 20–23, 2007. doi: [10.2514/6.2007-6705](https://doi.org/10.2514/6.2007-6705)
 90. Williams, P., Lansdorp, B., Ockels, W. J.: Nonlinear Control and Estimation of a Tethered Kite in Changing Wind Conditions. *AIAA Journal of Guidance, Control and Dynamics* **31**(3) (2008). doi: [10.2514/1.31604](https://doi.org/10.2514/1.31604)
 91. Vermillion, C., Grunnagle, T., Kolmanovsky, I.: Modeling and control design for a prototype lighter-than-air wind energy system. In: *Proceedings of the 2012 American Control Conference*, pp. 4405–4410, Montréal, QC, Canada, June 27–29, 2012
 92. Terink, E., Breukels, J., Schmehl, R., Ockels, W.: Flight Dynamics and Stability of a Tethered Inflatable Kiteplane. *Journal of Aircraft* **48**(2), 503–513 (2011). doi: [10.2514/1.C031108](https://doi.org/10.2514/1.C031108)
 93. Vermillion, C., Cobb, M., Fagiano, L., et al.: Electricity in the air: Insights from two decades of advanced control research and experimental flight testing of airborne wind energy systems. *Annual Reviews in Control* **52**(March), 330–357 (2021). doi: [10.1016/j.arcontrol.2021.03.002](https://doi.org/10.1016/j.arcontrol.2021.03.002)
 94. Ranneberg, M.: Direct Wing Design and Inverse Airfoil Identification with the Nonlinear Weissinger Method. [arxiv:1501.04983 \[physics.flu-dyn\]](https://arxiv.org/abs/1501.04983), 1–13 (2015)
 95. Hess, J. L.: Panel Methods in Computational Fluid Dynamics. *Annual Review of Fluid Mechanics* **22**(1), 255–274 (1990). doi: [10.1146/annurev.fl.22.010190.001351](https://doi.org/10.1146/annurev.fl.22.010190.001351)
 96. Katz, J., Plotkin, A.: *Low-speed Aerodynamics: From Wing Theory to Panel Methods*. McGraw-Hill Series in Population Biology. McGraw-Hill (1991)
 97. Erickson, L. L.: *Panel Methods: An introduction*, NASA Ames Research Center, Moffett Field, CA, United States, Dec 1990
 98. Katz, J.: Convergence and Accuracy of Potential-Flow Methods. *Journal of Aircraft* **56**(6), 2371–2375 (2019). doi: [10.2514/1.C035483](https://doi.org/10.2514/1.C035483)

99. Drela, M.: XFOIL: An Analysis and Design System for Low Reynolds Number Airfoils. In: Mueller, T. J. (ed.) *Low Reynolds Number Aerodynamics*, vol. 54, Lecture Notes in Engineering, pp. 1–12. Springer, Berlin-Heidelberg (1989). doi: [10.1007/978-3-642-84010-4_1](https://doi.org/10.1007/978-3-642-84010-4_1)
100. Drela, M., Giles, M. B.: Viscous-inviscid analysis of transonic and low Reynolds number airfoils. *AIAA Journal* **25**(10), 1347–1355 (1987). doi: [10.2514/3.9789](https://doi.org/10.2514/3.9789)
101. Castro-Fernández, I., Borobia-Moreno, R., Cavallaro, R., Sánchez-Arriaga, G.: Three-Dimensional Unsteady Aerodynamic Analysis of a Rigid-Framed Delta Kite Applied to Airborne Wind Energy. *Energies* **14**(23), 8080 (2021). doi: [10.3390/en14238080](https://doi.org/10.3390/en14238080)
102. Fasel, U., Keidel, D., Molinari, G., Ermanni, P.: Aerostructural optimization of a morphing wing for airborne wind energy applications. *Smart Materials and Structures* **26**(9), 095043 (2017). doi: [10.1088/1361-665X/aa7c87](https://doi.org/10.1088/1361-665X/aa7c87)
103. Aerodynamic analysis of Ampyx airborne wind energy system. *Journal of Physics: Conference Series* **1037**(6), 062008 (2018). doi: [10.1088/1742-6596/1037/6/062008](https://doi.org/10.1088/1742-6596/1037/6/062008)
104. Folkersma, M., Viré, A.: Flow transition modeling on two-dimensional circular leading edge airfoils. *Wind Energy* **22**(7), 908–921 (2019). doi: [10.1002/we.2329](https://doi.org/10.1002/we.2329)
105. Folkersma, M., Schmehl, R., Viré, A.: Steady-state aeroelasticity of a ram-air wing for airborne wind energy applications. *Journal of Physics: Conference Series* **1618**(3), 032018 (2020). doi: [10.1088/1742-6596/1618/3/032018](https://doi.org/10.1088/1742-6596/1618/3/032018)
106. Prandtl, L.: Tragflügeltheorie. II. Mitteilung. *Nachrichten von der Gesellschaft der Wissenschaften zu Göttingen, Mathematisch-Physikalische Klasse* **1919**, 107–137 (1919)
107. Tollmien, W., Schlichting, H., Görtler, H., Riegels, F. W.: Über Tragflügel kleinsten induzierten Widerstandes. In: Riegels, F. W. (ed.) *Ludwig Prandtl Gesammelte Abhandlungen*, pp. 556–561. Springer Berlin Heidelberg, Berlin, Heidelberg (1961). doi: [10.1007/978-3-662-11836-8_40](https://doi.org/10.1007/978-3-662-11836-8_40)
108. Abbott, I. H., Doenhoff, A. E.: *Theory of wing sections*. Dover Publications (1959)
109. Starnes, J. H., Haftka, R. T.: Preliminary Design of Composite Wings for Buckling, Strength, and Displacement Constraints. *Journal of Aircraft* **16**(8), 564–570 (1979). doi: [10.2514/3.58565](https://doi.org/10.2514/3.58565)
110. Vosteen, L. F.: *Composite Aircraft Structures BT - Fibrous Composites in Structural Design*. In: Lenoë, E. M., Oplinger, D. W., Burke, J. J. (eds.), pp. 7–24. Springer US, Boston, MA (1980). doi: [10.1007/978-1-4684-1033-4_2](https://doi.org/10.1007/978-1-4684-1033-4_2)
111. Shirk, M. H., Hertz, T. J., Weisshaar, T. A.: Aeroelastic tailoring - Theory, practice, and promise. *Journal of Aircraft* **23**(1), 6–18 (1986). doi: [10.2514/3.45260](https://doi.org/10.2514/3.45260)
112. Weisshaar, T. A.: Aeroelastic Tailoring of Forward Swept Composite Wings. *Journal of Aircraft* **18**(8), 669–676 (1981). doi: [10.2514/3.57542](https://doi.org/10.2514/3.57542)
113. Weisshaar, T.: Aeroelastic tailoring - Creative uses of unusual materials. In: 28th Structures, Structural Dynamics and Materials Conference, Reston, Virginia, Apr 1987. doi: [10.2514/6.1987-976](https://doi.org/10.2514/6.1987-976)
114. Krohn, S.: The wind energy pioneers: The gedser wind turbine. Published by The Danish Wind Turbine Manufacturers Association on the Internet: <http://www.windpower.dk/pictures/juul.htm> **2000** (1998)
115. Mishnaevsky, L., Branner, K., Petersen, H., et al.: Materials for Wind Turbine Blades: An Overview. *Materials* **10**(11), 1285 (2017). doi: [10.3390/ma10111285](https://doi.org/10.3390/ma10111285)
116. Brøndsted, P., Lilholt, H., Lystrup, A.: Composite Materials for Wind Power Turbine Blades. *Annual Review of Materials Research* **35**(1), 505–538 (2005). doi: [10.1146/annurev.matsci.35.100303.110641](https://doi.org/10.1146/annurev.matsci.35.100303.110641)
117. Kennedy, G., Martins, J.: A Regularized Discrete Laminate Parametrization Technique with Applications to Wing-Box Design Optimization. *AIAA Paper 2012-1519*. In: 53rd AIAA/ASME/ASCE/AHS/ASC Structures, Structural Dynamics and Materials Conference, Honolulu, HI, USA (2012). doi: [10.2514/6.2012-1519](https://doi.org/10.2514/6.2012-1519)
118. Bauchau, O., Craig, J.: *Structural Analysis: With Applications to Aerospace Structures*. Solid Mechanics and Its Applications. Springer Netherlands (2009)
119. Dorbath, F., Nagel, B., Gollnick, V.: Comparison of Beam and Shell Theory for Mass Estimation in Preliminary Wing Design. 2nd Aircraft Structural Design Conference October, 26–28 (2010)
120. Hodges, D. H., Dowell, E. H.: Nonlinear equations of motion for the elastic bending and torsion of twisted nonuniform rotor blades, 1974, D–7818, NASA, December 1974
121. Librescu, L., Thangitham, S.: Analytical studies on static aeroelastic behavior of forward-swept composite wing structures. *Journal of Aircraft* **28**(2), 151–157 (1991). doi: [10.2514/3.46004](https://doi.org/10.2514/3.46004)
122. Librescu, L., Song, O.: On the static aeroelastic tailoring of composite aircraft swept wings modelled as thin-walled beam structures. *Composites Engineering* **2**(5-7), 497–512 (1992). doi: [10.1016/0961-9526\(92\)90039-9](https://doi.org/10.1016/0961-9526(92)90039-9)
123. Librescu, L., Simovich, J.: General formulation for the aeroelastic divergence of composite swept-forward wing structures. *Journal of Aircraft* **25**(4), 364–371 (1988). doi: [10.2514/3.45572](https://doi.org/10.2514/3.45572)
124. Gern, F. H., Librescu, L.: Aeroelastic Tailoring of Composite Wings Exhibiting Nonclassical Effects and Carrying External Stores. *Journal of Aircraft* **37**(6), 1097–1104 (2000). doi: [10.2514/2.2718](https://doi.org/10.2514/2.2718)
125. Lobitz, D., Veers, P. S., Eisler, G. R., et al.: The Use of Twist-Coupled Blades to Enhance the Performance of Horizontal Axis Wind Turbines, Sandia National Laboratories (SNL), Albuquerque, NM, and Livermore, CA (United States), May 2001. doi: [10.2172/783086](https://doi.org/10.2172/783086)

-
126. Volovoi, V., Hodges, D., Cesnik, C., Popescu, B.: Assessment of beam modeling methods for rotor blade applications. *Mathematical and Computer Modelling* **33**(10-11), 1099–1112 (2001). doi: [10.1016/S0895-7177\(00\)00302-2](https://doi.org/10.1016/S0895-7177(00)00302-2)
 127. Wijnja, J., Schmehl, R., Breuker, R. de, Jensen, K., Vander Lind, D.: Aero-elastic analysis of a large airborne wind turbine. *Journal of Guidance, Control and Dynamics* **41**(11), 2374–2385 (2018). doi: [10.2514/1.G001663](https://doi.org/10.2514/1.G001663)
 128. Fasel, U., Keidel, D., Molinari, G., Ermanni, P.: Aeroservoelastic Optimization of Morphing Airborne Wind Energy Wings. In: *AIAA Scitech 2019 Forum*, January, Reston, Virginia, Jan 2019. doi: [10.2514/6.2019-1217](https://doi.org/10.2514/6.2019-1217)
 129. Fasel, U., Tiso, P., Keidel, D., Molinari, G., Ermanni, P.: Reduced-Order Dynamic Model of a Morphing Airborne Wind Energy Aircraft. *AIAA Journal* **57**(8), 3586–3598 (2019). doi: [10.2514/1.J058019](https://doi.org/10.2514/1.J058019)
 130. Eijkelhof, D., Rapp, S., Fasel, U., Gaunaa, M., Schmehl, R.: Reference Design and Simulation Framework of a Multi-Megawatt Airborne Wind Energy System. *Journal of Physics: Conference Series* **1618**(3) (2020). doi: [10.1088/1742-6596/1618/3/032020](https://doi.org/10.1088/1742-6596/1618/3/032020)
 131. Collar, A. R.: The expanding domain of aeroelasticity. *The Aeronautical Journal* **50**(428), 613–636 (1946)
 132. Fung, Y.: *An Introduction to the Theory of Aeroelasticity*. Dover books on engineering and engineering physics. Dover Publications (1969)
 133. Katz, J., Plotkin, A.: *Low-speed aerodynamics*. 2nd ed. Cambridge University Press (2001)
 134. National, T. S. B.: *Pilot/Operator Aircraft Accident/Incident Report*. NTSB Form 6120.1, NTSB, Washington, DC, 2017
 135. Drela, M.: Integrated simulation model for preliminary aerodynamic, structural, and control-law design of aircraft. In: *40th Structures, Structural Dynamics, and Materials Conference and Exhibit*, c, Reston, Virginia, Apr 1999. doi: [10.2514/6.1999-1394](https://doi.org/10.2514/6.1999-1394)
 136. Sivells, J. C., Neely, R. H.: Method for calculating wing characteristics by lifting-line theory using nonlinear section lift data. *NACA Technical Note 1269*, Langley Memorial Aeronautical Laboratory, Langley, VA, USA, Apr 1947
 137. Weissinger, J.: *The Lift Distribution of Swept-Back Wings*. NACA Technical Memorandum No. 1120., 1947
 138. Dam, C. van: The aerodynamic design of multi-element high-lift systems for transport airplanes. *Progress in Aerospace Sciences* **38**(2), 101–144 (2002). doi: [10.1016/S0376-0421\(02\)00002-7](https://doi.org/10.1016/S0376-0421(02)00002-7)
 139. Dam, C. P. van, Vander Kam, J. C., Paris, J. K.: Design-Oriented High-Lift Methodology for General Aviation and Civil Transport Aircraft. *Journal of Aircraft* **38**(6), 1076–1084 (2001). doi: [10.2514/2.2875](https://doi.org/10.2514/2.2875)
 140. Leloup, R., Roncin, K., Bles, G., et al.: Estimation of the Lift-to-Drag Ratio Using the Lifting Line Method: Application to a Leading Edge Inflatable Kite. In: Ahrens, U., Diehl, M., Schmehl, R. (eds.) *Airborne Wind Energy, Green Energy and Technology*, Chap. 19, pp. 339–355. Springer, Berlin Heidelberg (2013). doi: [10.1007/978-3-642-39965-7_19](https://doi.org/10.1007/978-3-642-39965-7_19)
 141. Dupont, C., Deberque, M., Leroux, J.-B., Roncin, K., Jochum, C.: Local Results Verification of a 3D Non-Linear Lifting Line Method for Fluid-Structure Interactions Simulation on a Towing Kite for Vessels. *High-Performance Marine Vehicles*, 79–97 (2017). doi: [10.1007/978-981-10-1947-0_4](https://doi.org/10.1007/978-981-10-1947-0_4)
 142. Gaunaa, M., Paralta Carqueija, P. F., Réthoré, P.-E. M., Sørensen, N. N.: A Computationally Efficient Method for Determining the Aerodynamic Performance of Kites for Wind Energy Applications. In: *Proceedings of the European Wind Energy Association Conference*, Brussels, Belgium, Mar 14–17, 2011
 143. Gallay, S., Ghasemi, S., Laurendeau, E.: Sweep effects on non-linear Lifting Line Theory near Stall. In: *52nd Aerospace Sciences Meeting*. (2014). doi: [10.2514/6.2014-1105](https://doi.org/10.2514/6.2014-1105)
 144. Piszkin, S., Levinsky, E.: Nonlinear lifting line theory for predicting stalling instabilities on wings of moderate aspect ratio, 1976, AD-A027 645
 145. Damiani, R., Wendt, F. F., Jonkman, J. M., Sicard, J.: A Vortex Step Method for Nonlinear Airfoil Polar Data as Implemented in KiteAeroDyn. In: *AIAA Scitech 2019 Forum*. (2019). doi: [10.2514/6.2019-0804](https://doi.org/10.2514/6.2019-0804)
 146. Ranneberg, M.: Viiflow—A New Inverse Viscous-Inviscid Interaction Method. *AIAA Journal* **57**(6), 2248–2253 (2019). doi: [10.2514/1.J058268](https://doi.org/10.2514/1.J058268)
 147. Breukels, J., Schmehl, R., Ockels, W.: Aeroelastic Simulation of Flexible Membrane Wings based on Multibody System Dynamics. In: Ahrens, U., Diehl, M., Schmehl, R. (eds.) *Airborne Wind Energy, Green Energy and Technology*, Chap. 16, pp. 287–305. Springer, Berlin Heidelberg (2013). doi: [10.1007/978-3-642-39965-7_16](https://doi.org/10.1007/978-3-642-39965-7_16)
 148. Chandra, R., Stemple, A. D., Chopra, I.: Thin-walled composite beams under bending, torsional, and extensional loads. *Journal of Aircraft* **27**(7), 619–626 (1990). doi: [10.2514/3.25331](https://doi.org/10.2514/3.25331)
 149. Eastep, F. E., Tischler, V. A., Venkayya, V. B., Khot, N. S.: Aeroelastic Tailoring of Composite Structures. *Journal of Aircraft* **36**(6), 1041–1047 (1999). doi: [10.2514/2.2546](https://doi.org/10.2514/2.2546)
 150. Guo, S., Cheng, W., Cui, D.: Aeroelastic Tailoring of Composite Wing Structures by Laminate Layup Optimization. *AIAA Journal* **44**(12), 3146–3150 (2007). doi: [10.2514/1.20166](https://doi.org/10.2514/1.20166)
 151. Kaw, A.: *Mechanics of Composite Materials*. 2nd ed. Mechanical Engineering Series. CRC Press, Boca Raton, FL (2005). doi: [10.1201/9781420058291](https://doi.org/10.1201/9781420058291)
 152. Kulfan, B. M.: Universal Parametric Geometry Representation Method. *Journal of Aircraft* **45**(1), 142–158 (2008). doi: [10.2514/1.29958](https://doi.org/10.2514/1.29958)

153. Straathof, M. H.: Shape Parameterization in Aircraft Design: A Novel Method, Based on B-Splines. (2012)
154. Mansfield, E., Sobey, A.: The Fibre Composite Helicopter Blade. *Aeronautical Quarterly* **30**(2), 413–449 (1979). doi: [10.1017/s0001925900008623](https://doi.org/10.1017/s0001925900008623)
155. Librescu, L., Song, O.: Thin-walled composite beams: Theory and application, vol. 131, pp. 1–633. (2006)
156. Hibbeler, R. C.: *Mechanics of materials*. Prentice Hall, Boston (2011)
157. Megson, T. H. G.: *Aircraft Structures for Engineering Students*, pp. i–ii. Elsevier (2013). doi: [10.1016/b978-0-08-096905-3.00065-6](https://doi.org/10.1016/b978-0-08-096905-3.00065-6)
158. Ferede, E., Abdalla, M.: Cross-sectional modelling of thin-walled composite beams. In: 55th AIAA/ASME/ASCE/AHS/ASC Structures, Structural Dynamics, and Materials Conference, vol. January, pp. 1–16, National Harbor, MD, USA, Jan 2014. doi: [10.2514/6.2014-0163](https://doi.org/10.2514/6.2014-0163)
159. Simo, J. C., Fox, D. D.: On a stress resultant geometrically exact shell model. Part I: Formulation and optimal parametrization. *Computer Methods in Applied Mechanics and Engineering* **72**(3), 267–304 (1989)
160. Soden, P.: Lamina properties, lay-up configurations and loading conditions for a range of fibre-reinforced composite laminates. *Composites Science and Technology* **58**(7), 1011–1022 (1998). doi: [10.1016/s0266-3538\(98\)00078-5](https://doi.org/10.1016/s0266-3538(98)00078-5)
161. Massa, J. C., Barbero, E. J.: A Strength of Materials Formulation for Thin Walled Composite Beams with Torsion. *Journal of Composite Materials* **32**(17), 1560–1594 (1998). doi: [10.1177/002199839803201702](https://doi.org/10.1177/002199839803201702)
162. Stemple, A. D., Lee, S. W.: A finite element model for composite beams undergoing large deflection with arbitrary cross-sectional warping. *International Journal for Numerical Methods in Engineering* **28**(9), 2143–2160 (1989). doi: [10.1002/nme.1620280911](https://doi.org/10.1002/nme.1620280911)
163. Saravanos, D., Varelis, D., Plagianakos, T., Chrysochoidis, N.: A shear beam finite element for the damping analysis of tubular laminated composite beams. *Journal of Sound and Vibration* **291**(3-5), 802–823 (2006). doi: [10.1016/j.jsv.2005.06.045](https://doi.org/10.1016/j.jsv.2005.06.045)
164. Kim, T., Hansen, A., Branner, K.: Development of an anisotropic beam finite element for composite wind turbine blades in multibody system. *Renewable Energy* **59**, 172–183 (2013). doi: [10.1016/j.renene.2013.03.033](https://doi.org/10.1016/j.renene.2013.03.033)
165. Yu, W., Hodges, D., Volovoi, V., Cesnik, C.: On Timoshenko-like modeling of initially curved and twisted composite beams. *International Journal of Solids and Structures* **39**(19), 5101–5121 (2002). doi: [10.1016/S0020-7683\(02\)00399-2](https://doi.org/10.1016/S0020-7683(02)00399-2)
166. Carrera, E., Giunta, G., Nali, P., Petrolo, M.: Refined beam elements with arbitrary cross-section geometries. *Computers & Structures* **88**(5-6), 283–293 (2010). doi: [10.1016/j.compstruc.2009.11.002](https://doi.org/10.1016/j.compstruc.2009.11.002)
167. Carrera, E., Petrolo, M.: Refined One-Dimensional Formulations for Laminated Structure Analysis. *AIAA Journal* **50**(1), 176–189 (2012). doi: [10.2514/1.J051219](https://doi.org/10.2514/1.J051219)
168. Przemieniecki, J. S.: *Theory of matrix structural analysis*. English. McGraw-Hill, New York SE - 468 pages illustrations 23 cm (1967)
169. Wempner, G.: Finite elements, finite rotations and small strains of flexible shells. *International Journal of Solids and Structures* **5**(2), 117–153 (1969). doi: [10.1016/0020-7683\(69\)90025-0](https://doi.org/10.1016/0020-7683(69)90025-0)
170. Battini, J.-M., Pacoste, C.: Co-rotational beam elements with warping effects in instability problems. *Computer Methods in Applied Mechanics and Engineering* **191**(17-18), 1755–1789 (2002). doi: [10.1016/S0045-7825\(01\)00352-8](https://doi.org/10.1016/S0045-7825(01)00352-8)
171. Anderson, D. G.: Iterative Procedures for Nonlinear Integral Equations. *Journal of the ACM* **12**(4), 547–560 (1965). doi: [10.1145/321296.321305](https://doi.org/10.1145/321296.321305)
172. Echeverri, P., Fricke, T., Homay, G., Tucker, N.: Energy Kite technical report: Selected Results From the Design, Development and Testing of Makani's Airborne Wind Turbines Part I, Makani, 2020
173. Bowyer, A.: Computing Dirichlet tessellations. *The Computer Journal* **24**(2), 162–166 (1981). doi: [10.1093/comjnl/24.2.162](https://doi.org/10.1093/comjnl/24.2.162)
174. Diaconu, C., Sato, M., Sekine, H.: Feasible region in general design space of lamination parameters for laminated composites. *AIAA Journal* **40**(3), 559–565 (2002). doi: [10.2514/3.15097](https://doi.org/10.2514/3.15097)
175. Hammer, V., Bendsoe, M., Lipton, R., Pedersen, P.: Parametrization in laminate design for optimal compliance. *International Journal of Solids and Structures* **34**(4), 415–434 (1997). doi: [10.1016/S0020-7683\(96\)00023-6](https://doi.org/10.1016/S0020-7683(96)00023-6)
176. Setoodeh, S., Abdalla, M., Gurdal, Z.: Approximate Feasible Regions for Lamination Parameters. AIAA Paper 2006-6973. In: Proceedings of 11th AIAA/ISSMO Multidisciplinary Analysis and Optimization Conference, Portsmouth, VA, USA, Sept 2006. doi: [10.2514/6.2006-6973](https://doi.org/10.2514/6.2006-6973)
177. Bloomfield, M., Diaconu, C., Weaver, P.: On feasible regions of lamination parameters for lay-up optimization of laminated composites. *Proceedings of the Royal Society A: Mathematical, Physical and Engineering Sciences* **465**(2104), 1123–1143 (2009). doi: [10.1098/rspa.2008.0380](https://doi.org/10.1098/rspa.2008.0380)
178. Tsai, S., Hahn, H.: *Introduction to composite materials*. English. Technomic Pub., Westport, CT (1980)
179. Kövesdi, P., Dreier, J.-E.: Drive train and method for drives having widely spaced operating points. German Patent WO/2015/032491, 2015

-
180. Bormann, A.: CyberKite, an Automated Ram Air Hybrid Kite-system. Presented at the High Altitude Wind Power Conference, Chico, CA, USA, Nov 6, 2009
 181. Stoll, W., Fischer, M., Bormann, A., Skutnik, S.: CyberKite. http://www.festo.com/net/SupportPortal/Files/42084/CyberKite_en.pdf. Accessed 02/28/2013
 182. Gambier, A.: Projekt OnKites : Untersuchung zu den Potentialen von Flugwindenergieanlagen (FWEA). Final Project Report, Fraunhofer Institute for Wind Energy and Energy System Technology IWES, Bremerhaven, Germany, 2014. 155 pp. doi: [10.2314/GBV:81573428X](https://doi.org/10.2314/GBV:81573428X)
 183. Bormann, A., Skutnik, S., Fischer, M.: HeiDAS UH - Flying with Superheated Steam. AIAA Paper 2007-7816. In: Proceedings of the 17th LTA Systems Technology Conference, AIAA, Belfast, Northern Ireland, Sept 18–20, 2007. doi: [10.2514/6.2007-7816](https://doi.org/10.2514/6.2007-7816)
 184. Bormann, A., Skutnik, A., Llado, J. M.: A new era in flying with hot air. Principles, performances and economics of insulated hot-air balloons and hot-airships. Presented at the 7th International Airship Convention, Friedrichshafen, Germany, Oct 9–11, 2008
 185. Hussen, K. van, Dietrich, E., Smelink, J., et al.: Study on Challenges in the commercialisation of airborne wind energy systems. ECORYS Report PP-05081-2016, European Commission, Brussels, 2018. doi: [10.2777/87591](https://doi.org/10.2777/87591)
 186. Faggiani, P.: Pumping Kites Wind Farm. M.Sc.Thesis, Delft University of Technology, Dec 19, 2014
 187. Rieck, B., Ranneberg, M., Candade, A., Bormann, A., Skutnik, S.: Comparison of Launching & Landing Approaches. In: Diehl, M., Leuthold, R., Schmehl, R. (eds.), The International Airborne Wind Energy Conference 2017: Book of Abstracts, Freiburg, Germany (2017)
 188. Prandtl, L.: Tragflügeltheorie. I. Mitteilung. Nachrichten von der Gesellschaft der Wissenschaften zu Göttingen, Mathematisch-Physikalische Klasse, 451–477 (1918)
 189. Horten, R., Selinger, P. F.: Nurflügel: Die Geschichte der Horten-Flugzeuge 1933-1960. Weishaupt (1987)
 190. Bormann, A., Skutnik, S., Gebhardt, C., Ranneberg, M.: Tethered wing system for wind energy use. US Patent US20150225080A1, 2013
 191. Aircraft Design Certification GmbH: AD&C Project EnerKite/ATALOG. <http://www.aircraftdc.de/en/projects/80-enerkite-atalog.html> (2017).

List of publications

Candade, A. A., Heinecke, F., Breipohl, F., et al.: Aero-structural design tailoring of composite AWE wings. In: Schmehl, R., Fagiano, L., Croce, A., Thoms, S. (eds.), 9th international Airborne Wind Energy Conference (AWEC 2021): Book of Abstracts, Milano, Italy, May 2022

Candade, A. A., Ranneberg, M., Schmehl, R.: Aero-structural Design of Composite Wings for Airborne Wind Energy Applications. *Journal of Physics: Conference Series* **1618**(3), 032016 (2020). doi: [10.1088/1742-6596/1618/3/032016](https://doi.org/10.1088/1742-6596/1618/3/032016)

Candade, A. A., Ranneberg, M., Schmehl, R.: Structural Analysis and Optimization of a Tethered Swept Wing for Airborne Wind Energy Generation. *Wind Energy* **23**(November 2019), we.2469 (2020). doi: [10.1002/we.2469](https://doi.org/10.1002/we.2469)

Candade, A. A., Ranneberg, M., Schmehl, R.: Development of a Toolchain for Aero-structural Design of Composite AWE Kites. In: Abstract from AWEC 2019: 8th international Airborne Wind Energy, Glasgow, United Kingdom, Oct 2019. doi: [10.4233/uuid:57fd203c-e069-11e9-9fcb-441ea15f7c9c](https://doi.org/10.4233/uuid:57fd203c-e069-11e9-9fcb-441ea15f7c9c)

Candade, A. A., Ranneberg, M., Schmehl, R.: Modelling, design and optimisation of composite structures for AWE wings. In: Wind Energy Science Conference, University College Cork, Cork, Ireland, June 2019

Candade, A. A., Ranneberg, M., Schmehl, R.: Structural Analysis and Optimization of an Airborne Wind Energy System. In: Diehl, M., Leuthold, R., Schmehl, R. (eds.), The International Airborne Wind Energy Conference 2017: Book of Abstracts, Freiburg, Germany (2017). doi: [10.4233/uuid:d801586f-063b-4c54-8e3a-db411a295344](https://doi.org/10.4233/uuid:d801586f-063b-4c54-8e3a-db411a295344)

Rieck, B., Ranneberg, M., Candade, A. A., Bormann, A., Skutnik, S.: Comparison of Launching & Landing Approaches. In: Diehl, M., Leuthold, R., Schmehl, R. (eds.), The International Airborne Wind Energy Conference 2017: Book of Abstracts, Freiburg, Germany (2017). doi: [10.4233/uuid:746d1263-9685-452a-b26b-d26b6a138c65](https://doi.org/10.4233/uuid:746d1263-9685-452a-b26b-d26b6a138c65)

Acknowledgments

*In the realm of AWE, I set sail,
On this journey, I'd unveil—
With ebbs and flows, my path was fraught,
Through sleepless nights and battles fought.
The journey was long, but I found my trajectory,
With patience, perseverance, and some bravery.—
In the end, I did emerge, stronger nay wiser?
A question to ponder, lies yet unanswered.*

This dissertation is the culmination of a few years of research and many more weekends of writing. It has been a wholesome learning experience, with its share of peaks and valleys, and it wasn't achieved in isolation. I greatly appreciate my committee for their time to evaluate my thesis and participate in my defence. I want to thank Gerard van Bussel for his guidance and wisdom, which have vastly improved this dissertation. I would also like to extend my gratitude to Roland Schmehl for all the advice. His dedication to the field of airborne wind energy is unparalleled. My thanks to Sylvia Willems for all the support and coordination through the years, in Delft and from Berlin.

My time in Delft, though short, was highly enlightening, thanks to my wonderful colleagues. Sebastian, Mikko, Bruce, Mark, Navi, Julia, Vinit, thanks for all the conversation and strategies to win President. I also thank the people from the AWESCO group for our multi-country exchanges and travels. Apart from the period at Delft, the majority of this journey was spent at EnerKite in Berlin. I want to thank the entire team, who have contributed both directly and indirectly to this thesis. My time at EnerKite has enabled me to see my research translated to solve real-world challenges, for which I am very grateful. The constant travelling between Berlin and Delft wouldn't have been possible without the support of my friends. Everyone at JvB, thanks for a *gezellig* getaway in Delft. I must thank my long list of flatmates for their patience while lending a sympathetic ear to the troubles of juggling an industrial PhD.

I would not be here today without the foundation from the giants whose shoulders I have grown up on—my family. Like an iceberg, this achievement is not only my own, but a product of their years of stabilising submerged wisdom. And finally, Prarth, my rock of support who has been by my side through all these years. For all the knowledge I could gain, there will always be much left to learn from you. Thank you for all your encouragement in the valleys, excitement at the peaks, and the courage to see this through.

*Ashwin Candade
Berlin, 2022*

Curriculum vitae

Ashwin Candade was born in 1990 in Chennai, India. He finished his schooling in 2007, following which he began his studies in Mechanical Engineering at SRM University. After obtaining his Bachelor's degree in 2011, he joined the National Trisonic Aerodynamic Facilities of the National Aerospace Laboratories (NAL) as a Project Assistant. He then moved to The Netherlands in 2013 to pursue a Master's degree in Aerospace Engineering at TU Delft. During his master's studies, he focused on aircraft design and optimisation methods. For his thesis, he experimentally investigated a tip-mounted tractor propeller's aeroacoustic and aerodynamic interaction effects.

In late December 2015, he commenced his PhD research at the Aerodynamics, Wind Energy, Flight Performance and Propulsion (AWEP) Department at TU Delft. Within the framework of the Marie Skłodowska-Curie doctoral network Airborne Wind Energy System Modelling, Control and Optimisation (AWESCO), this research was performed as an industrial researcher located at EnerKite, Berlin until 2018, and continued as a PhD researcher based at TU Delft. Since 2020, he has been employed at EnerKite, where he works on designing and optimising composite wings for airborne wind energy (AWE).

